MULTI-HAZARD PERFORMANCE CRITERIA FOR NON-DUCTILE REINFORCED CONCRETE FRAME BUILDINGS RETROFITTED WITH AN FRP COLUMN JACKETING SYSTEM

A Dissertation
Presented to
The Academic Faculty

by

Jiuk Shin

In Partial Fulfillment
of the Requirements for the Degree
Doctor of Philosophy in the
School of Civil and Environmental Engineering

Georgia Institute of Technology
August 2017

MULTI-HAZARD PERFORMANCE CRITERIA FOR NON-DUCTILE REINFORCED CONCRETE FRAME BUILDINGS RETROFITTED WITH AN FRP COLUMN JACKETING SYSTEM

Approved by:

Dr. David W. Scott, Advisor
School of Civil and Environmental
Engineering
Georgia Institute of Technology

Dr. Reginald DesRoches
Department of Civil and Environmental
Engineering
Rice University

Dr. Chuang-Sheng Yang
School of Civil and Environmental
Engineering
Georgia Institute of Technology

Dr. Lauren K. Stewart, Co-Advisor
School of Civil and Environmental
Engineering
Georgia Institute of Technology

Dr. Seung-Kyum Choi
The George W. Woodruff School of
Mechanical Engineering
Georgia Institute of Technology

Date Approved: [July 17, 2017]

To my lovely wife Hwayeong, and my sweet daughter Jimin

ACKNOWLEDGEMENTS

I would like to express my deepest appreciation to my advisors, Dr. David W. Scott and Dr. Lauren K. Stewart, for their support, patience, direction, and encouragement. I will always remember what Yoda said: "*Do or do not, there is no try.*" I am extremely grateful to my thesis committee members, Dr. Reginald DesRoches, Dr. Chuang-Sheng (Walter) Yang, and Dr. Seung-Kyum Choi, for their time and valuable comments.

This research would not have been possible without the help of my colleagues. I would like to give special thanks to Timothy R. Wright, who helped me complete full-scale dynamic testing. I would also like to extend my gratitude to my research group members, Seo-Hun Lee, Javaid Anwar, and Genevieve Pezzola, for sharing encouragement and many ideas. Special thanks also go to Walter, who gave me valuable advice on research, career, and life.

I would like to extend my sincere thanks to Dr. Kihak Lee, Dr. Seong-Hoon Jeong, and Dr. JunHee Kim, who motivated me to study abroad in the US. I must also thank one of my best friends, Young-Jun Lim who has supported me over the last four years. I would like to thank all members of Georgia Tech Korean Student Association at Civil and Environmental Engineering, especially Jong-Su Jeon and Sung-Hu Kim.

I am deeply indebted to my parents, Kyung-Ja Kang and Young-Nam Shin, and my brother, Seoung-Wook Shin, for their unwavering support and love. I hope I made them proud. I would also like to extend my gratitude to my parents-in-law, Soon-Ja Baek and Joon-Sik Choi.

Finally, I would like to express my deepest gratitude to Hwayeong Choi, who is my wife, best friend, assistant, and the mother of my child. She is the strongest person I have ever met. For

last four years, when I always said to her, *"I want you to be happy,"* she replied, *"I am already happy."* Now, I am really happy because she is still with me and is the mother of my lovely daughter, Ellie Shin. I could not have done this work without her; I hope it is deserving of her sacrifices.

TABLE OF CONTENTS

LIST OF TABLES

LIST OF FIGURES

xiv

xvi

LIST OF SYMBOLS

$\bar{a}$	Activation value
b	Column width
$\bar{b}$	Threshold or bias value
CR_{min}	Minimum value of confinement ratio
D	Damage demand (index)
D_B	Blast energy-based damage demand
D_{Bi}	Blast energy-based damage limit at i performance level
D_i	Local damage index at location i
D_M	Multi-hazard energy-based damage demand
D_{Mi}	Multi-hazard energy-based damage limit at i performance level
D_n	Damage parameter at n^{th} step
D_S	Seismic energy-based damage demand
D_{Si}	Seismic energy-based damage limit at i performance level
D_{S_i}	Seismic energy-based damage demand at i^{th} story
D_{S_T}	Total seismic damage demand in entire structural model
D_{story}	Each story damage index
D_y	Y-translational degree-of-freedom in the global coordinate system
DCF_i	Drift concentration factor in the ith story
DL	Dead load
dE	Incrementally absorbed hysteretic energy
E	Elastic modulus
E_a	Elastic modulus in a-principal axis

E_i	Energy absorbed at location i
E_{BD}	Energy dissipation of the column element
E_{SD_i}	Hysteretic energy dissipation at i^{th} story for a given seismic load
E_{SD_T}	Total hysteretic energy dissipation for a given seismic load
e	Exponent
$F(t)$	Shaker force in terms of time
F_{u_col}	Yielding lateral force of RC columns
F_{y_col}	Ultimate lateral force of RC columns
$f(\bullet)$	Transfer or activation function
f_c'	Unconfined concrete strength
f_{cc}'	Peak confined concrete strength
f_{cu}'	Ultimate confined concrete strength
f_g	Unconfined compressive strength of non-shrink grout material
f_{g_max}	Maximum training point of compressive strength of grout material
f_{g_min}	Minimum training point of compressive strength of grout material
f_{g_n}	Nominal training point of compressive strength of grout material
f_h	Lateral confining pressure for existing transverse reinforcement detailing
f_{ju}	Ultimate tensile strength of FRP jacket
f_{ju_max}	Maximum training point of ultimate jacket strength
f_{ju_min}	Minimum training point of ultimate jacket strength
f_{ju_n}	Nominal training point of ultimate jacket strength
f_u	Ultimate stress of steel materials
f_y	Yeilding stress of steel materials
G	Shear modulus

G_{ab}	Shear modulus in a- and b-principal axes
G_s	Bond shear modulus
g	Gravity acceleration
H	Height of structure
h	Column depth
h_{dmg}	Damage curve exponential coefficient
h_i	i^{th} story height
ID	Inner diameter of fiber-reinforced polymer column jacketing system
$ID_{\_min}$	Minimum training point of column inner diameter
$ID_{\_max}$	Maximum training point of column inner diameter
$ID_{\_n}$	Nominal training point of column inner diameter
LL	Live load
l_1	Bottom and top regions in fiber-reinforced polymer-retrofitted column
l_2	Middle region in FRP-retrofitted column
M^*	Mass of the equivalent single-degree-of-freedom system
M_i	i^{th} story mass
$\tilde{M}_{ij}$	Performance (or damage) zone in i^{th} row and j^{th} column
M_w	Moment magnitude
MCR_{mean}	Mean value of modified confinement ratio
MCR_{min}	Minimum value of modified confinement ratio
m	Control weighing factor for the component
m_s	Mass of the linear shaker
n	Incremental step
P	Hydrostatic pressure
Q	Quantities in multiple-degree-of-freedom system

Q^*	Quantities in single-degree-of-freedom system
Q_y	Yield strength
PL_{Bi}	Blast performance at i level
PL_{Mi}	Multi-hazard performance at i level
PL_{Si}	Seismic performance at i level
R_x and R_z	X- and Z-rotational degrees-of-freedom in the global coordinate system
R_D	Standoff distance
R_H	Standoff height
R_μ	Ductility reduction factor
RL	Retrofit location
r	Radius of FRP jacket
S	1/4 scale factor
S_a	Spectral acceleration
S_{ae}	Elastic spectral acceleration
S_{au}	Ultimate spectral acceleration
S_{ay}	Yielding spectral acceleration
S_{a_max}	Maximum training point for peak spectral acceleration
S_{a_min}	Minimum training point for peak spectral acceleration
S_{a_n}	Nominal training point for peak spectral acceleration
S_{a_peak}	Peak spectral acceleration
S_{DS}	Design short-period response acceleration
S_d	Spectral displacement
S_{dm}	Spectral displacement demand

S_{du}	Ultimate spectral displacement
S_{dy}	Yielding spectral displacement
S_{MS}	Maximum considered earthquake short-period response acceleration
S_{M1}	Maximum considered earthquake spectral response acceleration at a period of 1.0 second
s	Spacing of column ties
$\tilde{s}$	Bond slip displacement
$\tilde{s}_{max}$	Maximum elastic slip
T	Period
T^*	Effective elastic period of single-degree-of-freedom system
$\tilde{T}$	Finite element-based demand (target value)
T_o	Transition period
t_j	Fiber-reinforced polymer jacket thickness
t_{j_max}	Maximum value of jacket thickness
t_{j_min}	Minimum value of jacket thickness
t_{j_n}	Nominal value of jacket thickness
V^*	Base shear in single-degree-of-freedom system
V_a	Shear strength by axial loading
V_{base}	Base shear of structure
V_c	Shear strength by concrete
V_{if}	Ideal flexural strength given by the sectional analysis
V_s	Shear strength by existing transverse reinforcement
V_u	Ultimate base shear
V_y	Yielding base shear
V_y^*	Yielding force in single-degree-of-freedom system

W_i	Weighing factor of element i
W_{TNT}	Equivalent mass of TNT
w_{ij}	Weight coefficient
w_1	Weight of steel rails distributed over the second floor
w_2	Weight of steel rails distributed over the third floor
x_i	Input from the earlier layer of neuron
x_j	Output from the next layer of neuron connecting with the ith neuron
$\ddot{x}_s(t)$	Absolute acceleration of the shaker in terms of time
$\tilde{Y}$	Fast running model-based demand (calculated value)
y_i	Output value in the artificial neural network
Z_s	Scaled distance for the quarter-scale
α_s	Parameter to control a dynamic increase factor for steel material
β	Coefficient for cyclic loading effect
Γ	Modal participation factor
$\Delta_{\text{As-built}}$	Inter-story drift of as-built frame
Δ_i	i^{th} inter-story drift
Δ_{iv} and Δ_{jv}	Vertical displacement measured from two opposite sides of a column surface
$\Delta_{\text{As-built}}$	Maximum deformation
$\Delta_{\text{Retrofitted}}$	Inter-story drift of as-built frame
$\Delta\tilde{s}_p$	Increment of plastic slip displacement
Δ_u	Ultimate deformation capacity under static loading
$\Delta\sigma_m$	Maximum shear failure surface
$\Delta\sigma_r$	Residual shear failure surface
$\Delta\sigma_y$	Yield shear failure surface

δ_m	Displacement demand of multiple-degree-of-freedom system
δ_{mi}	Displacement demand at the ith story
$\delta_{peak\_as\text{-}built}$	Peak blast displacement for as-built finite element model
$\delta_{peak\_retrofitted}$	Peak blast displacement for retrofitted finite element model
$\delta_{residual\_as\text{-}built}$	Residual blast displacement for as-built finite element model
$\delta_{residual\_retrofitted}$	Residual blast displacement for retrofitted finite element model
δ_{roof}	Roof story displacement
δ_u	Ultimate displacement
δ_{u_col}	Ultimate displacement for RC columns
δ_y	Yielding displacement
δ_{y_col}	Yielding displacement for RC columns
δ^*	Displacement in single-degree-of-freedom system
δ_y^*	Yielding displacement in single-degree-of-freedom system
$\dot{\varepsilon}$	Strain rate
ε_{cu}	Ultimate concrete axial strain
ε_{ju}	Ultimate strain for FRP jacket
$\dot{\varepsilon}_{sc}$	30×10^{-6} s^{-1} for static strain rate in compression
$\dot{\varepsilon}_{st}$	10^{-6} s^{-1} for static strain rate in tension
$\eta(\lambda)$	Damage function in terms of effective plastic strain
$\theta_{As\text{-}built}$	Maximum normalized column rotation of the as-built frame
θ_{col}	Column hinge rotation
$\theta_{Retrofitted}$	Maximum normalized column rotation of the retrofitted frame
λ	Effective plastic strain
λ_m	Effective plastic strain corresponding to $\Delta\sigma_m$
μ	Displacement ductility demand

μ_0	Ductility of as-built column
μ_{blast}	Blast displacement ductility demand
μ_{target}	Target ductility of column
ν	Poisson's ratio
ν_{ab}	Poisson's ratio in a- and b-principal axes
σ	Axial stress
σ_R	Confining pressure
τ	Bond stress
τ_{max}	Maximum bond stress
ϕ_{f}	Flexural strength reduction factor of 0.9
ϕ_{ij}	j^{th} normalized mode vector at the ith story
ϕ_{n}	Mode shape vector in the roof
ϕ_{v}	Shear strength reduction factor of 0.85
ϖ	Parameter to control shear dilation

LIST OF ABBREVIATIONS

ACI	American Concrete Institute
ADRS	Acceleration-displacement response spectrum
ALE	Arbitrary Lagrangian-Eulerian
ANN	Artificial neural network
ASCE	American Society of Civil Engineers
ATC	Applied Technology Council
CFRP	Carbon fiber-reinforced polymer
CP	Collapse prevention
CR	Confinement ratio
CSM	Capacity spectrum method
CSP	Concrete surface profile
DCF	Drift concentration factor
DIF	Dynamic increase factor
DOF	Degrees-of-freedom
EC	El Centro
EMS	Eccentric mass shaker
FE	Finite element
FEMA	Federal Emergency Management Agency
FRP	Fiber-reinforced polymer
FRM	Fast running model
FSI	Fluid-structure interface
GLD	Gravity load designed

ICRI	International Concrete Repair Institute
IDR	Inter-story drift ratio
IO	Immediate occupancy
K&C	Karagozian and Case
KCC	Karagozian and Case concrete
LBE	Load Blast Enhanced
LMA	Levenberg-Marquardt Algorithm
LOP	Level of protection
LS	Life safety
MCE	Maximum considered earthquake
MCR	Modified confinement ratio
MDOF	Multi-degree-of-freedom
MM-ALE	Multi-Material Arbitrary Lagrangian-Eulerian
MSE	Mean squared error
NEES	The National Science Foundation George E. Brown Jr. Network for Earthquake Engineering Simulation
Q-Q	Quantile-Quantile
RC	Reinforced concrete
SCWB	Strong column-weak beam
SDC	Seismic design category
SDOF	Single-degree-of-freedom
SP	Sinusoidal pulse
WCSB	Weak column-strong beam

SUMMARY

Many existing reinforced concrete building structures that were designed in accordance with pre-1971 codes have non-seismically detailed columns and beam-column joints. These seismically-deficient details can lead to premature failure under natural and man-made disasters (e.g., earthquakes and blast events). Some premature failures resulting from these events could potentially be prevented by a fiber-reinforced polymer column jacketing system, which provides additional confining pressure and enhances both the flexural capacity and ductility of existing columns. These retrofits can be used to ensure that existing structures have adequate seismic and blast performance levels as specified in current design codes. However, code-defined performance criteria are composed of different structural demand limits depending on the loading type. These different demand limits may lead to retrofit designs that are insufficient for multi-hazard loading or are overly conservative and therefore not cost-effective. The objective of this dissertation is to propose a multi-hazard performance criteria with energy-based damage limits for non-ductile RC frames retrofitted with fiber-reinforced polymer jacketing systems.

A series of full-scale dynamic experiments were performed on a non-ductile reinforced concrete test frame that had been retrofitted with a fiber-reinforced polymer jacketing system in the first story columns to measure realistic dynamic behavior and quantify the effectiveness of the retrofit system. The measured dynamic responses were utilized to propose and verify a numerical modeling methodology that represents a more realistic assessment of bond-slip effects between reinforcing bars and surrounding concrete. Additionally, blast responses on the frame were considered using finite element models, which included bond-slip effects between

reinforcing bars and surrounding concrete as well as an advanced blast load modeling technique. The blast modeling method was verified by comparing the simulated response developed in the present work with experimental responses from previous research. The finite element model, verified using the seismic and blast experimental results, was then incorporated into the development of fast running models using an artificial neural network. The fast running models provided reliable structural demands for the non-ductile concrete frame that had been retrofitted with fiber-reinforced polymer column jacketing systems (i.e., inter-story drift ratio and displacement ductility demands related to code-defined limits, and seismic and blast energy-based damage demands related to energy-based damage limits). Finally, a multi-hazard performance criteria that integrated the energy-based damage demands was derived using the fast running models in order to determine seismic and blast damage limits that correspond to code-defined performance levels. Based on the combined damage limits, this study developed four-by-four performance evaluation matrices for the as-built and retrofitted conditions. These performance matrices can be used for the performance evaluation of non-ductile reinforced concrete building structures and the selection of retrofit schemes to ensure a desired target performance level under seismic and blast loading.

CHAPTER 1. INTRODUCTION

1.1 Problem Description and Motivation

Existing reinforced concrete (RC) building structures that were constructed in the 1950s-1970s were typically only designed for gravity loads (e.g., the load combination $1.4DL + 1.7LL$, where DL = dead load and LL = live load), in accordance with the editions of the American Concrete Institute (ACI) 318 design code published before 1971 (hereafter referred to as "pre-1971 ACI codes"). Since the pre-1971 ACI codes have no specific provisions for seismic design, many RC building structures designed and constructed with non-seismically detailed columns and beam-column joints are still in service today. These seismically deficient details result in non-ductile behavior of the existing building structures [Aycardi et al. 1994, Bracci et al. 1995a, El-Attar et al. 1997, Corley et al. 1998, and Osteraas 2006]. Post-disaster building damage reconnaissance [Corley et al. 1996, Osteraas et al. 1996, Aschheim et al. 2000, and Sezen et al. 2000] has demonstrated the ways in which non-ductile RC building structures are potentially vulnerable to to natural and man-made disasters, often referred to as "multi-hazard events."

Previous earthquakes have demonstrated the seismic vulnerability of non-ductile RC frame buildings. For example, the 1999 Kocaeli earthquake in Turkey injured or killed more than 17,000 people, and damaged or collapsed approximately 18,000 buildings [Aschheim et al. 2000]. Among them, the RC frame buildings commonly suffered shear and lap-splice failure in the columns (Figure 1.1(a)), significant damage in beam-column joints (Figure 1.1(b)), and soft-story mechanisms in lower stories (Figure 1.1(c)). Additionally, the 1994 Northridge earthquake in California caused significant damage to non-ductile RC frame buildings built prior to the

1970s, mainly due to brittle shear failure in RC columns. However, RC building structures designed according to modern seismic codes (i.e., ductile RC frame buildings) resisted the earthquake without significant damage [Osteraas 1996].

(a) (b) (c)
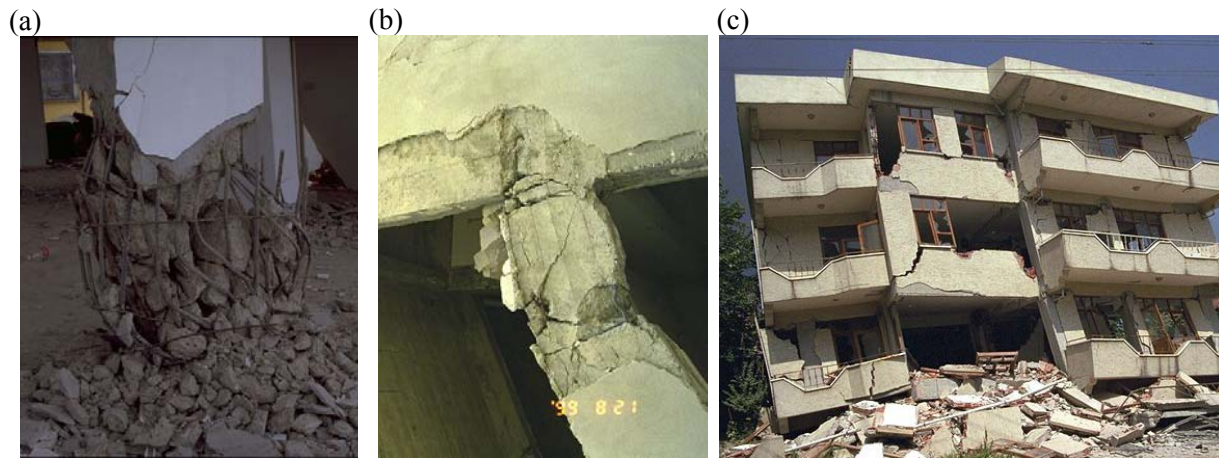
Figure 1.1. Damage of non-ductile RC frame buildings subjected to the Kocaeli earthquake: (a) lap-splice failure in RC column; (b) damage in beam-column joint; (c) soft-story mechanism [Earthquake Engineering Online Archive, NISEE E-Library]

The Alfred P. Murrah Federal Building (hereafter referred to as "the Murrah Building") in Oklahoma City, Oklahoma was a nine-story, non-ductile RC building structure (i.e., non-seismic detailing) constructed in the 1970s. On April 19, 1995, a bomb was detonated on the north side of the Murrah Building, which led to major loss of life and injuries, significant structural damage, and partial collapse of the building itself. The bomb also inflicted varying amounts of blast damage on other buildings located nearby. The Federal Emergency Management Agency (FEMA) was tasked with investigating the blast damage and failure mechanism of the Murrah Building. According to the FEMA-277 report [Corley et al. 1996], major structural damage and building collapse occurred at the north side of the building, which directly faced the blast effects. The direct effects of blast abruptly failed three columns in shear. The column shear failure triggered the subsequent progressive collapse. In order to mitigate the

2

column damage in the immediate area where a blast occurs, Corley et al. [1996 & 1998] recommended the installation of column jacketing systems for existing building structures.

To prevent the premature failure of non-ductile RC frames under seismic and blast loads, a number of retrofit techniques are available. Column retrofit systems have been developed using a range of materials and fabrication techniques, including concrete, steel, fiber reinforced polymer (FRP) wraps, and prefabricated FRP shapes. Steel jackets on RC columns can result in the addition of significant weight, increased construction time, and potential future corrosion issues [Lan et al. 1998, and Teng et al. 2003]. Given the problems associated with the use of steel in these types of applications, FRP column jacketing systems have been proposed as an alternative to improve the seismic performance of RC columns. In addition, FRP column jacketing systems have been used to enhance the blast resistance of RC building structures and prevent building collapse [Crawford et al. 1995 & 1997, Corley et al. 2004, Malvar et al. 2007, and Crawford 2011]. Thus, to retrofit seismically vulnerable columns in a non-ductile RC frame, this study selected a prefabricated FRP jacketing system from the various RC column jacketing techniques.

The current state of practice in the retrofit of non-ductile RC frames under seismic and blast events involves the separate determination of critical limit states for each type of loading. This is because current design codes for seismic and blast loads such as FEMA-356 [2000] and American Society of Civil Engineers (ASCE) 59-11 [2011] provide performance criteria with different demand parameters, such as drift-based performance criteria for seismic loads and displacement ductility-based performance criteria for blast loads. When existing building structures are required to exhibit adequate seismic and blast performance, the conflicts between performance criteria in seismic and blast design codes may lead to retrofit designs that are

insufficient for multi-hazard loading or are overly conservative and therefore not cost-effective. For this reason, multi-hazard performance criteria with identical demand parameters are needed. Generating these performance criteria will allow structural engineers to estimate current damage levels and develop a retrofit scheme satisfying a target performance level for seismic and blast loading.

1.2 Research Objective

The main objective of this research is to propose multi-hazard performance criteria for non-ductile RC frames that have been retrofitted with an FRP column jacketing system and are subjected to seismic and blast loads. To derive the multi-hazard performance criteria, energy-based damage demands corresponding to existing code-defined limits were determined, and the seismic and blast damage limits were combined. This research program involved the following tasks:

- Perform a series of seismic dynamic tests on full-scale two-story non-ductile RC test frames, designed for only gravity loads, in non-retrofitted (referred to as "as-built") and retrofitted configurations in order to investigate the dynamic responses under seismic loading. By comparing the dynamic responses between the as-built and retrofitted test frames, the effectiveness of the retrofit system was quantified in terms of damage distribution and reduction in drift and column rotation.

- Propose a numerical modeling methodology for seismic loads. Finite element (FE) models were developed using the well known FE computer program LS-DYNA

[LSTC 2013] for both the as-built and retrofitted configurations, and verified with the full-scale experimental responses.

- Develop FE models that incorporate a numerical modeling methodology for blast loads. The numerical modeling methodology was verified in previous experiments [Woodson and Baylot 1999] and was implemented to the as-built and retrofitted FE frame models in order to investigate the blast response of each.

- Generate fast running models for seismic and blast loads based on numerical datasets obtained from FE simulations using an artificial neural network to predict energy-based damage demands. By using the fast running models, a combining methodology between seismic and blast energy-based damage limits was proposed, and multi-hazard performance criteria was derived.

1.3 Dissertation Outline

The dissertation is organized into the following chapters as follows:

Chapter 2 presents a literature review of critical background information on the seismic and blast responses of existing non-ductile RC frames, seismic and blast retrofits using FRP materials, seismic testing methodologies, and existing performance criteria for blast and seismic loads.

Chapter 3 examines the results of a full-scale seismic load test of an RC building frame that was retrofitted with an FRP column jacketing system. In addition, the effectiveness of the

FRP column jacketing system is investigated by comparing the experimental dynamic responses of the as-built and retrofitted test frames.

Chapter 4 presents the process used to develop FE models for the as-built and retrofitted test frames for seismic loads. To reproduce the measured dynamic responses using the FE frame models, bond-slip effects between surrounding concrete and steel reinforcing bars, characterized based on the experimental responses in bond-slip zones, applied to the FE frame models, which were then verified using the full-scale experimental responses in the as-built and retrofitted configurations.

Chapter 5 presents the process used to develop FE models for blast loads. To verify the modeling development process, results from a prior experimental study performed by Woodson and Baylot [1999] were compared with the simulated results from the FE column model utilizing the proposed development process. After the modeling process was verified, the FE frame models described in Chapter 4 were analyzed under blast loads.

Chapter 6 describes the development of fast running models using artificial neural networks to predict the structural demands (e.g., inter-story drift ratio and displacement ductility demands for current code-defined performance criteria, and energy-based damage demands) for the non-ductile concrete frame subjected to seismic and blast loads. The fast running models were trained based on numerical datasets with varying loading, geometric and material parameters, which were computed using the FE frame models described in Chapters 4 and 5. A variety of test cases were used to verify the fast running models.

Chapter 7 proposes a combined seismic and blast damage criteria using the fast running models developed in Chapter 6, which leads to the development of a multi-hazard performance

criteria for the as-built and retrofitted non-ductile RC frames investigated in this study. In addition, parametric studies for geometric and material parameters associated with the FRP column jacketing system were carried out to demonstrate the effects of the parameters, and the retrofit scheme satisfied with a desired target performance level was established for a given non-ductile RC frame.

Chapter 8 presents the conclusions found in the present research, and recommendations for future study.

CHAPTER 2. LITERATURE REVIEW

2.1 Non-Ductile RC Frame Building Design

Figure 2.1 shows typical detailing for RC columns designed according to pre-1971 ACI codes compared to RC columns designed according to modern design codes (e.g., ACI 318-14 [2014]). The non-seismically detailed column includes the following design features: small-diameter transverse reinforcements; large spacing between column ties (approximately equal to the minimum column dimension); 90º L-shaped corner hooks for rectangular column ties; short lap-splices without an additional confinement above each story level; and locations of lap-splices where the column moments are maximized [Bracci et al. 1995a, Sause et al. 2004, Jeon et al. 2015, and Wright 2015]. The small diameter and large spacing of column ties lead to less buckling resistance of the longitudinal reinforcement, poor concrete confinement, and low shear capacity in the RC columns. Additionally, once the concrete cover is spalled, the 90º L-shaped corner hook provides neither confining pressure to the concrete core nor buckling restraint to longitudinal reinforcements, as illustrated in Figure 2.2 [Sause et al. 2004]. The inadequate column lap-splices result in bond slip failure. Bond slip failure along lap-splices manifests in vertical cracks on the column faces adjacent to the failed bars. The concrete cracks cause a sudden loss of confinement in the lap-splice regions and rapidly reduce the bond strength between the concrete and lap-splices [Haroun et al. 2005, and Luccioni et al. 2005]. Thus, columns with short lap-splices suffer premature failure before reaching expected flexural capacities. Such non-ductile behavior of existing RC columns has been demonstrated in previous experimental studies. For example, Aycardi et al. [1992] tested non-ductile RC columns with and without column lap-splices located in potential plastic hinge zones. When compared to the

8

column specimens without the lap-splices (i.e., continuous longitudinal bars), the RC columns with inadequate lap-splices, which are composed of shorter lengths than those from modern seismic code and are located at the ends of the columns where moments are maximized, showed poor energy dissipation. This is attributed to the effect of bond slip between the concrete and lap-splice bars. Lynn et al. [1996] tested eight full-scale columns that were designed in accordance with pre-1971 ACI codes. The column specimens demonstrated a limited flexural ductility followed by the loss of lateral resistance due to shear failure. To identify the main parameters contributing to shear failure and gravity load collapse of RC columns, Sezen [2002] tested full-scale RC columns with insufficient transverse reinforcement under cyclic lateral loads with low and high axial loading conditions in double bending. Column specimens under high axial loads lost lateral and vertical load carrying capacities (i.e., shear and axial failure) at the low ductility level, estimated as the ductility of 1.5 to 2.0 for the non-ductile RC columns.
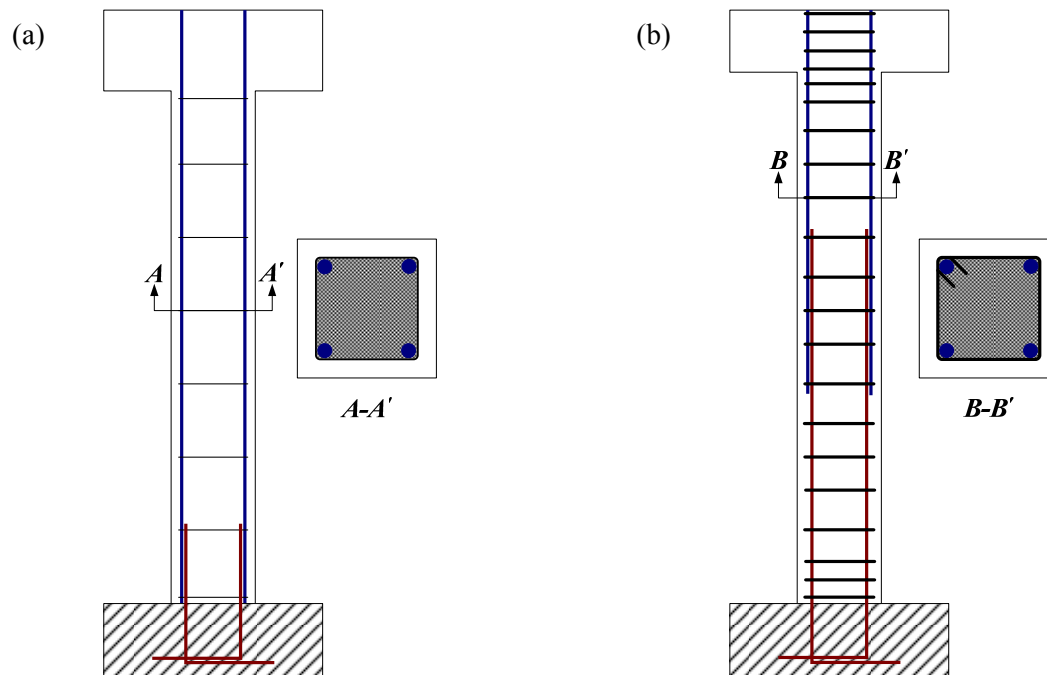
Figure 2.1. Typical RC column details for pre-1971 ACI codes and current design codes: (a) non-seismically detailed column; (b) seismically detailed column

9
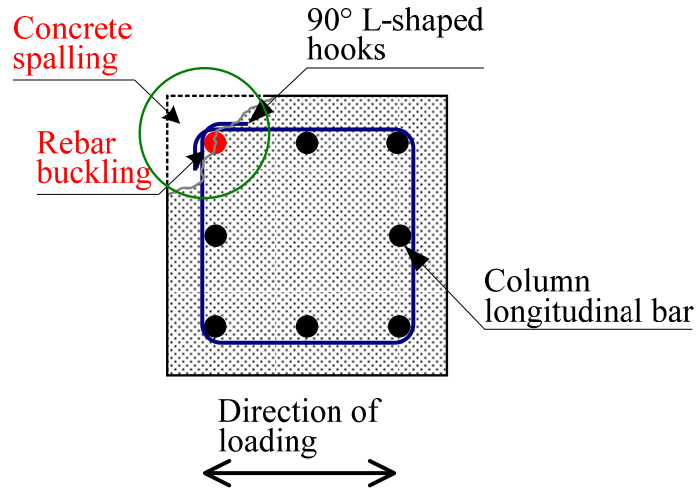
Figure 2.2. Failure of a non-ductile RC column with 90 degree L-shaped column ties

Figure 2.3 illustrates the typical details of exterior and interior RC beam-column joints designed according to pre-1971 ACI codes, as well as RC beam-column joints designed according to modern design codes (e.g., ACI 318-14 [2014]). Unlike the seismically detailed beam-column joints (Figure 2.3(b)), the non-seismically detailed exterior beam-column joints have no transverse reinforcement in panel zones, which leads to inadequate shear resistance in the beam-column joints. Additionally, the non-seismically exterior and interior beam-column joints are designed with the straight anchorage of positive (bottom) beam reinforcement and discontinuous positive (bottom) beam reinforcement, respectively [Pessiki et al. 1990, Beres et al. 1996, and Hakuto et al. 2000]. These anchorage details in the beam-column joint result in the pull-out of bottom reinforcement as shown in Figure 2.4 [Wright 2015]. In addition to poor reinforcement details, the columns are weaker than the adjacent beams (i.e., weak column-strong beam, hereafter referred to as "WCSB"), which can potentially lead to a soft story or column sidesway mechanism. Aycardi et al. [1992] tested non-seismically detailed exterior and interior beam-column joints, such as column lap splices in potential plastic hinge zones, a lack of transverse reinforcement in the beam-column joints, and inappropriate anchorage of positive

beam reinforcement. They concluded that these seismic deficiencies led to an undesirable WCSB mechanism. Moreover, to identify the failure mechanisms of beam-column joints designed with non-ductile reinforcement details, El-Amoury [2004] tested shear and bond-deficient beam-column joint specimens. These specimens suffered combined joint shear and bond-slip failure (i.e., pull-out failure) with severe strength and stiffness degradations at low levels of ductility. These previous experimental studies indicate that inadequate detailing of RC columns and beam-column joints as specified in the pre-1971 ACI codes could result in the premature failure of building structures under seismic loads.

(a)

Interior beam-column joint

Exterior beam-column joint

(b)

Interior beam-column joint

Exterior beam-column joint
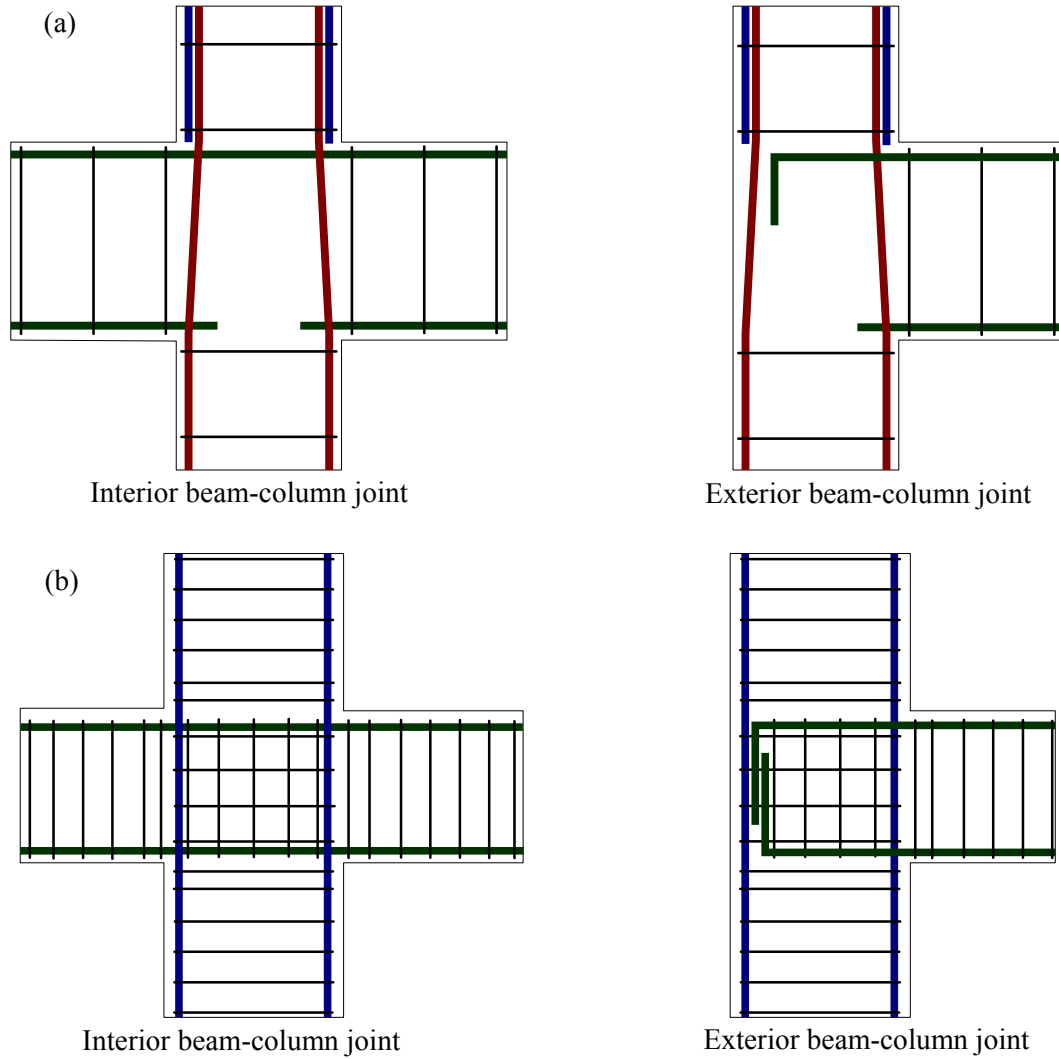
Figure 2.3. Typical RC beam-column joint details for pre-1971 ACI codes and current design codes: (a) non-seismically detailed beam-column joints; (b) seismically detailed beam-column joints
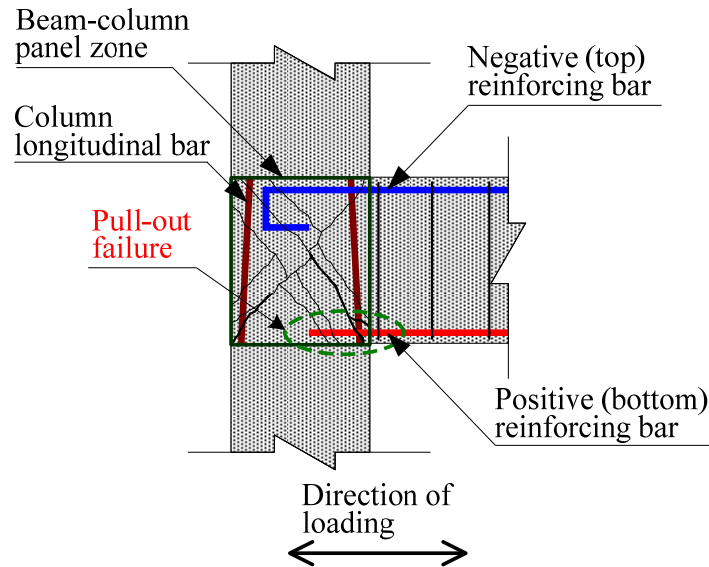
Figure 2.4. Failure for a typical non-ductile beam-column joint

2.2 Seismic Response of RC Frames: Soft Story Mechanism

Non-ductile RC building structures are typically dominated by the soft-story mechanism due to seismically deficient detailing in the columns and beam-column joints. El-Attar et al [1991] conducted a shaking table test for a 1/8 scale three-story lightly RC building under seismic loads. They demonstrated that gravity load designed (GLD) RC frames developed plastic hinges in the first story columns and exhibited a soft-story failure mechanism. Bracci et al. [1995a] tested a three-story 1:3 reduced-scale model of a GLD RC frame subjected to simulated earthquakes which represented low to moderate earthquake zones. To determine the damage state in individual elements, an analysis was performed using a deformation and energy-based damage model proposed by Park and Ang [1985]. The results of the damage analysis showed the most severe damage was concentrated in the interior columns in the first story, and the damage in interior columns triggered progressive failure in the structures.

Typical building collapse mechanisms are shown in Figure 2.5. Figure 2.5(a) illustrates a typical soft-story failure mechanism (i.e., column sidesway mechanism) that is common for the WCSB system. The soft-story mechanism can frequently lead to severe damage in the lower stories, while the upper stories remain undamaged. In other words, the drift of the structure can be more prevalent on the lower stories (i.e., non-uniform story drift distribution), with high column rotations [Aycardi et al. 1994, Bracci et al. 1995a, Beres et al. 1996, Kurama 1996, and Priestley 1997]. Current design codes require a strong column-weak beam (SCWB) system for RC moment-resisting frames to ensure ductile behavior of the structure [Aycardi et al. 1994, El-Attar et al. 1997, Priestley 1997, and Hakuto et al. 2000]. Such building structures can develop a beam sidesway mechanism or a mixed sidesway mechanism, as shown in Figure 2.5(b) and Figure 2.5(c), respectively. These sidesway mechanisms tend to distribute plastic hinges in the beams along the entire height or around 2/3 of the height of the structure, mitigating the damage being concentrated in the lower story columns.
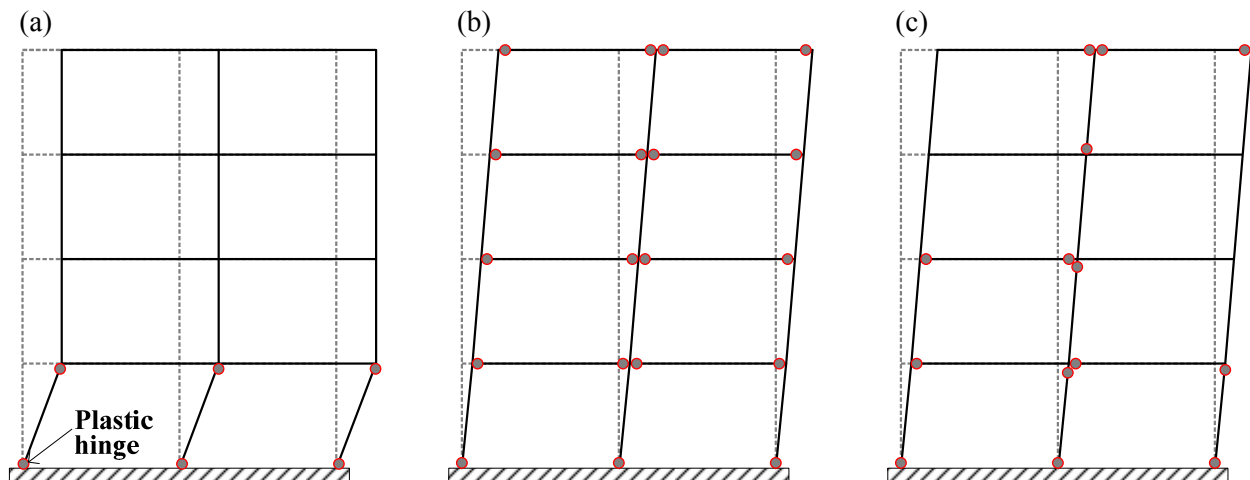
Figure 2.5. Collapse mechanisms of building structure: (a) soft-story mechanism (column sidesway mechanism); (b) beam sidesway mechanism; (c) mixed sidesway mechanism [after Priestley 1997]

2.3 Blast Response: Non-Ductile RC Column

Non-ductile RC columns are significantly vulnerable to blast loads due to inadequate column detailing (Figure 2.1(a)). The inadequate detailing can result in several brittle failure modes for non-ductile RC columns, including: (1) diagonal shear failure, (2) axial failure, and (3) direct shear failure [Buchan and Chen. 2007, Bao and Li 2010, and Crawford 2011]. In particular, the diagonal shear failure mode is closely related to inadequate transverse reinforcement details (e.g., large spacing and small diameter of column ties, and 90º L-shaped corner hooks). These reinforcement details lead to extensive diagonal shear cracks, which can often be observed at the bottom and top of the column. These shear cracks contribute to exposing the concrete core in RC columns. Since the exposed concrete core cannot be fully confined due to inadequate column ties, a sudden loss of an axial load carrying capacity (i.e., axial failure) occurs in the RC column. This is another major form of brittle failure. A third brittle failure mode is the direct shear failure, which is less common than other failure modes. This failure mode is caused by the lack of longitudinal reinforcement between the column and foundation [Crawford et al. 2011]. Crawford et al. [1995] studied the failure mechanisms of a non-ductile RC column under blast loads using full-scale field tests.

To capture the blast responses of the RC columns, engineers at Karagozian and Case (K&C) developed a specialized concrete material model [Crawford et al. 2012]. The K&C concrete (KCC) model has been implemented in a high-fidelity physics-based computer finite element program, LS-DYNA [LSTC 2013]. The KCC model is based on plasticity theory, and it uses a damage function to model the hardening and softening behavior of concrete. The details of the KCC model will be described in Chapter 4.

To investigate the effect of blast loading on the RC column details, Bao and Li [2010] performed an extensive parametric study under short standoff blast loads. The study investigated the parametric effects such as transverse reinforcement ratios, long-term axial load ratios, longitudinal reinforcement ratios, and column aspect ratios (the ratio of column height to depth) on the residual capacities of RC columns. This study indicated that the transverse reinforcement ratio significantly influences the blast resistance and failure modes of the column.

The failure modes of the RC column are also affected by an increase in the longitudinal reinforcement ratios. The increase in longitudinal reinforcement can lead to shifting from a ductile flexural failure to a brittle shear failure because the flexural demand of an RC column with a high longitudinal reinforcement ratio may exceed the shear demand. Additionally, the effect of the axial load ratios is more significant for shear-critical columns (i.e., non-ductile RC columns) than for flexure-critical columns. William et al. [2009] tested square and circular RC columns with different column details, such as seismically-deficient details (i.e., designed only for gravity loads), seismic details, and blast-resistant details. This experimental study demonstrated that the use of a circular column is relatively beneficial to decrease blast pressure and impulse, compared to a square column of the same size. Moreover, although all column specimens experienced shear and flexural cracks, the RC columns with the blast-resistant details exhibited a less brittle response than other columns.

2.4 FRP Retrofit

2.4.1 FRP column jacketing system

FRP column jacketing systems have been used to strengthen existing RC structures since the mid-1980s in Europe, Japan, Canada, and the United States. The typical structural behavior for RC columns with and without the FRP column jacketing system is illustrated in Figure 2.6. The FRP jacket or wrap confines the dilation of concrete columns under axial compression, and provides a passive radial stress or confining pressure (σ_R). Consequently, the confinement effect resulting from the confining pressure contributes to the enhancement of concrete compressive strength (f_{cc}', confined concrete strength) and ultimate axial strain (ε_{cu}) as shown in Figure 2.6(a). The confining pressure is computed using Equation (2.1):

$$\sigma_R = f_{ju} t_j / r \tag{2.1}$$

where

f_{ju} = ultimate tensile strength of the FRP jacket

t_j = thickness of the FRP jacket

r = radius of the FRP jacket

The confined concrete strength (f_{cc}') is a function of the unconfined concrete strength (f_c') and the confining pressure (σ_R) as given in Equation (2.2):

$$f_{cc}' = f_c' \left(2.254 \sqrt{1 + \frac{7.94 \sigma_R}{f_c'}} - \frac{2 \sigma_R}{f_c'} - 1.254 \right) \tag{2.2}$$

Based on these equations, the confinement effect is affected by FRP material properties, FRP jacket thickness, and the radius of the FRP jacket (i.e., the section size of the FRP jacketed RC column). Through the confinement effect, the seismic and blast responses for an RC column retrofitted with the FRP material can be improved as shown in Figure 2.6(b) with additional flexural capacity as well as an increase in stiffness and ductility [Mander et al. 1988, Saatcioglu and Razvi 1992, Xiao and Wu 2000, and Fam and Rizkalla 2001].
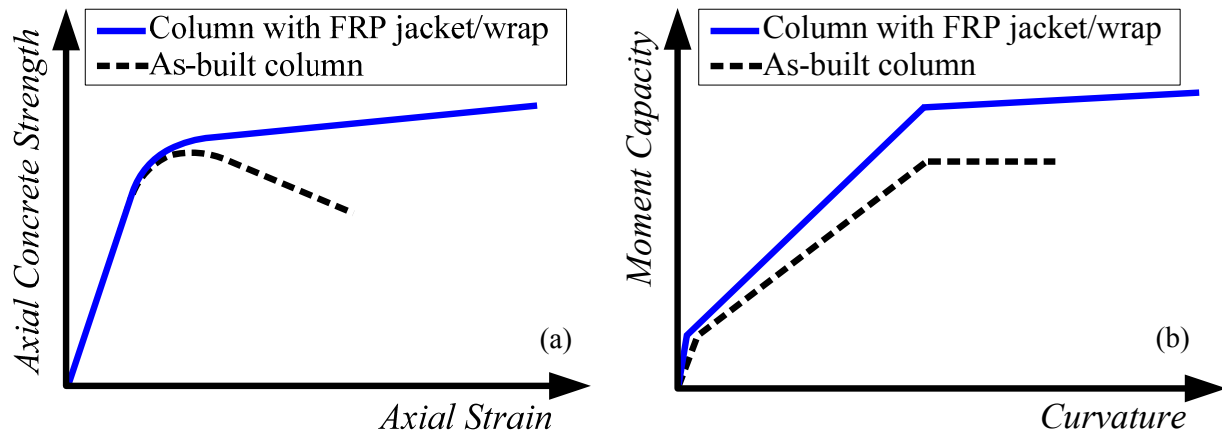
Figure 2.6. Typical behavior of RC columns with and without FRP retrofitting system: (a) axial stress-strain response; (b) moment-curvature response [Mander et al. 1988, Saatcioglu and Razvi 1992, Xiao and Wu 2000, and Fam and Rizkalla 2001]

Figure 2.7 illustrates two typical FRP column retrofit systems. The FRP column retrofitting system shown in Figure 2.7(a), an FRP column jacketing system, is composed of non-shrink grout materials for section enlargement and prefabricated FRP materials for wrapping around the column. The system shown in Figure 2.7(b) typically involves wrapping uncured FRP materials around a column after rounding off the edges of the column. Obviously, the cross-sectional shapes of RC columns significantly affect confinement [Haroun et al. 2003, Yan and Pantelides 2006a & 2006b, Al-Salloum 2007, and Wang and Wu 2008]. To evaluate the effectiveness of FRP jacketing systems with respect to the shape of the cross-sections, Haroun et

al. [2003] tested circular and rectangular RC columns retrofitted with FRP jacketing systems. The test results showed that the square and rectangular sections were less effective than their circular or elliptically-shaped counterparts because the rectangular section was not uniformly confined by the FRP jackets, and the confinement effect was greatly reduced. Accordingly, to maximize the confinement effect, section enlargement from a rectangular or square shape to a circular or elliptical shape was accomplished using FRP jackets with non-shrink grout filling the annular space, as shown in Figure 2.7(a).

ElGawady et al. [2010] demonstrated that the application of shape enlargement with circular FRP jackets in the plastic hinge region of rectangular RC columns significantly improved the displacement ductility, energy dissipation, and lap-splice capacity for RC columns with deficient lap-splices. When including the modification of sectional shapes using the section enlargement, the corner rounding at the column edges of the rectangular RC columns significantly influences confinement. This is because the corner rounding contributes to the size of confined areas with the FRP jackets, as shown in Figure 2.8. Wang and Wu [2008] and Wu and Wei [2010] tested FRP-retrofitted column specimens with a variety of corner radius ratios. The test results demonstrated that the confined area increased with increases in the corner radius ratio, and that the increase in the confined area contributed to the increase in the confined concrete strength. To maximize the confined area, the authors recommended rounding off the corner with a large corner radius ratio, as shown in Figure 2.8(b). Additionally, corner rounding prevents the failure of composite materials due to stress concentrations at the edges of the cross-sections. Al-Salloum [2007] demonstrated that edge sharpness reduced the ductility of FRP jacketed RC columns because of the premature rupture of the FRP under axial loading.

19
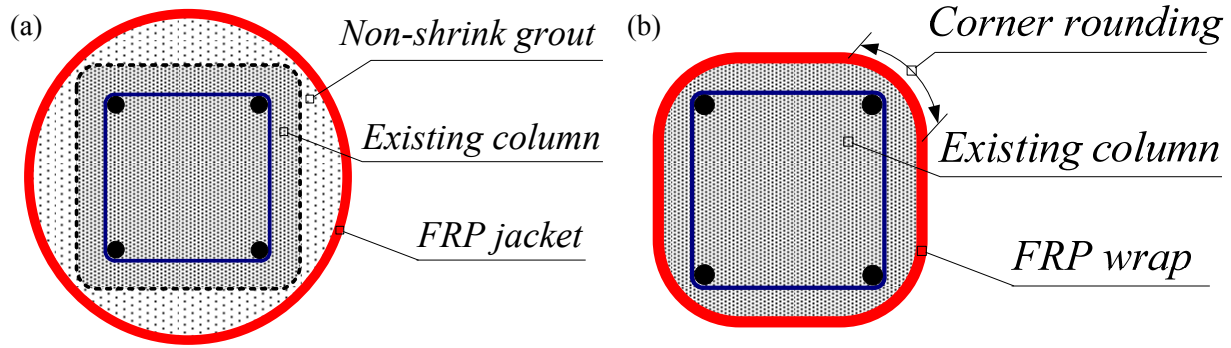
Figure 2.7. Typical FRP column retrofit systems: (a) FRP Jacketing [ElGawady et al. 2010]; (b) FRP Wrapping [Al-Salloum 2007, and Wang and Wu 2008]
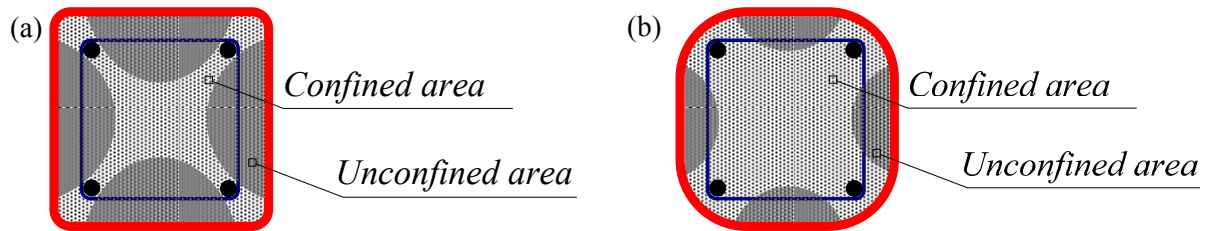
Figure 2.8. Effect of corner rounding on confined and unconfined areas: (a) small corner radius ratio; (b) large corner radius ratio [Wang and Wu 2008, and Wu and Wei 2010]

2.4.2 Seismic Retrofit

To prevent shear, flexural, and lap-splice failure modes of seismically vulnerable RC columns, seismic retrofit techniques using FRP materials have been widely used. Seible et al. [1994, 1995a & 1995b] conducted quasi-static tests for column specimens retrofitted with a variety of FRP materials, and demonstrated that FRP retrofit schemes can be effective at preventing certain failure modes in non-ductile RC columns. Based on these experimental studies, a retrofit design process of FRP jacketing or wrapping systems was proposed and validated by Seible et al. [1995c & 1997].

In addition, the prefabricated FRP jacketing system is expected to have significant advantages related to constructability in terms of quality control and the speed of installation [Xiao and Ma 1997, Ma 1999, and Xiao et al. 1999]. Xiao et al. applied prefabricated FRP jackets to existing circular RC columns to enhance the shear strength and lap-splice capacity of non-ductile RC bridge columns designed according to pre-1971 ACI codes. The test results indicated that the prefabricated FRP jackets completely prevented shear failure and contributed to stable ductile behavior without any significant degradation in stiffness and strength. Additionally, Ma demonstrated that the use of prefabricated FRP shells delayed the premature lap-splice failure of non-ductile RC columns. Although gradual degradation of load carrying capacity for the retrofitted column was observed, the FRP retrofit allowed the section to behave in a ductile fashion.

A number of studies of non-ductile RC building columns were conducted to investigate the effectiveness of FRP column retrofit systems for the most common possible failure modes (i.e., axial-flexural failure [Sause et al. 2004], lap-splice failure [Harries et al. 2006], and shear failure [Patel 2000]). In each case, the retrofit design was based on the procedure proposed by Seible et al. [1995c & 1997]. These experimental investigations indicate that the FRP column retrofit systems can provide a sufficient confinement pressure to improve the flexural, shear, and lap-splice capacities of the RC columns and increase longitudinal reinforcement buckling resistance.

2.4.3 Blast Retrofit

The use of FRP retrofits to enhance the blast resistance of existing RC structures has become more prevalent since the 1990s. Crawford et al. [1995 & 1997] demonstrated

numerically that the installation of an FRP column jacketing system in multi-story building structures with the potential for column shear failure would be effective in preventing building collapse. In addition, Karagozian and Case (K&C) proposed a retrofit design procedure using FRP materials [Morrill et al. 1999]. This proposed retrofit design procedure was validated in full-scale blast tests and quasi-static laboratory tests. Crawford et al. [2012] carried out the full-scale field tests for non-retrofitted and FRP-retrofitted columns in an RC frame building. Since the FRP retrofit provided sufficient shear capacity and ensure ductile behavior, the retrofitted RC column avoided brittle shear failure, and thus remained elastic without permanent deformation under blast loads. Rodriguez-Nikl [2006] tested non-ductile and FRP-retrofitted RC columns under blast-like shock loading, using ultra-fast hydraulic actuators called Blast Generators. The Blast Generator produces impulsive loads without explosive materials on large-scale structures by impacting the specimen with a mass in a controlled manner. The blast responses of the RC column specimens under the simulated blast loads in the laboratory tests were similar to the full-scale field test. Additionally, the FRP-retrofitted RC column specimens behaved in a ductile manner without any significant damage, whereas the non-ductile RC column specimens suddenly failed in diagonal shear. ASCE 59-11 [2011] recommends the blast retrofit of RC columns using FRP materials shall comply with all details specified in ACI 440.2R [2017] and achieve a ductility ratio of at least 6 for the design blast loads.

2.5 Shake Table Testing

To investigate the seismic response and modal properties for RC building structures, a variety of shake table tests (e.g., El-Attar et al. [1991 & 1997], Bracci et al [1995a & 1995b], Di Ludovico et al. [2008], Garcia et al. [2010], and Koutromanos et al. [2013]) have been performed

to simulate seismic loading. In these shake table tests, the size, weight and strength of test specimens were necessarily limited due to the capacities of available shake table equipment [Yu et al 2008]. Consequently, previous experimental studies typically used reduced-scale specimens in their testing programs. The first shake table test of a non-ductile RC frame, designed for gravity load only, was conducted by El-Attar et al. [1991 & 1997]. Bracci et al. [1995a & 1995b] tested one-third scale models of a full-scale prototype building with and without a seismic retrofit system. Prior to these studies, researchers [Hudson 1960, and Galambos and Mayes 1979] conducted field testing of full-scale RC structures subjected to ambient and low-level forced vibrations in order to measure the modal properties of real structures and calibrate analytical models. However, those forced vibration tests were performed in the linear elastic range. In order to overcome those limitations, the National Science Foundation George E. Brown Jr. Network for Earthquake Engineering Simulation (NEES) established the University of California, Los Angeles NEES Equipment Site, which developed a mobile shaker system for lateral excitation simulating earthquake motions on full-scale structures [NEES 2015]. Yu et al. [2008] excited a real four-story RC building, which was damaged during the 1994 Northridge Earthquake, beyond yielding using the mobile shaker system. This in-situ vibration test was conducted to calibrate numerical models based on the experimental results and to better understand the dynamic responses of the real structure.

2.6 Performance Criteria for Seismic and Blast Loads

To evaluate the seismic performance of building structures, FEMA-356 [2000] specifies three performance levels: immediate occupancy (IO), life safety (LS), and collapse prevention (CP). These performance levels are defined by an inter-story drift ratio associated with the

damage status of frame systems. ASCE 59-11 [2011] provides blast performance criteria for structural elements, which are quantified by displacement ductility or support rotation, in terms of three damage levels (level of protection, LOP): superficial, moderate, and heavy damage. The performance criteria specified in the seismic and blast design codes are defined by different demand parameters depending on loading types. Because of these differences in the design codes, multi-hazard performance criteria are needed to develop a retrofit scheme ensuring adequate performance of building structures subjected to both seismic and blast loads.

To estimate the structural damage of RC building structures, Park and Ang [1985] proposed a combined damage model, hereafter referred to as the "Park-Ang damage model." This model consists of a simple linear combination of normalized deformation and energy absorption parameters as given in Equation (2.3).

$$D = \frac{\Delta_m}{\Delta_u} + \frac{\beta}{Q_y \Delta_u} \int dE \tag{2.3}$$

where

Δ_m = maximum deformation

Δ_u = ultimate deformation capacity under static loading

Q_y = yield strength

dE = incrementally absorbed hysteretic energy

β = coefficient for cyclic loading effect

The β value depends on laboratory or field testing data. This study assumes the β value is 0.05 for RC components [Park and Ang 1985, and Jeong 2005]. The structural damage characterized by current code-defined limits, such as FEMA-356 and ASCE 59-11, is determined using only maximum deformation in the structure. However, the Park-Ang damage model includes effects of cyclic responses as well as maximum responses. For this reason, the performance criteria derived from the Park-Ang damage model can represent more accurate damage conditions than the current performance criteria (e.g., FEMA-356 and ASCE 59-11). Additionally, the Park-Ang damage model has been widely used to quantify the structural damage to non-ductile RC structures with and without retrofit systems at the component and structural levels [Park et al. 1987, Kunnath et al. 1990, Bracci et al. 1995a & 1995b, Jeong 2005, Güneyisi and Altay 2008, Seifi et al. 2017]. Therefore, the present work utilizes the Park-Ang damage model to develop multi-hazard performance criteria by combining the energy-based damage limits for the seismic and blast loading conditions.

In addition, to quantify the global damage of an RC structure, Park et al. [1987] derived the global damage index for each story of a building structure from the local damage index, as given in Equation (2.4):

$$D_{story} = \frac{\sum D_i E_i}{\sum E_i} \tag{2.4}$$

where

D_{story} = each story damage index

D_i = local damage index at location i

E_i = energy absorbed at location i

In addition, Park et al. defined five damage levels with respect to the damage indices based on the damage observation of RC buildings (see Table 2.1). The proposed limit states were utilized by Kunnath et al. [1990 & 1992] to perform an inelastic damage analysis of RC frame-wall structures. Chung et al. [1990] also used the global damage index proposed by Park et al. to estimate the damage of a numerical RC frame model.

Bracci et al. [1989] introduced the effect of gravity loads supported by the local component of story damage index as given in Equation (2.5):

$$D_{story} = \frac{\sum W_i D_i^{m+1}}{\sum W_i D_i^m} \tag{2.5}$$

where

W_i = weighing factor of element i

D_i= maximum local damage index at element i

m = control weighing factor for the component

The m factor can be introduced to place emphasis on severely damaged local components. Assuming that the gravity loads are uniformly distributed over the structure, the present study uses $m = 1.0$. Based on experimental studies on columns and scaled three- and six-story frame models, Bracci et al. suggested damage limit states correlated with the damage indices given in Table 2.2.

Table 2.1. Limit states of RC frame proposed by Park et al. [1987]

Damage index	Damage level	Damage description
$D < 0.1$	Slight Damage	No damage or localized minor cracking
$0.1 \leq D < 0.25$	Minor Damage	Light cracking throughout, and partial crashing of concrete in columns
$0.25 \leq D < 0.4$	Moderate Damage	Extensive large cracks, and spalling of concrete in weaker elements
$0.4 \leq D < 1.0$	Severe Damage	Extensive crashing of concrete, and disclosure of buckled reinforcement
$D \geq 1.0$	Collapse Damage	Total or partial collapse of building

Table 2.2. Limit states of RC frame proposed by Bracci et al. [1989]

Damage index	Damage level
$D \leq 0.33$	Serviceable state
$0.33 < D \leq 0.66$	Repairable state
$0.66 < D \leq 1.0$	Irrepairable state
$D > 1.0$	Collapse state

CHAPTER 3. FULL-SCALE DYNAMIC TESTING OF NON-DUCTILE RC FRAME RETROFITTED WITH FRP COLUMN JACKETS

3.1 Overview

Four identical full-scale two-story two-bay non-ductile RC test frames were constructed at the Georgia Institute of Technology Structural Engineering & Materials Research Laboratory, as shown in Figure 3.1(a). The test frames were representative of low-rise RC office buildings in the eastern United States built in the 1950s-1970s without consideration of seismic loads. A mobile shaker system was utilized to vibrate the full-scale test frames beyond their linear elastic behavior. For the first dynamic test, one of four frames was tested in an as-built configuration (hereafter referred to as the "as-built test frame"). After the damage observed in the as-built test frame, seismic retrofit schemes were developed for the three remaining test frames. These test frames were retrofitted with three different retrofit technologies: near surface mounted reinforcing bars with carbon FRP (CFRP) wraps, a prefabricated CFRP column jacketing system, and a shape memory alloy bracing system. This chapter focuses on the dynamic responses of the retrofitted frame with the prefabricated CFRP column jacketing system in the first story (hereafter referred to as the "retrofitted test frame"), as shown in Figure 3.1(b). Additionally, to estimate the effectiveness of the FRP jacketing system, the retrofitted test frame was compared to the as-built test frame.

(a)

(b)

Figure 3.1. Full-scale, two-story two-bay non-ductile RC test frames: (a) four identical full-scale test frames; (b) FRP jacketed column in retrofitted test frame

3.2 Experimental Program

3.2.1 Test setup and specimen details

The material properties of the as-built and retrofitted test frames are summarized in Table 3.1, where the concrete strengths are average compressive values, and the steel strengths are yielding values. In addition, the strength of the FRP jacket is given as the tensile stress (i.e., the ultimate tensile strength of the FRP jacket) corresponding to the ultimate strain ($\varepsilon_{ju} = 0.011$) in the material at rupture. The material properties given in Table 3.1 were determined in accordance with relevant ASTM standards [2013, 2014, 2015a & 2015b].

Table 3.1. Summary of material properties [Wright 2015]

Material type	Location/rebar type	Strength (MPa)		ASTM standards
		As-built test frame	Retrofitted test frame	
Concrete	First story column	32.8	31.4	ASTM-C39 [2015a]
	First story beam/slab	26.5	26.5	ASTM-C39 [2015a]
	Second story column	25.0	30.3	ASTM-C39 [2015a]
	Second story beam/slab	23.5	23.5	ASTM-C39 [2015a]
Steel	ϕ 10 rebar (Diameter = 10 mm)	520	520	ASTM-A615 [2015b]
	ϕ 19 rebar (Diameter = 19 mm)	445	445	ASTM-A615 [2015b]
	ϕ 25 rebar (Diameter = 25 mm)	541	541	ASTM-A615 [2015b]
FRP	First story column	No-retrofit	1080	ASTM-D3039 [2014]
Grout	First story column	No-retrofit	40.0	ASTM-C109 [2013]

Figure 3.2 provides a schematic illustration of the test setup and test frame details. Note that a complete description of the design and construction of the RC frames is given by Wright [2015]. To simulate gravity loading, steel rails weighing approximately 9.30 kN/m and 7.72 kN/m (w_1 and w_2 in Figure 3.2) were distributed over the second and top (third) floors, respectively. As shown in Figure 3.2, two shakers were utilized to perform the full-scale dynamic experiment. In this study, a 334 kN hydraulic linear shaker was anchored to the middle of the top floor to apply the lateral forces to the roof. In addition, a portable eccentric mass shaker (EMS) with a maximum capacity of 110.7 kN-mm was fixed on the second floor (between B13 and B14 in Figure 3.2) to estimate modal properties of the test frames. The hydraulic linear shaker and portable EMS are shown in Figure 3.3. The as-built RC test frame was designed for gravity loads only in accordance with the 1963 edition of ACI design code [ACI 318-63 1963]. The relative dimensions of each test specimen are consistent with construction practices in the eastern United States from 1950-1970. Due to a limitation in the availability of period-specific materials, ASTM 615 Grade 60 steel reinforcement (f_y = 414 MPa) and concrete with a 28-day compressive strength (f_c') of 25.8 MPa were used in the design. The first story columns for both the RC test frames were built with lap-splice lengths of 610 mm at the column base and non-ductile transverse reinforcement detailing (spacing @ 305 mm and 90 º column ties). These configurations are often found in building structures constructed in the United States prior to the 1970s.

To compensate for the non-ductile RC columns in the first story, prefabricated FRP jackets were installed on the three columns in the first story of the retrofitted frame. Unlike the first story columns, the second story columns were designed with a relatively narrow transverse reinforcement spacing (178 mm) and longer lap-splice lengths (914 mm). Column ties with a

specified angle of 135 º were used in the second story center column (between C32 and C42 in Figure 3.2). This was intended to transfer vibration loads from the second story to the first story, avoiding unexpected failure while the shaker applied the loads.
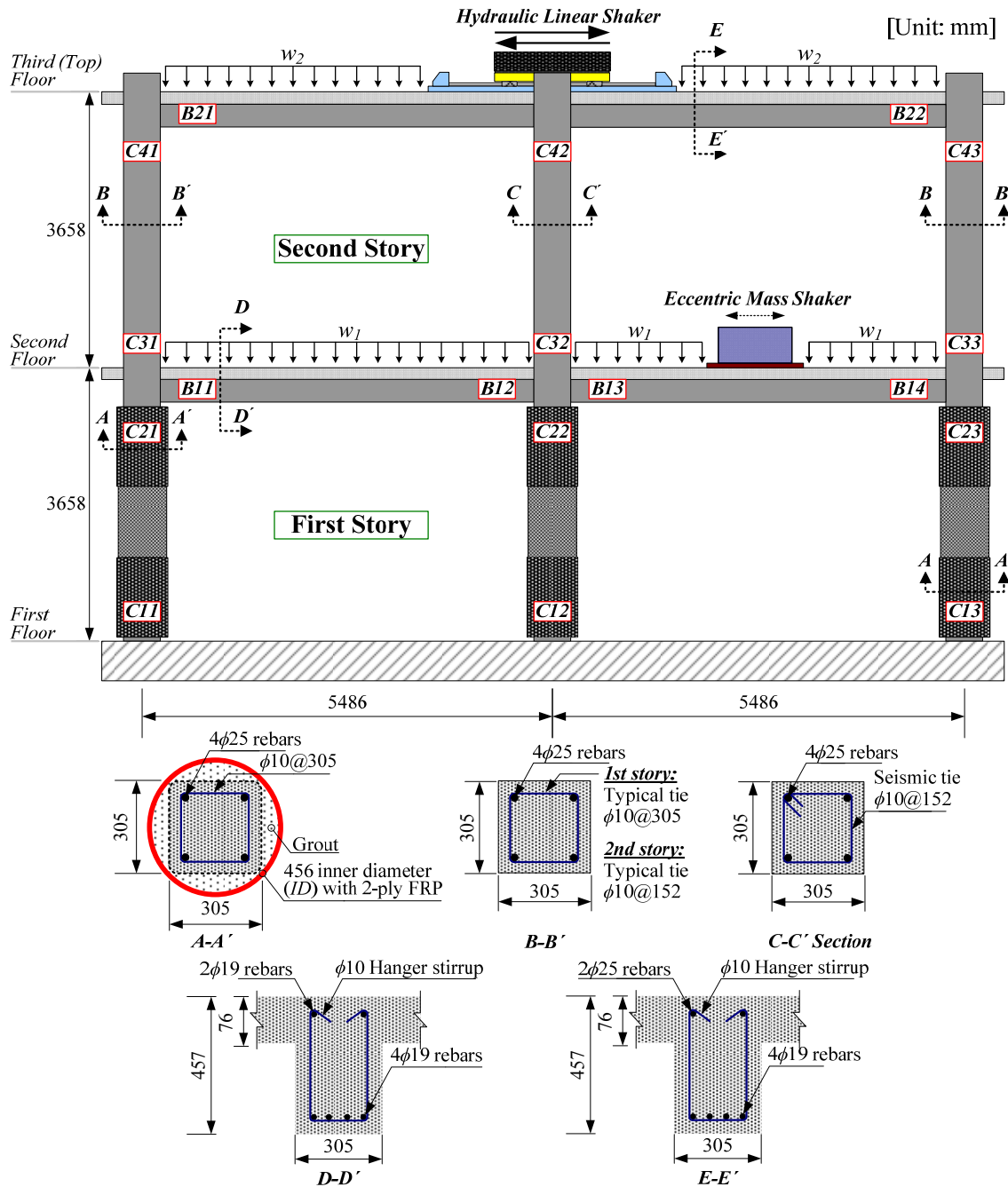
Figure 3.2. Test frame details

(a)

(b)

Figure 3.3. Mobile shakers: (a) hydraulic linear shaker; (b) portable eccentric mass shaker

(a)

Hydraulic Linear Shaker

B21   C42   B22
C41   Tension only brace   C43

Eccentric Mass Shaker

C31   C32   C33

B11   B12   B13   B14
C21   Gravity collapse prevention frame   C23
C22

Wide-flanged beam
C11   C12   C13

(b)

Collapse prevention frame

Tension only brace

Wide-flanged beams

(c)
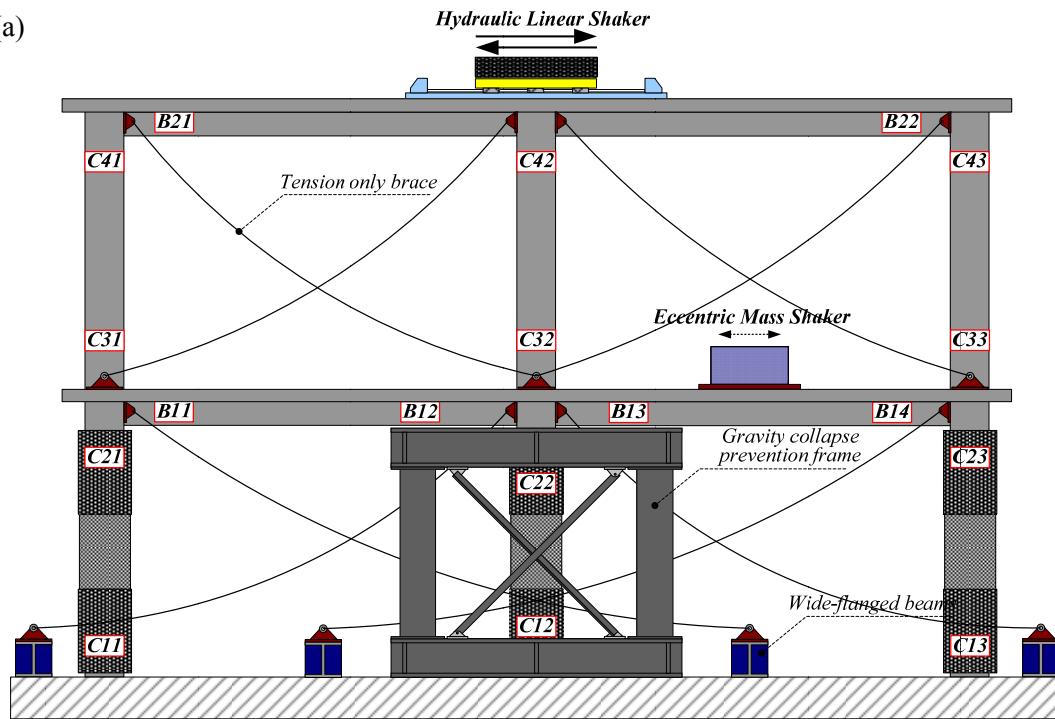
Figure 3.4. Additional test setup for collapse prevention: (a) schematic view of safety equipment; (b) first story; (c) second story

Figure 3.4(a) shows the safety equipment that was installed to prevent structural collapse during the dynamic testing. A steel frame was installed around an interior column on the first story, as illustrated in Figure 3.4(b). This steel frame was designed to support the weight of the entire structure. Additionally, tension-only cable x-braces were installed on the first and second stories (Figures 3.4(b) and 3.4(c)). The cable braces were designed to restrain additional deformation of the test frame once the structure reached a 3.0 % inter-story drift ratio (IDR).

3.2.2 Loading sequences

The hydraulic linear shaker on the roof imparted two different phases of excitations to the test frames: seismic vibration and sinusoidal pulses. Each input excitation corresponded to a target displacement of the linear shaker [Wright 2015]. Table 3.2 presents the loading sequences of the as-built and retrofitted test frames for two different excitation phases with specified target displacements, the 1940 El Centro (EC) earthquake (Phase 1) and single or double sinusoidal pulse (SP) vibration (Phase 2). To compare the dynamic responses between the as-built and

retrofitted test frames, the loading sequences for the two test frames were identical until SP 12 (Table 3.2). During Phase 1 (EC 1 to EC 8), the target displacement of the linear shaker increased from 25.4 mm to 203 mm. The seismic loading sequences (Phase 1) were scaled from actual ground motion displacement time histories. During SP 4 and SP 8 in Phase 2, the shaker generated excitations with a single sinusoidal pulse, while SP 12 to SP 20 generated vibrations with double sinusoidal pulses. The linear shaker displacement increased from 102 mm to 508 mm. The maximum velocities of the seismic and sinusoidal vibration loads were 1.51 and 1.83 m/sec, respectively.

Table 3.2. Summary of loading sequences

Phase	Loading sequences		Vibration type	Shaker displacement
	As-built test frame	Retrofitted test frame		
Phase 1	EC 1	EC 1	1940 El Centro earthquake	25 mm (1 in)
	EC 2	EC 2		51 mm (2 in)
	EC 4	EC 4		102 mm (4 in)
	EC 6	EC 6		152 mm (6 in)
	EC 8	EC 8		203 mm (8 in)
Phase 2	SP 4	SP 4	Single sinusoidal pulse	102 mm (4 in)
	SP 8	SP 8		203 mm (8 in)
	SP 12	SP 12	Double sinusoidal pulses	305 mm (12 in)
	None	SP 16		406 mm (16 in)
	None	SP 20		508 mm (20 in)

3.2.3 Retrofit design and construction of FRP jacketing system

To develop a seismic retrofit strategy for the test frame using the FRP column jacketing system, a visual damage inspection of the as-built test frame was conducted. The complete results of the test on the as-built frame were given by Wright [2015]. A visual inspection of the as-built frame after loading was completed revealed a range of observable damage as shown in Figure 3.5. During Phase 1 of loading sequences (El Centro earthquake loads), no visible damage was detected. However, the ultimate loading sequence in the as-built test frame led to splitting cracks at the column bases, which represented the initiation of lap-splice failure, and shear cracks within lap-splice regions (610 mm from the column bases). Additionally, the pullout failure of the bottom beam reinforcement in the exterior beam-column joints was demonstrated using the relationship between hinge rotation and reinforcement strain, as illustrated in Figure 3.6 [Wright 2015]. The strains of the bottom reinforcement (positive bar in Figure 3.6) have almost constant values before reaching the yielding strain of the reinforcing bar when the beam hinge rotations increased from 0.005 rad to 0.008 rad. After that, the strains dropped significantly. This indicates that the initiation of pullout failure occurred for the bottom reinforcement in the exterior beam-column joint. Similarly, the experimental results demonstrated the lap-splice failure in the first story columns in the as-built test frame.

This study also utilized the same approach to investigate bond-slip behavior in the lap-splice column and beam-column joint areas in the retrofitted test frame, and more detailed information related to the bond-slip effects will be described in Chapter 4. The visual inspection and measured results found that the damage to the as-built test frame was concentrated in the first story column bases. The installation of the FRP jackets on the first story columns was expected to mitigate some of this damage accumulation.

(a) Damage location
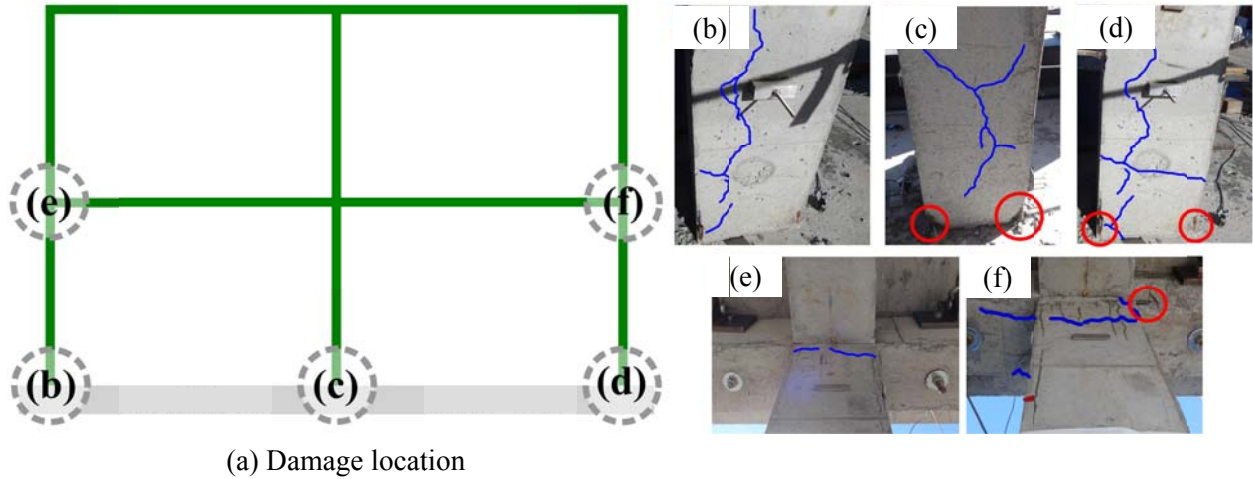
Figure 3.5. Damage inspection of as-built test frame
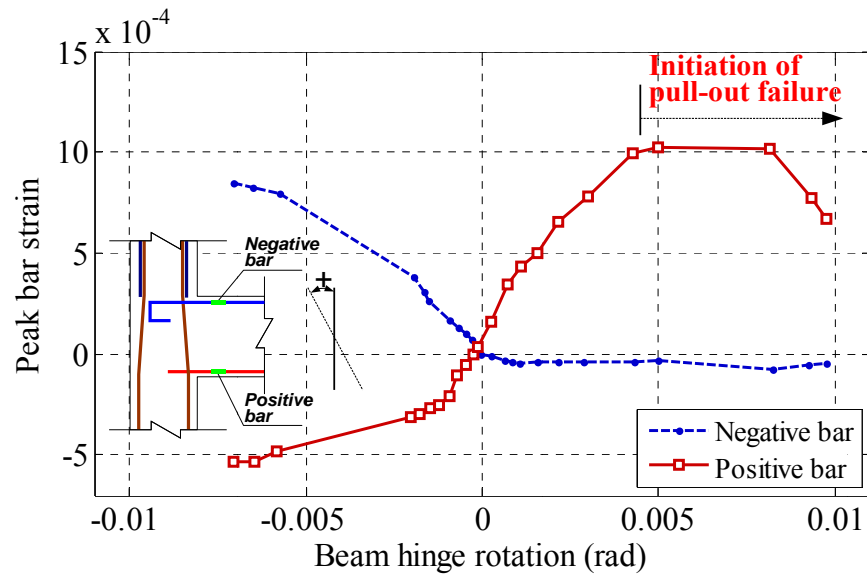
Figure 3.6. An example of hinge rotation-peak bar strain relationship [after Wright 2015]

Figure 3.7 shows the details of an RC column in the as-built frame (Figure 3.7(a)) and an FRP jacketed RC column in the retrofitted frame (Figure 3.7(b)). The present work followed the retrofit design process proposed by Seible et al. [1995c & 1997]. The first step in the design process was to estimate the lateral resisting capacity, ductility, shear strength, and lap-splice failure for the as-built column details, using a sectional analysis performed by a Response-2000

program developed by Bentz and Collins [2001]. The sectional analysis can estimate the strength

and ductility of an RC cross-section subjected to shear, moment, and axial loading conditions. A

moment-curvature relation of the as-built column was developed from the sectional analysis, and

the ductility of the as-built column (μ_0) was calculated as the ratio of ultimate curvature to

yielding curvature ($\mu_0 = 2.25$). After performing the sectional analysis of the as-built column, a

target ductility ($\mu_{target} = 4.50$) twice that of μ_0 was established. The confined concrete

compressive strength was conservatively assumed as 1.5 times the unconfined concrete strength

($f_{cc}' = 1.5\ f_c' \approx 47.1$ MPa), in accordance with previous research [Ma et al. 2000]. Under these

assumptions, the number of FRP plies required to prevent all three possible failure modes

described in Section 2.4.2 (flexural failure, shear failure, and lap-splice failure) was determined.

For the flexural failure mode, the required ultimate axial strain of the FRP-confined concrete

material using the target ductility was assumed and the jacket thickness preventing the premature

failure was computed using Equation (3.1):

$$t_f = \frac{0.09 ID(\varepsilon_{cu} - 0.004) f'_{cc}}{\phi_f f_{ju} \varepsilon_{ju}} = 1.29 \text{mm} \ (\approx 2 \text{ plies})$$
(3.1)

where

ID = inner diameter of the FRP column jacketing system

ϕ_f = flexural strength reduction factor of 0.9

f_{ju} = ultimate tensile strength of 1080 MPa for the FRP jacket

ε_{ju} = ultimate strain of 0.011 for the FRP jacket

To enhance the shear capacity of the RC column, the thickness of FRP jacket at the plastic hinge regions (i.e., ends of the RC column) was determined using Equation (3.2):

$$t_v = \frac{1.5V_{if}/\phi_v - (V_c + V_s + V_a)}{\frac{\pi}{2} \times 0.004 E_j ID} = 0.58 \text{mm} \ (\approx 1 \text{ ply})$$ (3.2)

where

V_{if} = ideal flexural strength given by the sectional analysis

ϕ_v = shear strength reduction factor of 0.85

V_c = shear strength by concrete ($\approx$ 53.1 kN)

V_s = shear strength by exsting transverse reinforcement ($\approx$ 20.9 kN)

V_a = shear strength by axial loading ($\approx$ 19.7 kN)

The jacket thickness to improve the lap-splice capacity was calculated based on the required clamping pressure ($f_l \approx 1.02$ MPa), which can prevent lap-splice bond slips, using Equation (3.3):

$$t_s = \frac{500ID(f_l - f_h)}{E_j} = 1.07 \text{mm} \ (2 \text{ plies})$$ (3.3)

In this equation, f_h is the lateral confining pressure for the existing transverse reinforcement detailing and is estimated as 0.31 MPa. More detailed examples of the retrofit design process using the FRP jacket can be found in Seible et al. [1997a].

As shown in Figure 3.7(b), the jacketing system was installed with a two-ply FRP jacket (1.32 mm in thickness) and one-ply FRP jacket (0.66 mm in thickness) in the l_1 and l_2 regions,

respectively. Based on the sectional analysis of the retrofitted column, the FRP jackets increased the flexural stiffness of the retrofitted columns by approximately 88.0 % (54 kN/m in the as-built column and 101 kN/m in the retrofitted column) compared to the as-built columns, and increased the lateral load resisting capacity by approximately 68.0 % (112 kN-m in the as-built column and 189 kN-m in the retrofitted column).
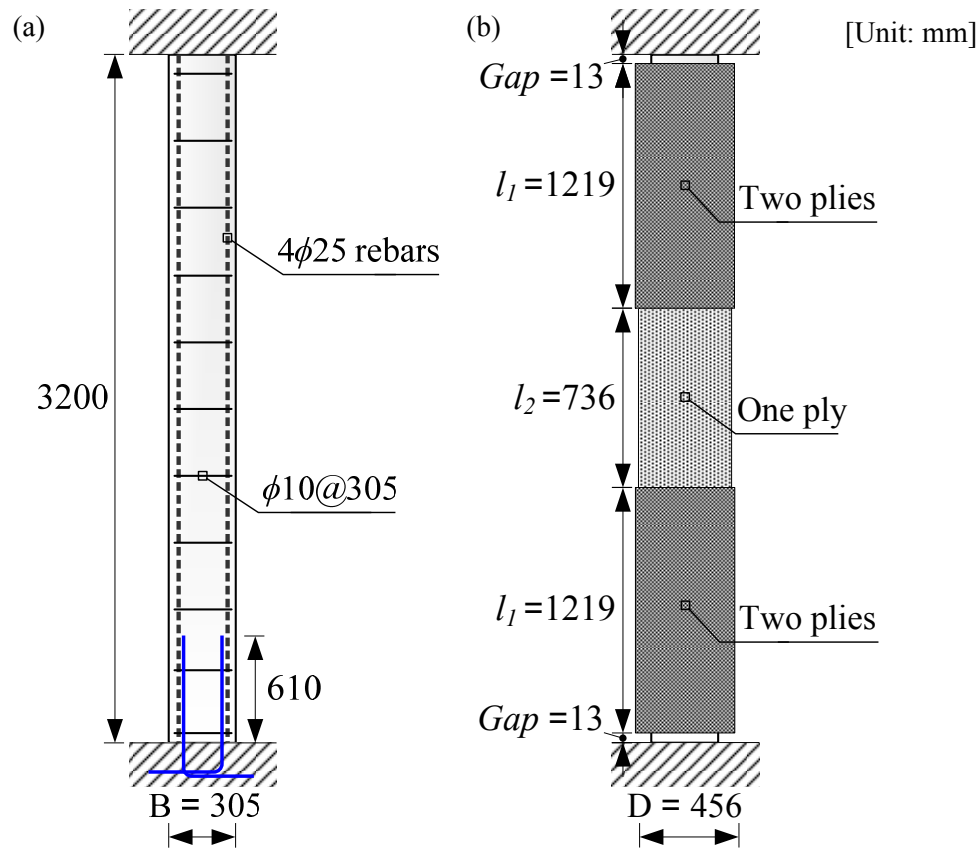
Figure 3.7. RC column details before and after installation of FRP jacketing system: (a) as-built column; (b) retrofitted column

FEMA-547 [2006] provides a general construction guideline for column jacketing systems. In this guideline, the surface of the existing concrete must be appropriately roughened to ensure sufficient bonding between new and existing materials. These guidelines were used in conjunction with the manufacturer's recommendations [Ehsani and Tipnis 2011] for the

installation of the commercially available jacketing system. Neither guideline gave specific criteria for the substrate concrete surface profile (CSP), which represents the roughness of a concrete surface. As such, recommendations given by the International Concrete Repair Institute (ICRI) were followed. ICRI recommends a CSP of 7 to 9 to ensure adequate bonding between the substrate concrete and the retrofit material; this was accomplished using hand-held concrete breakers [ICRI 2014]. Prior to application of the FRP shells, the column surface was cleaned with a high-pressure air gun. High strength epoxy resin was applied to the surface of the prefabricated FRP sheets. Next, the prefabricated FRP sheets were used to form a circular shape around the existing square columns. Several ratchet straps were used to fix the diameter of the shell and prevent it from unraveling before the epoxy cured. After curing of the epoxy, a hole was created at the top of the FRP shells to fill the annular space between the jacket and column with a non-shrink grout. Additionally, as recommended in FEMA-547, gaps of approximately 13 mm were left at the column top and bottom to inhibit the interaction between the FRP jacket and the adjacent elements (e.g., slab, beam, and foundation).

3.2.4 Instrumentation plan

The dynamic response of the full-scale test frames was recorded using 87 sensors (38 LVDTs, 6 string potentiometers, 34 uniaxial accelerometers, and 9 triaxial accelerometers) installed throughout the frame, as illustrated in Figure 3.8. The accelerometers were installed to estimate modal properties. The string potentiometers were mounted on the bottom of the slab to measure global displacement at each story level. As an example, the sensor configuration at the C22 and C32 beam-column joint (Figure 3.2) is shown in Figure 3.9. To measure the hinge rotations of the left and right beams at the expected plastic hinge locations, four LVDTs were

42

installed horizontally on the top and bottom surfaces of the beam or slabs. Four vertical LVDTs were installed at two opposite sides of the columns to monitor the hinge rotations of the columns. The column hinge rotation was computed as given in Figure 3.10, where θ_{col} is the column hinge rotation; Δ_{iv} and Δ_{jv} are vertical displacements measured from the two opposite sides of the columns; and ID is the column diameter. Beam-column hinge rotations were calculated in a similar manner as the column hinge rotation.
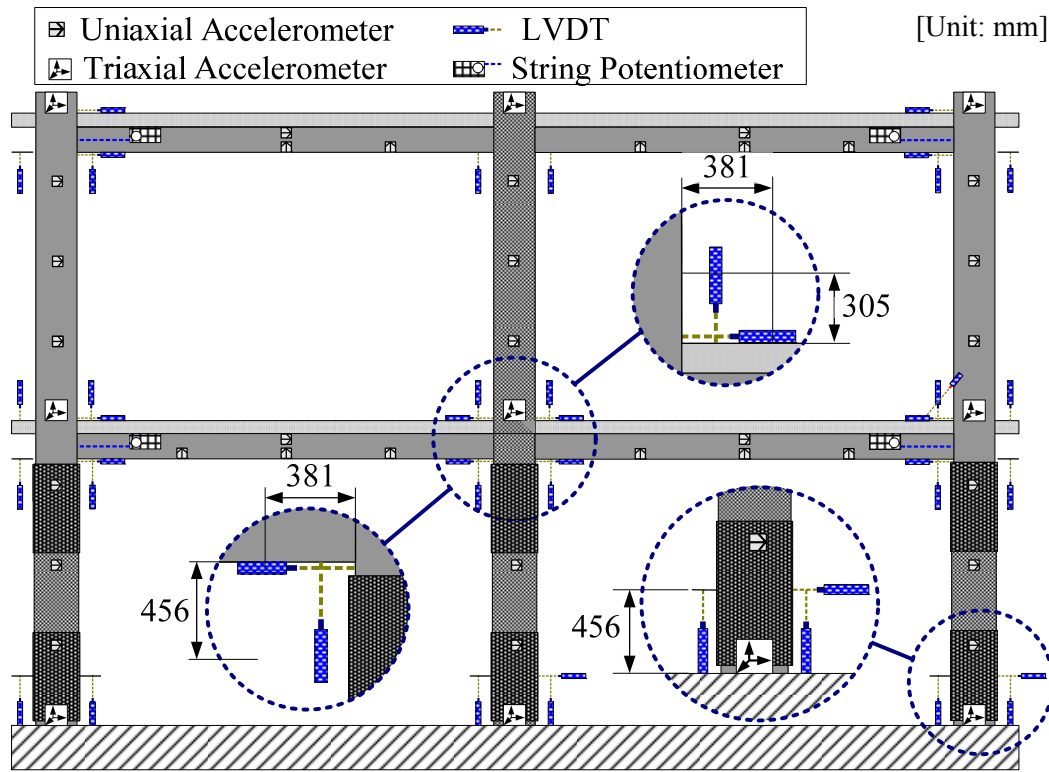
Figure 3.8. Schematic view of LVDTs, string potentiometers, and accelerometers
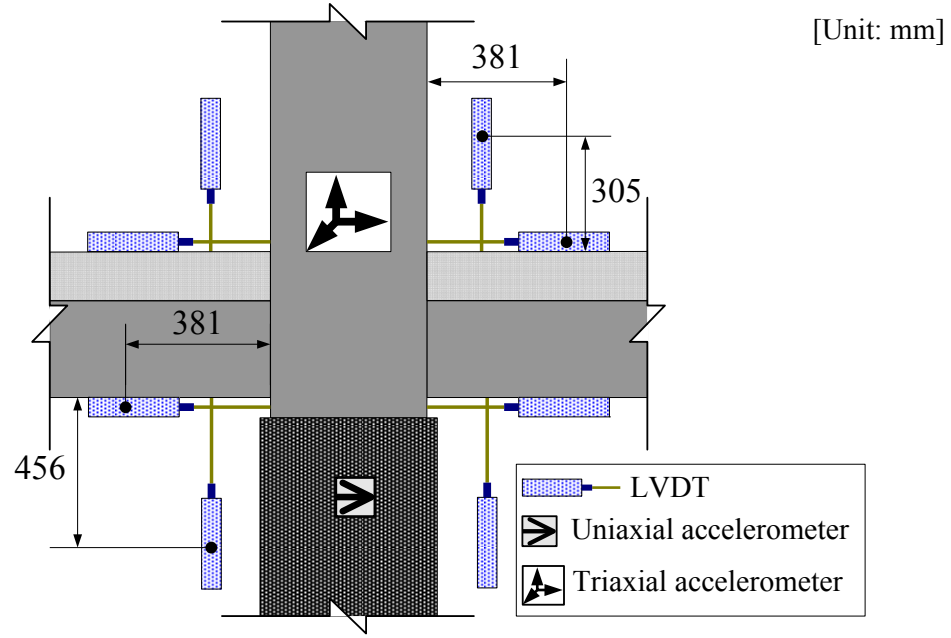
Figure 3.9. Sensor configuration at C22 and C32 (Figure 3.2)

$$\theta_{col} = (\Delta_{iv} + \Delta_{jv})/ID$$
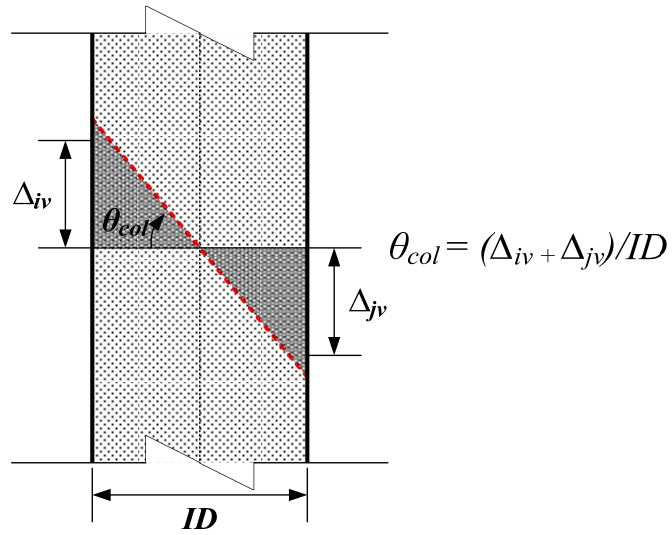
Figure 3.10. Calculation of column hinge rotation

3.3 Experimental Results of Retrofitted Test frame with FRP Jacketing System

3.3.1 Modal responses and damage observed in retrofitted frame

To obtain the natural frequencies of the retrofitted frame, the EMS shaker installed on the second floor was used to produce ambient vibrations before and after the loading sequences applied by the hydraulic linear shaker on the roof. The measured natural frequencies of the first and second modes for the retrofitted frame for each loading sequence are shown in Figure 3.11. The initial natural frequencies (i.e., prior to the first loading sequence) for the first and second modes were 1.88 Hz and 4.70 Hz, respectively. In general, the natural frequencies decreased gradually as the loading sequences progressed. At the end of Phase 1, no visible damage was observed in the structure, and the natural frequencies decreased by approximately 8.0 %. During the application of the sinusoidal pulses (Phase 2), the visible damage was observed after SP 8, as shown in Figure 3.12. An approximately 2 mm joint crack in the slab immediately adjacent to the column was observed, and longitudinal reinforcement at the column base was exposed due to concrete cover spalling. This damage resulted in a reduction in natural frequency compared to initial measured values of 12.8 % for the first and 23.4 % for the second modes. Following the final loading sequence (SP 20), the measured natural frequencies in the retrofitted frame decreased from the initial measured values by 20.2 % and 36.2 %.
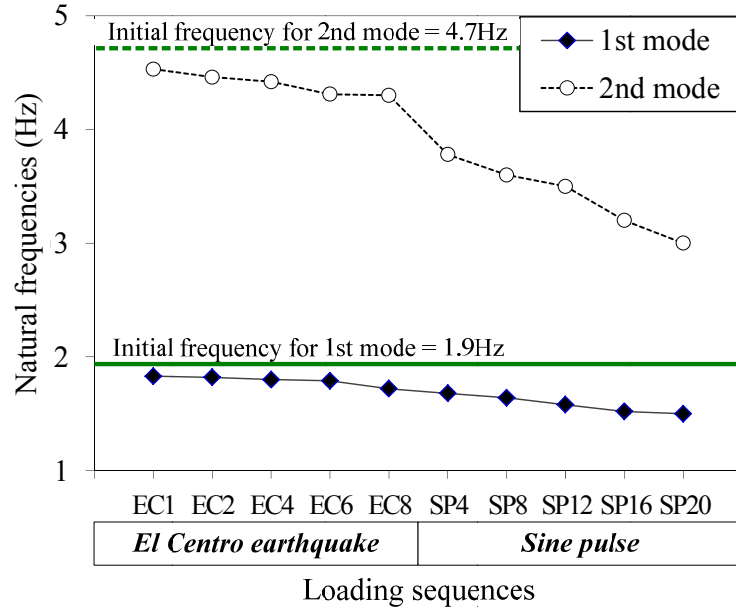
Figure 3.11. Natural frequencies of retrofitted test frame
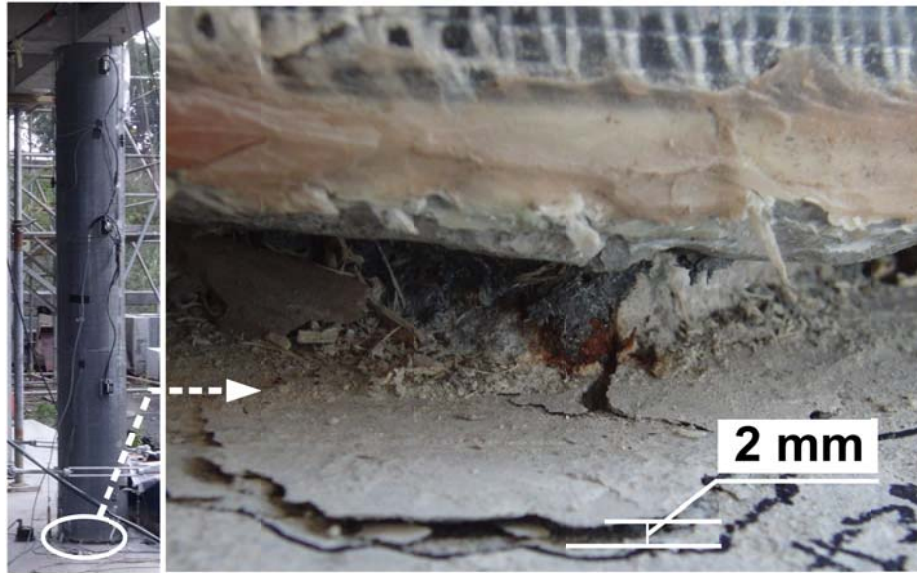
Figure 3.12. Damage observed near the column base (C13 in Figure 3.2) after SP 8

3.3.2 Dynamic response of retrofitted test frame

In this study, the damage levels of the retrofitted frame with respect to the inter-story drift ratio (IDR) were defined according to the three performance levels of the RC frames specified in

FEMA-356 [2000]. Additionally, the performance levels for rotation of beams and columns were adopted from ASCE 41-13 [2014]. This study employed these rotational limits to identify the damage progression of the retrofitted frame under the loading sequences. The drift and rotational limits with respect to the performance levels are summarized in Table 3.3. This table includes the summary of damage conditions for each performance level, specified in FEMA-356 and ASCE 41-13. Those limit states are useful for determining the target performance of building structures with respect to seismic hazard levels in a rehabilitation design process. However, this study utilized the performance levels to indicate the damage status of the test frames in each loading sequence because the shaker loads gradually increased until the shaker capacity was reached and the building target performance was not specified in the FRP retrofit design process.

Story displacements were recorded using string potentiometers located at the corners of each story. The peak inter-story drift ratios are shown in Figure 3.13 under selected loading sequences: Phase 1 (EC 1 to EC 8) in Figure 3.13(a) and Phase 2 (SP 4 to SP 20) in Figure 3.13(b). For simplicity, only representative test results are shown in Figure 3.13. The peak inter-story drift ratio increased as the shaker's target displacement increased. During Phase 1 (Figure 3.13(a)), the peak inter-story drift ratio was within the immediate occupancy (IO) level without visible damage. However, after the visible damage was observed during SP 8, the peak inter-story drift ratio of the first story in the retrofitted frame reached the life safety (LS) level, as shown in Figure 3.13(b). The change in the performance level from IO to LS was attributed to the joint crack and concrete cover spalling between the C13 column base and slab. In the final loading sequence (SP 20), the peak inter-story drift ratios on both stories were within the LS level, but no additional visible damage was observed on the first and second stories.

Table 3.3. Drift and rotational limit states [FEMA-356 2000, and ASCE 41-13 2014]

Performance level	Drift limits (%)	Rotational limits (rad)		Damage conditions
		Column	Beam	
Immediate occupancy (IO)	≤ 1.0	≤ 0.005	≤ 0.005	Minor hairline cracking; no crushing
Life safety (LS)	≤ 2.0	≤ 0.027	≤ 0.020	Minor spalling in non-ductile column, joint cracks < 3.2 mm
Collapse prevention (CP)	≤ 4.0	≤ 0.034	≤ 0.030	Splice failure in some non-ductile columns
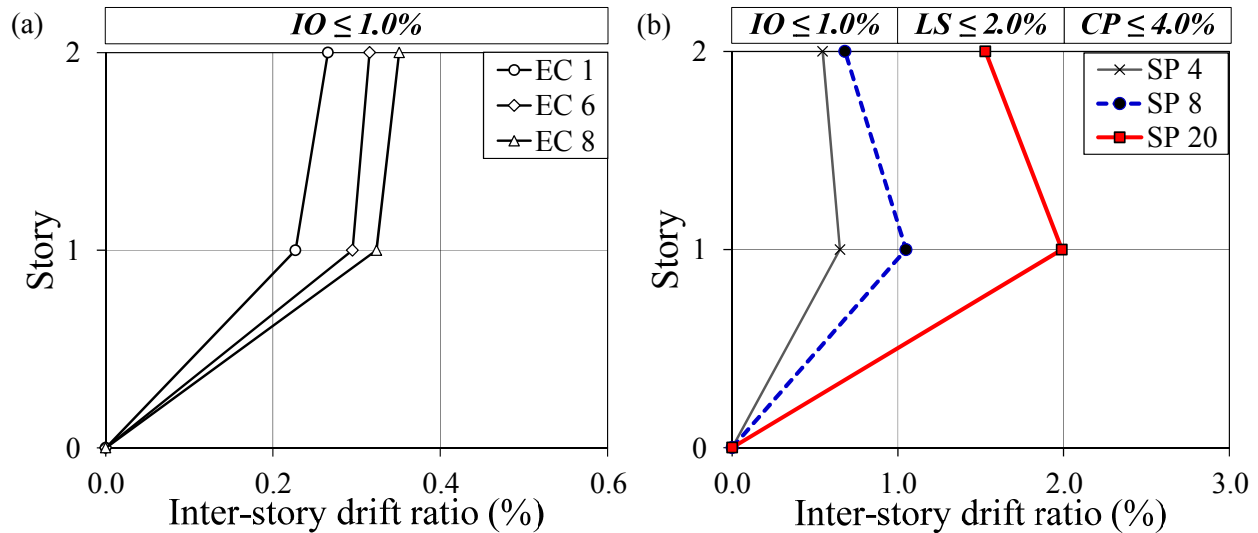
Figure 3.13. Peak inter-story drift ratio for selected loading sequences: (a) Phase 1 (El Centro earthquake); (b) Phase 2 (sinusoidal pulse vibration)

The maximum hinge rotations of column and beam components under selected loading sequences are shown in Figure 3.14. The rotational demands of the beams and columns in the retrofitted frame reveal that the top and bottom of the first story columns reached the LS level first; these were the most vulnerable components, followed by the second story column bases and the first story beam portions near the exterior joints.
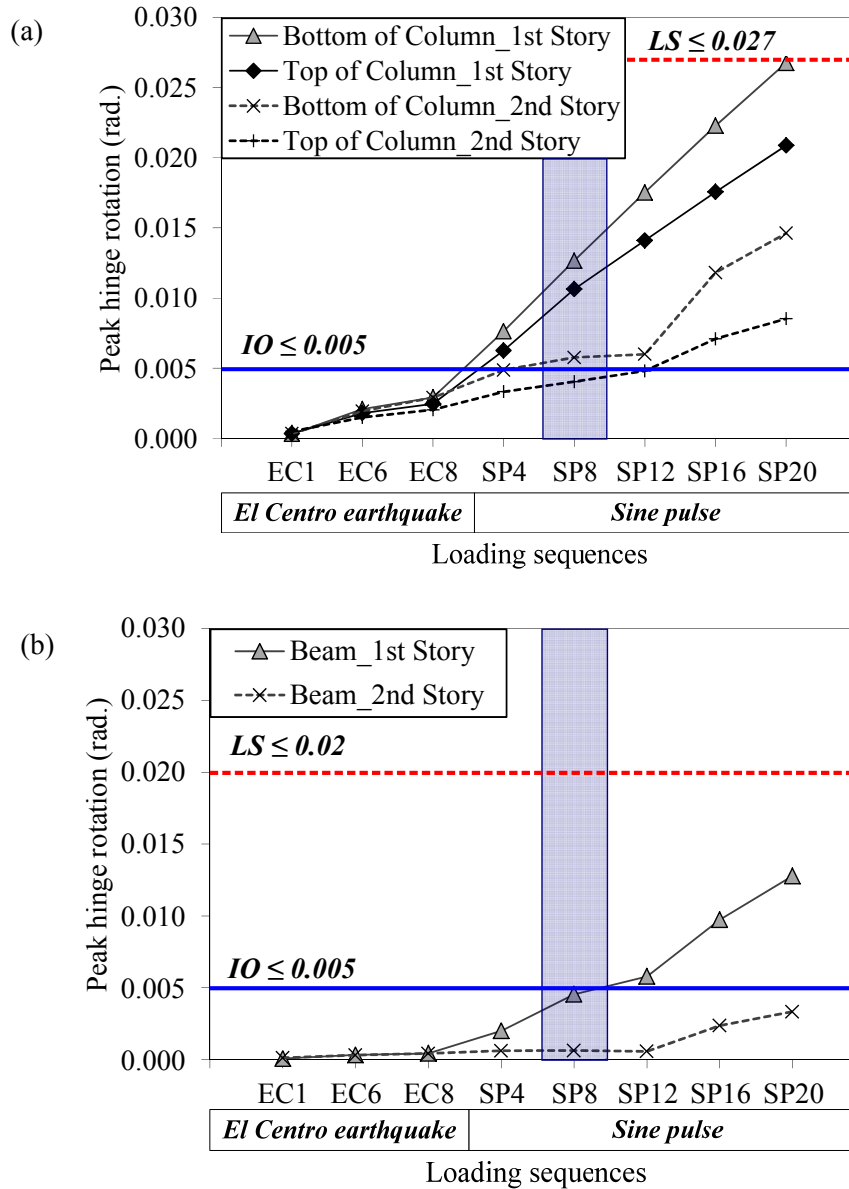
Figure 3.14. Maximum hinge rotations of column and beam for selected loading sequences: (a) column hinge rotations; (b) beam hinge rotations

3.4 Effectiveness of FRP Column Jacketing System

3.4.1 Drift reduction

Prior to dynamic testing of the RC frame retrofitted with the FRP jacketing system, an as-built RC frame without any retrofits was tested in a similar fashion [Wright 2015] to provide a

basis for comparison. The dynamic responses obtained from the as-built frame were compared to those of the retrofitted frame under selected loading sequences, as shown in Table 3.2. The drift reduction ratios for the first story, where the FRP jacketing system was installed, are shown in Figure 3.15. The drift reduction ratio is defined in Equation (3.4):

$$\text{Drift reduction ratio (\%)} = (\Delta_{As\text{-}built} - \Delta_{Retrofitted}) / \Delta_{As\text{-}built} \times 100 \qquad (3.4)$$

where

$\Delta_{As\text{-}built}$ = peak inter-story drift of the as-built frame

$\Delta_{Retrofitted}$ = peak inter-story drift of the retrofitted frame

A positive value for the drift reduction ratio represents a reduction in the inter-story drift. As shown in Figure 3.15, the FRP jackets reduced the inter-story drift ratios in the first story for all loading sequences applied in Phase 1. This reduction in inter-story drift ratio can be attributed to the increase in stiffness of the frame system by means of the installation of the FRP jackets and the section enlargement in the first story columns.
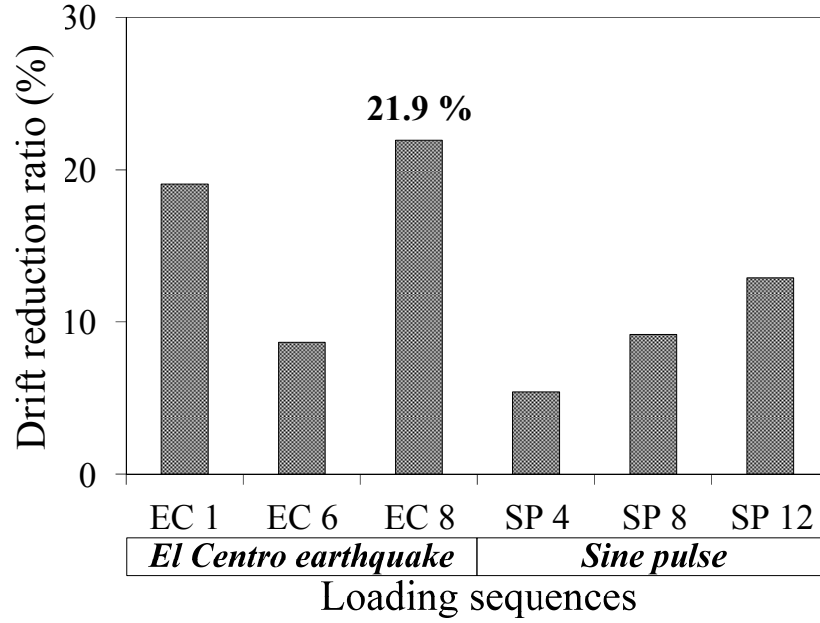
Figure 3.15. Reduction of drift in the first story

3.4.2 Column rotation reduction

The effectiveness of the FRP jacketing system can also be demonstrated by comparing the column hinge rotations in the first story between the as-built and retrofitted frames. To properly compare the column hinge rotations between those frames, the rotation values must be normalized by dividing the rotations by the corresponding measurement geometry for the LVDTs used; the change in the section size due to the column jackets in the retrofitted structure precludes a one-to-one comparison of rotations between the frames. The rotation reduction ratios on the top and bottom of the first story columns are shown in Figure 3.16. The rotation reduction ratio of a column was calculated using Equation (3.5):

$$\text{Rotation reduction ratio (\%)} = (\theta_{As\text{-}built} - \theta_{Retrofitted})/\theta_{As\text{-}built} \times 100 \tag{3.5}$$

where

51

$\theta_{As\text{-}built}$ = maximum normalized column rotation of the as-built frame

$\theta_{Retrofitted}$ = maximum normalized column rotation of the retrofitted frame

A positive value represents the reduction in the column rotation induced by the FRP jacketing system. As shown in Figure 3.16, the FRP jacketing system reduced the measured column rotations at the bottoms and tops of the first story columns, with maximum reductions of approximately 60.0 % and 40.0 %, respectively. Although the retrofitted frame experienced a stiffness reduction due to the damage observed after loading sequence SP 8, the FRP jacketing system in the first story still reduced the first story column rotations by more than 40.0 %. A similar reduction can also be observed in the larger excitation of loading sequence SP 12.
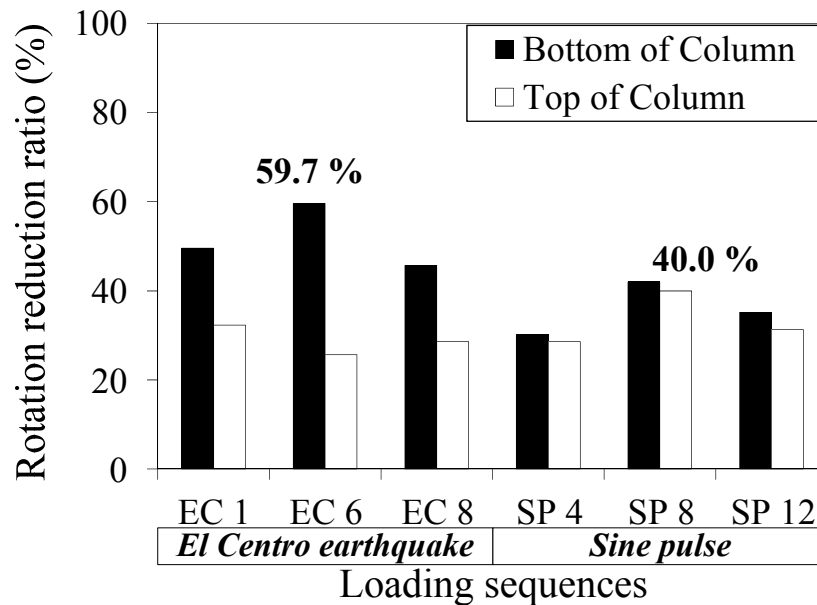
Figure 3.16. Reduction of column rotations in the first story

3.4.3 Damage sequence

Figure 3.17 compares damage sequences between the as-built and retrofitted test frames in terms of the rotation-based performance (or damage) levels given in Table 3.3. The damage levels for column and beam components are determined by comparing the measured column and beam hinge rotations with the rotation limit values of the damage levels specified in ASCE 41-13 [2014]. As illustrated in Figure 3.17, collapse prevention (CP) level damage occurred in the first story when the as-built test frame was subjected to the ultimate loading sequence. However, the retrofitted test frame did not experience the CP level damage at any level, and the LS level damage was uniformly distributed over the entire structure.
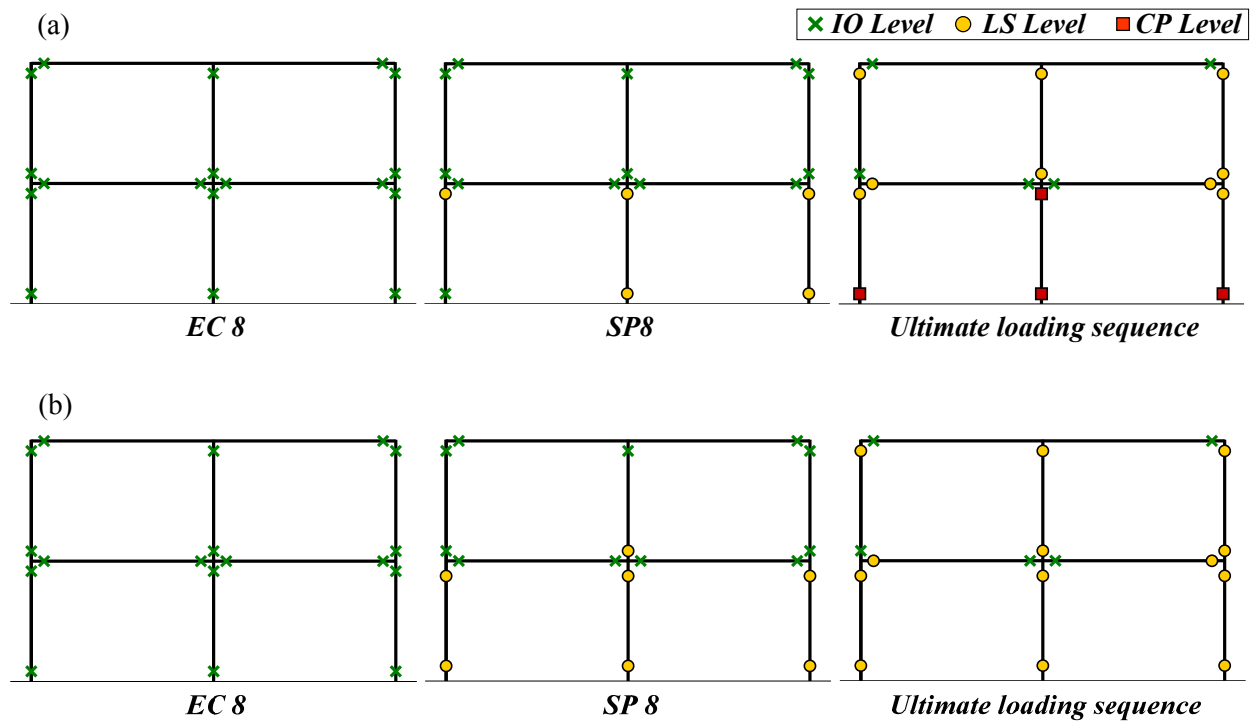
Figure 3.17. Damage sequence: (a) as-built test frame; (b) retrofitted test frame

3.4.4 Drift concentration factor

To quantify the uniformity of inter-story drifts over the entire structure, the drift concentration factors (*DCF*s) for the as-built and retrofitted frames were evaluated. The *DCF* for a story is defined as the ratio of the peak inter-story drift ratio for the considered story to the roof drift ratio [Ji et al. 2009, and Qu et al. 2011]. Values for *DCF* may be determined using Equation (3.6):

$$DCF_i = (\Delta_i / h_i) / (\delta_{roof} / H) \qquad (3.6)$$

where

DCF_i = *DCF* in the ith story

Δ_i = i^{th} inter-story drift

δ_{roof} = roof story displacement

h_i = i^{th} story height

H = entire height of the structure

Based on this definition, if the *DCF* values for all stories are equal to 1.00, the structure will develop a uniform story drift distribution, as shown in Figure 3.18(a). However, if the structure is dominated by a soft-story mechanism, as shown in Figure 3.18(b), specific stories with concentrated drift will have *DCF*s larger than 1.0 and values for stories with less damage will be closer to zero. The *DCF*s in the first and second stories (DCF_1 and DCF_2) for the as-built and retrofitted frames are shown in Figure 3.19. For the as-built frame, DCF_1 ranges between 1.5 and

1.7, and DCF_2 varies from 0.3 to 0.5. The DCFs of the as-built frame thus show evidence of a potential soft story mechanism. However, the FRP jacketing system reduced DCF_1 and simultaneously increased DCF_2, leaving both the DCF_1 and DCF_2 values closer to 1.0. It is reasonable to infer that the FRP jacketing system installed in the first story helped generate a more uniform story drift distribution for the frame, mitigating the drift or damage concentration in the first story.
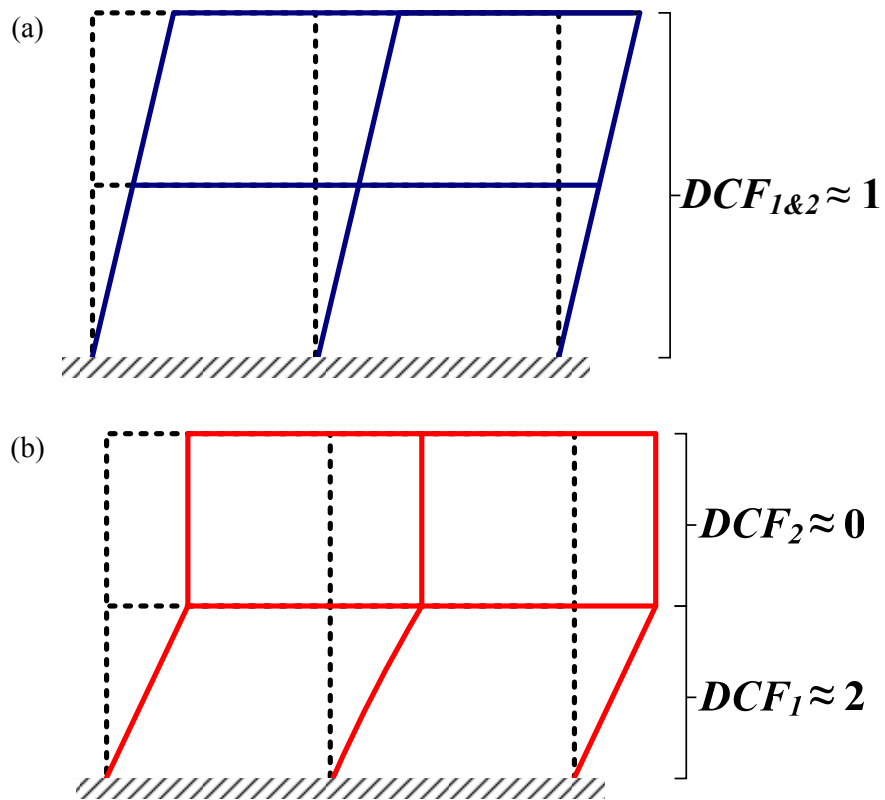
Figure 3.18. Schematic diagrams for drift distributions: (a) idealized uniform story drift distribution; (b) soft story mechanism, using drift concentration factors (*DCF*s)
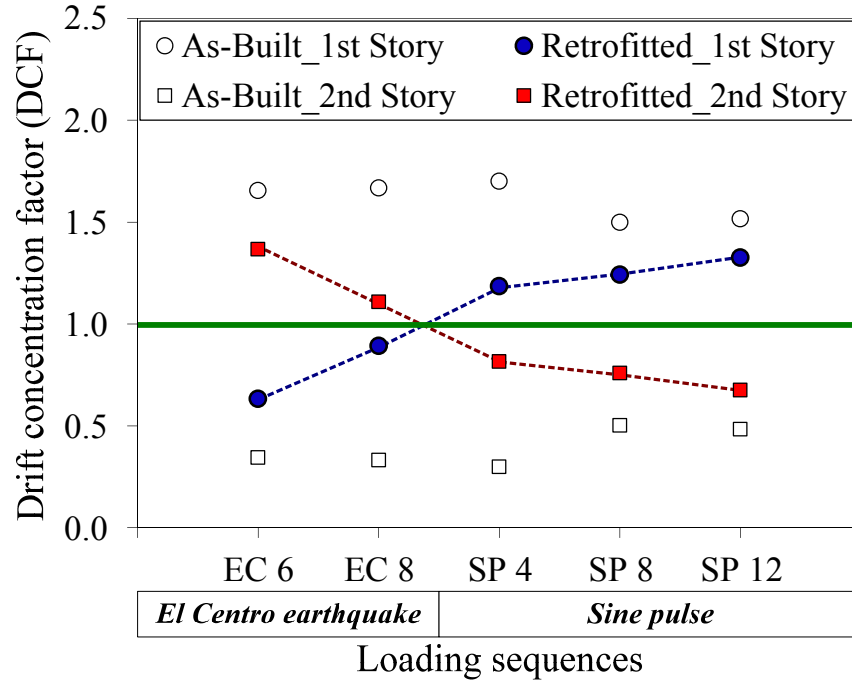
Figure 3.19. Drift concentration factors (*DCF*s) for as-built and retrofitted test frames

3.5 Summary

This chapter investigated the dynamic response of a two-story two-bay non-ductile RC frame retrofitted with an FRP jacketing system on columns in the first story. The effectiveness of the FRP jacketing system in improving the dynamic performance of the frame was evaluated by comparing its performance under seismic loading to an identical RC frame that had not been retrofitted.

As dynamic loading was increased on the retrofitted test frame during the Phase 1 sequence, the natural frequencies of the retrofitted frame decreased slightly. No visible damage was observed during this stage of the loading. Additionally, the peak inter-story drift ratios of the retrofitted frame were within the immediate occupancy (IO) level (inter-story drift ratio ≤ 1.0 %, as defined in FEMA-356 [2000]). During the Phase 2 loading sequence (sinusoidal pulse

excitation), the peak inter-story drift ratio of the first story reached the drift life safety (LS) level after observed concrete cracking and cover spalling in the slab immediately adjacent to the first story. Consistent with the drift LS level, the maximum hinge rotation of the first story columns reached the rotation LS level. Following the loading sequence where visible damage was observed in the structure, the second story columns reached the LS level. After further loading sequences were applied to the structure, the beam rotations near the two exterior joints in the first story reached the rotation LS level. This damage sequence indicates that the most vulnerable components in this structural system are the first story columns, followed by the second story column base, and then the beam elements near the exterior joints.

By comparing the dynamic responses between the as-built and retrofitted test frames, the installation of the FRP jacketing system in the first story was shown to be effective in reducing both story drift (maximum drift reduction ≈ 22 %) and column rotations in the first story (maximum rotation reduction ≈ 60 %). This improvement in performance in the retrofitted frame may be attributed to two factors: an increase in concrete confinement in the first story columns, and the section enlargement of those columns, which enhanced their lateral strength, stiffness, and ductility compared to the as-built configuration.

The installation of the FRP jacketing system on the first story columns brought the drift concentration factors (*DCF*s) for the retrofitted frame closer to 1.0. This indicates that the retrofitted frame had a more uniform drift distribution than the as-built frame, which is a better scenario to avoid damage due to a soft story mechanism. Therefore, the retrofit scheme employed in this study can help mitigate the soft-story mechanism commonly existing in RC frames designed according to pre-1971 codes for structural concrete.

CHAPTER 4. DEVELOPMENT AND VALIDATION OF FINITE ELEMENT MODEL FOR SEISMIC LOADS

4.1 Overview

The as-built test frame described in Chapter 3 represents a typical non-ductile reinforced concrete frame and has significant seismic vulnerabilities due to inadequate reinforcing details. Adequately characterizing the performance of these details is critical to the development of useful numerical and analytical models. This chapter proposes a methodology to simulate the response of such frames with and without the FRP column jacketing system installed on the first story. To reproduce the experimental responses obtained from the full-scale dynamic testing, as-built and retrofitted finite element (FE) frame models were developed using the software LS-DYNA [LSTC 2013]. The bond-slip effects between reinforcing bars and the surrounding concrete, observed in column lap-splice and beam-column joints, were modeled with one-dimensional slide line models in LS-DYNA. The model was defined by failure modes and bonding conditions observed in full-scale dynamic tests and was validated using measured experimental responses.

4.2 Structural Geometry Modeling

A three-dimensional FE frame model representing the RC frames tested in the experimental program is given in Figure 4.1. The FE frame models were developed using a half-symmetry condition, which was employed to reduce computational demands. To enforce the plane of symmetry, the two rotational degrees-of-freedom (DOF) parallel to the symmetry plane (R_x and R_z in the global coordinate system) and the translational degree-of-freedom (DOF)

perpendicular to the symmetry plane (D_y in the global coordinate system) were restrained. Additionally, the foundation bases were restrained in all translational and rotational directions, which simulated a fixed condition. Live loads in the experiment were simulated by placing steel rails on the second and third floors of the frame. These weights were converted to masses, and then equally distributed as nodal masses on each element of the floor slab using the option Element_Mass in LS-DYNA.
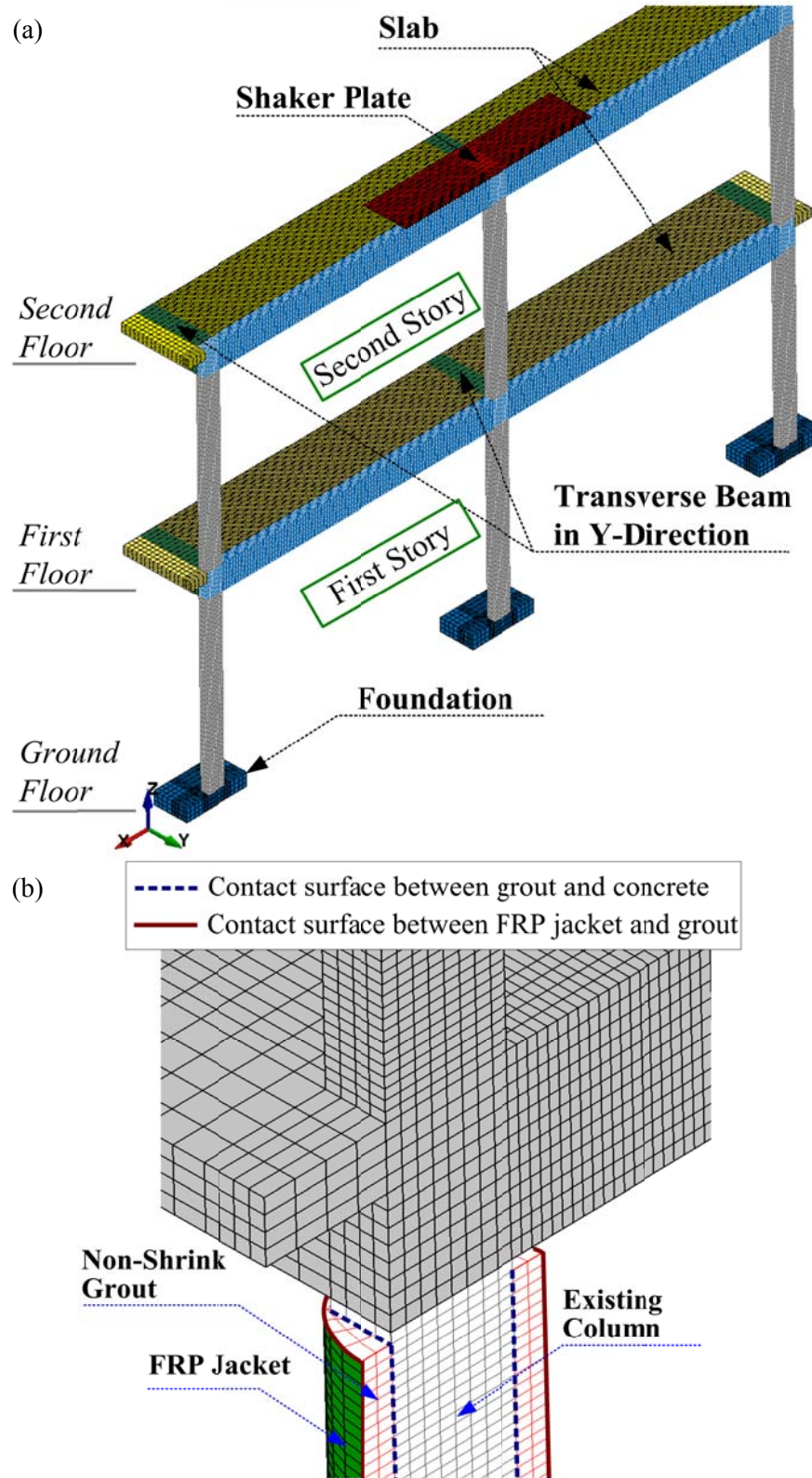
Figure 4.1. Three-dimensional view of FE frame models: (a) as-built FE frame model; (b) first story column of retrofitted FE frame model

The concrete column and beam models in the longitudinal direction (X-direction) utilized eight-node solid elements with single point integration. All reinforcing bars were modeled using two-node Hughes–Liu beam elements. The longitudinal and transverse reinforcing bars in the column and beam elements were connected to the concrete mesh nodes. The nodes that link the concrete and reinforcement mesh were shared. These shared nodes were fully bonded; however, to capture bond slip effects, the lap-splice bars in columns and straight anchorages in joint regions had separate nodes from the concrete mesh nodes. These separate nodes were linked with one-dimensional slide lines. Since the foundation, slab, and transverse beam had no significant damage during the dynamic tests, those elements were modeled using shell elements with an elastic material model (MAT001 in LS-DYNA) in order to develop a more efficient model. The elastic material model was reduced by stiffness reduction factors specified in ASCE 41-13 [2014]. To impose the shaker forces measured from the full-scale dynamic testing, a shaker plate was placed on the top of the FE frame model. The shaker plate was represented using solid elements with a rigid material (MAT020 in LS-DYNA).

Figure 4.1(b) shows the model of the FRP column jacket system on one of the first story columns for the retrofitted frame, consisting of non-shrink grout and an FRP composite shell. The non-shrink grout model utilized solid elements to provide additional confining pressures. The FRP jacket, placed on the surface of the grouting model, was modeled using shell elements with thicknesses corresponding to the FRP jackets of the retrofitted test frame. A two-ply FRP jacket (1.32 mm in thickness) on the top and bottom of the column, and a one-ply FRP jacket (0.66 mm in thickness) in the middle of the column as described in Chapter 3 were included in the model. Additionally, as illustrated in Figure 4.1(b), the FRP jacket system is assumed to have two different interface surfaces: a contact surface between the concrete and the non-shrink grout

61

models, and a contact surface between the non-shrink grout and the FRP jacket models. These interface surfaces were simulated using the LS-DYNA function CONTACT AUTOMATIC SURFACE-TO-SURFACE (referred to as "surface-to-surface contact") developed by Tabiel and Wu [2000]. In this contact function, the frictional coefficients of interface surfaces were assumed to be 0.8. This assumption allowed the model to simulate imperfect bonding in each interface surface.

4.3 Material Model

4.3.1 Concrete material

To predict concrete behavior, LS-DYNA provides several material models, such as WINFRITH_CONCRETE (MAT084, often referred to as the "Winfrith model") [Broadhouse 1986], CSCM (MAT159, referred to as the "CSC model") [Schwer and Murray 1994] and CONCRETE_DAMAGE_REL3 (MAT072R3) [Malvar et al. 1997, and Crawford et al. 2012], which is well known as the Karagozian and Case (K&C) concrete model (referred to hereafter as the "KCC model"). These models have a default parameter generation function (e.g., the unconfined compressive strength of the concrete), and capture post-peak strain softening, shear dilation, and confinement effects in concrete behavior. Wu and Crawford [2015] examined the tri-axial behavior of a single solid element modeled with three different concrete constitutive models, and compared the simulated results with tri-axial compression tests. The numerical study demonstrated that the KCC model can reproduce concrete damage behavior, softening, modulus reduction, shear dilation, and confinement effect under a wide range of confining pressures. Additionally, this KCC model has been extensively compared to experimental responses obtained from quasi-static, blast, and high-velocity impact loading tests [Wu and Crawford

62

2015]. Therefore, this study selected the KCC model to simulate the concrete behavior among the various concrete constitutive models provided in LS-DYNA.

The KCC model is characterized by three independent shear failure surfaces: the maximum surface ($\Delta\sigma_m$), yield surface ($\Delta\sigma_y$), and residual surface ($\Delta\sigma_r$). The strain hardening-softening responses in axial stress-strain behavior are established by the combination of three independent shear surfaces and a damage function, as given in Equation (4.1) and Equation (4.2) [Malvar et al. 1997, and Wu and Crawford 2015]:

$$\sigma=\eta(\lambda)\cdot[\Delta\sigma_m(P)-\Delta\sigma_y(P)]+\Delta\sigma_y(P) \text{ (strain hardening)} \qquad \lambda\leq\lambda_m \qquad (4.1)$$

$$\sigma=\eta(\lambda)\cdot[\Delta\sigma_m(P)-\Delta\sigma_r(P)]+\Delta\sigma_r(P) \text{ (strain softening)} \qquad \lambda>\lambda_m \qquad (4.2)$$

where

σ = axial stress

P = hydrostatic pressure

$\eta(\lambda)$ = damage function

λ = effective plastic strain

λ_m = effective plastic strain corresponding to $\Delta\sigma_m$

The KCC model can simulate shear dilation using a parameter ϖ. This parameter can capture the expansion of concrete as it cracks. If high confinement effects occur due to the FRP jacket, the ϖ parameter can contribute to providing a confining pressure - increasing strength

and ductility [Crawford et al. 2012]. In other words, the ϖ parameter plays a critical role in the reasonable simulation of confinement effects. Crawford et al. [2013] suggested $\varpi = 0.9$ for well-confined concrete components (FRP jacketed RC column), and $\varpi = 0.5$ or 0.75 for poorly-confined concrete components (non-ductile RC column). Based on these previous studies, this study employed a ϖ parameter of 0.9 for the retrofitted columns, and a ϖ parameter of 0.5 for the as-built columns. Table 4.1 shows the main material parameters of the KCC model for as-built and retrofitted FE frame models.

Table 4.1. Main material parameters of KCC model

Story levels	Element	As-Built FE frame		Retrofitted FE frame	
		Concrete strength (MPa)	ϖ	Concrete strength (MPa)	ϖ
First story	Column	31.5	0.5	32.8	0.9
	Beam	25.0	0.5	26.5	0.5
Second story	Column	28.5	0.5	30.3	0.5
	Beam	23.5	0.5	23.5	0.5

4.3.2 Steel material

The LS-DYNA material models, such as PLASTIC_KINEMATIC (MAT003, referred to as "elasto-plastic material model") and PIECEWISE_LINEAR_PLASTICITY (MAT024, referred to as "piecewise linear plasticity material model"), have been widely used to simulate steel behavior. The steel stress-strain curve of the elastic-plastic material model represents bilinear behavior with linear isotropic hardening. The piecewise linear plasticity material model allows the user to input an arbitrary stress-strain curve [Hallquist 2007]. The piecewise linear

plasticity material model was used in the present work to provide a more realistic simulation of the steel reinforcing bars. The parameters of this material model were defined based on the quasi-static testing results for each rebar size embedded in the test frames. The yield strengths and elastic modulus for ϕ 10, ϕ 19, and ϕ 25 steel reinforcing bars are summarized in Table 4.2. The strain corresponding to the ultimate strength was assumed to be approximately 15.0 % [Malvar 1995]. After reaching the ultimate strength, the steel material models represented softening behavior until 25.0 % strains. As shown in Figure 4.2, the selected material model was verified with the material tests discussed in Chapter 3 for ϕ 10, ϕ 19, and ϕ 25 steel reinforcing bars.

Table 4.2. Main parameters of steel material model

Rebar	Yield strength (MPa)	Ultimate strength (MPa)	Elastic modulus (GPa)
ϕ 10 (Diameter = 10 mm)	520	739	197
ϕ 19 (Diameter = 19 mm)	445	734	194
ϕ 25 (Diameter = 25 mm)	541	663	209
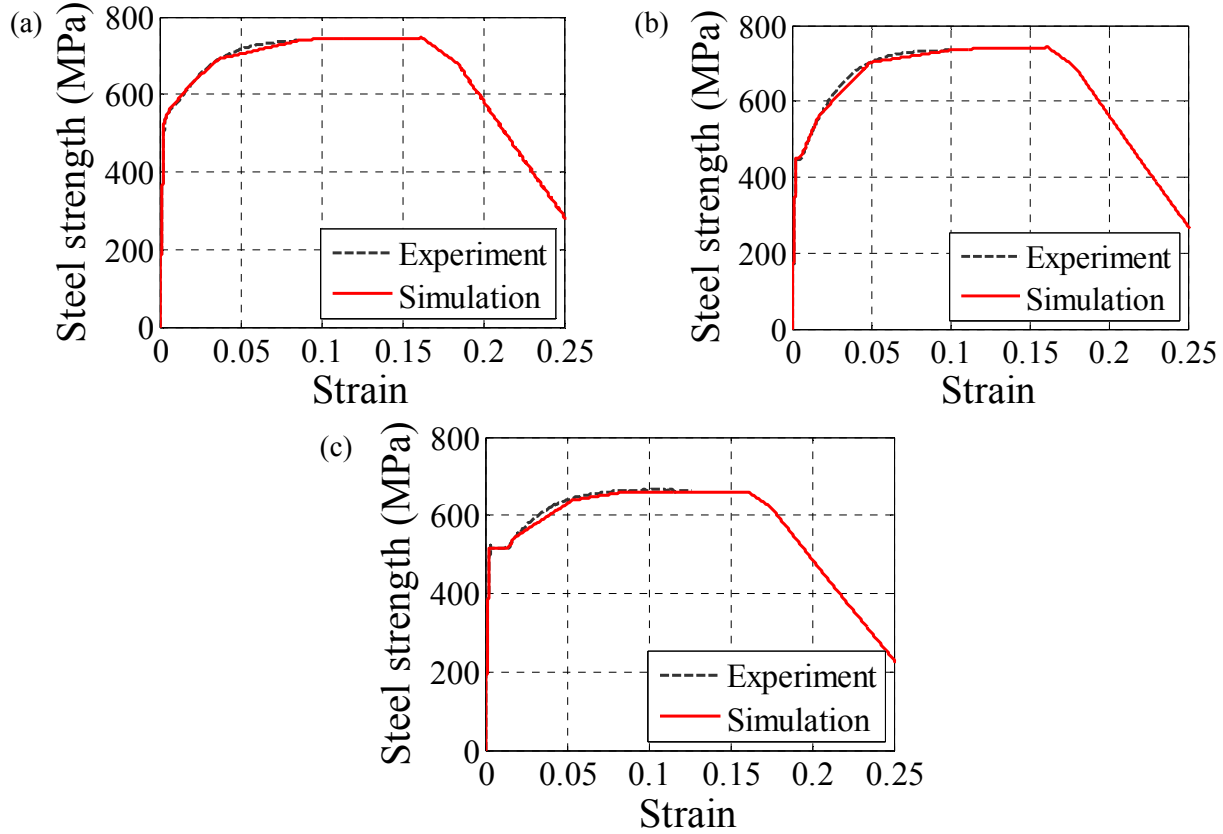
Figure 4.2. Comparison of experimental results to simulation for steel stress-strain behavior: (a) ϕ 10 steel rebar; (b) ϕ 19 steel rebar; and (c) ϕ 25 steel rebar

4.3.3 FRP composite material

This study models the prefabricated FRP jackets on the first story columns using the ORTHOTROPIC_ELASTIC (MAT002, referred to as "orthotropic material") model in LS-DYNA. This material model is characterized by an elastic modulus (E), shear modulus (G), and Poisson's ratio (v) in terms of the three local principal axes (a-, b-, and c-principal axes). Thus, the orthotropic material can simulate the directional characteristics of FRP materials [LSTC 2013]. The main parameters (E_a, G_{ab}, and v_{ab}) of the orthotropic material in the hoop direction used in this study are 95.5 GPa, 4.5 GPa, and 0.28, respectively. These modeling parameters for the FRP material were taken from the product data sheet for PileMedic^{TM} PLC150.10 [PileMedic

2009]. The failure criterion of the FRP material model was assigned 1.1 % ultimate strain using the EFFEPS card in the MAT_ADD_EROSION, which allows users to set up material failure criteria. Recent studies [Nam et al. 2009, Mutalib and Hao 2010, and Youssf et al. 2014] have utilized the orthotropic model to simulate and verify the FRP material behavior for FRP-strengthened RC structures. In particular, Youssf et al. [2014] verified the material behavior of FRP-confined concrete by using the orthotropic model for the FRP materials, which indicates that the orthotropic material is able to predict the confining pressure provided to the concrete by the FRP jacket.

4.4 Bond-Slip Model

The bond-slip effects between the steel reinforcing bars and concrete can significantly affect the structural response of RC structures [Spacone and Limkatanyu 2000, Luccioni et al. 2005, and Bao et al. 2008]. The non-ductile RC frame used in the present study had short lap-splice reinforcing bars in the columns, straight anchorage of positive (bottom) beam reinforcing bars, and no transverse reinforcement in the beam-column joint regions. Since such inadequate reinforcing details can lead to poor bonding conditions in RC structures, the bond-slip effects are critical to develop the FE frame models.

4.4.1 One-dimensional slide line model

A one-dimensional slide line model provided by LS-DYNA [LSTC 2013] can transfer interfacial shear forces between the slave nodes of the reinforcing bar beam elements and the master nodes of the concrete solid elements. The interfacial forces are proportional to the slip displacement between the slave nodes and master nodes. These one-dimensional slide line

models can simulate bond-slip effects by defining the bond shear modulus (G_s), maximum elastic

slip ($\tilde{s}_{max}$) and damage curve exponential coefficient (h_{dmg}), as given in Equation (4.3):

$$\tau \;=\; \begin{array}{ll} G_s \tilde{s}, & \tilde{s} \leq \tilde{s}_{max} \\ \tau_{max} e^{-h_{dmg} D}, & \tilde{s} > \tilde{s}_{max} \end{array} \tag{4.3}$$

The h_{dmg} parameter decays the bond shear stress with the increment of plastic slip displacement (

$\Delta \tilde{s}_p$), and D_n is the damage parameter at n^{th} step, the sum of the absolute values of $\Delta \tilde{s}_p$ (i.e.,

$D_{n+1} = D_n + \Delta \tilde{s}_p$, where n is an incremental step). As defined in Equation (4.3), the bond-slip

behavior is assumed to be bilinear, and the bond stress deterioration is initiated after reaching

τ_{max} (= $G_s \cdot \tilde{s}_{max}$).

Shi et al. [2008] modeled bond-slip interface behavior between beam elements and

surrounding concrete solid elements in an RC column using the one-dimensional slide line in LS-

DYNA for blast loading. The FE column model with bond-slip effects gives a better prediction

of the blast responses than the numerical model calibrated by Woodson and Baylot [1999]. Shi et

al. [2009] modeled bond-slip effects with the one-dimensional slide line model to simulate pull-

out responses in RC beam elements and validated the responses with experimental results. The

bond-slip parameters in the one-dimensional slide line model were calibrated based on the

experimental results. The calibrated FE models agreed well with the pull-out testing results.

Additionally, to characterize nonlinear behavior in RC beam-column assemblies, Bao et al.

[2008] developed FE models that incorporate bond-slip effects. These bond-slip effects were also

simulated with one-dimensional slide line models between beam longitudinal bars and

surrounding concrete in the panel zone. The FE models appropriately predicted the large deformation responses related to progressive collapse of the beam-column assemblies.

4.4.2 Experimental response for bond-slip

A previous experimental study on a non-ductile RC test frame [Wright 2015] identified bond-slip behavior in column lap-splice and straight anchorage (positive beam reinforcing bars in beam-column joint areas), using test results obtained from a full-scale dynamic experiment. The bond-slip behavior in the lap-splice and joint areas was identified by comparing measured hinge rotations in beams or columns to reinforcing bar strain in those areas under dynamic loads. The relationships between the peak hinge rotations and corresponding bar strains are summarized in Figures 4.3 and 4.4, respectively, for each loading sequence for the as-built and retrofitted test frames. Figure 4.3(a) shows the relationship between peak column hinge rotations in first story column bases and the corresponding bar strains for each loading sequence. If no bond-slip failure in the lap-splice regions is observed, then the peak column hinge rotations should continuously increase in accordance with the shaker force increment. Further, the bar strains should also keep increasing prior to yielding of steel reinforcing bars. However, it was observed in the experiment that the lap-splice bar strain decreased after reaching the peak bar strain, which occurred before the yielding of steel reinforcing bars. This phenomenon is believed to have occurred due to concrete cracks in the lap-splice regions (e.g., splitting cracks along the column reinforcing bars and shear cracks) that contributed to the loss of interface forces between the lap-splice bars and surrounding concrete. Figure 4.3(b) demonstrates the pull-out behavior in the positive beam reinforcing bars in the first story exterior beam-column joints. However, the maximum bar strains in the negative beam reinforcement were continuously increased due to 180º anchorage

hooks. More detailed test results of the bond-slip behavior for the as-built test frame can be found in Wright [2015].

Through the full-scale dynamic testing of the retrofitted test frame, the bond-slip responses were also observed using the same approach as the as-built test frame. Figure 4.4(a) indicates that the installation of an FRP column jacket system in first story columns can help delay the bond-slip of the column lap-splice bars since the maximum bar strains keep increasing with the peak column hinge rotations. This is due to the additional confining pressures provided by the FRP jacket system. As shown in Figure 4.4(b), strain reading in bottom reinforcing bars taken near an exterior beam-column joint indicated a decrease in bar strains after they reached a maximum value but before yielding in the bar. This decrease indicated pull-out failure in the exterior beam-column joints. Based on these observations in the full-scale dynamic tests, the bonding conditions and failure modes can be approximated for the locations where bond-slip effects are significant.
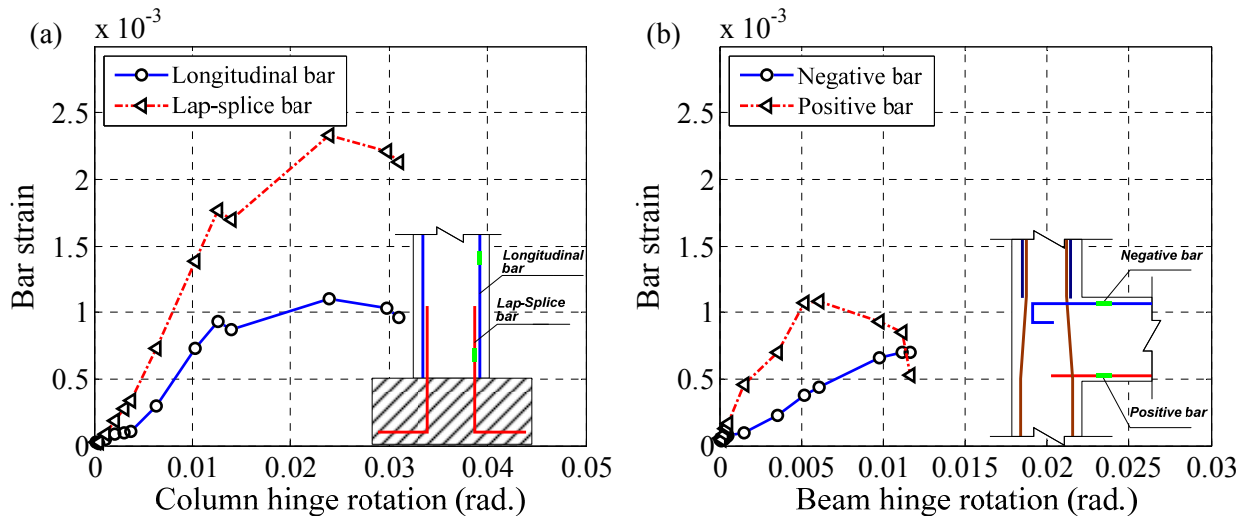
Figure 4.3. Relationships between peak hinge rotations and bar strains for the as-built test frame: (a) first story column; and (b) first story exterior beam-column joint

70
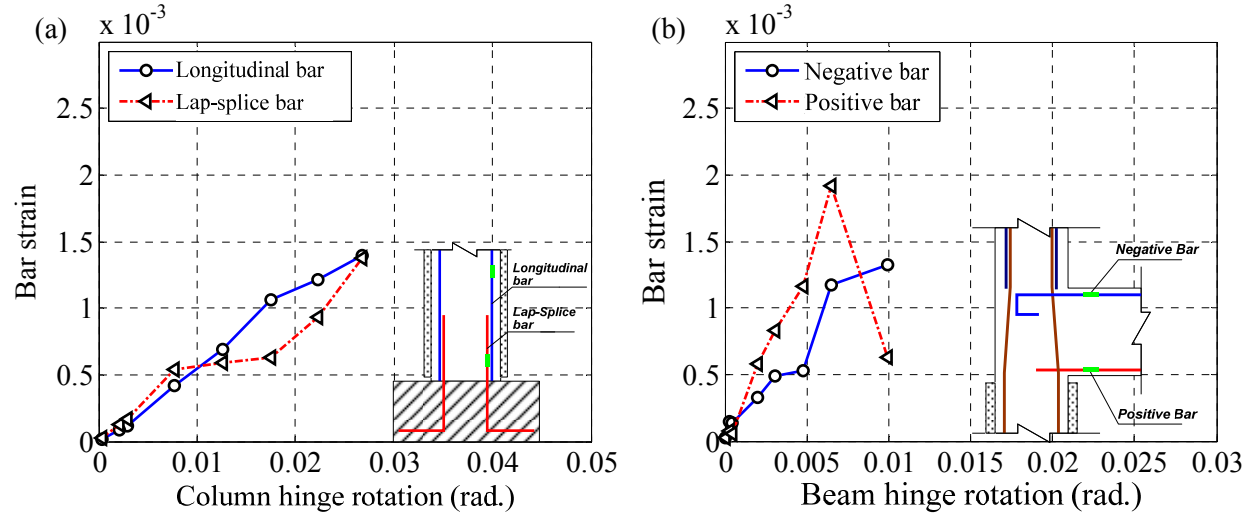
Figure 4.4. Relationships between peak hinge rotations and bar strains for the retrofitted test frame: (a) first story column; and (b) first story exterior beam-column joint

4.4.3 Numerical bond-slip model

The bond-slip performance in the FE frame models was characterized using the CEB-FIP Model Code [1990]. The model code defines the bond stress-slip relationship depending on failure modes (e.g., splitting or pull-out failure modes) and bonding conditions (e.g., good or poor conditions). The bonding condition can be determined by confining pressures regarding concrete cover and reinforcement detailing, such as column lap-splice length, transverse reinforcing details, and anchorage details in beam-column joints. Figure 4.5 compares the bond stress-slip relationships between the model code and the one-dimensional slide line model in LS-DYNA. The bond stress deterioration was captured by using the h_{dmg} parameter discussed in Section 4.4.1. The values of h_{dmg} in terms of the failure modes and bonding conditions were found by calibrating the residual bond stresses of the model code with those of the one-dimensional slide line model. The values of the h_{dmg} for good and poor bonding conditions in the

71

lap-splice failure were 0.25 and 0.065, respectively, and the value of the h_{dmg} for good and poor bonding conditions in the pull-out failure was 0.01.
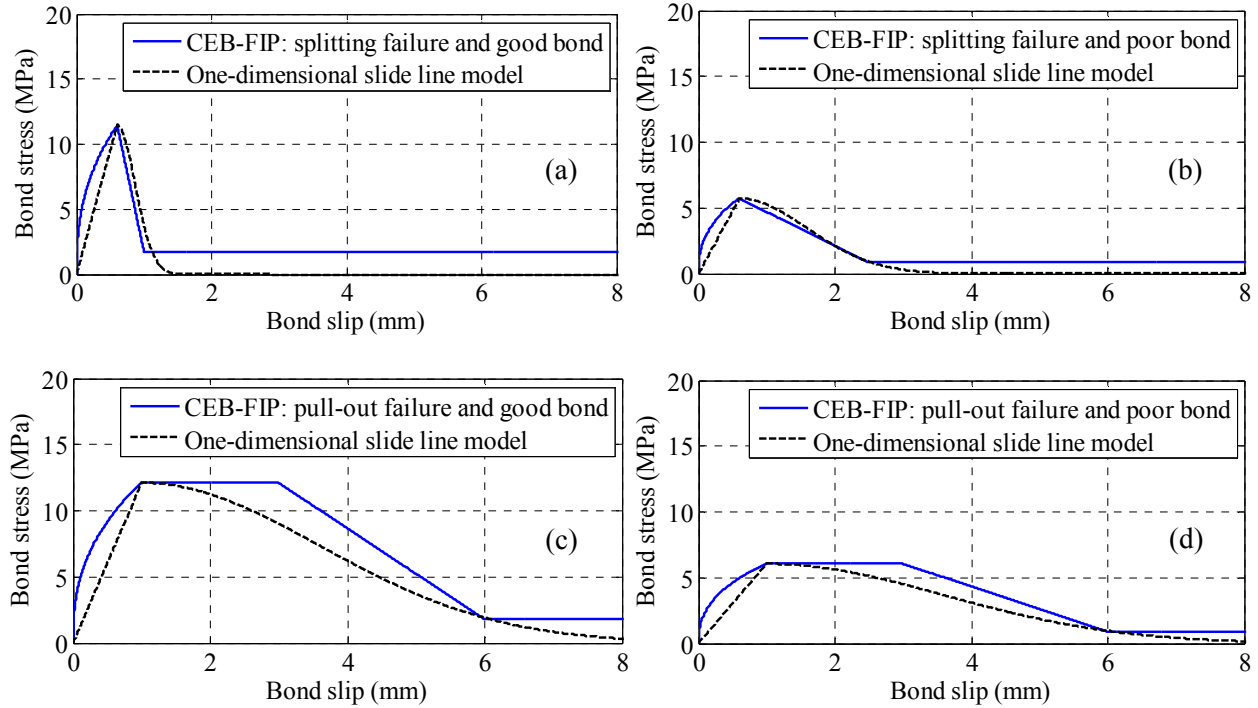
Figure 4.5. Comparisons of bond stress-slip relations between CEB-FIP Model Code and one-dimensional slide line model in LS-DYNA: (a) splitting failure and poor bond; (b) splitting failure and good bond; (c) pullout failure and good bond; and (d) pullout failure and poor bond

Figure 4.6 shows representative bond-slip modeling used in the FE frame models with respect to the failure modes and bonding conditions determined based on the full-scale experimental studies. Figure 4.7 indicates locations where bond-slip effects are thought to occur. As shown in Figures 4.6(a) and 4.6(b), the bond-slip models in the first story as-built columns and positive beam reinforcing bars were defined based on the full-scale dynamic testing results (Figures 4.3 and 4.4). The test results also demonstrated that the installation of the FRP jackets improved the bonding condition of the column lap-splice bars (Figure 4.4(a)). Thus, as shown in Figure 4.6(c), the bond-slip effects in the column lap-splice regions of the retrofitted FE frame

model were simulated with the bond stress-slip response determined by the splitting failure mode and good bonding condition. The second story columns had a longer lap-splice length and smaller spacing of column ties with seismic detailing (i.e., 135º specified angle), in order to transfer the vibration loads from the second story to the first story without an unexpected failure during the experiment. Thus, the bond-slip behavior of lap-splice zones in second story columns was modeled with a splitting failure mode and good bonding condition, as given in Figure 4.6(d).

No instrumentation was installed inside panel zones for the RC frames tested in this study, and transverse beams supporting slabs inhibited any visible inspection on the surface of panel zones during the full-scale dynamic testing. As such, this study assumes a set of failure modes and bonding conditions between the column reinforcing bars and the surrounding concrete inside the panel zones. Previous experimental studies [Engindeniz 2008, Akguzel 2011, and Park and Mosalam 2012] on non-ductile beam-column joints constructed prior to 1970s, which have no transverse reinforcing bars inside the panel zones, detected visible damage such as shear cracks and splitting cracks along column reinforcing bars. In particular, the splitting cracks resulted in confinement losses between the column reinforcing bars and surrounding concrete, and these confinement losses can produce significant bond-slip effects. The second story panel zones, as shown in Figures 4.6(e) and 4.7, had transverse beam reinforcing bars, similar to current seismic design requirements. These can minimize bond-slip effects for the column reinforcing bars inside panel zones. Therefore, this study assumes bond-slip conditions for the column reinforcing bars in the panel zones as the splitting failure mode with poor bonding condition in the first story (Figure 4.6(b)) and the splitting failure mode with good bonding condition in the second story (Figure 4.6(e)).
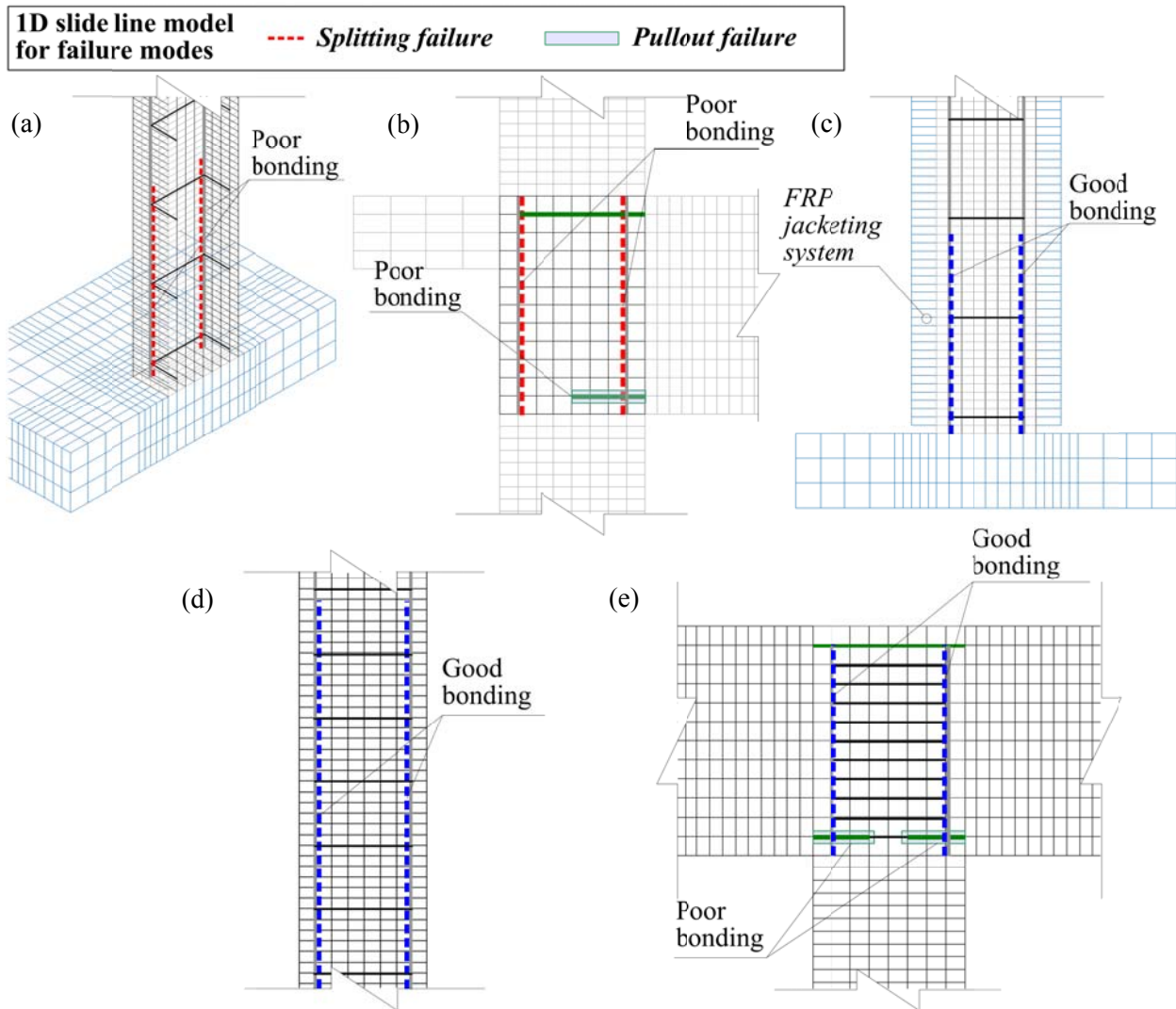
Figure 4.6. Examples of bond-slip modeling for failure modes and bonding conditions in LS-DYNA: (a) first story as-built column; (b) first story exterior beam-column joint; (c) first story retrofitted column; (d) second story column; and (e) second story interior beam-column joint
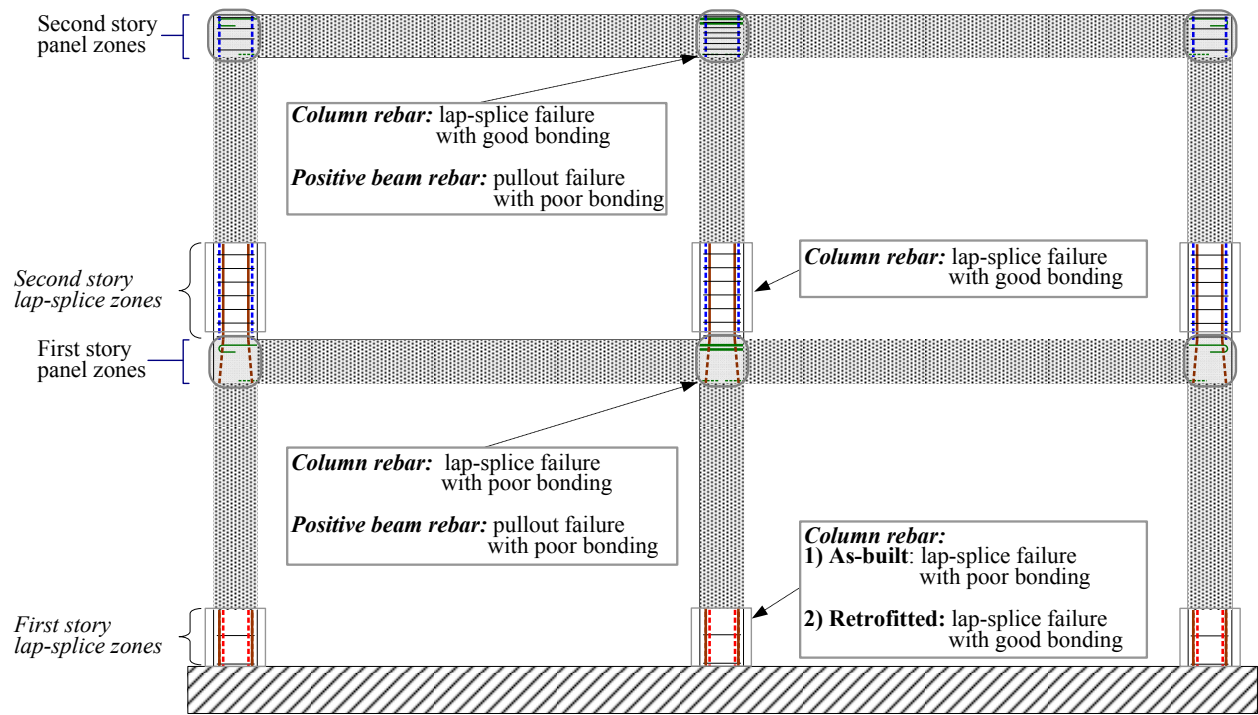
Figure 4.7. Bond-slip model locations for the FE frame models

4.5 Validation of As-Built and Retrofitted Frame Models

4.5.1 Shaker forces

During full-scale dynamic testing, the test frames were vibrated by forces induced from a hydraulic linear shaker on the roof. The linear shaker generated two different types of excitations: seismic and sine vibrations. The amplitudes of the shaker force in each input excitation were scaled by the increase in the target displacement of the linear shaker. To verify elastic and inelastic responses, this study selected two different types of loading scenarios for each FE frame model: the 1940 El Centro (EC) earthquake with 203 mm (≈ 8 inch) target displacement (EC 8) and double sine pulse (SP) vibration with 660 mm (≈ 26 inch) target displacement (SP 26, ultimate loading scenario) for the as-built FE frame model, and EC 8 and double sine pulse (SP) vibration with 508 mm (≈ 20 inch) target displacement (SP 20, ultimate

75

loading scenario) for the retrofitted FE frame model. The seismic and sine vibrations were applied to the rigid plates of the FE frame models as shaker forces. These shaker forces ($F(t)$) were computed as given in Equation (4.4):

$$F(t) = -m_s \ddot{x}_s(t) \tag{4.4}$$

where

$F(t)$ = Shaker force

m_s = Mass of the linear shaker

$\ddot{x}_s(t)$ = Absolute acceleration of the shaker

This acceleration data was measured by an accelerometer, which was mounted directly to the shaker mass in the in-plane direction. To eliminate noise in the measured acceleration, the acceleration data was filtered using a median filter function provided in MATLAB [MathWorks 2014]. The filtered and measured shaker accelerations for the as-built test frame are plotted in Figure 4.8 with EC 8 in Figure 4.8(a) and SP 26 in Figure 4.8(b).
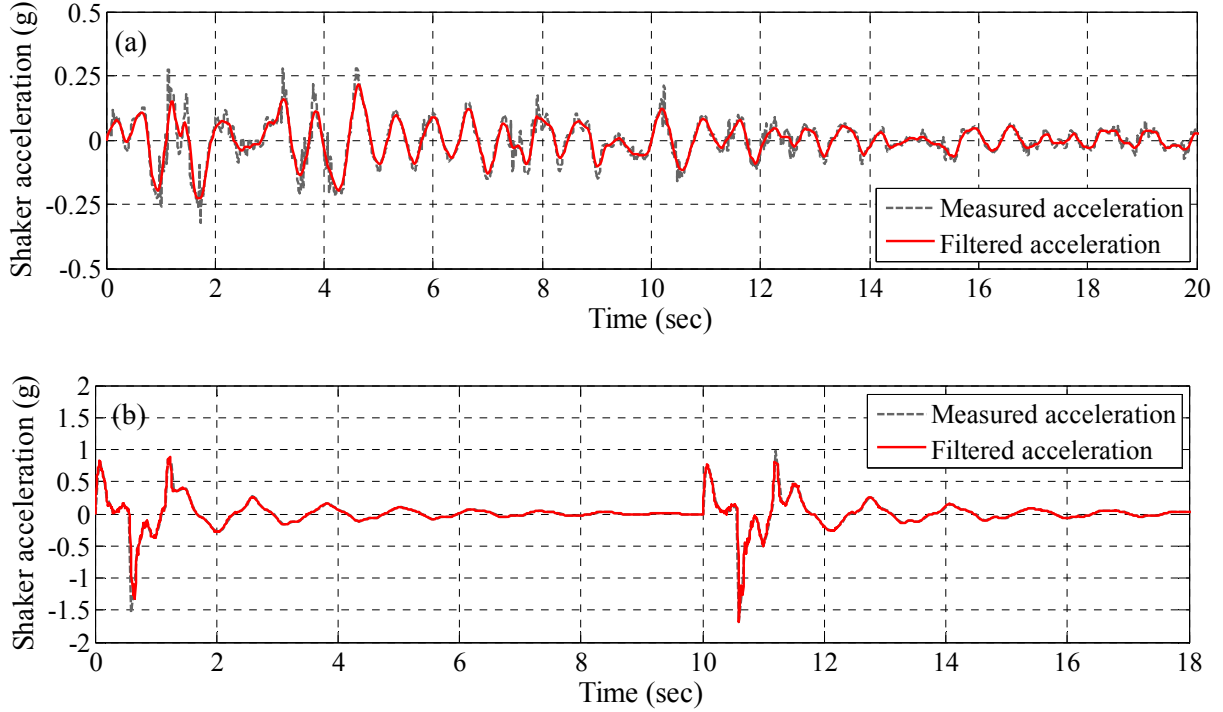
Figure 4.8. Measured and filtered shaker accelerations: (a) seismic excitation, 1940 El Centro earthquake (EC 8); and (b) double sine pulses (SP 26)

4.5.2 As-built FE frame model

Figure 4.9 compares displacement time history responses between the experimental and simulated results in the first and second stories for the as-built RC frame under the EC 8 loading. As observed in the full-scale dynamic tests, this loading scenario did not produce any significant damage in the structure [Wright 2015]. Thus, the bond-slip effects were expected to be marginal in this loading scenario, which is used to attempt to identify the dynamic behavior of the frame within the elastic range. The as-built FE frame model predicted the experimental results in terms of the response period over the full range of time. The maximum absolute story displacement of experimental and simulated responses at t_1 (= 1.33 seconds) and t_2 (= 4.19 seconds) are plotted in Figures 4.10(a) and 4.10(b), where t_1 and t_2 denote the time at which the first and second stories had the maximum displacements in the displacement time history responses measured from the

experiment, respectively. The FE frame model underestimated the maximum displacement at time t_1 by approximately 10.0 % (Figure 4.10(a)), and it overestimated the maximum displacement at time t_2 by approximately 9.0 % (Figure 4.10(b)). Figure 4.11 shows the peak inter-story drift ratios obtained from the experiment and simulation. The peak inter-story drift ratios of the simulated results were plotted at the time when the maximum drift response occurred for each story level. While the peak inter-story drift ratio in the first story was approximately 4.0 % lower than the experimental results, the peak inter-story drift ratio in the second story was approximately 10.0 % higher than the experimental results.
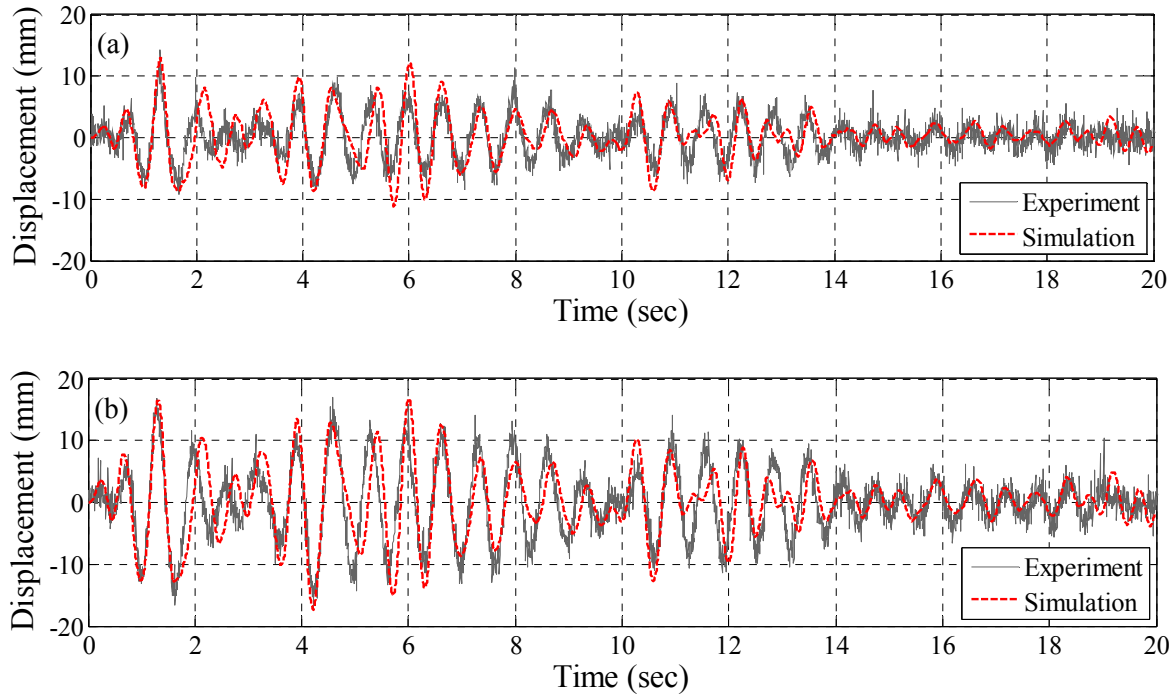
Figure 4.9. Comparison of time-history responses for the as-built FE frame model between experimental and simulated responses: (a) first story; (b) second story
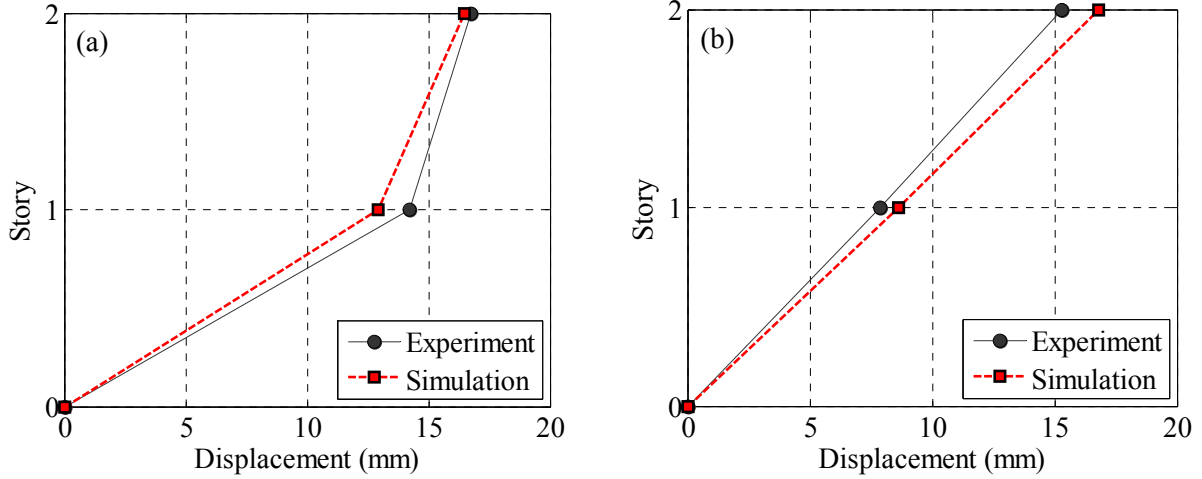
Figure 4.10. Comparison of story displacements for the as-built FE frame model between experimental and simulated responses: (a) t_1 time step; (b) t_2 time step
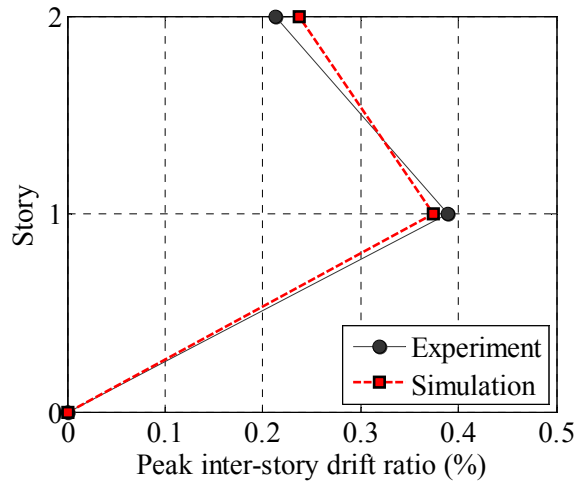
Figure 4.11. Comparison of peak inter-story drift ratios for the as-built FE frame model between experimental and simulated responses under EC 8

Figure 4.12 shows the experimental and simulated time history responses in the first and second stories under the SP 26 loading. Overall, the simulated and experimental results were in good agreement in terms of the response periods. The maximum absolute story displacements for the first and second stories were found at $t_1 = 11.44$ seconds and $t_2 = 11.50$ seconds, respectively. The story displacements at times t_1 and t_2 are plotted in Figures 4.13(a) and 4.13(b), respectively.

The maximum simulation variation for the story displacements of the FE frame model at times t_1 and t_2 was approximately 7.0 % and 8.0 %, respectively. Figure 4.14 compares the peak inter-story drift ratios between experiment and simulation. The peak inter-story drift ratio in the second story was overestimated by approximately 9.0 %.
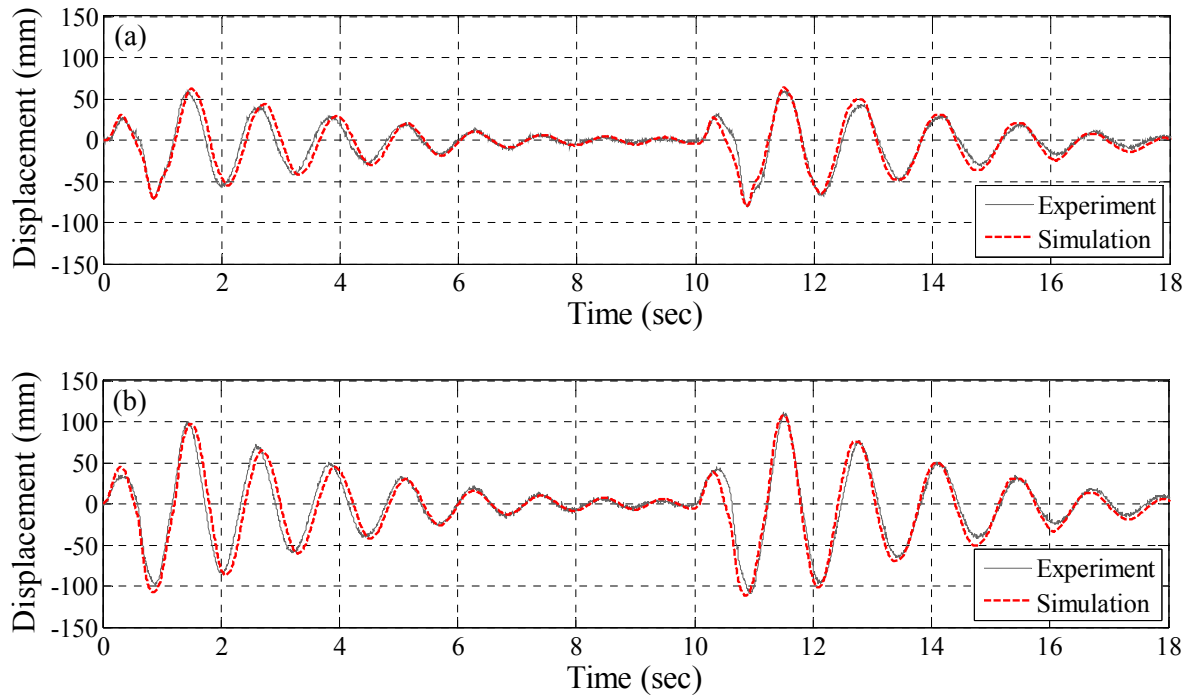
Figure 4.12. Comparison of time-history responses for the as-built FE frame model between experimental and simulated responses under SP 26: (a) first story; (b) second story
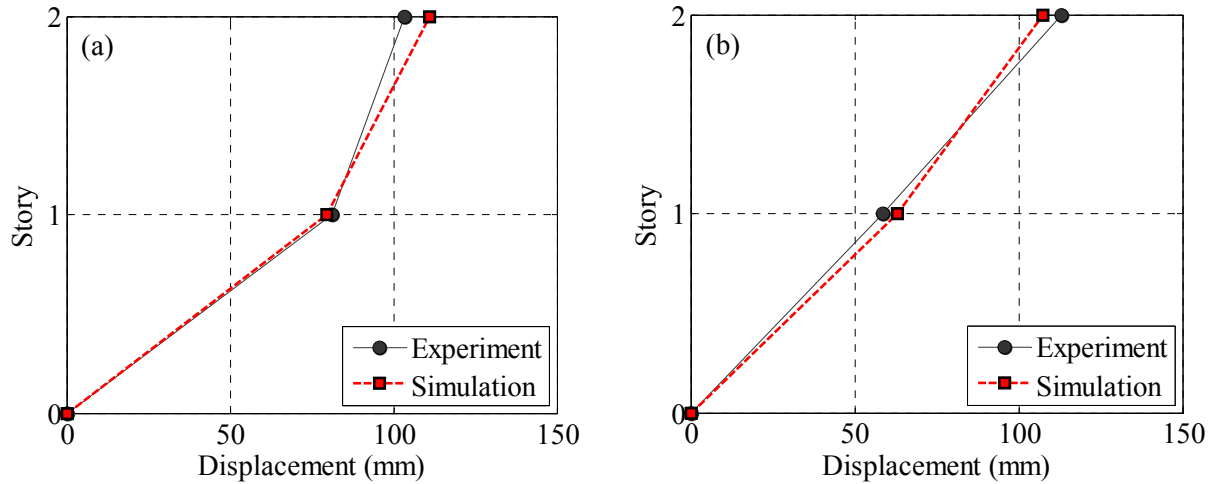
Figure 4.13. Comparison of story displacements for the as-built FE frame model between experimental and simulated responses under SP 26: (a) t_1 time step; (b) t_2 time step
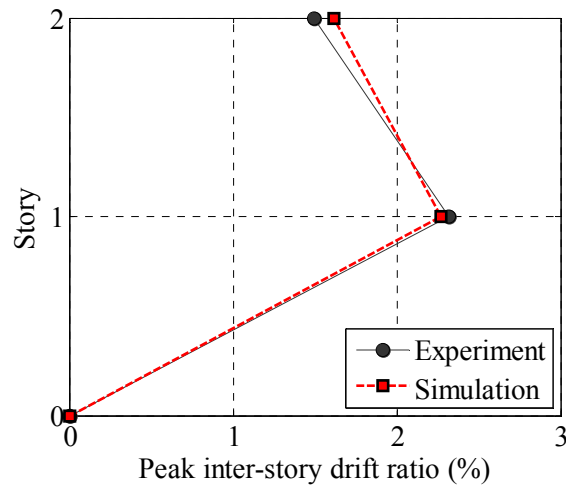
Figure 4.14. Comparison of peak inter-story drift ratios for the as-built FE frame model between experimental and simulated responses under SP 26

Overall, the variation between the simulated and experimental responses is estimated to be below 10.0 %. This variation is attributed to some of the assumptions made in the FE frame model. First, while the steel rails placed on the first and second floors to simulate live loads slid along the slab slightly during the experiments, the masses in the FE frame model were modeled to be fixed (i.e., fixed mass condition). Secondly, the test frame was vibrated under sequential

81

loading scenarios. However, the FE frame model was assumed to be non-damaged under the selected loading scenarios. Finally, to reduce the computational time of the FE frame model, slab, transverse beam, and foundation elements (i.e., non-critical elements where no significant damage was found from the full-scale dynamic testing), were simplified using an effective stiffness. The effect of these assumptions would be expected to lead to slight variations between experimental and simulated responses. Nevertheless, the FE frame model was able to capture the dynamic responses in terms of the response periods, story displacements, and inter-story drift ratios. In particular, the full-scale dynamic tests demonstrated that the dynamic responses of the as-built test frame were significantly affected by bond-slip behavior in the first story column bases and exterior beam-column joints under the SP 26 loading. Simulations using the bond-slip modeling procedure employed in the present work result in maximum displacements in the model within 10.0 % of those observed during the experimental investigation under SP 26 loading.

4.5.3 Retrofitted FE frame model

The dynamic responses of the retrofitted FE frame model were evaluated using the same basic approach that was applied to the as-built FE frame model. The experimental responses of the retrofitted test frame were gathered from the full-scale dynamic test described in Chapter 3. Figure 4.15 shows experimental and simulated displacement time history responses of the retrofitted frame under the EC 8 loading. As illustrated in Figures 4.15(a) and 4.15(b), the retrofitted FE frame model captureed the experimental results in terms of the response period in entire time steps. The maximum absolute story displacements at $t_1 = 1.06$ seconds and $t_2 = 4.40$ seconds are plotted in Figures 4.16(a) and 4.16(b), respectively. The first story displacement at

time t_1 was underestimated by approximately 9.8 % in the simulation, while the the first story displacement at time t_2 was underestimated by approximately 6.7 % in the FE frame model. Figure 4.17 compares the peak inter-story drift ratios of the retrofitted frame between the experiment and simulation. The maximum variation for the inter-story drift ratio was estimated within 10.0 %.
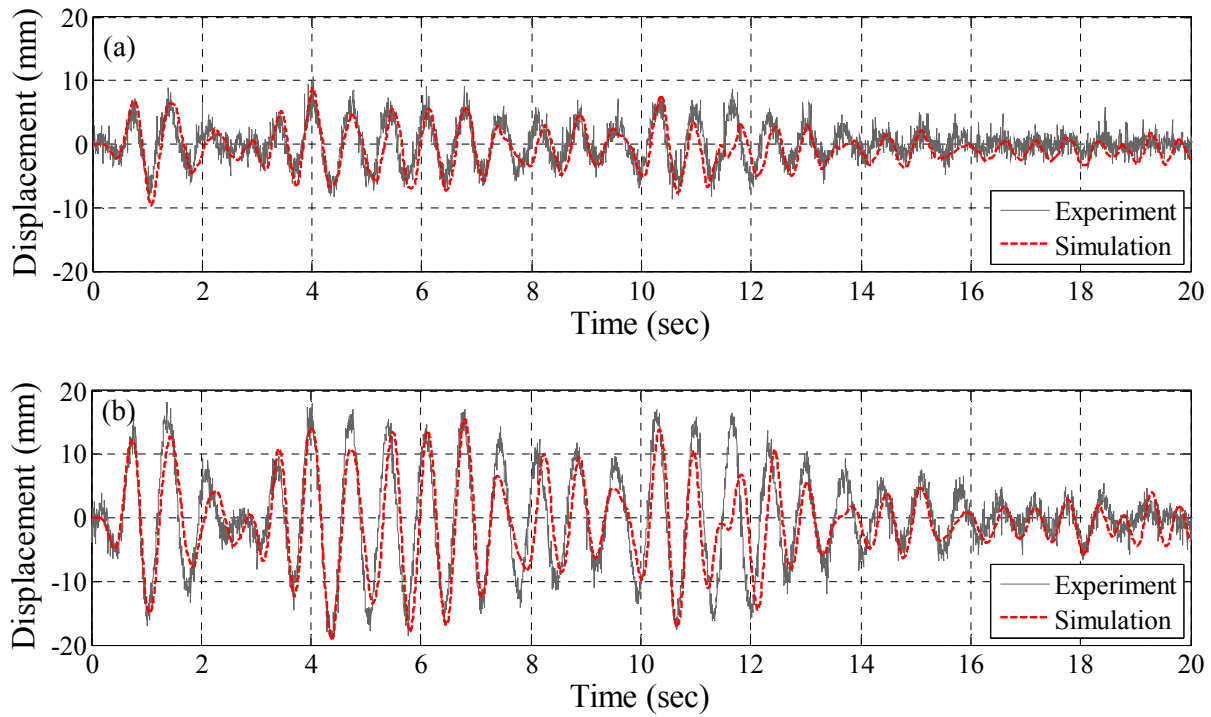
Figure 4.15. Comparison of time-history responses for the retrofitted FE frame model between experimental and simulated responses under EC 8: (a) first story; (b) second story
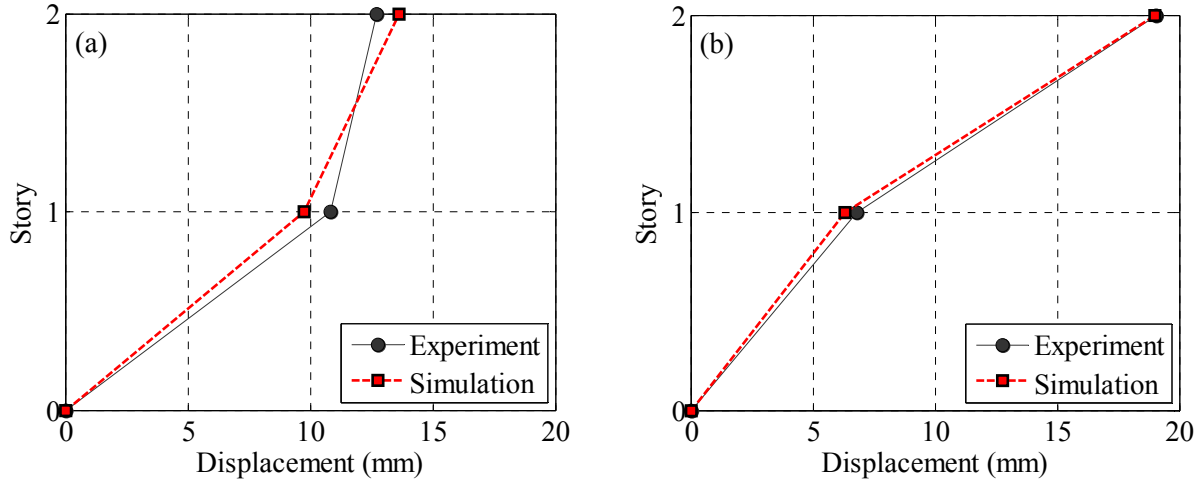
Figure 4.16. Comparison of story displacements for the retrofitted FE frame model between experimental and simulated responses under EC 8: (a) t_1 time step; (b) t_2 time step
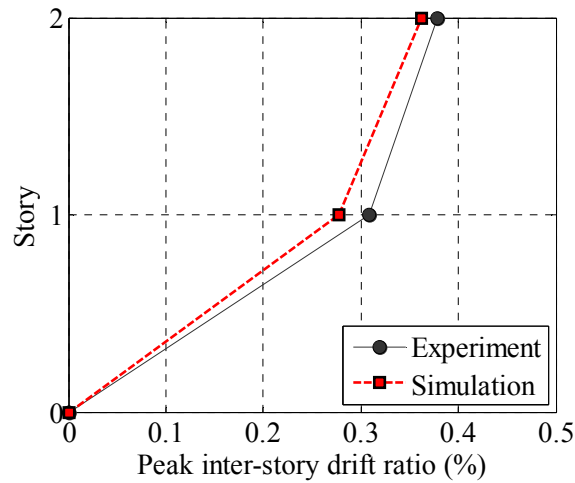
Figure 4.17. Comparison of peak inter-story drift ratios for the retrofitted FE frame model between experimental and simulated responses under EC 8

Figure 4.18 illustrates displacement time history responses under SP 20 (the ultimate loading scenario for the retrofitted test frame). The FE frame model can capture the response periods before the beginning of a second loading cycle. However, the response periods were slightly overestimated during the second loading cycle under SP 20. This is thought to be due to structural damage accumulation induced by the first loading cycle under SP 20. Figure 4.19

compares experimental and simulated story displacements at t_1 = 6.18 seconds and t_2 = 6.23 seconds. The FE frame model underestimates the maximum story displacement by approximately 5.5 % at time t_1, while it overestimates the maximum story displacement by approximately 4.8 % at time t_2. Figure 4.20 shows the experimental and simulated peak inter-story drift ratios. The peak inter-story drift ratio was underestimated by approximately 11.5 % when compared to the experimental results in the second story. This variation in the peak inter-story drift ratio is acceptable because the previous studies on numerical modeling of large-scale RC structures [Kunnath et al. 1990, Martinelli and Filippou 2009, Deaton 2013, Abdelkarim and ElGawady 2015] accepted 10.0 % to 20.0 % variations between experimental and simulated responses.
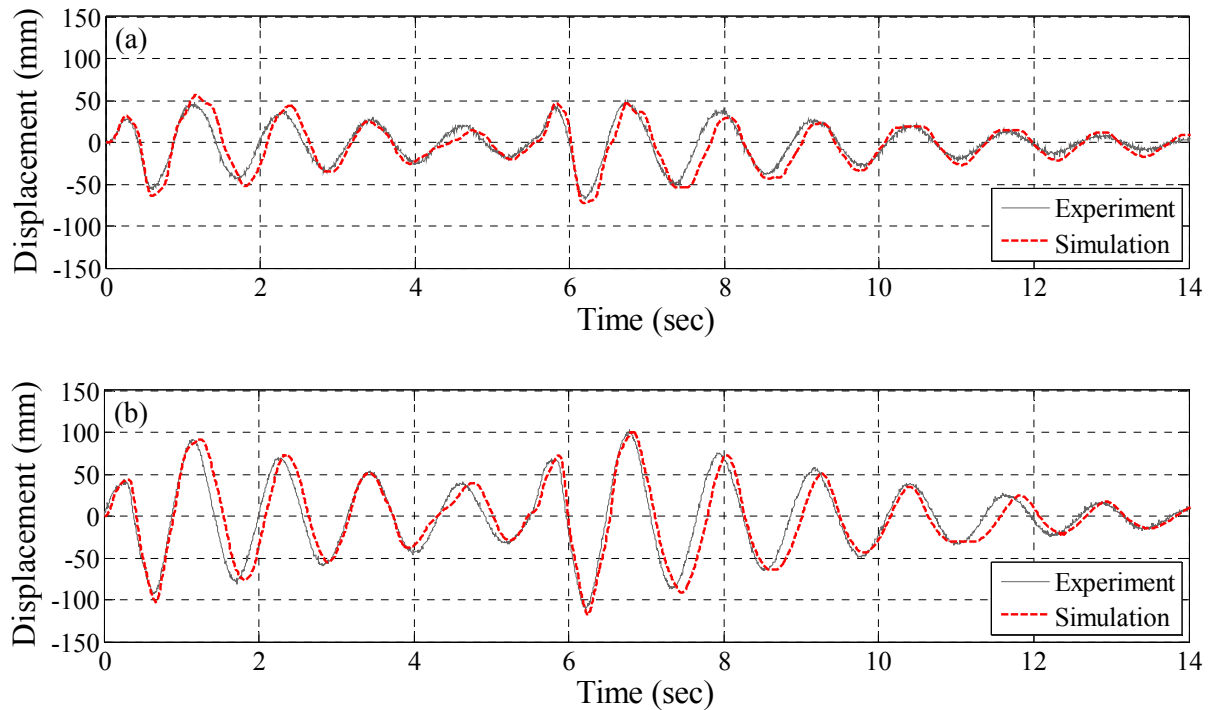
Figure 4.18. Comparison of time-history responses for the retrofitted FE frame model between experimental and simulated responses under SP 20: (a) first story; (b) second story
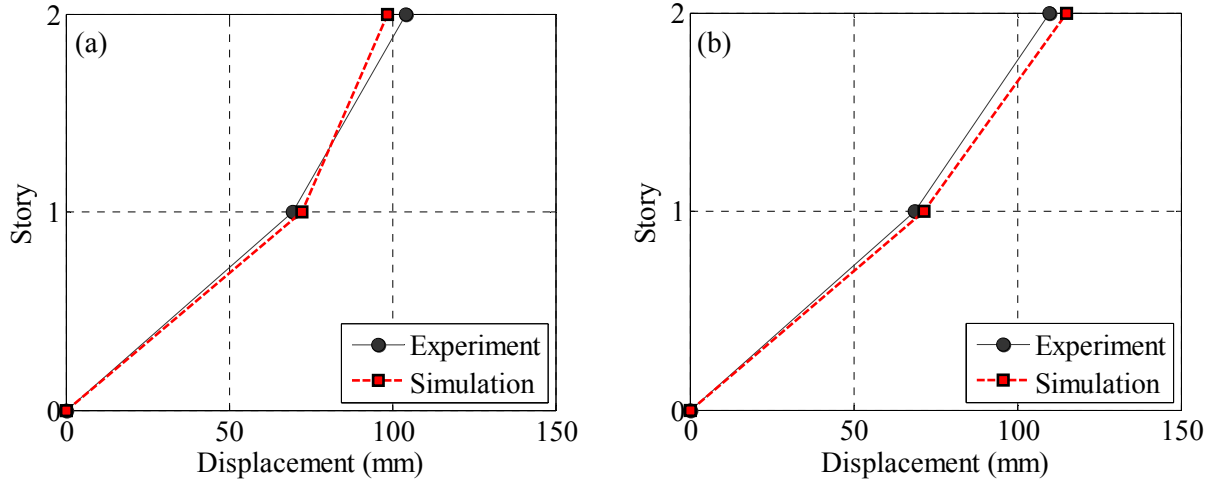
Figure 4.19. Comparison of story displacements for the retrofitted FE frame model between experimental and simulated responses under SP 20: (a) t_1 time step; (b) t_2 time step
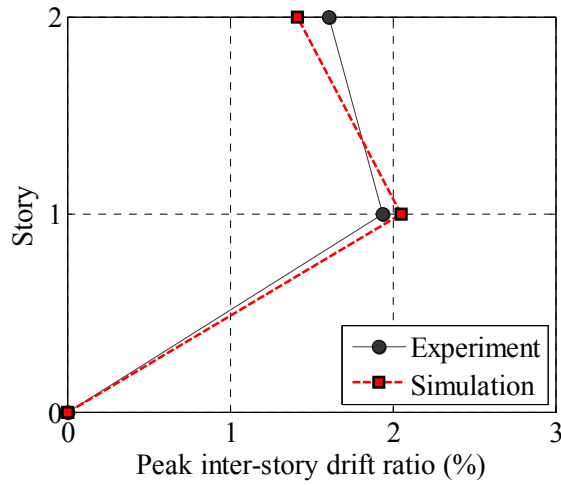
Figure 4.20. Comparison of peak inter-story drift ratios for the retrofitted FE frame model between experimental and simulated responses under SP 20

4.6 Effects on Bond-Slip Modeling

To investigate the necessity of including bond-slip performance in simulations, the dynamic responses of the FE frame models described in the previous sections (referred to as "true bond-slip") were compared to those of FE frame models with two different bond-slip conditions: (1) full bond-slip effects with all good bonding conditions (referred to as "good bond-slip"), and (2)

no bond-slip effects because of perfect bonding between reinforcing bars and surrounding concrete (referred to as "no bond-slip"). True bond-slip models, described in Section 4.4.3, have combinations of good and poor bonding conditions based on reinforcing detailing in column lap-splice and panel zones. Good bond-slip models use the good bonding condition in all possible areas where bond-slip effects occur, regardless of the reinforcing detailing. No bond-slip models deactivate the one-dimensional slide line models in the column lap-splice and panel zones, and the beam elements are merged with the nodes of concrete solid elements (i.e., perfect bonding between reinforcing bars and concrete material). Those effects were estimated under each ultimate loading scenario (i.e., SP 26 for as-built FE frame model, and SP 20 for retrofitted FE frame model) because bond-slip effects were marginal in the elastic range due to negligible slip displacements between the reinforcing bars and surrounding concrete.

Figure 4.21 shows roof time-history responses of the true bond-slip, good bond-slip, and no bond-slip models. Figure 4.22 compares maximum simulated responses of true bond-slip models with those of the no bond-slip models for the first and second sine vibrations. For the as-built frame models, as shown in Figure 4.21(a), the overall responses of the no bond-slip model were significantly less than those of the true bond-slip model. The maximum response of the no bond-slip model in the first sine vibration was approximately 39.0 % lower than that of the true bond-slip model (Figure 4.22). The main reason for this significant difference is that the models which used no bond slip effects exhibited perfect bonding between the steel reinforcing bars and the surrounding concrete in the lap-splice and panel zones, which greatly exaggerated the overall stiffness of the area.

The dynamic responses of the good bond-slip model were also less than those of the true bond-slip model. The maximum differences between the true bond-slip and good bond-slip

models for first and second sine vibrations were approximately 22.0 % and 17.0 %, respectively (Figure 4.22). The good bond-slip model used the good bonding condition in poor bonding regions such as first story lap-splice and panel zones, and this inappropriate bonding condition resulted in higher bonding stiffness and stresses between reinforcing bars and surrounding concrete in these areas.

As shown in Figure 4.21(b), the overall responses of the no bond-slip and good bond-slip models were slightly lower than the response simulated using the true bond-slip model for the retrofitted frame. In particular, during the first sine vibration of the simulations, the maximum responses of the no bond-slip and good bond-slip models were approximately 13.0 % and 8.0 % lower than those of the true bond-slip model. These slight differences are due to the effectiveness of the FRP column jacket system in the first story columns, which delayed bond-slip effects by minimizing concrete damage within the first story lap-splice and panel zones in the early steps of the simulations. In other words, during the early run-time, the effects of bond-slip models for the retrofitted FE frame models were marginal. However, as the loading increased, the dynamic response of the no bond-slip model was approximately 25.0 % less than that of the true bond-slip model. This is because the assumption of the no-bond slip model, in which the reinforcing bars are perfectly bonded with the surrounding concrete in the lap-splice and panel zones, exaggerated bonding stiffness in all possible bonding zones.

Figure 4.22 shows the variation between the good bond-slip model and the true bond-slip model during the second sine vibration; the variation was higher than that which was measured during the first sine vibration because of the use of a bond-slip model with inappropriate bonding conditions in the first story panel zones. This modeling assumption failed to appropriately predict reasonable bond-slip behavior during the second sine vibration.
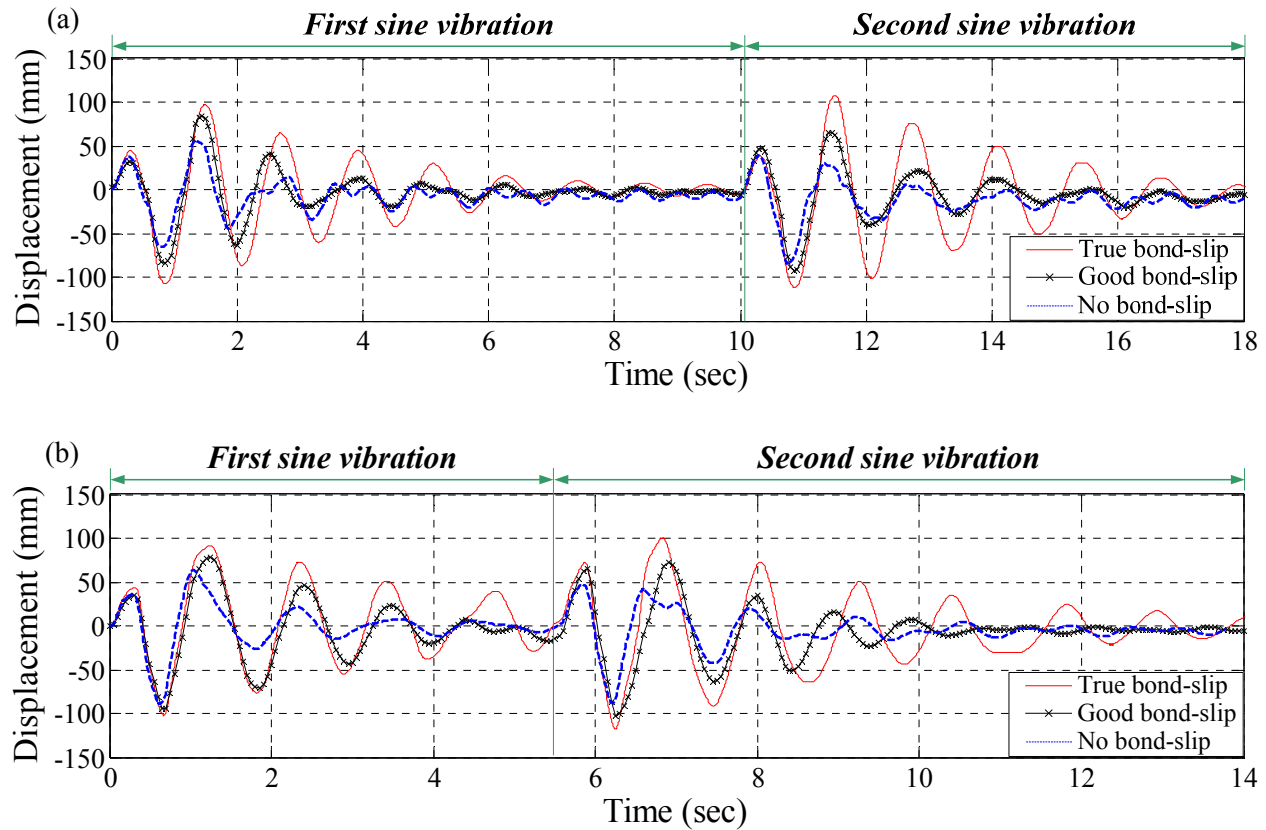
Figure 4.21. Roof time-history responses of true bond-slip, good bond-slip, and no bond-slip models: (a) as-built FE frame model; and (b) retrofitted FE frame model
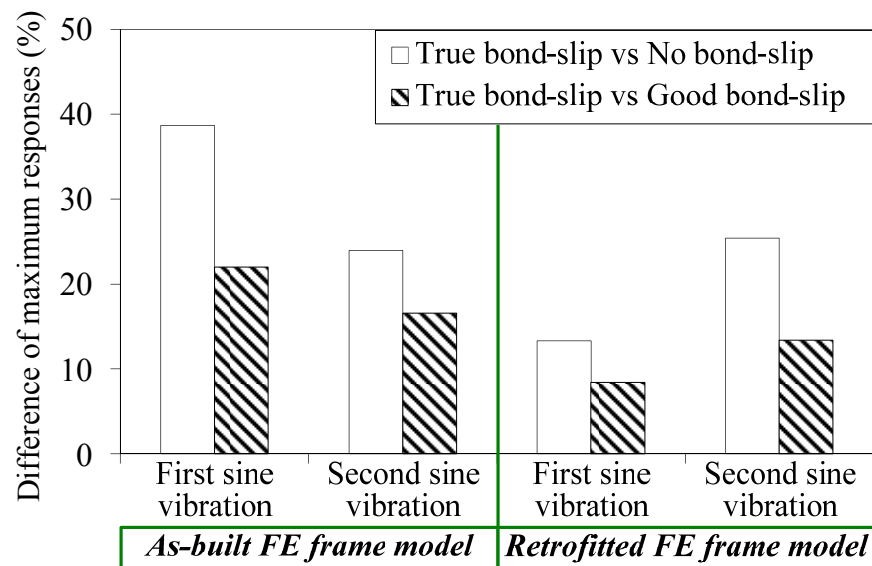
Figure 4.22. Comparison of maximum responses for first and second sine vibrations

4.7 Summary

This chapter described the development of finite element models of the full-scale as-built (non-ductile) and retrofitted test frames subjected to dynamic loads using LS-DYNA [LSTC 2013]. Results from the full-scale experiments indicated that bond-slip effects significantly contributed to the soft-story behavior of the as-built test frame. Based on these full-scale experiments, specific bonding performance conditions and failure modes were identified for locations where bond-slip effects were expected. The bond-slip behavior was modeled using one-dimensional slide line models between the reinforcing bars and surrounding concrete. The developed FE frame models with appropriate bonding conditions in the lap-splice and panel zones (i.e., true bond-slip models) were simulated under seismic and sine vibrations (ultimate loading sequences) measured from the full-scale dynamic tests. The simulated results were compared with the experimental responses for the frames under seismic and sine vibrations. For story displacements and inter-story drifts, the variation between the simulated and experimental results was found to be within 12.0 %.

In order to explore the effect of the bond-slip models on the simulated responses, the frame models with various bonding performance conditions (i.e., true bond-slip, good bond-slip, and no bond-slip models in Section 4.6) were simulated under the ultimate loading sequences, which induced bond-slip behavior in lap-splice and/or panel zones in the full-scale dynamic testing. The simulated results for the good bond-slip and no bond-slip models were underestimated compared to the true bond-slip models because the inappropriate bond-slip models exaggerated the bonding properties in lap-splice and panel zones, where the bond-slip behavior occurred. Therefore, the experiment-based bond-slip modeling process utilized in this study is useful in developing an accurate numerical model.

CHAPTER 5. DEVELOPMENT AND VALIDATION OF FINITE ELEMENT MODEL FOR BLAST LOADS

5.1 Overview

This chapter presents a methodology to simulate the blast response of FE frame structures with and without FRP column jackets using LS-DYNA [LSTC 2013]. Various blast modeling techniques were initially reviewed and the techniques capable of reproducing accurate blast loading parameters were selected. A previous experimental study using high explosives was used to verify the modeling methodology. Additionally, to predict blast responses of as-built and retrofitted FE frame models, the modeling methodology developed in Chapter 4 was applied to the FE frame models. This chapter also briefly investigates the effectiveness of the FRP column jacketing system by comparing blast responses between the as-built and retrofitted FE frame models.

5.2 Blast Load Modeling Technique

Figure 5.1 illustrates blast wave interactions with a target structure. After blast waves such as incident waves or ground reflected waves impact the target structure, some portions of the blast waves are immediately reflected from the target, and the remaining waves are diffracted around the target. The reflected waves can increase the magnitude of the overpressure by merging the shock waves, which may lead to significant damage on the target structure. The diffracted waves create trailing vortices behind the target. Such blast wave interaction affects the blast loading parameters, such as peak reflected pressure, peak impulse, and duration [Ofengeim

et al. 1997, Tai et al. 2005, and Shi et al. 2007]. To predict accurate blast responses of structures, reproducing the effects of the blast wave interaction is needed in numerical simulations.
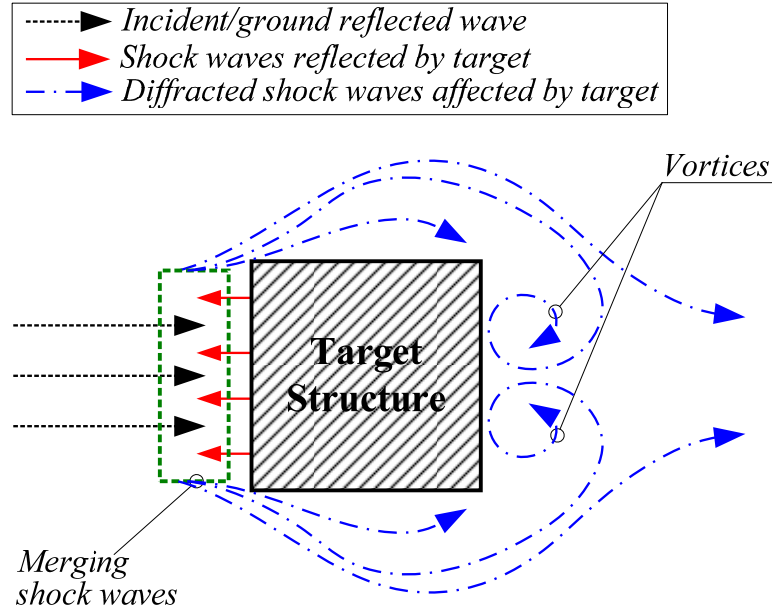
Figure 5.1. Blast wave interaction with a target structure

Blast loads can be simulated by several modeling techniques in LS-DYNA: (1) Load Blast Enhanced (LBE) modeling method [LSTC 2013], (2) Multi-Material Arbitrary Lagrangian-Eulerian (MM-ALE) method [Olovsson and Souli 2000], and (3) a coupled method between LBE and MM-ALE [Slavik 2009]. The LBE method computes an air blast pressure using an empirical blast equation calibrated by extensive explosive air blast experiments. The function of the air blast pressure is determined based on an equivalent mass of TNT (W_{TNT}) and relative distance between the explosives and target structures (i.e., standoff distance, R_D). The blast modeling method is based on a pure Lagrangian formulation; in other words, the blast pressure produced by the LBE method is directly applied to the segments on a given surface of the target structure. Therefore, the advantage of the pure Lagrangian approach is computational efficiency.

However, during a simulation using the modeling method, the blast pressure vector always stays normal to the surface of the target structure. If the pressure causes large deformation in the target structure, the surface mesh facing the pressure can be distorted, and thus the numerical results may not be reasonable [Børvik et al 2009]. Because of this, the LBE approach is not valid for cases where the scaled distance (Z) is less than approximately 0.4 m/kg$^{1/3}$, which is not available for near-contact charges [Geneviève and Amal 2010, and LSTC 2013]. An additional limitation of the LBE model is that it cannot generate the blast wave interactions illustrated in Figure 5.1 (e.g., merging reflected waves by a target structure, the diffracted blast waves in front of the target structure, and the effect of trailing vortices along the back sides of the target structure) because the air blast pressure produced by the LBE model is applied on the blast-faced surfaces of the target structure [Prada and Fink 1994, Geneviève and Amal 2010, Wojciechowski et al. 2011, Rigby 2012, and Haladuik 2014].

To overcome the limitations of the LBE model, blast loads can be modeled with the MM-ALE modeling method. The ALE formulation in the MM-ALE method allows modeling the blast in an Eulerian system. The MM-ALE approach is required to model a Lagrangian mesh and two separate Eulerian meshes: a target structure serves as the Lagrangian mesh, while explosive and surrounding air models function as the Eulerian meshes [Williams 1999]. To reproduce high explosive burn and shock propagation, the explosive meshes are directly modeled inside the surrounding air meshes while assuming a constant atmospheric pressure. The surrounding air meshes are fully coupled with the Lagrangian target structure using a fluid-structure interface (FSI) algorithm, which allows air to flow on and around the structure. In other words, the coupled air mesh serves as a compressible medium between the explosive and the target structures, making it possible to transfer the blast waves to the target structure immediately after

the explosive charge has occurred. While traveling in the air mesh, the incident waves produced by a detonation of the explosive material interact with any reflected waves from ground and target surfaces. Thus, the main advantage of the MM-ALE modeling method is that it can reproduce the proper blast wave interactions that are illustrated in Figure 5.1. Additionally, unlike the LBE method, the MM-ALE approach can predict near contact explosions because the explosive materials are modeled directly in the air [Schwer et al. 2015]. The limitation of the MM-ALE modeling method is that it is computationally more expensive than the LBE modeling method. This is mainly due to large amounts of elements in the air, a small mesh size of the explosive model, and reductions in time step size for the coupling computations [Slavik 2009, Schwer 2010, Wojciechowski et al. 2011, and Trajkovski et al. 2014].

To ensure a good balance between accuracy and computational efficiency, a coupled method between the empirical blast load function (LBE method) and the MM-ALE method (hereafter referred to as "coupled LBE-ALE") is available in LS-DYNA. The coupled LBE-ALE approach is illustrated in Figure 5.2. This figure also shows a comparison between the coupled LBE-ALE and MM-ALE methods. As shown in Figure 5.2, the coupled LBE-ALE method is composed of a Lagrangian target structure, an air model, and a single layer of ambient elements. The air model surrounding the target structure and the ambient element immediately adjacent to the air model are modeled with an ALE domain. The ambient air element transfers a blast pressure time-history computed by the LBE method (Figure 5.2) to the air model surrounding the target structure. The ALE air model allows the blast wave to travel, and it also allows interaction with the target structure by coupling using the FSI algorithm. As compared with the MM-ALE method, the coupled method (Figure 5.2) eliminates the explosive model and reduces the air

model, which results in a significant increase in computational effort. Therefore, this method is more computationally efficient.

Previous studies have investigated the balance between computational efficiency and accuracy in blast simulations. Among them, Tabatabaei et al. [2012] modeled a concrete panel under blast loading with a scaled distance (Z) of 0.51 m/kg$^{1/3}$. This Blast load was simulated with three different blast modeling methods: LBE, MM-ALE, and coupled LBE-ALE methods. Blast responses induced by the three blast modeling methods were compared against the experimentally-measured results, and the computation time in each modeling method was estimated. The MM-ALE and coupled LBE-ALE methods showed an excellent correlation with the experimental results. The coupled LBE-ALE method reduced computational time by a factor of 2 when compared to the MM-ALE method. In addition, Han and Liu [2015] simulated air blast loads using the coupled method and compared the simulated peak pressures and impulses under varying scaled distances to those of UFC 3-340-02 [2008]. The reflected pressures and impulses in the coupled LBE-ALE were very close to those in UFC 3-340-02. They also compared the effect of an air blast on a steel plate measured from a previous experimental study [Boyd 2000] to the simulated responses in the numerical model with different element sizes of the air model. The researchers found that, for the range of element sizes considered, the experimental responses of the steel plate were well captured by the coupled LBE-ALE, regardless of the element size of the air model used.
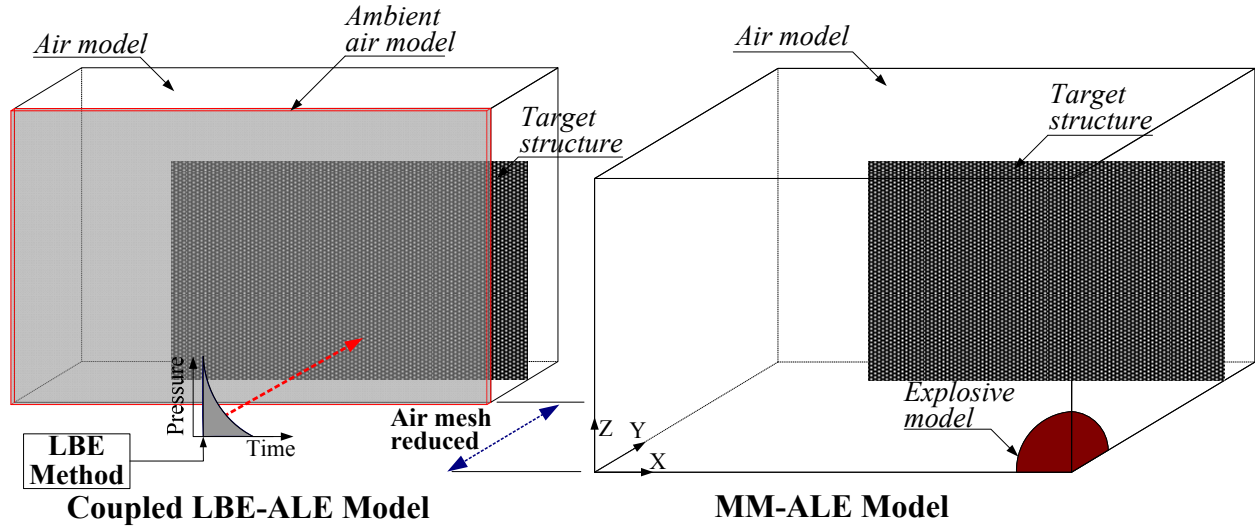
Figure 5.2. Comparison between coupled LBE-ALE and MM-ALE blast modeling methods [Slavic 2009]

5.3 Verification of Numerical Modeling Methodology for Blast Loading

5.3.1 Past experimental and numerical studies

Woodson and Baylot [1999] performed a series of experiments with two-story, two-bay RC frame specimens to investigate blast responses in an exterior RC column. They selected a typical RC frame structure common in low-seismic regions in the United States. The researchers designed and constructed quarter-scale RC frame specimens using geometric scaling via the law of similarity [Hosoya et al. 1999]. This geometric scaling is also consistent with the Hopkinson scaling law (cube root) of the blast pressure [Baker 1973]. By reducing the full-scale standoff distance and charge mass, the scaled distance of the quarter-scale model is set to be same as that of the full-scale model ($Z_s = S \cdot R_D/(S^3 \cdot W_{TNT})^{1/3} = R_D/W_{TNT}^{1/3} = Z$, where Z_s is the scaled distance for the quarter-scale; S is the 1/4 scale factor; and Z is the scaled distance for the full-scale structure). According to the Hopkinson scaling law, the scaled model has the same blast pressure

as the full-scale structure [Neubeger et al. 2007]. The material properties of the scaled models were assumed to be identical to those of the full-scale frame structure.
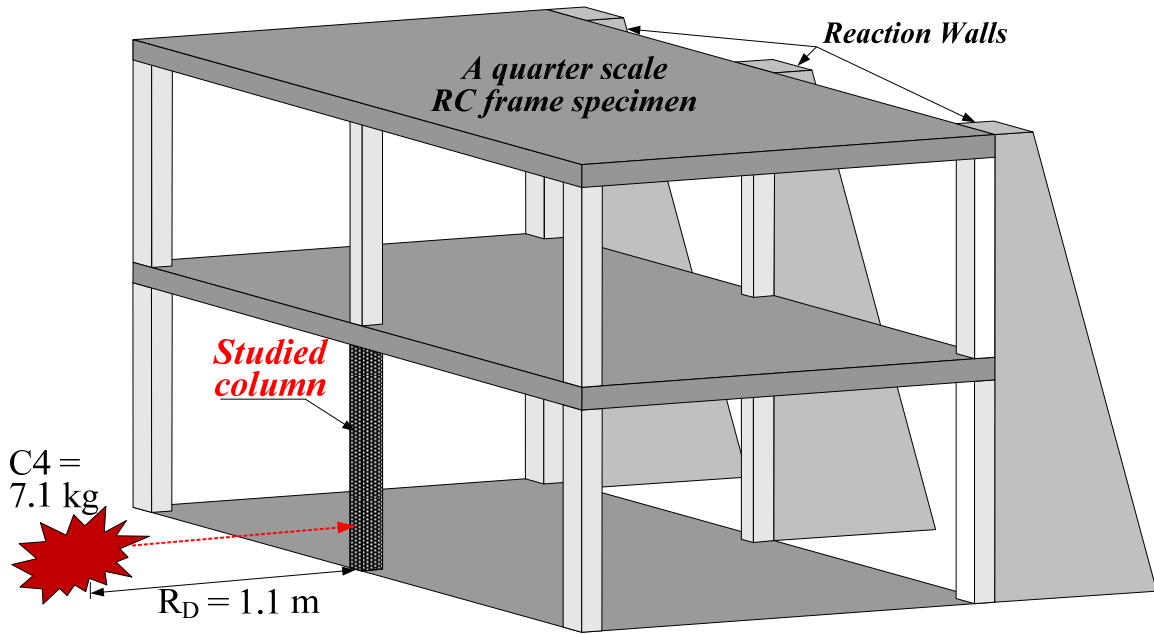
Figure 5.3. Schematic view of test setup for a quarter-scale RC frame specimen reproduced from [Woodson and Baylot 1999]

Figure 5.3 shows a schematic view of the experimental setup for the quarter-scaled RC frame specimen. Reaction walls, which were constructed behind the specimen, restrained horizontal motions of structural slabs to investigate the blast effects of a center front column (the studied column in Figure 5.3). A 7.1 kg hemisphere of C4 was detonated at a standoff distance (R_D) of 1.07 m and a standoff height (R_H) of 305 mm above the ground surface. The blast resulted in damage to the first story exterior column, with residual displacement of approximately 6.3 mm at the mid-height of the column. Additionally, displacement time history responses at the mid-height of the first story exterior column, peak pressure, and impulse on the column's front surface were also measured. These experimental responses were used to verify the numerical modeling methodology subjected to the blast load.

In previous numerical studies, Baylot and Bevins [2007] simulated entire quarter-scale specimens with and without infill walls to reproduce the experimental responses of the first story exterior column and investigated the effects of the infill walls. Additionally, to validate the accuracy of the RC column model under the blast loads, Shi et al. [2008 & 2010] verified their RC column modeling method under blast loads with experimental responses measured from Woodson and Baylot [1999]. In their simulation, they modeled only the quarter-scaled exterior columns in the first story (i.e., the studied column in Figure 5.3) and implemented bond-slip effects along the longitudinal reinforcing bars in the RC column model. The column model was analyzed under air blast loads reproduced by AUTODYN [2001]. It demonstrated a better prediction in peak and residual displacements compared to Baylot and Bevins's numerical model. Mutalib and Hao [2011] and Chen et al. [2015] also verified their modeling processes using experimental responses measured from Woodson and Baylot [1999]. After that, they utilized the modeling processes to develop FE models for an FRP-retrofitted column and a prestressed RC beam under blast loading.

5.3.2 Numerical modeling methodology for blast loading

Figure 5.4 illustrates a numerical modeling methodology to simulate blast responses of FE frame models. As discussed in Chapter 4, the as-built and retrofitted FE frame models under seismic loading were correlated with experimental responses by implementing the proper bond-slip models determined according to the reinforcing details in the lap-splice and panel zones. The development process of FE models for seismic loading is summarized in Parts I and II of Figure 5.4.

To verify the numerical modeling methodology for blast loading, this study compared blast experimental responses of the first story exterior RC column in the quarter-scale frame specimen measured from Woodson and Baylot [1999]. The numerical modeling methodology for seismic loading as well as dynamic increase factors (DIFs) for concrete and steel materials were applied to the exterior RC column model using LS-DYNA. The RC column model led to significant variation in peak and residual blast responses between the experimental and simulated responses. To reduce the variation, the RC column model was modified using the following steps: (1) expand bond-slip areas to longitudinal reinforcing bars, (2) increase maximum bond strength between concrete and steel reinforcing bars for high-speed loading conditions [Weatherby 2003, and Shi et al 2008], and (3) implement a coupled LBE-ALE model, as described in Part IV of Figure 5.4. More detailed information of the RC column model will be discussed in Section 5.3.3. Finally, after validating the RC column model under the blast effects, the modeling process for blast loads described in Part IV of Figure 5.4 was applied to the as-built and retrofitted FE frame models in order to investigate the blast responses (Part V of Figure 5.4).
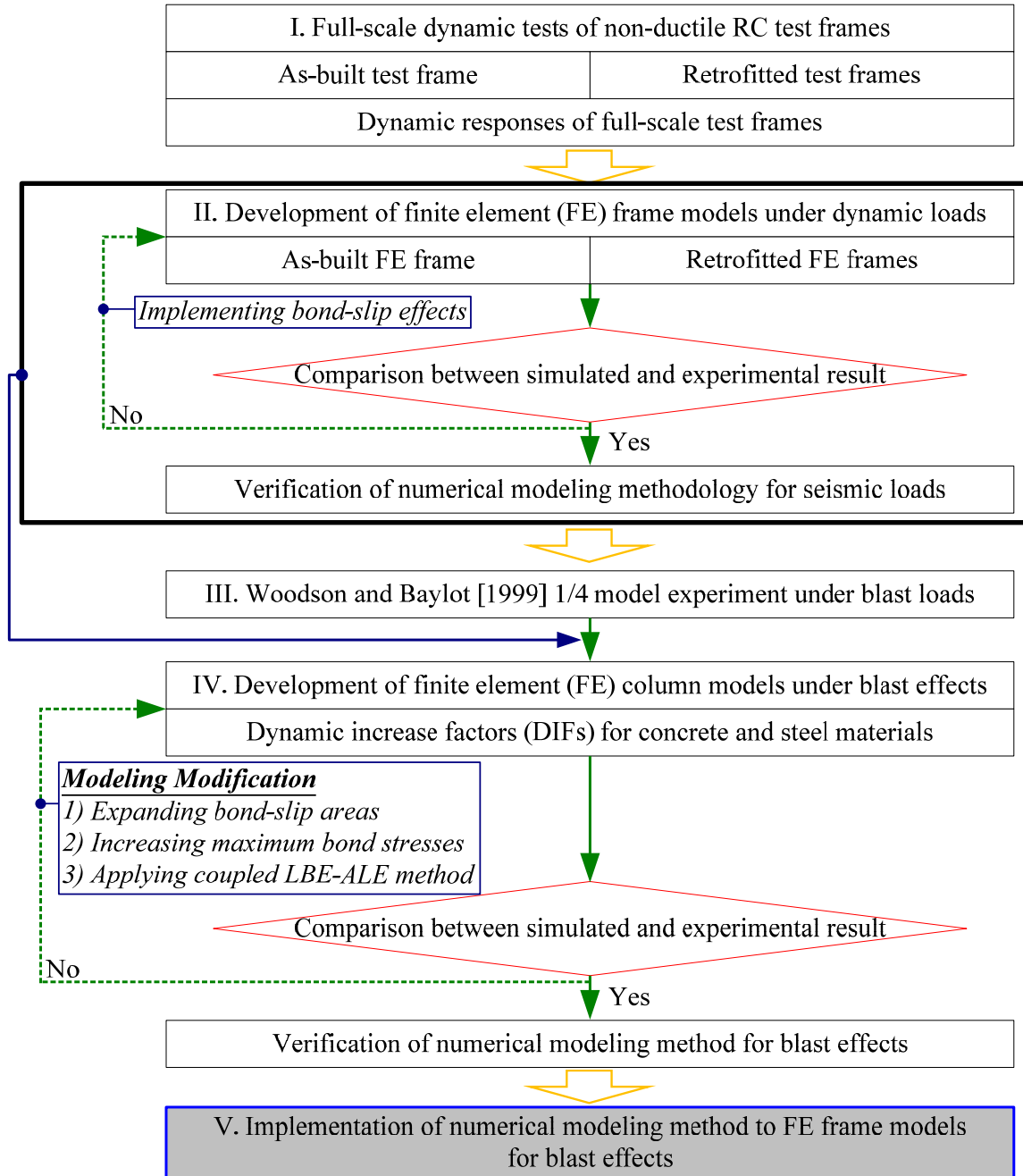
Figure 5.4. Development process of FE models for blast effects

5.3.3 Validation of Woodson and Baylot [1999]'s RC column model

To verify the modeling methodology for blast effects (Part IV of Figure 5.4), this study

selected an exterior RC column in the first story from the previous experimental study [Woodson

and Baylot 1999] (the studied column in Figure 5.3) and performed numerical simulation using LS-DYNA. The detailing of the first story exterior RC column is shown in Figure 5.5, where *H*, *b*, *h,* and *s* denote column height, width, depth and clear spacing of column and cross ties, respectively. The dimensions of the RC column are given in Table 5.1. The footing and header were modeled to provide higher fidelity for the column constraints. The outer vertical faces of the header were restrained in the *X*- and *Y*-translational directions. The boundaries at the header reproduced the structural slabs in the quarter-scaled RC frame specimen, which were constrained against horizontal motion by the reaction walls. The footing was restrained in all transitional and rotational directions to represent a fixed condition. The unconfined compressive strength (f_c') was assumed to be 42 MPa, and steel material properties for ϕ 3.2 and ϕ 1.6 are summarized in Table 5.2. The concrete was modeled using 25 mm solid elements with a single integration point, and the material behavior is captured by the Karagozian and Case (K&C) concrete (KCC) model discussed in Chapter 4. For the steel reinforcing bars in Figure 5.5, beam truss elements were utilized with the PLASTIC_KINEMATIC (MAT_003) material model. The parameters of the steel material model are given in Table 5.2.
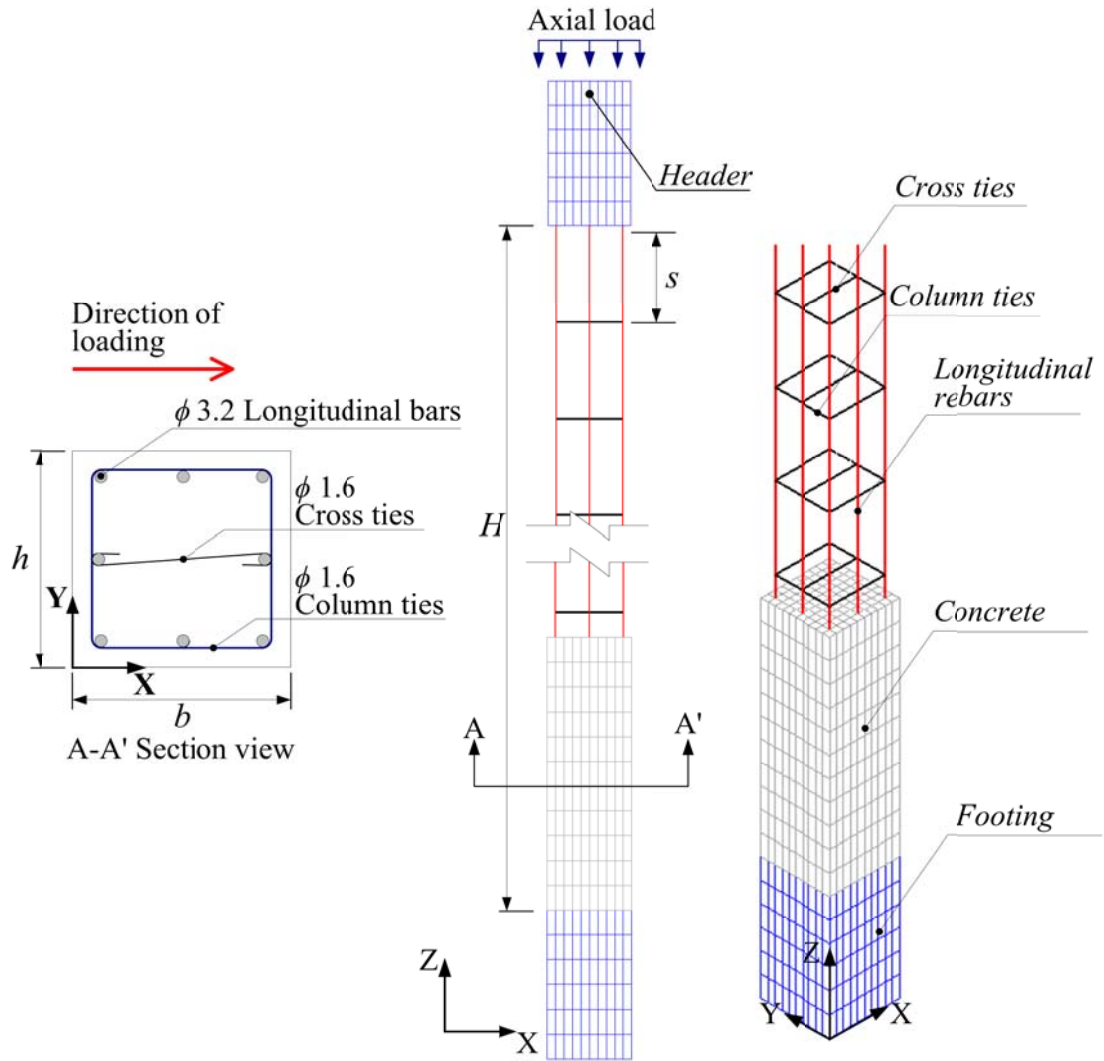
Figure 5.5. Details of RC column model selected in the quarter-scale RC frame

Table 5.1. Dimension of RC column model

Parameter	Dimension (mm)
Column height (H)	900
Column width (b)	89
Column depth (h)	89
Column and cross ties spacing (s)	100

Table 5.2. Steel material properties

Reinforcement	Area (mm^2)	Elastic Modulus (GPa)	Yielding strength (MPa)	Ultimate strength (MPa)
ϕ 1.6: Column and cross ties	2.01	2070	399	610
ϕ 3.2: Longitudinal bar	8.04	2070	449	513

To capture strain rate effects in the material models induced by high-speed blast loads, the concrete and steel material models included a dynamic increase factor (DIF), which is a ratio of the dynamic to static strength related to strain rates. The DIFs, which are characterized as a function of the strain rate, were incorporated into the KCC model in order to determine the concrete strain rate effects. The DIF function modifies the failure surface of the KCC model to reflect apparent changes in strength due to high loading speeds. The DIF functions for the concrete compressive and tensile strengths can be respectively derived as Equation (5.1) and Equation (5.2) [Crawford et al. 2012]:

$$DIF = \begin{cases} (\dot{\varepsilon}/\dot{\varepsilon}_{sc})^{1.026\alpha_s} & \varepsilon_s \leq 30\ s^{-1} \\ \gamma_s(\dot{\varepsilon}/\dot{\varepsilon}_{sc})^{1/3} & \varepsilon_s > 30\ s^{-1} \end{cases} \tag{5.1a}$$

with

$$\log(\gamma_s) = 6.156\ \alpha_s - 2 \tag{5.1b}$$

$$\alpha_s = 1/(5 + 0.9 f_c') \tag{5.1c}$$

where

$\dot{\varepsilon}$ = strain rate in s^{-1} (1/second)

$\dot{\varepsilon}_{sc} = 30 \times 10^{-6}$ s^{-1} for static strain rate in compression

f_c' = static compressive strength of concrete in megapascals

$$DIF = \begin{cases} (\dot{\varepsilon}/\dot{\varepsilon}_{st})^{\delta} & \varepsilon_s \leq 1.0\, s^{-1} \\ \\ \beta(\dot{\varepsilon}/\dot{\varepsilon}_{st})^{1/3} & \varepsilon_s > 1.0\, s^{-1} \end{cases} \tag{5.2a}$$

with
$$\log(\beta) = 6\delta - 2 \tag{5.2b}$$

$$\delta = 1/(1 + 0.8f_c') \tag{5.2c}$$

where

$\dot{\varepsilon}_{st}$ = 10^{-6} s^{-1} for static strain rate in tension

The PLASTIC_KINEMATIC steel material model can be incorporated with the DIF. The DIF amplifies yield and ultimate stresses of the steel materials as given in Equation (5.3) [Malvar and Crawford 1998]:

$$DIF = (\dot{\varepsilon}/10^{-4})^{\alpha_s} \tag{5.3}$$

where

$\alpha_s = 0.074 - 0.04 f_y/414$ for yielding stress of the steel material

$\alpha_s = 0.019 - 0.009 f_u/414$ for ultimate stress of the steel material

f_y = static yielding stress of the steel material in megapascals

f_u = static ultimate stress of the steel material in megapascals

It should be noted that Equation (5.3) is only valid for reinforcement with yield stresses between 290 MPa and 710 MPa.

The bond-slip effects between the surrounding concrete and steel reinforcing bars were reproduced using one-dimensional slide line models. The parameters in the one-dimensional slide line models, implemented along the longitudinal reinforcing bars, are characterized based on the detailing of the RC column, the splitting failure mode, and poor bonding condition with the damage curve exponential coefficient (h_{dmg}) of 0.065, as discussed in Section 4.4. To capture bond-slip effects for the high-speed loading condition, the maximum bonding stress between the surrounding concrete and the reinforcing bars was amplified based on pull-out experiments [Weatherby 2003, and Shi et al. 2008]. These previous experimental studies found that the maximum bond stresses were determined depending on the loading speeds (e.g., 6.6 MPa for quasi-static loading, 18.0 MPa for dynamic loading, and 22.0 MPa for impact loading).

The blast load, an approximate 7.1 kg hemisphere of C4 at a standoff distance (R_D) of 1.07 m with the standoff height (R_H) of 305 mm above the ground surface, was simulated using the coupled LBE-ALE and LBE methods. In the blast loading model, the equivalent TNT mass (W_{TNT}) was determined by multiplying the C4 mass by a conversion factor of 1.20. This factor is reasonable because a 1 kg mass of C4 produces the same impulse as a 1.19 kg of TNT and the same peak pressure as 1.37 kg of TNT [US Army 1985, and Baylot and Bevins 2007]. Figure 5.6 illustrates the implementation of the coupled LBE-ALE method on the target structure. The air and ambient layers were modeled with solid 10 mm cube using the multi-material ALE air elements. The blast load produced by the LBE model impacted the single layer of the ambient air model, and the ALE air model transferred the blast waves to the surrounding column model. The blast waves were reflected by the exterior boundary conditions of the air model in XY-, XZ- and

YZ-planes, and the unreasonable reflected waves were superposed with the incident waves in the air model. These unreasonable reflected waves may lead to the overestimation of the blast pressure and impulse. To avoid those reflections, this study applied non-reflecting boundaries on the exterior boundaries of the air model, as shown in Figure 5.6.
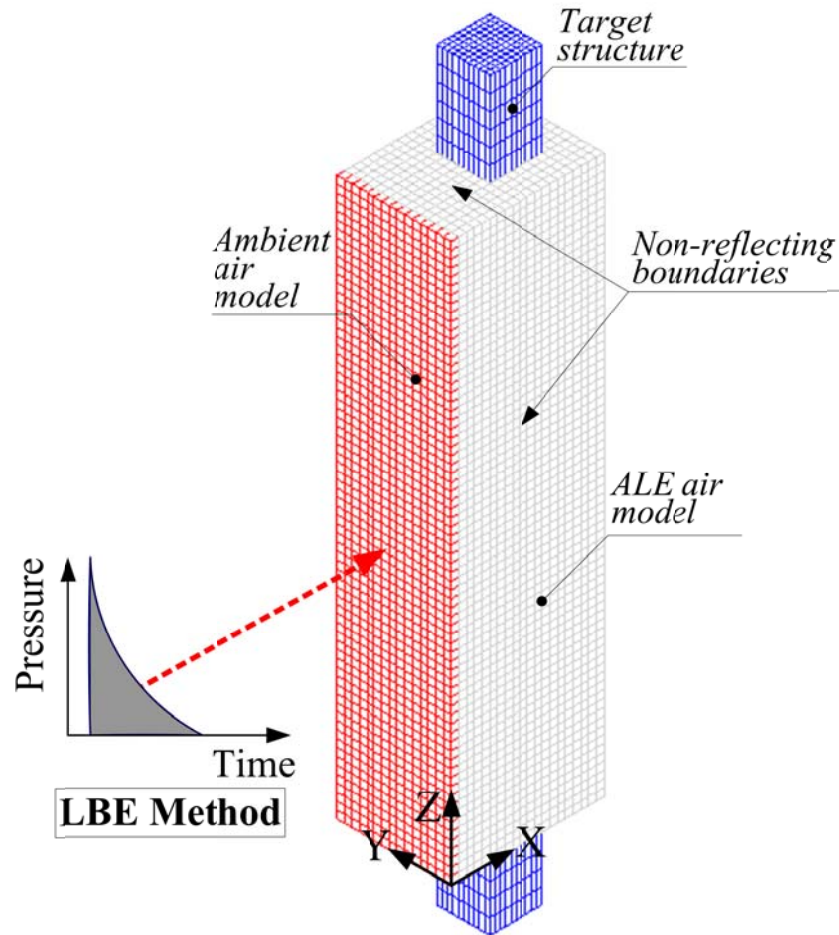
Figure 5.6. Implementation of coupled LBE-ALE method to RC column model

Figure 5.7 compares the displacement time histories at the middle height of the RC column between simulation and experiment. To estimate the effect of blast loading models, the figure also includes the simulated responses for the present numerical models using the LBE and coupled LBE-ALE methods, which are referred to as the "LBE model" and "Coupled LBE-ALE

model" in Figure 5.7, respectively. Additionally, simulated responses of the numerical models developed by previous research [Baylot and Bevins 2007, and Shi et al. 2008], which are referred to as the "Baylot model" and "Shi model," respectively, are compared to the coupled LBE-ALE model performed in this study. As shown in Figure 5.7, the peak displacement variation of the coupled LBE-ALE model and experimental responses was smaller than that of the LBE model (3.4 % variation for the coupled LBE-ALE model, and 13.8 % variation for the LBE model). This is because the coupled LBE-ALE method can capture the blast wave interaction with the structure and help reproduce more accurate blast loading parameters such as peak reflected pressure and peak impulse. The peak pressure of the blast load simulated by the coupled LBE-ALE method was 6680 kPa, while the impulse was 1082 kPa-msec. The simulated blast loading parameters were similar to the measured peak pressure and impulse in the column front surface in the previous experiment [Woodson and Baylot 1999] (i.e., peak pressure ≈ 7000 kPa, and impulse ≈ 1100 kPa-msec); the variation in the blast loading parameters is within 5.0 %.

In addition, the coupled LBE-ALE model developed in this study showed better predictions than the Baylot and Shi models in terms of the peak displacement and the time when the displacement is maximized. This is mainly due to the following modeling methods used in the coupled LBE-ALE model: (1) implementation of the bond-slip effects between surrounding concrete and longitudinal reinforcing bars compared to the Baylot model, and (2) better prediction of the blast wave interaction using the coupled LBE-ALE method compared to the Shi model. Therefore, the proposed modeling process for the blast effects described in Section 5.3.2 was verified with the experimental responses. This verified modeling process for blast effects was incorporated into the as-built and retrofitted FE frame models in Section 5.4.
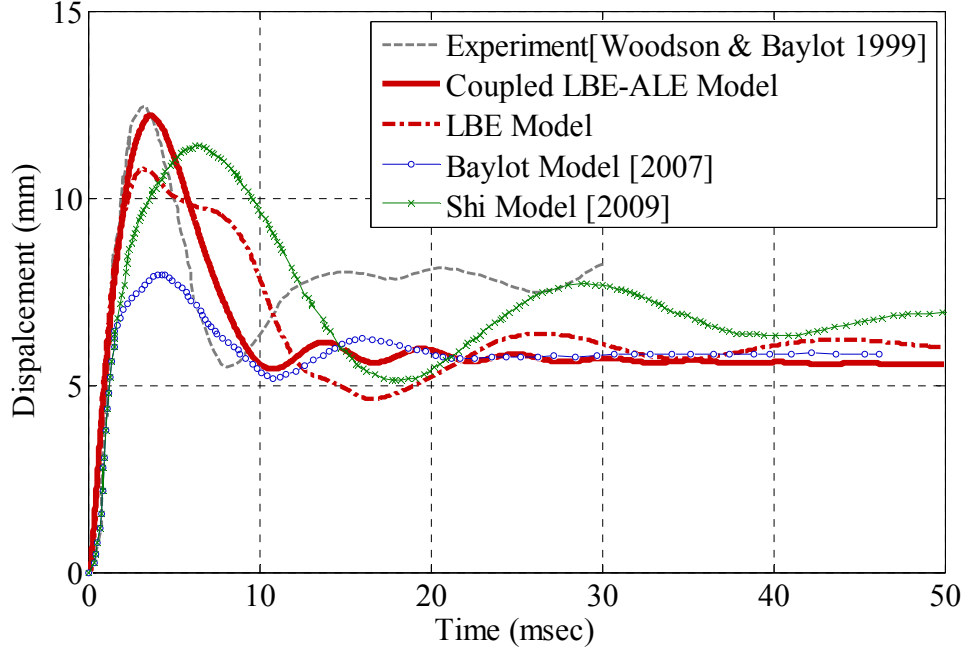
Figure 5.7. Comparison of mid-span displacement between simulations and experiment

5.4 Development of Finite Element RC Frame Model for Blast Effects

5.4.1 FE frame model with coupled LBE-ALE method

To predict blast responses of the as-built and retrofitted frames, the verified modeling methodology for the blast loads discussed in Section 5.3 (i.e., extension of bond-slip areas, and application of DIFs to the material models and coupled LBE-ALE model, shown in Figure 5.4) was applied to the FE frame models, which were developed and verified with the full-scale dynamic testing in Chapter 4. Figure 5.8 illustrates the as-built FE frame model combined with the coupled LBE-ALE blast modeling technique. The ALE air model extended from the corners of the target structure by 100 mm, except for the symmetric boundaries in the XZ-plane based on previous studies [Slavik 2010, Tai et al. 2011, and Han and Liu 2015], and the single layer of ambient air was directly modeled at the end surface of the air model in the YZ-plane. The ALE air model was coupled with the frame model using the FSI algorithm described in Section 5.2.

To eliminate the blast wave reflections from the boundaries of the air model in the XY-, XZ- and YZ-planes, non-reflecting boundaries were introduced around the outer perimeter of the air medium. The non-reflecting boundary in the base of the XY-plane activated the reflection of shear and dilatational waves from the ground surface to reproduce the wave reflections from the ground surface.
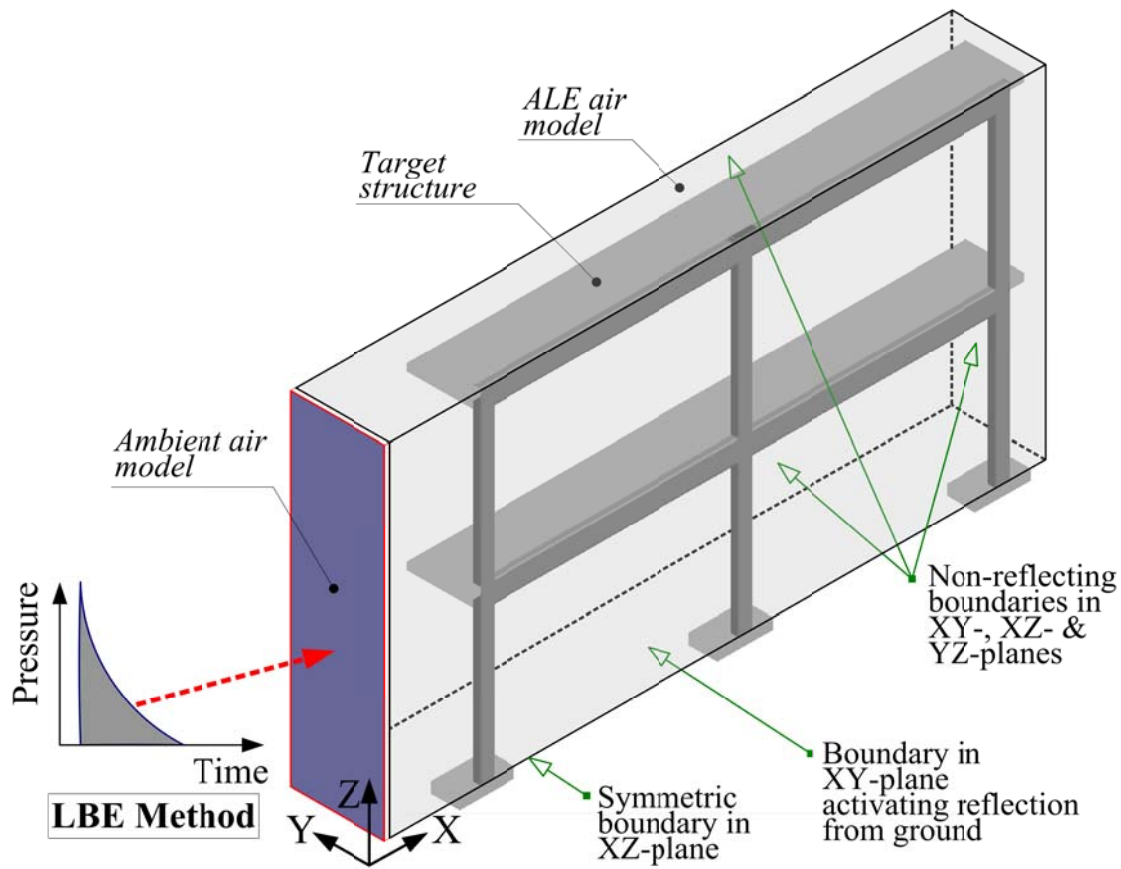
Figure 5.8. Incorporation of coupled LBE-ALE method into FE frame model

5.4.2 Mesh sensitivity analyses

The as-built FE frame model with the coupled LBE-ALE method was utilized to perform two mesh sensitivity studies: (1) target structure, and (2) ALE air model. These studies were carried out to determine an appropriate element size. Figure 5.9 shows the mesh sensitivity study

on the target structure. The target structure was modeled with various element mesh densities and subjected to a sample blast load, W_{TNT} = 680 kg; R_D = 7.0 m; and Z = 0.80 m/kg$^{1/3}$. The element mesh densities of the target structure were varied by reducing the element sizes from 25.4 mm to 3.12 mm (Mesh 1 to Mesh 4 in Figure 5.9). The element sizes were continuously reduced until the variation in peak displacement between the models with different element mesh densities became small. Figure 5.9 illustrates that the variation between Mesh 2 and Mesh 4 is significantly reduced by 7.2 % in the peak displacement, while the variation in the peak displacement between Mesh 1 and Mesh 2 is 20.3 %. Thus, this study selected the Mesh 2 (the solid element size of 12.5 mm) as the final mesh element size for the target structure.
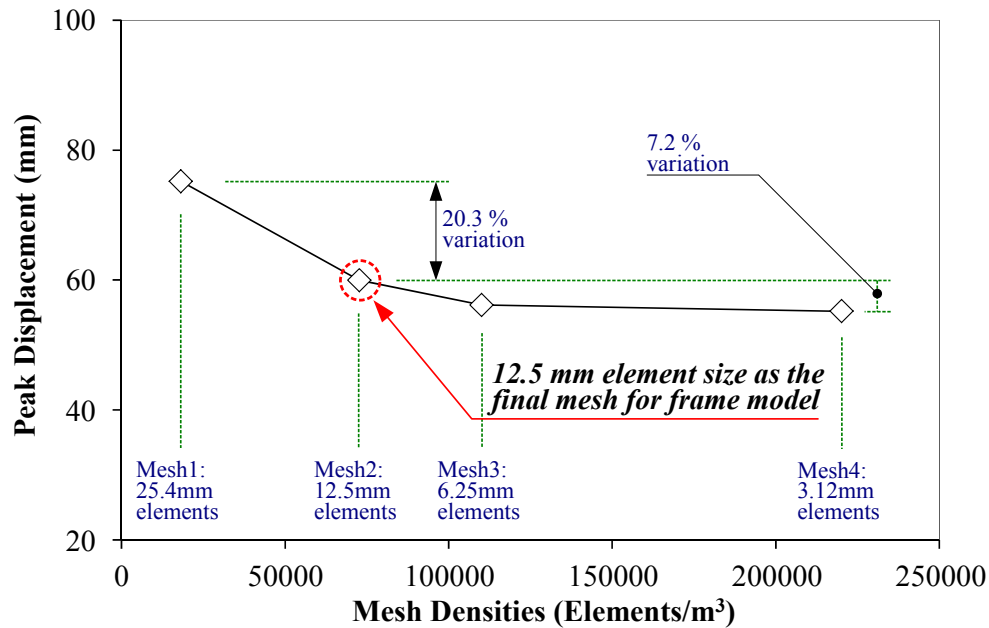
Figure 5.9. Mesh sensitivity study on FE frame model (target structure)

Figure 5.10 shows the mesh sensitivity study on the ALE air model with various element sizes from 63.5 mm to 12.7 mm, which corresponds to element mesh densities from 444,710 to 16,434,600 (Mesh 5 to Mesh 8 in Figure 5.10). This mesh sensitivity study also stopped reducing

the element mesh size of the air model when the variation in peak displacement between the numerical models with different mesh densities became small. The element size of the FE frame model was 12.5 mm, selected from the mesh sensitivity study for the target structure. The peak displacements gained from the numerical models with the various mesh densities of the air model were compared. As illustrated in Figure 5.10, while the variation in peak blast responses between Mesh 5 and Mesh 6 was approximately 53.1 %, the variation between Mesh 6 and Mesh 8 was within 10.0 % (≈ 8.1 % variation). Based on the simulated results, the element size of the air model was selected as Mesh 6 (solid element size of 38.0 mm).
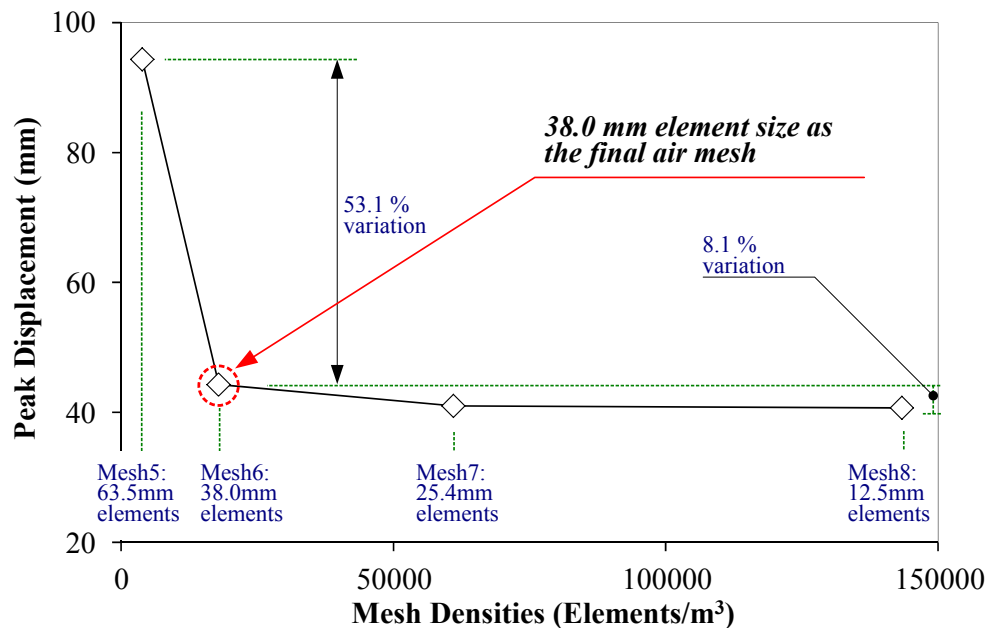
Figure 5.10. Mesh sensitivity study on ALE air model

5.4.3 Effectiveness of FRP column jacketing system for blast effects

The frame models were subjected to the sample blast load that was utilized in the mesh sensitivity analyses. The effectiveness of the FRP column jacketing system was investigated by comparing the displacement time histories of the as-built and retrofitted FE frame models. The

FRP column jacketing system in the retrofitted FE frame model, which is the same as the full-scale retrofitted frame specimen in Chapter 3, was designed for seismic loads to ensure a target ductility of 4.50. The details and modeling methods of the retrofit system are described in Chapters 3 and 4, respectively.

Figure 5.11 shows the displacement time histories and residual displacements in the as-built and retrofitted FE frame models. The peak displacement in the as-built FE frame model was 62.4 mm, while the peak displacement in the retrofitted FE frame model was 45.5 mm. The FRP column jacketing system thus reduced the peak displacement by 27.1 %. Additionally, the retrofit system resulted in a 41.0 % decrease in residual displacements. This reduction in peak displacements is attributed to an increase in the flexural stiffness by section enlargement of the column using the grout material, as well as an increase in the confining pressure produced by the FRP jackets. The retrofit also minimized the permanent damage on the front surface of the column, as evidenced by the reduction in residual displacements. The effectiveness of the retrofit system in reducing the peak and residual displacements can be affected by varying specific retrofit parameters, such as the number of FRP plies, FRP material properties, size of section enlargement, and grout material properties.
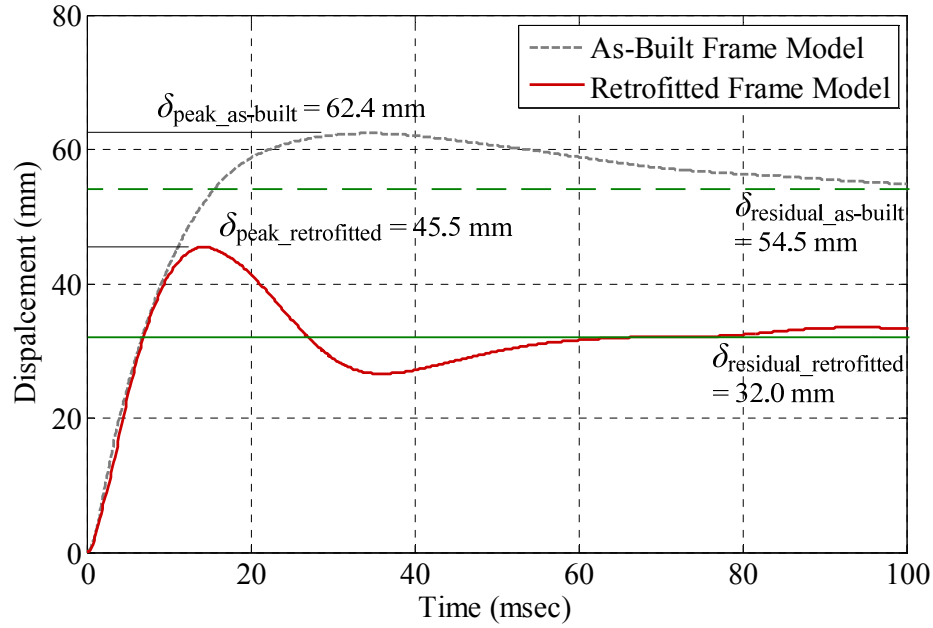
Figure 5.11. Displacement time histories in as-built and retrofitted FE frame models

5.5 Summary

This chapter presented a modeling methodology to simulate blast responses on frame structures. To verify the modeling methodology, results from a previous experimental study [Woodson and Baylot 1999] were utilized. The blast responses of the first story exterior RC column of the quarter-scale frame experiment were compared to the simulated responses reproduced from the numerical model that implemented the modeling processes for the blast effects. The numerical column model provided acceptable ranges of variation in peak displacement between the simulatation and experiment. The numerical model, which accounts for bonding effects with an advanced blast modeling technique, provides a better prediction than the numerical studies performed by previous researchers [Baylot and Bevins 2007, and Shi et al. 2008]. The well-verified modeling process for blast effects is incorporated with the as-built and retrofitted FE frame models described in Chapter 4.

The mesh element sizes in the target structure and air models were determined by mesh sensitivity analyses to be 12.5 mm for the target structure and 38.0 mm for the air models. To investigate the effectiveness of the FRP column jacketing system, the blast responses in terms of peak and residual displacements of the as-built FE frame model were compared to those of the retrofitted FE frame model. The retrofit system, designed for the seismic loads, reduced the peak and residual displacements by approximately 27.1 % and 41.0 %, respectively. This was mainly due to the increase in flexural stiffness and addition of the confining pressure for the first story columns that were retrofitted. It should be noted that these retrofit effects were limited, as the retrofit design was based only on seismic loading.

CHAPTER 6. FAST RUNNING MODELS FOR PREDICTING RESPONSE AND DAMAGE DEMANDS UNDER MULTI-HAZARD LOADS

6.1 Overview

This chapter presents the development of fast running models (FRMs) for consideration of seismic and blast loads; these models are referred to as "Seismic FRM" and "Blast FRM," respectively. The models were developed using an artificial neural network (ANN), which was trained with datasets obtained from simulations using the finite element (FE) frame models described in Chapters 4 and 5. To develop the numerical datasets for the model training, various input parameters associated with loading types along with geometric and material variables of an FRP column jacketing system were incorporated into the FE frame models. The trained models can be utilized to predict multiple outputs: (1) peak inter-story drift ratio (IDR), (2) blast displacement ductility demand (μ_{blast}), and (3) seismic and blast energy-based damage demands (D_S and D_B), computed from a Park-Ang damage model [Park and Ang 1987]. This chapter focuses on the development of the model, including the selection of input parameters, generation of output parameters, model training, and validation.

6.2 Artificial Neural Network

The FE modeling methodologies, verified with the experimental responses as described in Chapters 4 and 5, can accurately capture structural behavior in large deformation-induced loading conditions, such as seismic and blast loads. However, the FE-based simulation methodologies can be extremely time-consuming because the FE models must be highly detailed in order to accurately capture the structural damage on the system. The implementation of the FE

modeling methodologies to simulate inelastic dynamic behavior for multi-story buildings is often limited due to the need for a large number of elements representing geometric effects and nonlinear material behavior [Kim et al. 2005]. For example, the FE-based simulations for an as-built condition under the 1940 El Centro earthquake (Section 4.5) and sample blast load with a scaled distance (Z) of 0.80 m/kg$^{1/3}$ (Section 5.4) were completed in approximately 124 hours and 20 hours, respectively. More practical approaches, which allow the model to rapidly investigate the structural response of the frame under dynamic loadings, are required in order to overcome this limitation in the use of FE simulations.

The effectiveness of the FRP column jacketing system, identified as the retrofit system used in this investigation, can be affected by a number of parameters related to the design of the retrofit system. These parameters include the FRP jacket material properties (f_{ju}), the number of FRP plies (i.e., FRP jacket thickness, t_j), the section enlargement using a non-shrink grout (i.e., inner diameter of the FRP column jacketing system, ID), and the grout material properties (f_g) used for section enlargement. To accurately capture these parametric effects on structural behavior, well-verified FE models are necessary. However, a full parametric study requires hundreds of simulations varying these parameters. The generation of extensive simulated datasets using the FE-based models is not practical because of the enormous amount of computational time required. For this reason, this study utilizes an ANN approach to predict the simulated responses in given loading, geometric, and material conditions based on the datasets generated from the FE models [Stewart 2010].

An ANN is a statistical learning algorithm inspired by biological nervous systems like a human brain. The human brain has approximately 100 billion neurons, which communicate through electro-chemical signals, and the neurons are densely interconnected with synapses for

communication of the signals among the neurons. The neurons function as the primary unit of the nervous system to process, receive, and transmit information. The ANN was developed for use in other applications where large amounts of data must be processed and evaluated [Anderson and Rosenfeld 1988, Simpson 1990, and Kosko 1994]. The ANN learns the relationship between the input parameters and the controlled and uncontrolled variables by studying numerical or experimental datasets. This makes it possible to find solutions for large and complex systems that contain many interrelated parameters.

A multi-layer feedforward neural network (multi-layer perceptron) illustrated in Figure 6.1 is usually composed of input and output layers, and one or more hidden interconnecting layers between the two. In the neural network, each single artificial neuron computes activation $(\overline{a})$ and output values (x_j) using Equation (6.1):

$$x_j = f\left(\overline{a}_i\right) = f(\sum_j w_{ij} x_i - \overline{b})$$

(6.1)

where

i = earlier layer of neuron

j = next layer of neuron connecting with the ith neuron

x_i = input value in the neuron

$f(\bullet)$ = transfer or activation function

w_{ij} = weight coefficient that represents the degree of importance of the connection between the ith and j^{th} neurons

$$\sum w_{ij} x_i = \text{weighted summation}$$

$\bar{b}$ = threshold or bias value in the associated neuron

As given in Equation (6.1), the activation value is computed by subtracting the weighted summation from the threshold or bias value in the neuron. The weight (w_{ij}) and bias ($\bar{b}$) values can be modified during the training of the neural network in an iterative process. The activation value is passed through activation or transfer functions, such as log-sigmoid, tan-sigmoid, and/or linear transfer functions, to produce the output value (y_j in Figure 6.1). The output value is transmitted to the next neuron. Similar computational processes are repeated in all single neurons. The single neurons are interconnected with many elements in parallel, and then the multi-layer ANN is developed as illustrated in Figure 6.1.
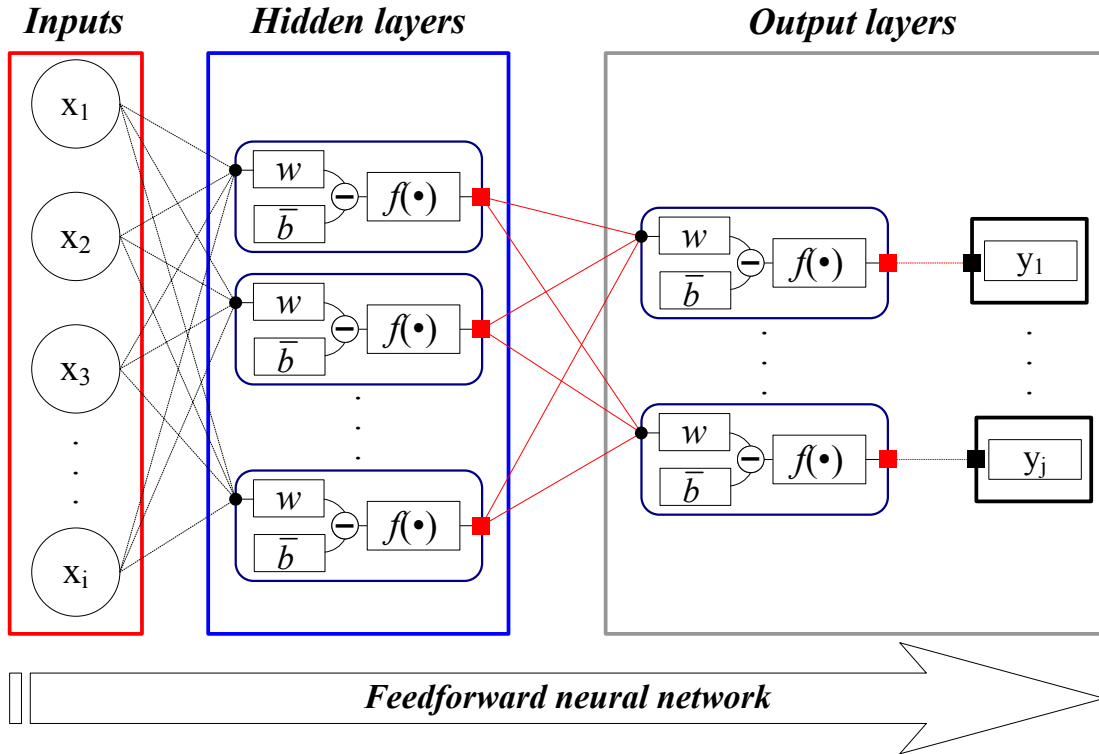
Figure 6.1. Multi-layer feedforward neural network reproduced from [Stewart 2010]

The feedforward neural network allows information transfer only from an earlier layer to the next consecutive layers. The neural network system is based on a supervised process, which knows actual outputs for the inputs utilized in the model training and provides calculated outputs by comparing the actual and calculated outputs. The neural networks developed in this study are based on the numerical simulations predicted using the FE models described in Chapters 4 and 5. If the actual outputs differ from the calculated outputs, the weight and bias in each single neuron are updated by one of the learning or teaching algorithms to match the calculated outputs with the actual inputs. These algorithms (e.g., back-propagation, Quasi-Newton and Levenberg-Marquardt algorithms) help the model minimize the difference between the actual and calculated outputs by automatically determining the weight and bias of the hidden and output layers (w and $\bar{b}$ in Figure 6.1) in the numerical or iterative method. Therefore, the neural network model can predict the best-fit values to the actual outputs for given input parameters.

6.3 Input Parameters

Two types of input parameters were selected for this neural network: (1) loading parameters for seismic and blast loads, and (2) geometric and material parameters associated with the design of an FRP column jacketing system. The geometric and material parameters for the FRP column jacketing system were selected as follows: (1) retrofit location (RL), (2) FRP material properties (f_{ju}), (3) jacket thickness (t_j), (4) column inner diameter enlarged by non-shrink grout (ID), and (5) grout material properties (f_g) used for section enlargement. This section describes the selection of the input parameters, as well as the selection of their training points that were used for the development of FRMs. The individual training points had a nominal, minimum, and maximum value within certain model ranges assumed in this study. The selection

119

of the three training points was based on a previous work [Stewart and Morrill 2015]. The nominal value is usually the most representative value of the sample. This is determined based on mean, median, code definition, and potentially experience aids. Table 6.1 summarizes all input parameters, their model ranges, and their training points (i.e., extreme and nominal values). The methods used to identify these ranges and training points for the various input parameters are given in the following sections.

Table 6.1. Summary of input parameters, ranges and training points

Parameter type	Parameter	Model range	Nominal	Extreme values	
				Minimum	Maximum
Loading	Peak spectral acceleration	0.5 to 3.0 g	1.5 g	0.5 g	3.0 g
	Scaled distance (standoff distance)	0.4 to 1.6 m/kg$^{1/3}$ (3.7 to 14.0 m)	0.8 m/kg$^{1/3}$ (7.0 m)	0.4 m/kg$^{1/3}$ (3.7 m)	1.6 m/kg$^{1/3}$ (14.0 m)
Geometric and material	Retrofit location	No-retrofit [a] to all-story retrofit	First-story retrofit	No-retrofit [a]	All-story retrofit
	Ultimate FRP jacket strength	166 to 1380 MPa	419 MPa	166 MPa	1380 MPa
	FRP jacket thickness	0 to 6.5 mm	3.6 mm	0.0 mm	6.5 mm
	Column inner diameter	444 to 559 mm	444 mm	No-retrofit [a]	559 mm
	Grout compressive strength	13.8 to 86.2 MPa (1-day to 28-day curing)	42.9 MPa	13.8 MPa	86.2 MPa

[a] No-retrofit = as-built condition.

120

6.3.1 Loading parameters

6.3.1.1 Seismic load

Seismic loads are characterized by peak spectral accelerations, which are referred to as "S_{a_peak}" in this study. FEMA-356 [2000] defines zones of high seismicity where there is a 10 % probability exceedance in 50 years (10 %/ 50 years, 475 year return period) to be higher than a 0.5 g design short-period response acceleration (S_{DS}). Based on this definition, the present work used a peak spectral acceleration of 0.5 g as the minimum training point for the seismic load (i.e., S_{a_min} = 0.5 g). Table 6.2 summarizes the maximum considered earthquake (MCE) spectral accelerations associated with seismic design categories (SDC) D, C, and B, specified in FEMA-P695 [2009]. Among the MCE spectral accelerations, the MCE short-period response acceleration (S_{MS}) in SDC D was defined as 1.5 g, and the MCE short-period acceleration was set as the nominal value of the peak spectral acceleration (i.e. S_{a_n} = 1.5 g). The reason for choosing the MCE short-period acceleration (S_{MS}) as the nominal spectral acceleration (S_{a_n}) is that low-rise building structures of the type used in this study have short periods within a given transition period (T_o) in SDC D (T_o = 0.6 seconds in Table 6.2 [FEMA-P695 2009]). Additionally, collapse intensities that indicate spectral accelerations are approaching collapse levels for building structures are generally higher than the MCE ground motions. FEMA-P695 recommends that the collapse intensity should be at least two times the MCE spectral acceleration. Therefore, this study assumed that the maximum training point of the peak spectral acceleration (S_{a_max}) is twice the MCE spectral acceleration (S_{MS} = 1.5 g) for the collapse intensity (i.e., S_{a_max} = 2 × 1.5 g = 3.0 g). This collapse intensity is needed to investigate the seismic responses of the frame models exceeding drift limit for a collapse prevention (CP) level

(i.e., CP drift limit > 4.0 %, as given in Table 3.3). Based on these assumptions, the peak spectral accelerations (S_{a_peak}) are within the range of 0.5 g to 3.0 g.

Table 6.2. MCE spectral accelerations and transition periods [FEMA-P695 2009]

Seismic design category (SDC)		Maximum considered earthquake (MCE)		Transition period (T_o, second)
Maximum	Minimum	S_{MS}[a] (g)	S_{M1}[b] (g)	
D	-	1.50	0.90	0.6
C	D	0.75	0.30	0.4
B	C	0.50	0.20	0.4
-	B	0.25	0.10	0.4

[a] S_{MS} = MCE spectral response acceleration at short periods
[b] S_{M1} = MCE spectral response acceleration at a period of 1.0 second

6.3.1.2 Blast load

As discussed in Chapter 5, the blast loads were modeled with a coupled method using both load blast enhanced (LBE) and Multi-Material Arbitrary Lagrangian-Eulerian (MM-ALE) methods (a coupled LBE-ALE method). The LBE method can characterize blast loads using three loading parameters: (1) charge weight (W_{TNT}), (2) standoff distance (R_D), and (3) standoff height (R_H). This study determined the range of the blast loads included by varying the scaled distance (i.e. $Z = R_D / W_{TNT}^{1/3}$). The charge weight and the standoff height were assumed as 680.4 kg and 0.9 m, respectively. The charge weight depends on the size and capacity of the vehicle [FEMA-426 2003]; the values selected represent typical vehicle bombs utilizing sedans to vans [FEMA-426 2003, and Stewart 2010]. After fixing the two loading parameters (i.e., charge weight and standoff height), the standoff distance varied from 3.7 m to 14.0 m (3.7 m $\leq R_D \leq$ 14.0 m). It should be noted that near contact charges closer than a standoff distance of 3.7 m (i.e.,

scaled distance < 0.4 m/kg$^{1/3}$) were not considered in the present work because the LBE method used for producing blast pressures is not acceptable below the scaled distance of 0.4 m/kg$^{1/3}$ [LSTC 2013]. Additionally, this study also excluded charges larger than the scaled distance of 1.6 m/kg$^{1/3}$ because blast loads beyond the scaled distance of 1.6 m/kg$^{1/3}$ produced marginal responses [Crawford et al. 1997]. For these reasons, the scaled distance (Z) used in this study ranged from 0.4 m/kg$^{1/3}$ to 1.6 m/kg$^{1/3}$. The nominal value of the scaled distance was selected as 0.8 m/kg$^{1/3}$, which corresponds to a standoff distance of 3.7 m, as given in Table 6.1.

6.3.2 Geometric and material parameters

6.3.2.1 Retrofit location

The experimental program discussed in Chapter 3 only involved a frame installed with the FRP jacketing system on the first story columns in order to minimize soft-story responses. However, a retrofit using FRP column jackets may be appropriate on multiple stories for structures affected by seismic and blast loading because the location of the retrofit system contributes to the increase or decrease in global stiffness of the structure. Therefore, the retrofit location is taken into account as a global geometric parameter of the retrofit system in the neural network models.

The retrofit location parameter has three training points, as given in Table 6.1. The nominal and maximum training points respectively represent a first-story retrofit installation and all-story retrofit installation. The minimum training point is set to be "No-retrofit," as given in Table 6.1. The minimum training point thus represents the as-built frame with no retrofit installed.

6.3.2.2 Ultimate tensile strength of the FRP jacket

The second parameter of the FRP column jacketing system is the ultimate tensile strength of the FRP jacket (f_{ju}). As discussed in Section 2.4.2, the ultimate jacket strength contributes to the amount of confining pressure on the concrete column, which directly influences concrete material behavior. Thus, the ultimate jacket strength was selected as one of the parameters associated with the retrofit system. The tensile strength of the FRP jacket is dependent on the type, amount, and orientation of the fiber material, along with the resin type. To determine the range of the FRP strength, product literature from a number of commercially available FRP jacket systems was examined. The collected commercial product datasheets are summarized in Table A.1. Table A.1 includes various fiber material types, such as glass, carbon, and aramid fiber materials. Based on the datasheets, the range of the ultimate jacket strength was selected as 166 MPa to 1380 MPa.

The nominal training point of the ultimate jacket strength was selected by investigating the confinement effect (i.e., the ratio of peak confined concrete strength to unconfined concrete strength, f_{cc}' / f_{co}) for the various jacket systems using the material datasheets displayed in Table A.1. The unconfined concrete strength (f_{co}), jacket thickness (t_j), and the inner diameter of the FRP column jacketing system (*ID*) were fixed as 31.4 MPa, 2.0 mm, and 444 mm, respectively. The peak confined strength (f_{cc}'), was calculated by Equation (2.2) in Section 2.4.1. Figure 6.2 demonstrates confinement effects compared to the ultimate tensile strength of FRP jackets. The FRP material, which provides confinement closest to the average of the confinement effects among the various FRP material systems examined, was determined to be the nominal value of the ultimate jacket strength (f_{ju_n}), which is 419 MPa. The extreme training points were set as the

minimum and maximum values among the datasheets (i.e. f_{ju_min} = 166 MPa, and f_{ju_max} = 1380 MPa).
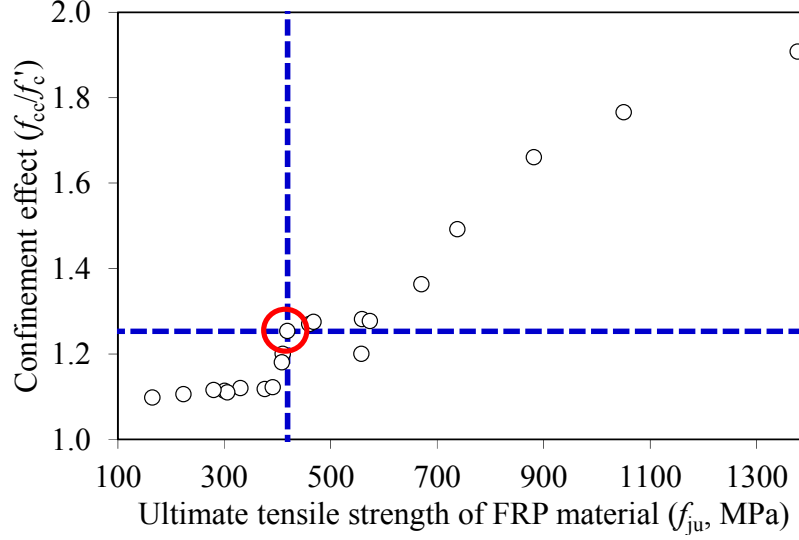
Figure 6.2. Confinement effect for FRP material properties

6.3.2.3 Thickness of FRP jacket

The next geometric parameter is the jacket thickness (t_j). An increase in the jacket thickness enhances confining pressure, as shown in Equation (2.1) in Section 2.4.1, and the enhanced confining pressure (σ_R) increases the peak confined concrete strength (f_{cc}'), as shown in Equation (2.2) in Section 2.4.1. To determine the range of jacket thicknesses used with the neural network model, the effects of the jacket thickness on a modified confinement ratio (MCR) were investigated. The MCR is given as shown in Equation (6.2):

$$\text{MCR} = \left(\frac{2r}{ID}\right) \cdot \frac{\sigma_R}{f_{co}}$$

(6.2)

where

r = corner radius

ID = inner diameter of the FRP column jacketing system

f_{co} = unconfined concrete strength.

For circular columns, the MCR is simply expressed as σ_R/f_{co}, which is the same as confinement ratio (CR). This is because the corner radius (r) is equal to the radius of the FRP column jacketing system (i.e., $r = ID/2$). Mirmiran et al. [1996] recommended a minimum MCR of 0.15 (i.e., $MCR_{min} = 0.15$). This minimum MCR ensures that the ultimate confined concrete strength (f_{cu}') is equal or greater to the peak confined concrete strength (f_{cc}'). Spoelstra and Monti [1999] also suggested a minimum value of 0.07 for the confinement ratio (i.e. $CR_{min} = 0.07$). Based on their experimental results, if the CR is less than 0.07 for a jacket system, the ultimate confined concrete strength (f_{cu}') will be less than the unconfined concrete strength (f_{co}). Thus, it should be noted that even though the minimum MCR is less than 0.15, the confining pressure can exceed the minimum value for the CR, and it can still enhance concrete behavior in terms of the peak confined concrete strength (f_{cc}') and the ultimate axial strain (ε_{cu}).

Since there is no maximum limit for the jacket thickness, this study calculated the MCR values with various jacket thicknesses and compared those values to the minimum MCR ($MCR_{min} = 0.15$) recommended by Rochette [1996] to determine the maximum thickness of the FRP jacket (t_{j_max}). Figure 6.3 shows the MCRs in terms of the minimum (f_{ju_min}), nominal (f_{ju_n}), and maximum (f_{ju_max}) training points of the FRP jacket strength determined in the previous section. As illustrated in Figure 6.3, the MCR value for the minimum jacket strength (f_{ju_min}) reaches the minimum MCR ($MCR_{min} = 0.15$ in Figure 6.3) for a jacket thickness of 6.5mm; thus, this value of jacket thickness was selected as the maximum training point. Since the MCR value

at the maximum jacket thickness still exceeds the minimum confinement ratio (CR) of 0.07 (CR_{min} = 0.07), the maximum jacket thickness can improve the concrete behavior in terms of the peak confined concrete strength (f_{cc}') and the ultimate axial strain (ε_{cu}) [Spoelstra and Monti 1999].

The nominal value of the jacket thickness (t_{j_n}) was also determined by investigating the MCR. The nominal jacket thickness is 3.6 mm (t_{j_n} = 3.6 mm in Figure 6.3), which corresponds to the mean value of the MCRs (MCR_{mean} = 0.21 in Figure 6.3) for the nominal jacket strength (f_{ju_n}) as shown in Figure 6.3. The minimum value of the jacket thickness (t_{j_min}) was assumed to be zero, which represents an as-built condition. This was intended to reduce sample cases in the datasets. Therefore, the jacket thicknesses used in the neural network model ranged from 0 mm to 6.5 mm.

Figure 6.4 shows the axial stress-strain behavior of FRP-confined concrete materials with respect to the three training points of the jacket thickness (t_{j_min}, t_{j_n} and t_{j_max}) in the minimum (f_{ju_min}), nominal (f_{ju_n}), and maximum (f_{ju_max}) FRP jacket strengths. The axial stress-strain behavior was derived from a passive confinement model proposed by Fam and Rizkalla [2001]. They combined Mander's confinement model [Mander et al. 1988] for concrete confined by transverse reinforcements with a variable confining pressure by changing material parameters to predict axial behavior on concrete-filled FRP tubes. This confinement model shows good correlation with experimental results for the axial behavior of the FRP-confined concrete. The confinement model was utilized in this study to confirm the change in concrete material behavior by applying FRP jackets assuming jacket thicknesses equal to each training point. As compared to the unconfined concrete behavior, the confining pressure produced by the nominal (t_{j_n}) and

maximum (t_{j_max}) training points of the jacket thicknesses significantly improved the material behavior.
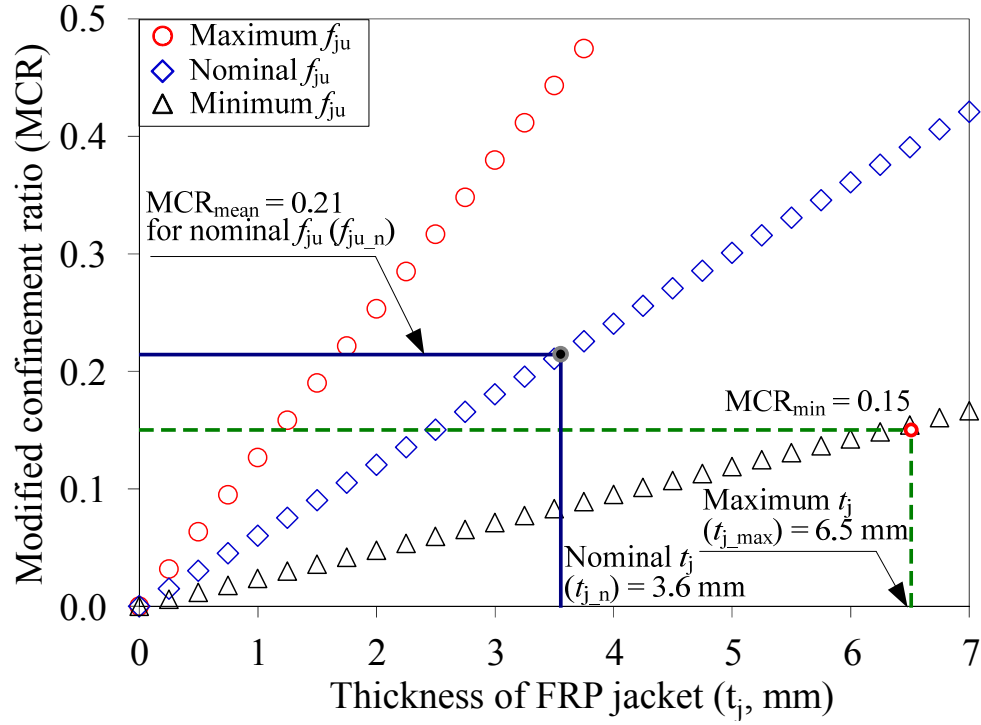
Figure 6.3. Modified confinement ratio (MCR) for minimum, nominal and maximum training points of FRP jacket strength (f_{ju_min}, f_{ju_n} and f_{ju_max})
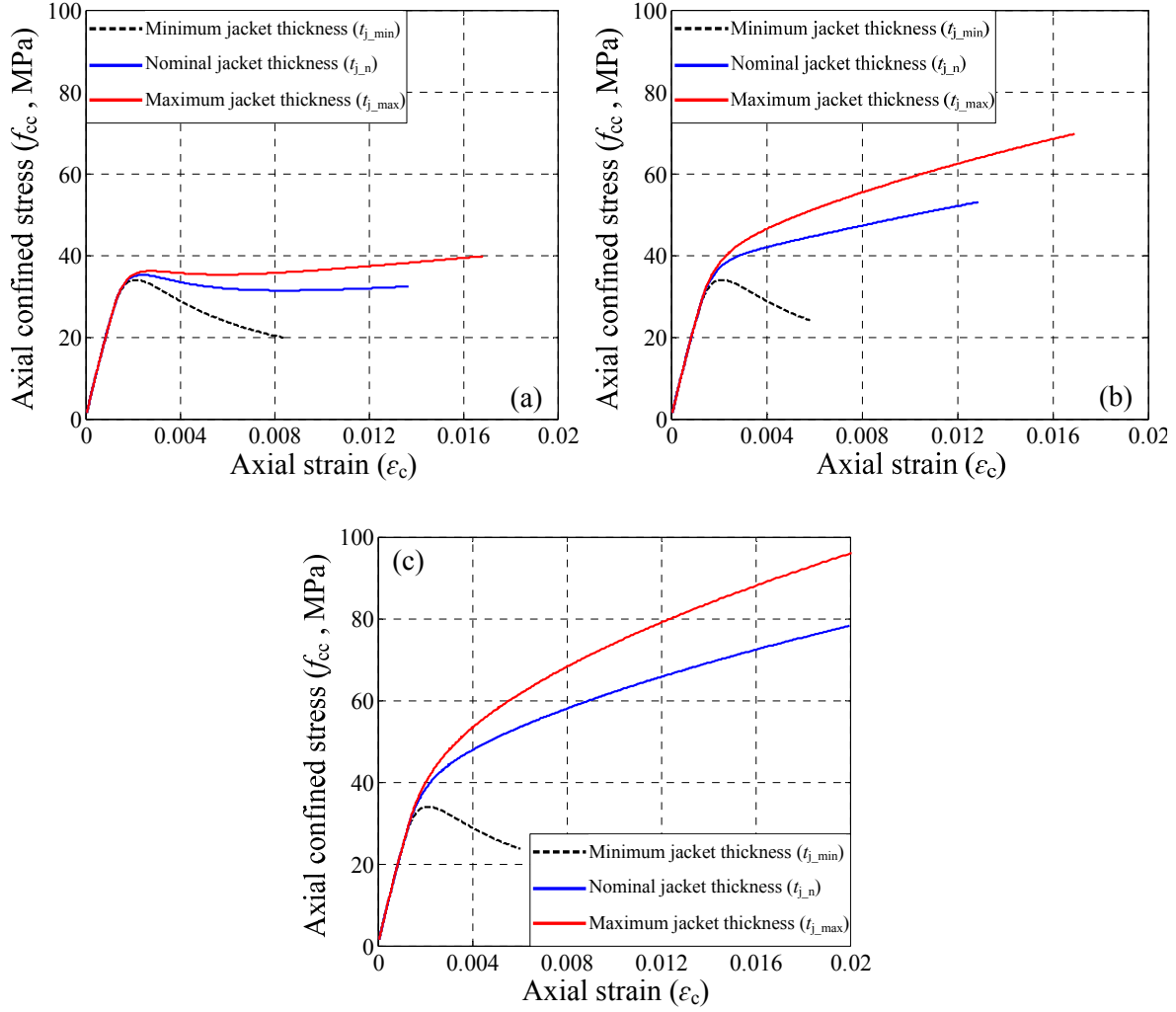
Figure 6.4. Axial stress-strain behavior of unconfined and confined concrete materials based on training points for jacket thicknesses: (a) minimum jacket strength (f_{ju_min}); (b) nominal jacket strength (f_{ju_n}); (c) maximum jacket strength (f_{ju_max})

6.3.2.4 Inner diameter of FRP column jacketing system

Cross-sectional shapes of existing RC columns are modified by section enlargement of rectangular or square shapes to circular or elliptical shapes, using non-shrink grout materials. The section enlargement contributes to maximizing confinement effects as well as increasing flexural stiffness in the existing RC columns, as discussed in Chapter 2. Additionally, the section enlargement results in a reduction in the confining pressure because of an increase in the radius

of the FRP jacketing system (r in Equation (2.1)). In practice, a typical size of the section enlargement from each edge of the existing concrete is within 69.5 mm to 127 mm [Teng et al. 2002, and FEMA-547 2006]. The minimum section enlargement required is due to the need to fill the annular space between the FRP jacket and the existing concrete column with a grout material [FEMA-547 2006]. The maximum section enlargement is determined considering a bond condition between the grout material and the existing concrete without mechanical anchorage [Teng et al. 2002]. The present work characterizes the effect of section enlargement using the size of the inner diameter (ID) of the FRP column jacketing system as one of the geometric parameters. Based on the typical range for section enlargement in structural retrofits, the range of the column inner diameter (ID) varies from 444 mm to 559 mm. The minimum value of the column diameter was set as the nominal training point (i.e., ID_n = 444 mm), and the maximum value was set as the maximum training point (i.e., ID_{max} = 559 mm). Additionally, the minimum training point (ID_{min}) was determined using the no-retrofit (as-built) configuration as given in Table 6.1.

6.3.2.5 Unconfined compressive strength of grout material

Material properties of the grout material used for the section enlargement will obviously affect the flexural stiffness in the retrofitted RC column. In the present investigation, the unconfined compressive strength of the grout material (f_g) was chosen as one of the material parameters associated with the FRP column jacketing system. To determine the range of the grout material properties to be used in the neural network models, product literature from a number of commercially available grout products were examined; these datasheets are shown in Table A.2. The table summarizes the 1-day and 28-day curing compressive strength values of the

grout materials for the collected product datasheets. Using the datasheets as a guide, the minimum value for grout strength was assumed to be 13.8 MPa (1-day curing compressive strength), and the maximum value was set as 89.6 MPa (28-day curing compressive strength). Therefore, the range of grout strengths varied between 13.8 MPa and 89.6 MPa. The minimum and maximum values were selected as f_{g_min} = 13.8 MPa and f_{g_max} = 89.6 MPa, respectively, as shown in Table 6.1. The nominal training point was assumed to be the average of the grout strength, f_{g_n} = 42.9 MPa, taken from the commercial datasheets given in Table A.2.

6.4 Combination of Training Points

To build the initial dataset, the training points of the input parameters described in Section 6.3 were combined in the systematic fashion described in Stewart [2010]. Based on this previous work, the present study utilized three different combining methods: (1) all nominal training points, (2) two fixed nominal training points while varying one parameter to an extreme, and (3) one fixed nominal training point while varying two parameters to extremes. These combining methods were integrated into the five input parameters (peak spectral acceleration or scaled distance, ultimate tensile strength of FRP jacket, jacket thickness, inner diameter of the FRP column jacketing system, and grout strength), and 34 sample cases with the first-story retrofit installation for each loading type were found. It should be noted that when the training points for minimum jacket thickness and inner diameter (i.e. t_{j_min} and $ID_{\_min}$) were combined with other parameters, the sample cases were excluded from the dataset because the sample cases with the minimum training points of the jacket thickness and inner diameter parameters represented the as-built condition.

To investigate the effects of the retrofit location parameter, an additional 34 sample cases for the all-story retrofit installation (found by the same combining manner) were included in the initial dataset. For the as-built condition, three sample cases, which were composed of the three training points of the loading parameters, were also added to the dataset. Thus, the total number of the initial sample cases was 71 for each of the loading types, as given in Table 6.3. In total, this study populated 142 sample cases for training, validating, and testing FRMs (Table 6.3). The seismic and blast initial datasets are summarized in Tables B.1 and B.2, respectively.

Table 6.3. Number of sample cases in seismic and blast initial datasets

Loading type	As-built frame	Retrofitted frame		Number of sample cases
		First-story retrofit	All-story retrofit	
Seismic loading	3	34	34	71
Blast loading	3	34	34	71
Total number of sample cases				142

6.5 Output Parameters

In this study, the FRMs were trained with multiple output parameters, which are composed of inter-story drift ratio (IDR in Section 3.3) and seismic energy-based damage demand (D_S) for the seismic FRM, and displacement ductility demand (μ_{blast}) and blast energy-based damage demand (D_B) for the blast FRM. The inter-story drift ratio was utilized to estimate the seismic performance level using the drift-based performance criteria in FEMA-356 [2000], which will be discussed in Chapter 7. In order to investigate the blast performance level in terms of the ductility-based limit states specified in ASCE 59-11 [2011], the displacement ductility

demand (μ_{blast}) was selected as one of the output parameters. To combine the seismic and blast performance criteria specified in the current design codes, the seismic (D_{S}) and blast (D_{B}) energy-based damage demands were computed using the Park-Ang damage model [Park and Ang 1987].

6.5.1 Seismic demand

To compute seismic demands such as inter-story drift ratio and seismic energy-based damage demand for the various input parameters in the initial seismic dataset, this study utilized a capacity spectrum method (CSM). The CSM approach was implemented into all sample cases given in Table B.1. To compute the seismic demands using the CSM approach, the as-built and retrofitted FE frame models described in Chapter 4 were varied with the training points of each input parameter. After that, nonlinear pushover and eigenvalue analyses were performed for the FE frame models with varying input parameters. Based on the simulated responses, the output parameters (IDR and D_{S}) associated with the seismic demands in the initial dataset were generated; these are given in Table B.3. To better understand the procedure of output generation used in this study, one of the cases, which represents the as-built configuration under the peak spectral acceleration ($S_{\text{a\_peak}}$) of 1.5 g (Case #2 in Table B.1), is detailed below as an example.

6.5.1.1 Capacity spectrum method

A CSM is one of the simplified analysis procedures presented in Applied Technology Council (ATC) 40 [1996] and FEMA-274 [1997], originally proposed by Freeman et al. (1975). The simplified approach has been widely used instead of time-history analyses to estimate seismic displacement demands when designing new structures and upgrading existing structures

[Chopra and Goel 2000, Fajfar 2000, and Miranda 2001]. Basically, the CSM approach determines seismic displacement demands for a given structure by finding the interaction point between the equivalent capacity and demand spectra, which is plotted in an acceleration-displacement response spectrum (ADRS) format, as illustrated in Figure 6.5. The capacity spectrum for the structure is based on a force-displacement curve obtained from a non-linear pushover analysis, and the pushover curve is converted to the ADRS format. The demand spectrum is defined by a response spectrum, which plots the spectral accelerations (S_a) against spectral displacements (S_d). To represent an inelastic spectrum, the response spectrum is reduced by an equivalent damping ratio or ductility. Previous studies [Chopra and Goel 1999, and Fajfar 1999] have improved the CSM approach to be more accurate and convenient than prior CSM approaches when estimating maximum seismic demands. The improved methods were verified by comparing results with seismic demands computed from prior CSM approaches [Chopra and Goel 1999] and reproducing the measured seismic demands [Fajfar 1999].
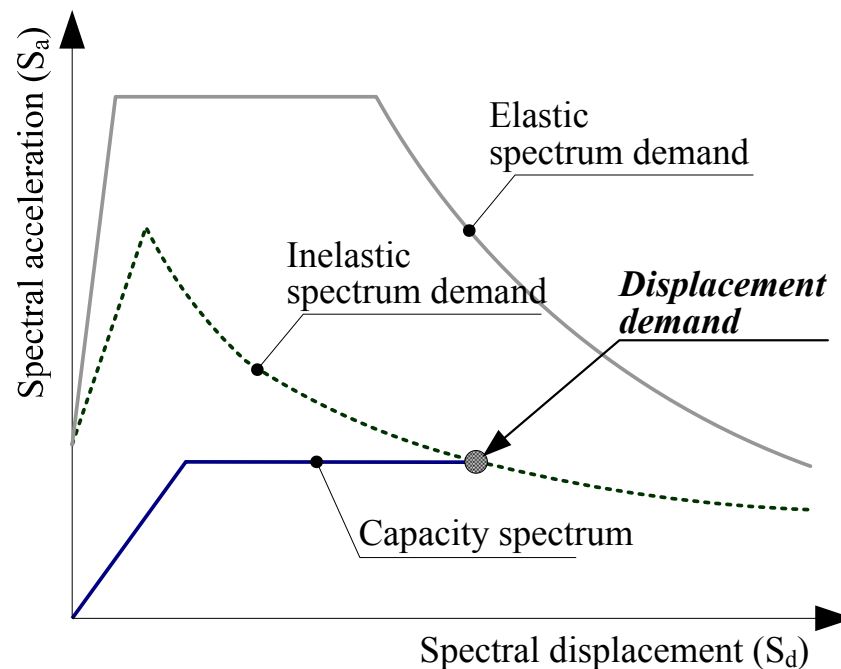
Figure 6.5. Capacity spectrum method (CSM)

134

6.5.1.2 Inter-story drift ratio

One of the seismic demands, the inter-story drift ratio (IDR), was generated using the improved CSM approach [Fajfar 1999]. This section describes the procedure for computing the IDR. First, a nonlinear pushover analysis was performed for the FE frame model. This simulation determined the relationship between base shear (V_{base}) and roof displacement (δ_{roof}), which is the pushover curve for a multi-degree-of-freedom (MDOF) system. Since the CSM was developed based on an equivalent single-degree-of-freedom (SDOF) system, the pushover curve for the MDOF system must be transformed to the SDOF system [Fajfar 1999, Gencturk and Elnashai 2008, and Rossetto 2016]. The pushover curve can be transformed from the MDOF to the SDOF using Equation (6.3) [Fajfar 1999]:

$$Q = \Gamma \cdot Q^* \tag{6.3}$$

where

Q^* = quantities in the SDOF system (e.g., base shear and displacement in the SDOF model, V^* and δ^*);

Q = corresponding quantities in the MDOF system

Γ = modal participation factor

The participation factor can be defined as Equation (6.4):

$$\Gamma = \frac{\sum M_i \phi_{ij}}{\sum M_i \phi_{ij}^2} \tag{6.4}$$

135

where

$M_i = i^{\text{th}}$ story mass

$\phi_{\text{ij}} = j^{\text{th}}$ normalized mode vector at the ith story, characterized by the eigenvalue analysis
for the FE frame model

After that, the pushover curve of the SDOF system was converted into a capacity spectrum curve in the ADRS format using Equation (6.5); this is represented by the blue dashed line in Figure 6.6.

$$S_a = \frac{V_{base}}{\Gamma \cdot M^*} \tag{6.5a}$$

$$S_d = \frac{\delta_{roof}}{\Gamma \cdot \phi_n} \tag{6.5b}$$

where

$M^* = $ mass of the equivalent SDOF system $(= \sum M_i \phi_{ij})$

$\phi_n = $ mode shape vector in the roof, assumed to be 1.0 in this study because the mode vectors are normalized with the value of the mode vector at the roof

To find the approximated yielding spectral displacement (S_{dy}) for the given structure, the capacity spectrum curve was idealized as a bilinear curve with no post-yield stiffness (i.e., an elastic-perfectly plastic form). This study followed the procedure of bilinear idealization specified in Paulay and Priestley [1992] and ATC-19 [1995]. Figure 6.6 shows capacity

spectrum curves for the as-built (Case #2) and retrofitted (Case #17) FE frame models. The idealization procedure assumed that the ultimate base shear (V_u) was the same as the yielding base shear (V_y). This indicates that the ultimate spectral acceleration (S_{au}) was equal to the yielding spectral acceleration (S_{ay}) in the capacity spectrum curve (i.e., $S_{ay} = S_{au}$). In the idealization procedure, the yielding displacement (δ_y) can be defined by an interaction between the yielding base shear and reduced stiffness, which was evaluated as the secant stiffness at 75.0 % of the yielding base shear ($S_{dy} = 23.4$ mm at the S_{ay} of 0.32 g in Figure 6.6(a), and $S_{dy} = 22.1$ mm at the S_{ay} of 0.48 g in Figure 6.6(b)). Additionally, this study assumed that the ultimate displacement (δ_u) corresponded to the displacement at the point of a 20.0 % strength reduction (i.e., $S_{du} = 75.0$ mm at 80.0 % of the S_{ay} in Figure 6.6(a), and $S_{du} = 112.4$ mm at 80.0 % of the S_{ay} in Figure 6.6(b)) based on FEMA-P695 [2009]. Through the idealization procedure, the spectral parameters, such as yielding and ultimate spectral displacement (S_{dy} and S_{du} in Figure 6.6) and yielding spectral acceleration (S_{ay} in Figure 6.6), were respectively estimated as 23.4 mm, 75.0 mm and 0.32 g for Case #2, as illustrated in Figure 6.6(a). Based on those response parameters, an effective elastic period of the SDOF system can be determined by Equation (6.6):

$$T^* = 2\pi \sqrt{\frac{M^* \delta_y^*}{V_y^*}} = \pi \sqrt{\frac{S_{dy}}{S_{ay} \cdot g}} \qquad (6.6)$$

where

T^* = effective elastic period of the SDOF system

δ_y^* = yielding displacement in the SDOF system

V_y^* = yielding force in the SDOF system

g = acceleration due to gravity
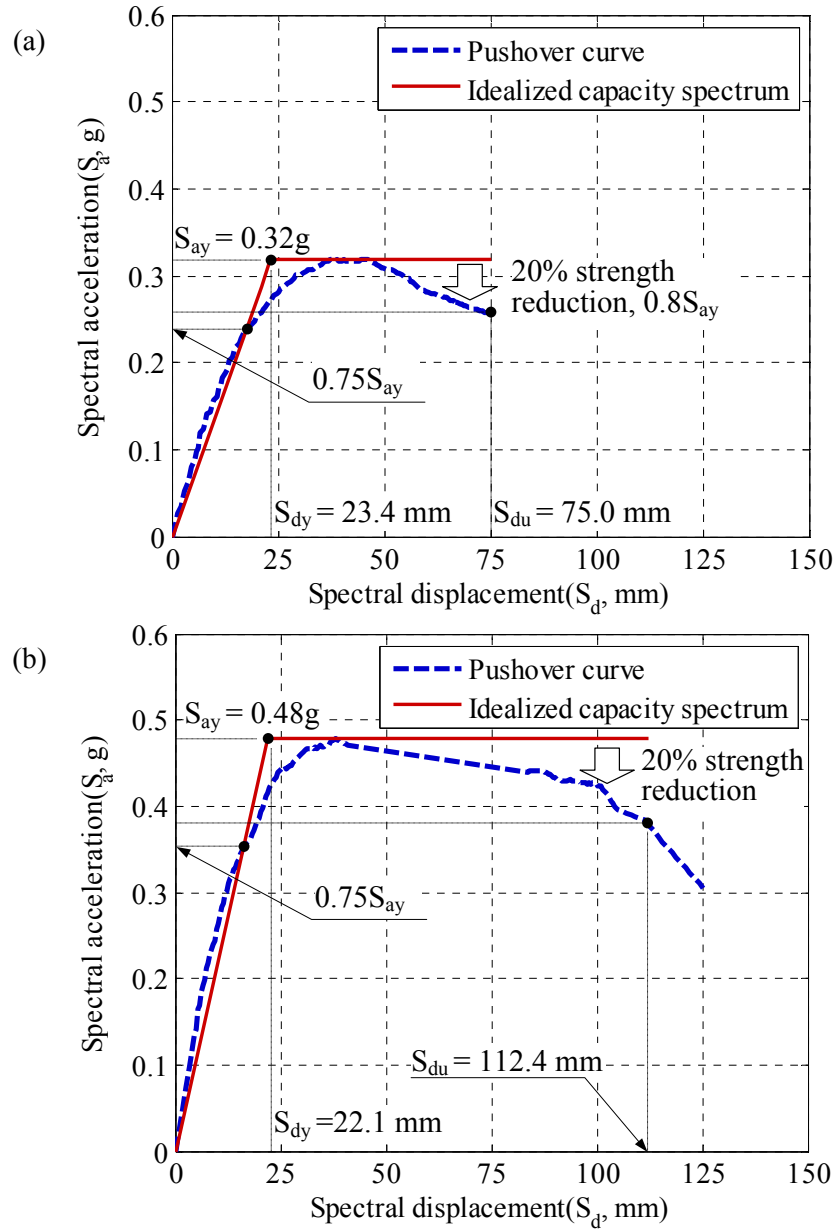
Figure 6.6. Capacity spectrum curves in acceleration-displacement response spectrum format: (a) Case #2 (as-built FE frame model); (b) Case # 5 (retrofitted FE frame model)

After building the idealized capacity spectrum curve, an elastic response spectrum was plotted in terms of period (T) and spectral acceleration (S_a) for the given peak spectral intensity (S_{a_peak} = 1.5 g for Case #2), as shown in Figure 6.7(a). For the elastic response spectrum, this

study assumed that the damping ratio and transition period (T_o) were equal to 5.0 % and 0.6 seconds, respectively [FEMA-P695 2009]. To build the elastic response spectrum with the transition period of 0.6 seconds, the maximum considered earthquake (MCE) one-period spectral response acceleration (S_{M1}) was assumed as 60.0 % of the MCE short-period spectral response acceleration (S_{MS}). The elastic response spectrum was transformed to an elastic spectrum demand curve in the ADRS format using Equation (6.7):

$$S_d = \frac{T^2}{4\pi^2} S_a$$

(6.7)

where

S_d = spectral displacement in the SDOF system

S_a = spectral acceleration in the SDOF system

The transformed elastic spectrum demand curve is shown in Figure 6.7(b). The figure also includes an inelastic spectrum demand curve with a ductility reduction factor (R_μ) of 4.71. This study defines the ductility reduction factor against a period (T) using Equations (6.8):

$$R_\mu = (\mu - 1)\frac{T}{T_o} + 1 \qquad \text{for } T \leq T_o$$

(6.8a)

$$R_\mu = \mu = S_{ae}/S_{ay} \qquad \text{for } T > T_o$$

(6.8b)

where

μ = displacement ductility demand

S_{ae} = elastic spectral acceleration
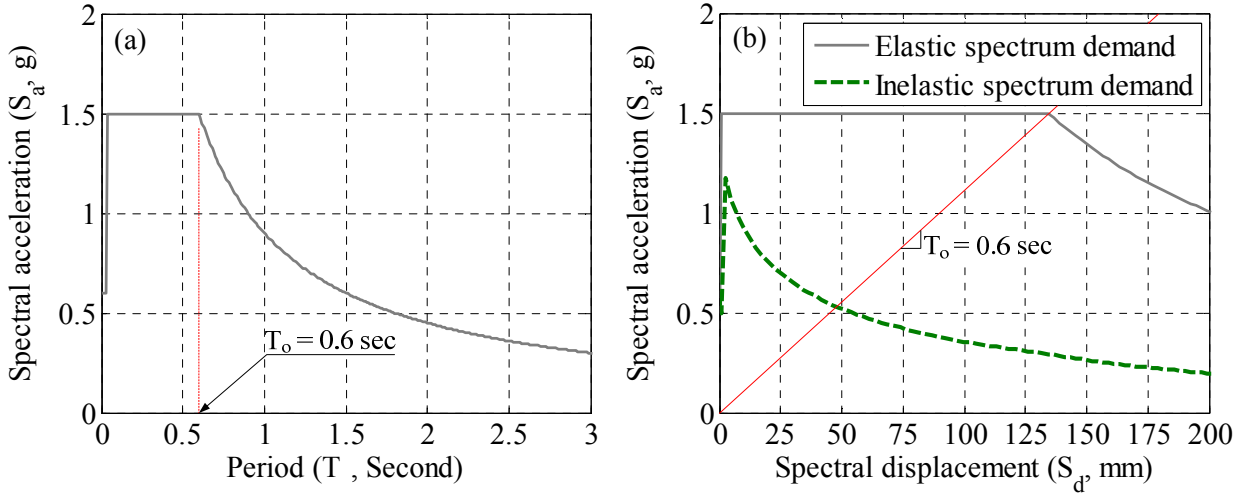
Figure 6.7. Demand spectrum curves for Case #2: (a) elastic response spectrum; and (b) elastic and inelastic spectrum demand curves in ADRS format

Next, the idealized capacity spectrum was compared to the elastic spectrum demand curve in the same plot as illustrated in Figure 6.8. An elastic spectral acceleration of 1.50 g (S_{ae} = 1.50 g in Figure 6.8) was detected at the interacted point between the elastic spectrum demand curve and the elastic period (T^*) of 0.54 second. The ductility reduction factor (R_μ) can be defined by the ratio of the elastic spectral acceleration to the yielding spectral acceleration (i.e., $R_\mu = S_{ae} / S_{ay} = 4.71$). The spectrum demand curve was reduced by the R_μ value of 4.71. For Case #2, since the elastic period (T^*) was less than the transition period (T_o) of 0.60 seconds, the displacement ductility demand (i.e., μ = 5.10) was calculated using Equation (6.9), which is rearranged from Equation (6.8).

$$\mu = (R_\mu - 1)\frac{T_o}{T^*} + 1 \qquad \text{for } T^* \le T_o \qquad (6.9a)$$

$$\mu = R_\mu \qquad\qquad \text{for } T^* > T_o \qquad\qquad (6.9b)$$

If the elastic period is higher than the transition period (e.g., a medium or high period range of structure), the spectral displacement demand (S_{dm}) is same as the displacement corresponding to the elastic spectral acceleration [Fajfar 1999]. However, since the frame models were less than the elastic period of 0.54 seconds (T^* of 0.54 seconds in Figure 6.8), the spectral displacement demand (S_{dm}) for Case #2 was computed by multiplying the displacement ductility demand (μ) and yielding spectral displacement demand (S_{dy}), as given in Equation (6.10):

$$S_{dm} = \mu \times S_{dy} = 119 \text{ mm} \qquad\qquad (6.10)$$

This value of the spectral displacement demand represents an interaction point between the inelastic spectrum demand reduced by the ductility reduction factor and the idealized capacity curves in Figure 6.8. It should be noted that this study selected 119 mm as the spectral displacement demand (S_{dm}), which is larger than the ultimate spectral displacement (S_{du}) of 75.0 mm in the capacity spectrum curve given in Figure 6.6(a), to generate inter-story drift demands reaching or exceeding a drift limit for a collapse prevention (CP) level (i.e., CP drift limit > 4.0 %). After calculating the spectral demand in the SDOF system, the spectral displacement of the SDOF (S_{dm}) was transformed to the displacement demand of the MDOF (δ_m) using Equation (6.11):

$$\delta_{mi} = \Gamma \times S_{dm} = 144 \text{ mm} \qquad\qquad (6.11)$$

where

Γ = modal participation factor to transform the spectral displacement of the SDOF to the displacement of the MDOF

δ_{mi} = story displacement demand at the ith story

To estimate a story displacement demand at the ith story (δ_{mi}), the present work distributed the MDOF displacement demand (δ_m) over the first and second stories using the first mode shape vector (ϕ_{i1}), obtained from the eigenvalue analyses of the FE frame model, as given in Equation (6.12):

$$\delta_{mi} = \delta_m \cdot \phi_{i1} = \delta_m \begin{bmatrix} \phi_{11} \\ \phi_{21} \end{bmatrix}$$

(6.12)

The rationale for only considering the first mode shape vector is that the dynamic behavior of low-rise building structures is mainly dominated by the first mode shape [Bracci et al. 1997, Akkar and Metin 2007, and FEMA-440 2005]. For Case #2, the first and second story displacement demands (δ_{m1} and δ_{m2}) were 80.9 mm and 144 mm, respectively, and the peak inter-story drift ratio was determined as 2.40 % in the first story, which corresponded to a collapse prevention (CP) level in FEMA-356 [2000]. This study chose the peak inter-story drift ratio as one of the output parameters to evaluate the seismic performance level using the drift-based limit states.
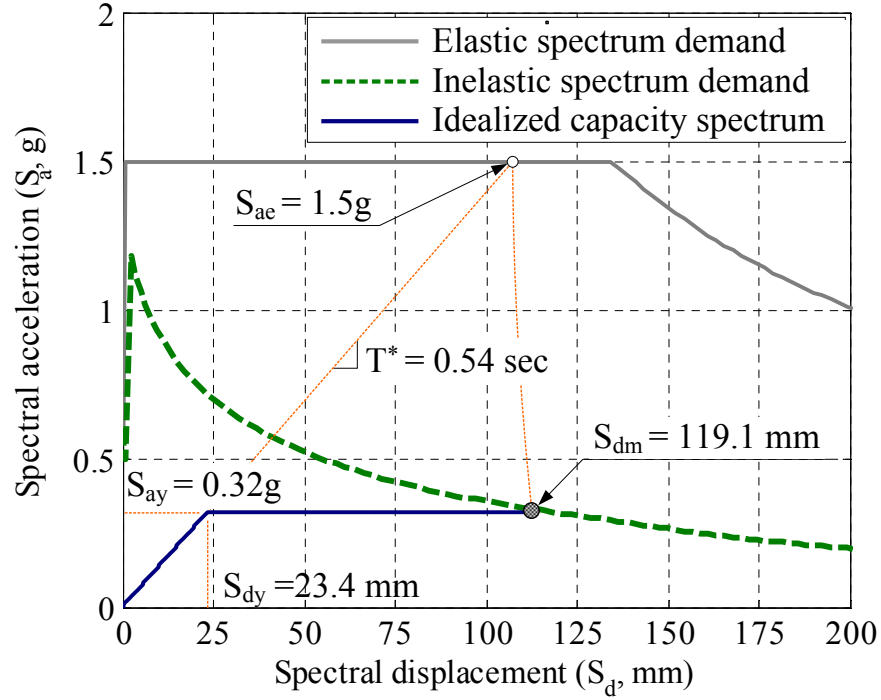
Figure 6.8. Calculation of seismic demand (S_{dm}) using CSM for Case #2

6.5.1.3 Energy-based damage demand

The seismic energy-based damage demand (D_S) was estimated using the Park-Ang damage model. The response parameters associated with the damage model were also obtained from the CSM approach. The total seismic damage demand in the entire structural model (referred to as "D_{S_T}") is defined in Equation (6.13a):

$$D_{S\_T} = \frac{\delta_m}{\delta_u} + \frac{\beta}{V_u \delta_u} E_{SD\_T} \qquad \text{in entire structure} \qquad (6.13a)$$

where

δ_m = roof displacement demand

δ_u = ultimate displacement and base shear of the entire structure

143

V_u = ultimate base shear of the entire structure

E_{SD_T} = total hysteretic energy dissipation for a given seismic load

The total hysteretic energy dissipation (E_{SD_T}) was computed by the area enclosed by a full hysteresis loop with the relationship between the base shear (V_{base}) and the roof displacement (δ_{roof}), as illustrated in Figure 6.9. It should be noted that the hysteresis loop was assumed to be elastic-perfectly plastic in this study. The damage demand in the first story (D_{S_1}) was estimated using Equation (6.13b):

$$D_{S\_1} = \frac{\delta_{m1}}{\delta_u} + \frac{\beta}{V_u \delta_u} E_{SD\_1} \qquad \text{in first story} \qquad (6.13b)$$

where

δ_{m1} = first story displacement demand computed by Equation (6.12)

E_{SD_1} = first story hysteretic energy dissipation

The second story energy-based damage demand (D_{S_2}) was determined by subtracting the first story damage demand (D_{S_1}) from the total damage demand of the structure (D_{S_T}) as given in Equation (6.13c):

$$D_{S\_2} = D_{S\_T} - D_{S\_1} \qquad \text{in second story} \qquad (6.13c)$$

The maximum value between the first story (D_{S_1}) and second story (D_{S_2}) damage demands was selected as the output parameter for the seismic energy-based damage demand (D_S).

Through the above procedure, the total (D_{S_T}), first story (D_{S_1}), and second story (D_{S_2}) damage demands for Case #2 were computed as 1.39, 0.93, and 0.46, respectively. The output parameter associated with the seismic energy-based damage demand (D_S) was selected as a maximum value between the first and second story damage demands (i.e., D_S for Case #2 = 0.93 in Table B.3).
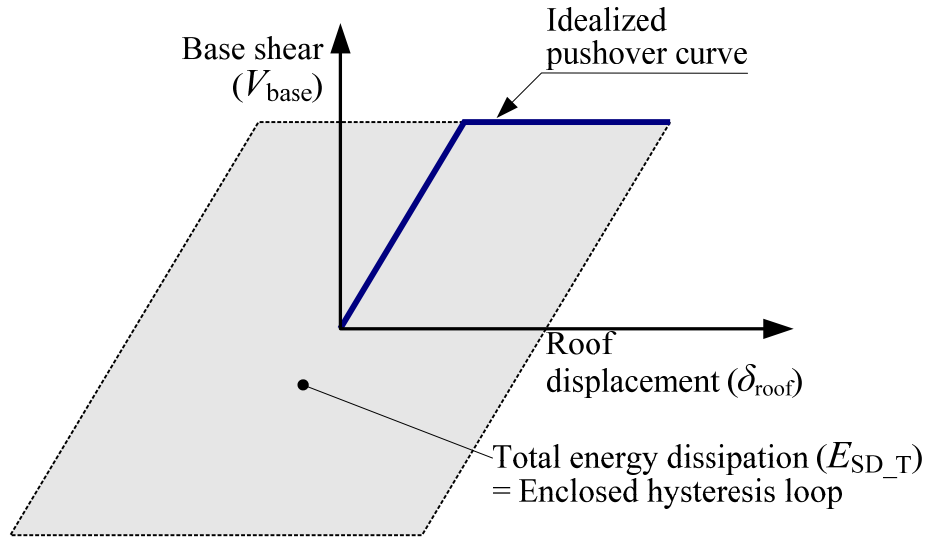
Figure 6.9. Estimation of energy dissipation demand for entire structure

6.5.2 Blast demand

Blast demands, such as displacement ductility (μ_{blast}) and energy-based damage (D_B) demands, were investigated based on simulated responses produced from the FE frame models. The as-built and retrofitted FE frame models were developed to simulate blast responses, using the methodology proposed and verified in Chapter 5. The FE frame models were modified with the input parameters in the initial ANN dataset given in Table B.2. The table summarizes output parameters for the blast loading. Case #73 in Table B.2, which represents the as-built frame model under the blast load with the scaled distance (Z) of 0.8 m/kg$^{1/3}$, is utilized here as an example to explain the blast demand calculations.

<u>6.5.2.1 Column capacity</u>

As-built and retrofitted RC columns were modeled with the input parameters to investigate the column capacities such as yielding displacement (δ_{y_col}), yielding or ultimate strength (F_{y_col} or F_{u_col}), and ultimate displacement (δ_{u_col}) for the column elements. These column capacities were estimated by applying nonlinear pushover analyses to the RC column models. As illustrated in Figure 6.10(a), fixed-sliding boundaries were modeled at the ends of the RC column model to reproduce a double-curvature configuration. The loading was applied in two different steps: (1) application of axial pressures as a gravity load to the top of the RC column models, and (2) application of lateral displacement to the RC column models for the pushover analysis. As shown in Figure 6.10(b), the column capacities were estimated using bilinear idealization [Paulay and Priestley 1992, and ATC-19 1995]. Figure 6.10(c) shows the simulated and idealized pushover curves for the column model associated with Case #73.
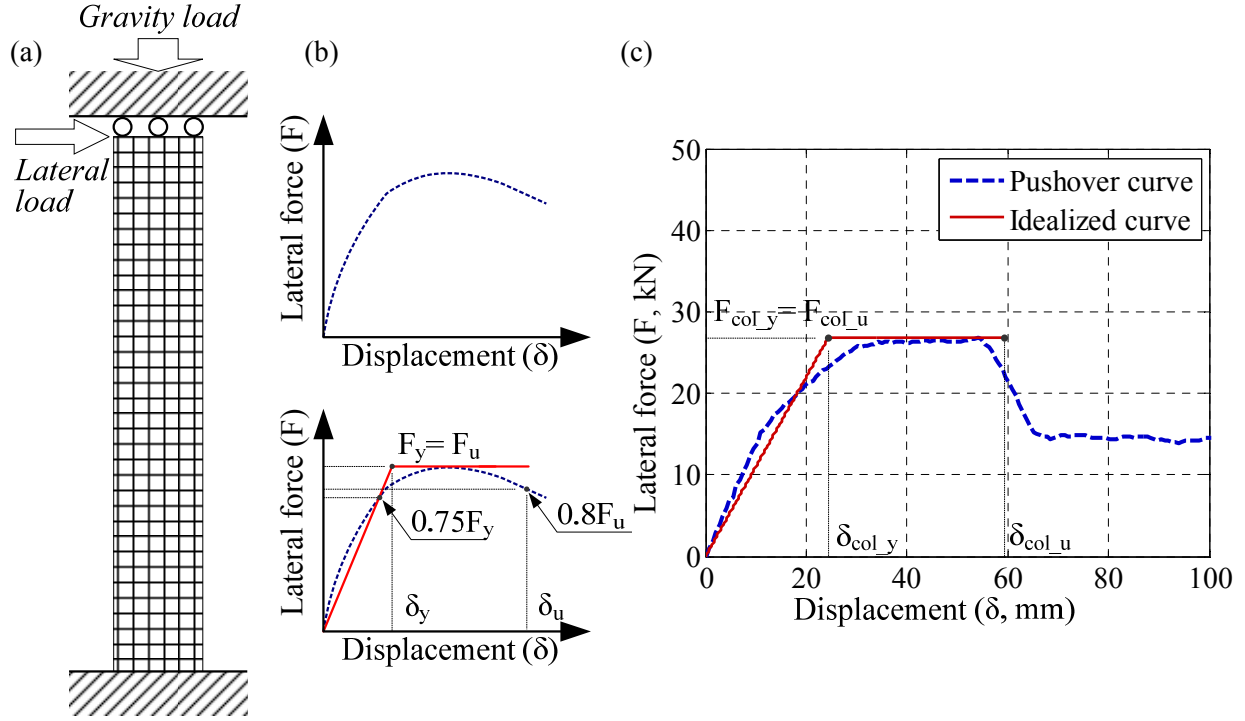
Figure 6.10. Estimation of the RC column model capacities: (a) schematic view of pushover simulation for RC column model; (b) bilinear idealization procedure; (c) pushover results for Case #73

6.5.2.2 Displacement ductility demand

Blast displacement ductility demand (μ_{blast}) to evaluate blast performance with ductility-based limits for non-seismic and FRP-retrofitted columns specified in ASCE 59-11 [2011] can be defined using Equation (6.14):

$$\mu_{blast} = \frac{\delta_{peak}}{\delta_{col\_y}}$$
(6.14)

where

δ_{peak} = peak displacement from the full-frame blast simulations

δ_{col_y} = yielding displacement of the RC column elements

147

Using the time history response of the FE frame model under a given blast load (a scaled distance of 0.8 m/kg$^{1/3}$), the peak displacement (δ_{peak}) was estimated to be 62.4 mm for Case #73, as illustrated in Figure 6.11. The column yielding displacement (δ_{col_y}) was 25.4 mm, which was determined by the pushover analysis of the first story exterior RC column for Case #73. Therefore, the maximum blast ductility demand was found at the first story exterior RC column and was approximated as 2.46. The maximum ductility demand was selected as the output parameter for Case #73, as given in Table B.4.
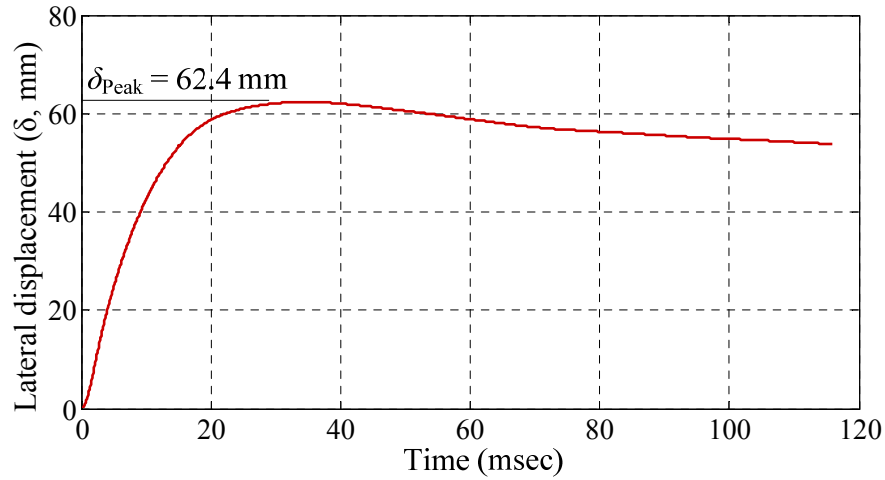
Figure 6.11. Displacement time history response for Case #73

6.5.2.3 Energy-based damage demand

As was done for seismic damage demand, the Park-Ang damage model was utilized to predict the blast energy-based damage demand (D_B) as given in Equation (6.15):

$$D_B = \frac{\delta_{peak}}{\delta_{col\_u}} + \frac{\beta}{F_{col\_u}\delta_{col\_u}}E_{BD} \qquad (6.15)$$

where

148

δ_{peak} = peak displacement

$\delta_{\text{col\_u}}$ = ultimate displacement of the RC column elements

β = coefficient to account for cyclic loading effects

$F_{\text{col\_u}}$ = ultimate lateral force of the RC column elements

E_{BD} = energy dissipation of the column element

The blast energy dissipation of the column element (E_{BD}) was computed as the summation of the area enclosed in the hysteresis loop. The blast energy-based damage demand (D_{B}) was computed for each column in the FE frame model, and the maximum value for blast damage demand was chosen as the output parameter. Figure 6.12 shows the lateral force-displacement hysteresis behavior at the exterior column in the first story, where the peak displacement (δ_{peak}) induced by the given blast loading was observed in Case #73. As shown in Figure 6.12, the peak displacement (δ_{peak}) and the energy dissipation (E_{BD}) for Case #73 were approximated as 62.4 mm and 2770 kN-mm, respectively. Based on the response parameters of the damage model, the maximum blast damage demand (D_{B}) was computed to be approximately 1.13, as given in Table B.4.
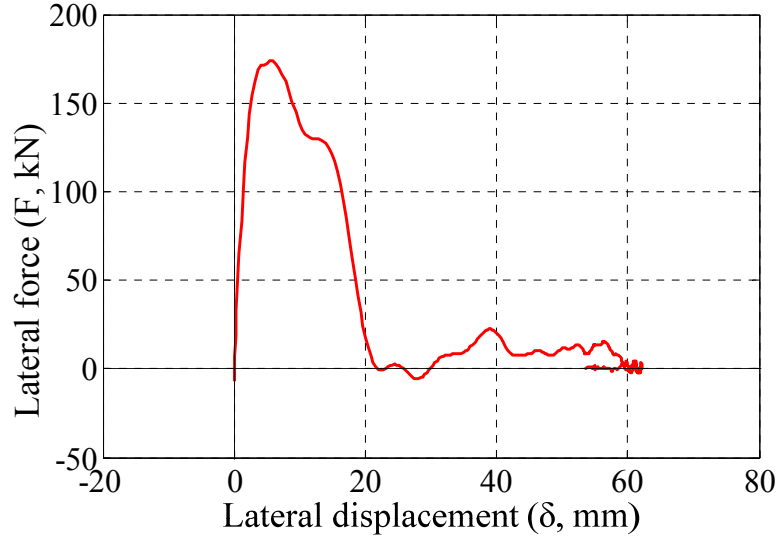
Figure 6.12. Lateral force-displacement hysteresis loop for Case #73

6.6 Development of Fast Running Models

To develop seismic and blast FRMs, the models were separately trained with their datasets, which included the initial dataset built in the previous sections, as well as the additional dataset described in Section 6.6.1. The model training for the two different FRMs based on the sample cases, which were randomly selected, was conducted by the same procedure as that presented in Section 6.6.2. After that, to verify the trained models, the predicted responses from the FRMs were compared to the FE simulated responses in the remaining sample cases in the datasets.

6.6.1 Additional dataset

Before training the models, the relationships of the various output parameters in each initial dataset (e.g., inter-story drift ratio (IDR), seismic damage demand (D_S), displacement ductility (μ_{blast}), and blast damage demand (D_B)) were investigated as shown in Figure 6.13. This was intended to determine if the output parameters of the initial datasets could represent the

structural responses corresponding to each performance level specified in FEMA-356 [2000] and ASCE 59-11 [2011]. Additionally, these relationships in Figure 6.13 helped ensure a uniform spread of values over the ranges of the structural demands used in current code-defined limits (i.e., the inter-story drift ratio and displacement ductility). As shown in Figure 6.13(a), the data points of the initial dataset for the as-built and retrofitted conditions could represent the drift-based limits in FEMA-356. However, since the initial dataset for the as-built condition has only three data points, seven data points varying peak spectral accelerations (S_{a_peak}) between 0.3 g and 2.8 g were added in Figure 6.13(a). The data points of the entire dataset had a better distribution than those of the initial dataset. For the dataset of a given blast loading, the maximum ductility demand (μ_{blast}) of the initial dataset for the retrofitted condition was approximately 4.5. Thus, there was no data point for blast ductility demand reaching or exceeding the code-defined ductility limit of 6, which represented a heavy damage level for an FRP-retrofitted column in ASCE 59-11. If the blast FRM is developed using solely the initial dataset, the model cannot accurately predict the blast demands after μ_{blast} reaches a value of 4.5. In order to add more data points representing the hazardous damage level, this study performed additional simulations on the FE frame models, varying the jacket thickness parameter (t_j) from a one-ply to two-ply jacket with respect to the three training points of the FRP tensile strength. This resulted in the jacket thickness varying from 0.66 mm to 2.0 mm. The additional simulations provided results very close to the blast ductility limit of 6 shown in Figure 6.13(b). Moreover, the six data points of the as-built condition (varying scaled distance (Z) within 0.65 m/kg$^{1/3}$ to 1.27 m/kg$^{1/3}$ corresponding to standoff distances within the range of 5.7 m to 11.2 m) were added to ensure a better distribution of the data points in the entire dataset. The additional

datasets for the seismic and blast loading types are summarized in Tables B.5 and B.6, respectively.
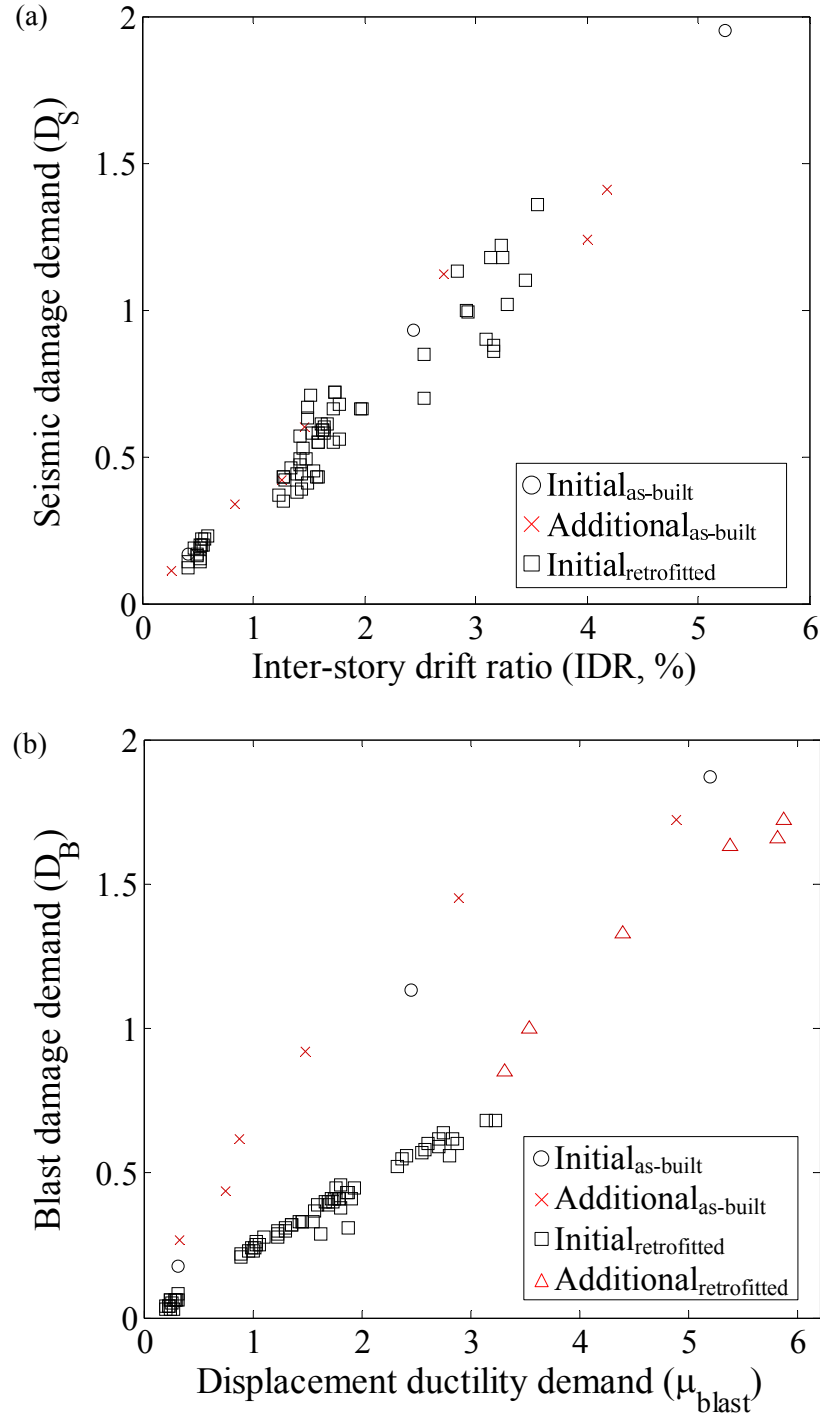
Figure 6.13. Relationships between multiple output parameters: (a) seismic output parameters; (b) blast output parameters

6.6.2 Model training and validation

After establishing the entire datasets, the output parameters were normalized with the maximum values of the structural demands. Figure 6.14 illustrates a structure of the neural network for the seismic and blast FRMs. The structure of the neural network was built with the six input parameters and the two output parameters for each loading type's FRM. The six input parameters included a loading parameter, three geometric parameters, and two material parameters associated with the FRP column jacketing system, as summarized in Table 6.4. The output parameters included structural responses (IDR = inter-story drift ratio, and μ_{blast} = blast displacement ductility demand in Figure 6.14) and energy-based damage demands (D_S = seismic damage demand, and D_B = blast damage demand in Figure 6.14) for the seismic and blast FRMs. The neural network is composed of five hidden layers. This was selected because the number of the hidden layers is recommended to be between the number of input and output parameters [Heaton 2008]. Additionally, a log-sigmoid transfer function is implemented into both the hidden layers and the output layers to restrict the normalized demands from 0 to 1. The transfer functions can prevent computing negative values from the neural network models.

Table 6.4. Summary of input parameter for training FRMs

Parameter types	Input parameter	
	Seismic	Blast
Loading	Peak spectral acceleration (S_{a_peak})	Scaled distance (Z)
Geometric	Retrofit location (RL)	
Material	Ultimate tensile strength of FRP jacket (f_{ju})	
Geometric	FRP jacket thickness (t_j)	
Geometric	Column inner diameter (ID)	
Material	Grout strength (f_g)	

This study utilized the feedforward neural network with a training algorithm of the Levenberg-Marquardt Algorithm (LMA) in MATLAB [MathWorks 2014]. The LMA provides the best-fit weight (w) and bias ($\bar{b}$) parameters to minimize a mean squared error (MSE) in an iterative process, which is the average squared error between the calculated demands (FRM-based demands) and the target demands (FE-based demands). The 78 sample cases in the seismic dataset and the 83 sample cases in the blast dataset were randomly selected for model training, validation, and testing. The LMA was trained with randomly-selected training samples until the MSE of the validation samples was minimized. The MSE values for the seismic FRM and the blast FRM were minimized at the 16th iteration and the 12th iteration, respectively.

To test the seismic FRM and the blast FRM, simple regression analyses were performed between the FE-based demands ($\tilde{T}$ = target values in Figure 6.15) and the FRM-based demands ($\tilde{Y}$ = calculated values in Figure 6.15), using the training sample cases. The slope and the intercept of the regression models in Figure 6.15 were set at 1.0 and 0.0, respectively (i.e. $\tilde{Y} = \tilde{T}$ in Figure 6.15). The regression models can be utilized to judge the adequacy of the FRMs with respect to the FE-based demands. As shown in Figure 6.15, the R^2-values for the seismic and blast FRMs were 0.98 and 0.99, respectively. This indicates that the seismic and blast FRMs were highly correlated with the seismic and blast FE-based demands. Additionally, the scatter-plots of the residuals, which describe the errors in the fit of the $\tilde{Y} = \tilde{T}$ regression model versus the FRM-based demands, are shown in Figure 6.16. The residual analyses proved that the FRM models were appropriate because the plots had a random pattern with small values of the residual, which indicates a good fit for the linear regression models.
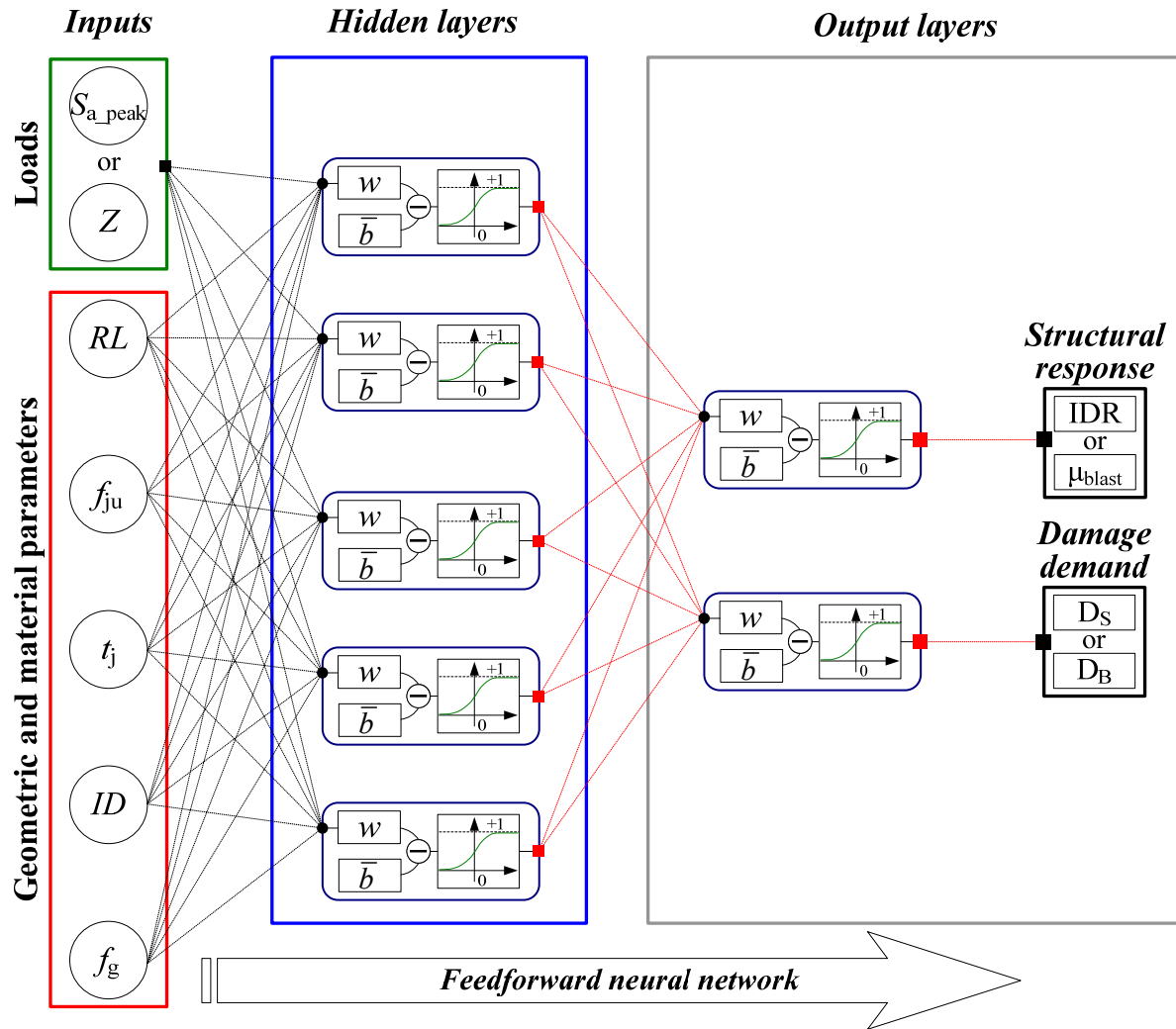
Figure 6.14. Neural network structure for predicting seismic and blast demands
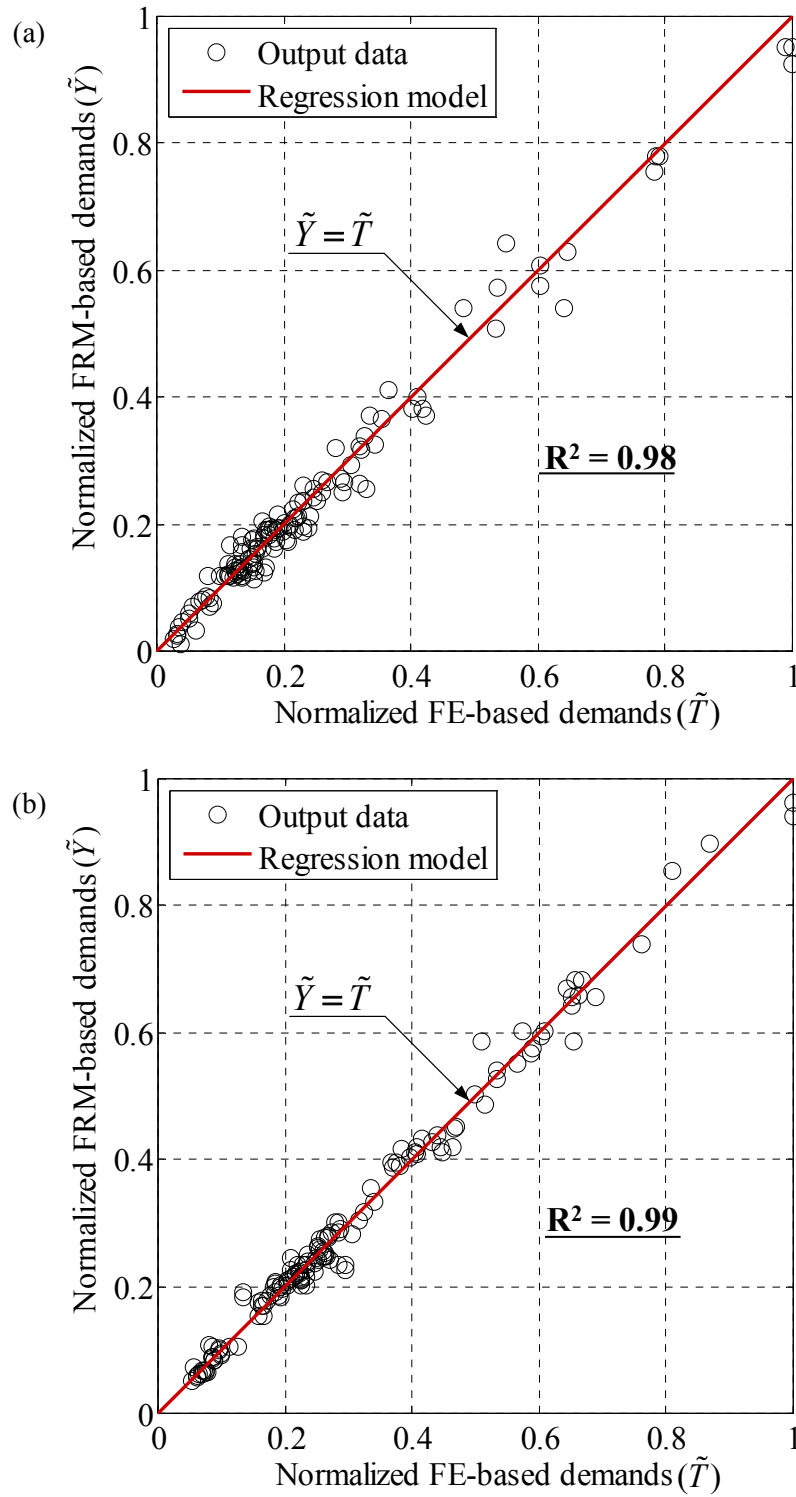
Figure 6.15. Regression analyses between FE- and FRM-based demands: (a) seismic FRM; (b) blast FRM
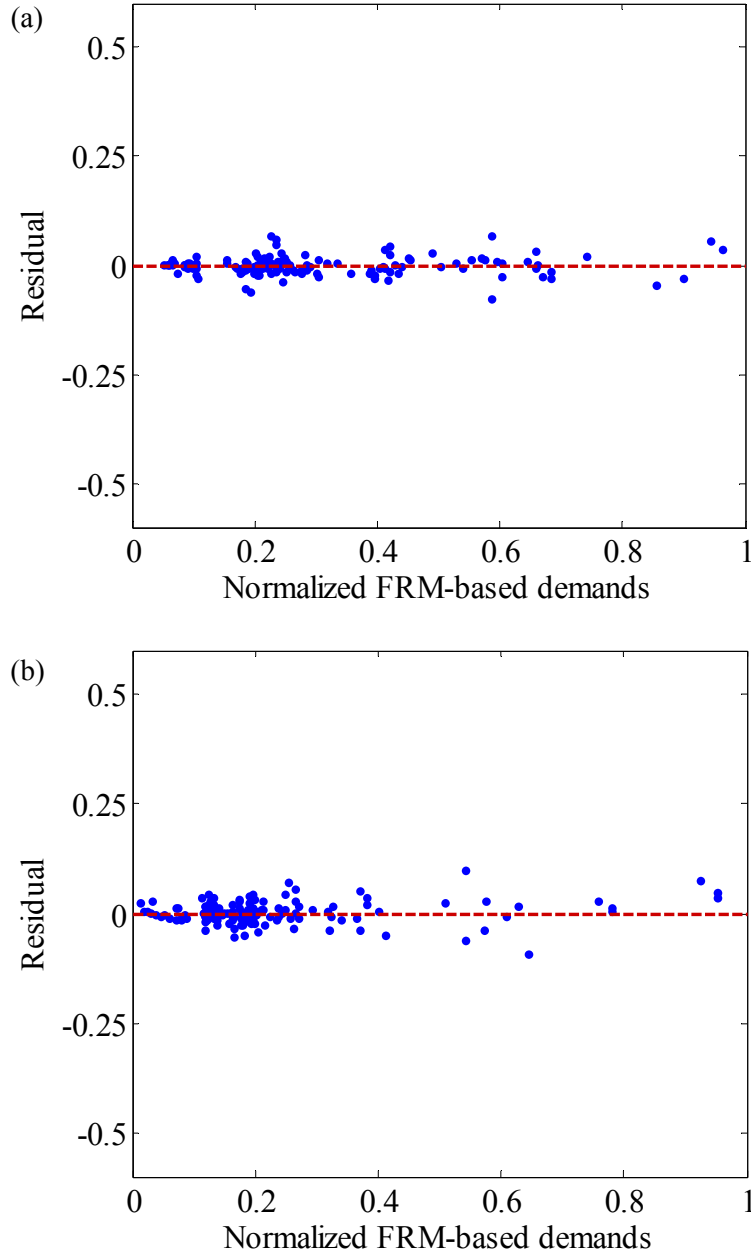
Figure 6.16. Diagnostic residual plots for FRM models: (a) seismic FRM; (b) blast FRM

6.6.3 Model testing

The trained models in the previous section were tested by comparing the FRM-based demands against the FE-based demands. For model testing, seven sample cases, which were not utilized in the model testing and validation, were randomly selected from each dataset. Tables

6.5 and 6.6 summarize the six input parameters for the 14 sample cases, along with the absolute variation between the FRM-based demands and the FE-based demands. The absolute variation for the seismic and blast FRMs was within 12.0 %, which was designated as an acceptable range of variation in this study. This study assumed the acceptable range within a 12.0 % variation, which was determined based on the variation between the simulated and experimental responses to verify the proposed FE modeling methodologies in Chapters 4 and 5.

Table 6.5. Model testing of seismic FRM

Case #	RL	S_{a_peak} (g)	f_{ju} (MPa)	t_j (mm)	ID (mm)	f_g (MPa)	|Variation (%)| IDR	|Variation (%)| D_S
8	First-story	1.5	1380	3.6	444	42.9	8.47	6.06
24	First-story	0.5	419	3.6	444	89.6	7.42	0.76
40	All-story	0.5	419	3.6	444	42.9	5.22	1.02
52	All-story	0.5	419	6.5	444	42.9	9.43	7.44
63	All-story	1.5	166	3.6	444	13.8	2.94	7.34
67	All-story	1.5	419	6.5	559	42.9	7.23	8.88
145	No-retrofit	2.0	No-retrofit	0.0	No-retrofit	No-retrofit	6.57	3.64

Table 6.6. Model testing of blast FRM

Case #	RL	Z (m/kg$^{1/3}$)	f_{ju} (MPa)	t_j (mm)	ID (mm)	f_g (MPa)	|Variation (%)| μ_{blast}	|Variation (%)| D_B
100	First-story	0.80	166	3.6	444	13.8	8.82	6.54
106	First-story	0.80	419	6.5	444	89.6	7.68	1.76
108	First-story	0.80	419	3.6	559	89.6	5.45	7.77
113	All-story	0.80	1380	3.6	444	42.9	4.73	3.29
121	All-story	1.52	1380	3.6	444	42.9	9.03	7.55

Case #	RL	Z $(m/kg^{1/3})$	f_{ju} (MPa)	t_j (mm)	ID (mm)	f_g (MPa)	|Variation (%)| μ_{blast}	D_B
123	All-story	0.80	419	6.5	444	42.9	8.38	0.72
155	No-retrofit	1.39	No-retrofit	0.0	No-retrofit	No-retrofit	6.48	7.83

6.7 Summary

This chapter developed two different fast running models (FRMs) for predicting seismic and blast demands using an artificial neural network (ANN) approach. To train, validate and test the FRMs, datasets composed of input and output parameters were established. The input parameters in the datasets included a loading parameter (e.g., peak spectral acceleration or scaled distance). In addition, five input parameters associated with the FRP column jacketing system (retrofit location, ultimate jacket strength, jacket thickness, inner diameter and grout strength) were used. The output parameters were selected as inter-story drift ratio, displacement ductility, and energy-based damage demands, which were computed from finite element (FE)-based simulations. The inter-story drift ratio and ductility demands can be utilized to determine seismic and blast performance levels in accordance with FEMA-356 [2000] and ASCE 59-11 [2011], respectively. The energy-based damage demands, computed from the Park-Ang damage model [Park and Ang 1987], can be utilized to combine seismic and blast code-defined limits. The procedure for output generation based on the FE models is described in this chapter. The seismic and blast datasets were built using 78 and 83 sample cases, respectively. Based on these datasets, the FRMs were trained to predict the output parameters.

The adequacy of the trained FRMs is proved using regression and residual analyses. Through these analyses, the models have a very high correlation between the FRM- and FE-

based results and also have small residuals with random patterns between their results. Additionally, the FRMs were tested using seven sample cases in each dataset by investigating an absolute variation between the FRM- and FE-based results. Since all absolute variations for the testing sample cases were less than 10.0 %, the seismic and blast FRMs are appropriate to predict the structural responses within the model ranges of the input parameters. Using the two FRMs, extensive seismic and blast responses will be generated with randomly-selected input parameters within the model ranges to derive the multi-hazard energy-based performance criteria presented in Chapter 7.

CHAPTER 7. ENERGY-BASED MULTI-HAZARD PERFORMANCE CRITERIA

7.1 Overview

This chapter presents the development of a methodology for a combined seismic/blast performance criteria formulated using fast running models (FRMs) developed and verified as described in Chapter 6. By implementing this combined methodology, multi-hazard damage limits composed of energy-based damage demands were derived with respect to three different multi-hazard performance levels. Based on the multi-hazard limits, performance evaluation matrices for the as-built and retrofitted conditions are proposed. The performance evaluation matrices can be utilized to examine the structural performance of non-ductile RC frames under combined seismic and blast loading regimes. This evaluation can then be used to determine retrofit schemes, which ensure a pre-determined target performance level for the structural system. Parametric studies were carried out to investigate the effects of critical geometric and material variables associated with prefabricated FRP column jacketing systems within the model ranges given in Table 6.1. An example is presented to demonstrate how this approach can be used to select a specific FRP jacket retrofit scheme for a given non-ductile RC frame.
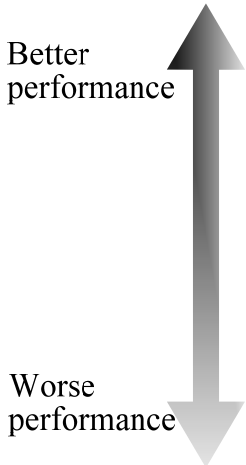
7.2 Combining Process of Seismic and Blast Performance Criteria using FRMs

Table 7.1 summarizes current code-defined drift and ductility limits in terms of three different performance levels specified in FEMA-356 [2000] and ASCE 59-11 [2011], respectively. These limit values were employed to identify multi-hazard energy-based damage limits as determined using the Park-Ang damage model, which correspond to code-defined

performance levels. This study assumed that structural demands exceeding collapse prevention

(CP) in FEMA-356 (i.e., a drift limit of 4.0 % for the RC frame) and "heavy" in ASCE 59-11

(i.e., displacement ductility limits of 0.9 and 6.0 for non-seismic and FRP-retrofitted RC columns)

reach a collapse level and an element failure level, respectively. Figure 7.1 defines multi-hazard

performance (or damage) levels along with the code-defined performance levels, which are

expressed as PL_S and PL_B for seismic and blast loads, respectively. As shown in Figure 7.1, PL_{Si}

is the seismic performance level from immediate occupancy (IO) to collapse (PL_{S1} to PL_{S4} in

Figure 7.1), PL_{Bi} is the blast performance level from superficial to element failure (PL_{B1} to PL_{B4}

in Figure 7.1), and PL_{Mi} is the multi-hazard performance level from minor to collapse or element

failure (PL_{M1} to PL_{M4} in Figure 7.1). A decrease in the integer i of each performance level (e.g.

PL_{B1} to PL_{B4} in Figure 7.1) indicates that a given structure reaches a better performance level.

Table 7.1. Code-defined drift and ductility limits [FEMA-356 2000, and ASCE 59-11 2011]

Level (i)	Seismic performance level (PL_{Si})		Drift limit Concrete frame	Blast performance level (PL_{Bi})		Ductility limit	
						Non-seismic	FRP-retrofitted
1	PL_{S1}	Immediate occupancy (IO)	≤ 1.0%	PL_{B1}	Superficial	≤ 0.7	≤ 1.0
2	PL_{S2}	Life safety (LS)	≤ 2.0%	PL_{B2}	Moderate	≤ 0.8	≤ 3.0
3	PL_{S3}	Collapse prevention (CP)	≤ 4.0%	PL_{B3}	Heavy	≤ 0.9	≤ 6.0
4	PL_{S4}	Collapse	> 4.0 %	PL_{B4}	Element failure	> 0.9	> 6.0

Performance Level			
Level (i)	Seismic	Blast	Multi-Hazard
1	$PL_{S1} = IO$	$PL_{B1} = Superficial$	$PL_{M1} = Minor$
2	$PL_{S2} = LS$	$PL_{B2} = Moderate$	$PL_{M2} = Moderate$
3	$PL_{S3} = CP$	$PL_{B3} = Heavy$	$PL_{M3} = Severe$
4	$PL_{S4} = Collapse$	$PL_{B4} = Element$ failure	$PL_{M4} = Collapse/$ element failure

Better performance

Worse performance

Figure 7.1. Definition of multi-hazard performance levels

A process to derive energy-based multi-hazard performance criteria by a combination of code-defined performance levels is proposed in the present work. Figure 7.2 outlines the combining process between seismic and blast performance criteria using FRMs. In the combining process, seven input parameters (RL = retrofit location, f_{ju} = ultimate tensile strength of FRP material, t_j = jacket thickness, ID = column inner diameter, f_g = grout strength, S_{a_peak} = peak spectral acceleration, and Z = scaled distance in Figure 7.2) were randomized within the model ranges given in Table 6.1, and these parameters were implemented into the FRMs to produce multiple outputs, such as inter-story drift ratio (IDR in Figure 7.2), blast displacement ductility demand (μ_{blast} in Figure 7.2), and energy-based damage demands (D_S and D_B demands in Figure 7.2). The IDR and μ_{blast} demands computed from the seismic and blast FRMs were compared to the code-defined limits given in Table 7.1, and the seismic and blast performance levels (PL_{Si} and PL_{Bi} in Figure 7.2) for the given input parameters were determined. The seismic and blast FRMs also provided the energy-based damage demands (D_S and D_B demands in Figure 7.2), which have performance levels determined by the code-defined limits. The worse performance level identified between the seismic (PL_{Si}) and blast (PL_{Bi}) performance criteria

was selected as one of the multi-hazard performance levels (PL_{Mi} in Figure 7.2) for the given input parameters. The seismic or blast energy-based damage demand (D_S or D_B demand in Figure 7.2) was then saved as a multi-hazard energy-based damage demand (D_M in Figure 7.2) for the multi-hazard performance level (PL_{Mi}). The multi-hazard performance level was determined by comparing the seismic and blast performance levels in a multi-hazard dataset, as illustrated in Figure 7.2. If a seismic performance level was identical to a blast performance level (e.g. $PL_{S2} = PL_{B2}$), a lower value between the D_S and D_B demands was saved as a multi-hazard damage demand (D_M) in the multi-hazard dataset. To extend the multi-hazard dataset, the above process was repeated until a user-defined repetition number (N in Figure 7.2) was reached. Since the input parameters were randomly varied within the model ranges for every repetition, the N-times outputs predicted from the FRMs were saved in the dataset. The extended multi-hazard dataset can be utilized to find the energy-based multi-hazard limits (D_{M1}, D_{M2}, and D_{M3} in Figure 7.2) in terms of three different performance levels, defined as minor, moderate, and severe (PL_{M1}, PL_{M2}, and PL_{M3} in Figure 7.2).
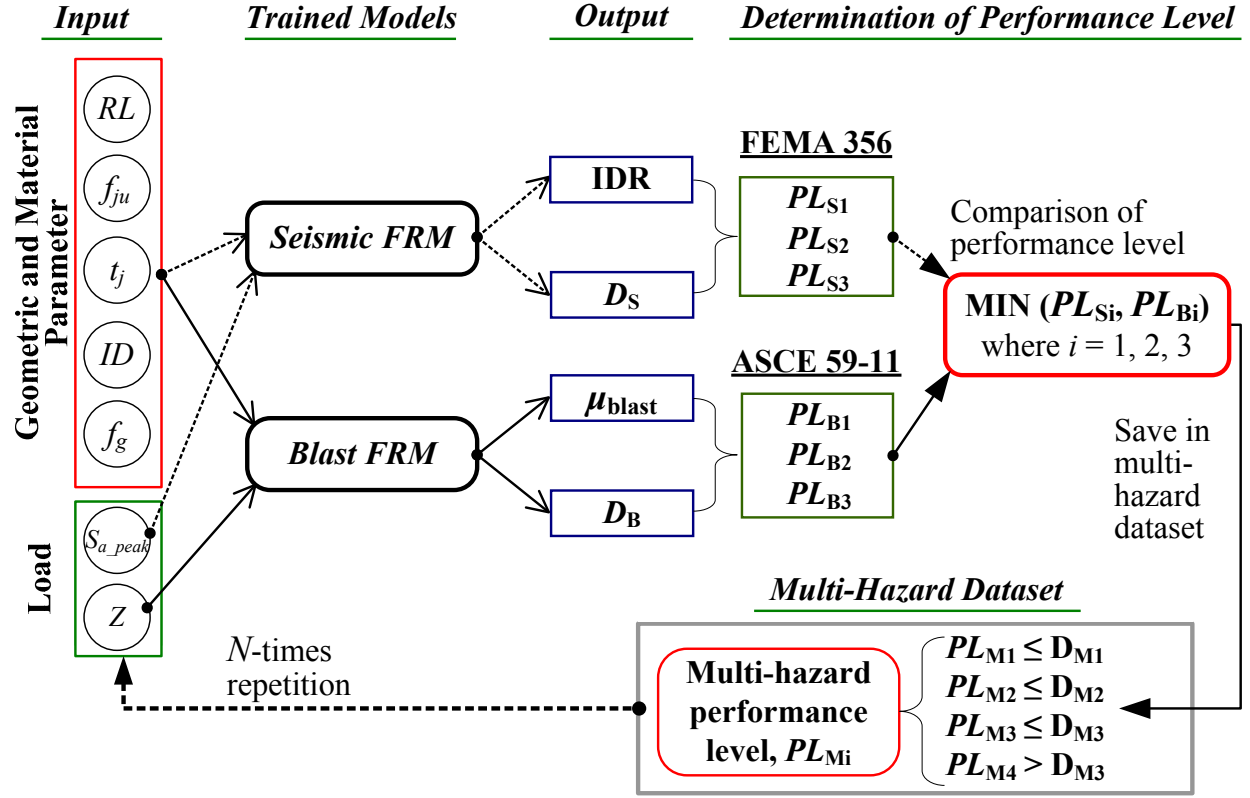
Figure 7.2. Procedure of combination between seismic and blast performance criteria

7.3 Energy-Based Performance Criteria

7.3.1 As-built frame

The combining process described in the previous section was implemented to derive multi-hazard performance criteria (PL_{Mi}) for the as-built frame building with non-seismic detailing tested in a previous study [Wright 2015]. The FRMs incorporated unretrofitted conditions for the input parameters of the FRP column jacketing system. The FRMs produced a thousand different outputs (1000 repetitions, i.e., $N = 1000$ in Figure 7.2) of the as-built condition varied within the ranges of the seismic and blast loading parameters (i.e., peak spectral accelerations from 0.5 g to 3.0 g, and scaled distance from 0.4 m/kg$^{1/3}$ to 1.6 m/kg$^{1/3}$) given in

Table 6.1. The repetition number ($N = 1000$) was determined to generate the multi-hazard dataset in order to directly determine the energy-based damage limits (D_{Mi} in Figure 7.2) that correspond to the code-defined performance levels. Using the multi-hazard dataset, the relationships between inter-story drift ratio (IDR) and seismic damage demand (D_S), as well as the relationships between displacement ductility demand (μ_{blast}) and blast damage demand (D_B), are shown in Figure 7.3. These relationships were utilized to identify the seismic and blast energy-based damage limits (i.e., D_{Si} and D_{Bi}) corresponding to the code-defined performance limits (i.e., drift- and ductility-based limits). The damage limits (D_{Si} and D_{Bi}) of the as-built condition in terms of the code-defined performance levels (PL_{Si} and PL_{Bi}) are summarized in Table 7.2. After identifying the D_{Si} and D_{Bi} limits, the energy-based damage limits (D_{Mi}) for multi-hazard performance levels (PL_{Mi}) were created by combining the seismic (PL_{Si}) and blast (PL_{Bi}) performance limits, as illustrated in Figure 7.4. The combined damage limits (D_{Mi}) in terms of the multi-hazard performance levels (PL_{Mi}) are given in Table 7.2. Figure 7.4 includes a four-by-four matrix composed of the energy-based damage limits (D_{Mi}) for each multi-hazard performance level. This four-by-four matrix represents 16 different performance (or damage) zones for the as-built condition, from $\tilde{M}_{11}$ to $\tilde{M}_{44}$, in Figure 7.4. This performance evaluation matrix can be used to evaluate the multi-hazard performance level of non-ductile RC frame buildings prior to the installation of retrofit schemes. For example, a damage demand within $\tilde{M}_{12}$ in Figure 7.4 denotes that the structure reaches minor seismic performance (PL_{S1}) and moderate blast performance (PL_{B2}), and another damage demand within $\tilde{M}_{33}$ in Figure 7.4 indicates that the structure has a severe performance level (PL_{S3} and PL_{B3}) for both seismic and blast loads, which may indicate that a retrofit system should be installed in the structure.
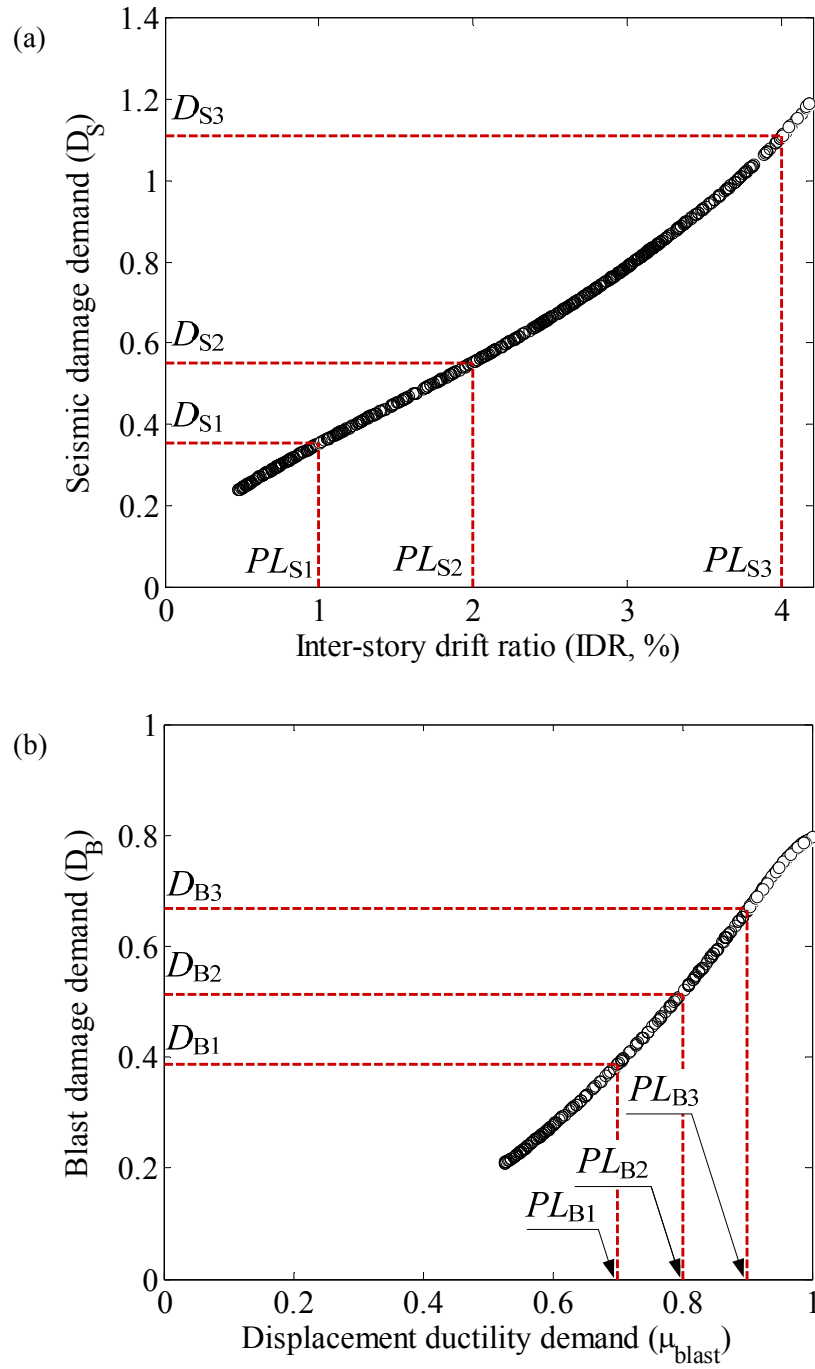
Figure 7.3. Seismic and blast energy-based damage limits for as-built frame: (a) IDR-D_S relationship; (b) μ_{blast}-D_B relationship (Table 7.2)
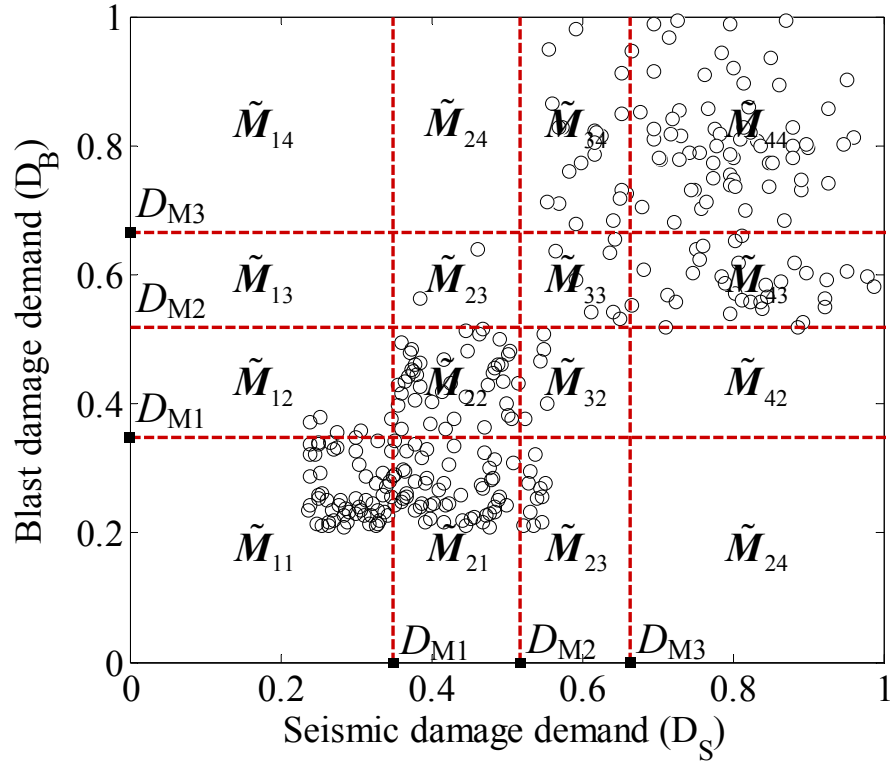
Figure 7.4. Four-by-four performance evaluation matrix for as-built frame (Table 7.2)

Table 7.2. Summary of energy-based damage limits for as-built frame structure

Seismic performance level (PL_{Si})		Energy-based damage limit (D_{Si})	Blast performance level (PL_{Bi})		Energy-based damage limit (D_{Bi})	Multi-hazard performance level (PL_{Mi})		Energy-based damage limit (D_{Mi})
PL_{S1}	IO	≤ 0.35	PL_{B1}	Superficial	≤ 0.39	PL_{M1}	Minor	≤ 0.35
PL_{S2}	LS	≤ 0.55	PL_{B2}	Moderate	≤ 0.52	PL_{M2}	Moderate	≤ 0.52
PL_{S3}	CP	≤ 1.11	PL_{B3}	Heavy	≤ 0.67	PL_{M3}	Severe	≤ 0.67
PL_{S4}	Collapse	> 1.11	PL_{B4}	Element failure	> 0.67	PL_{M4}	Collapse or element failure	> 0.67

7.3.2 Retrofitted frame

To derive multi-hazard energy-based performance criteria (PL_{Mi}) for the non-ductile frame structure retrofitted with an FRP column jacketing system, a multi-hazard dataset was

developed using two thousand input parameters varied within the model ranges given in Table 6.1 (2000 repetitions, i.e., $N = 2000$ in Figure 7.2). Similar to the as-built frame, the number of the repetitions ($N = 2000$) for the retrofitted frame was selected to generate the multi-hazard dataset, which can directly find the energy-based damage limits (D_{Si} and D_{Bi}) corresponding to the code-defined performance levels (PL_{Si} and PL_{Bi}). The relationships between inter-story drift ratio (IDR) and seismic damage demand (D_S), and between displacement ductility (μ_{blast}) and blast damage demand (D_B) are shown in Figures 7.5(a) and 7.5(b), respectively. By using the relationship of IDR-D_S, the seismic energy-based damage limits (D_{Si} in Figure 7.5(a)) corresponding to the code-defined drift limits were directly identified. The blast energy-based damage limits (D_{B1} and D_{B2} in Figure 7.5(b)) in terms of superficial and moderate performance levels (PL_{B1} and PL_{B2}) were also identified using the extended dataset, as shown in Figure 7.5(b). However, the extended dataset produced by the blast FRM had no data points reaching or exceeding the code-defined ductility limit ($\mu_{blast} = 6$ in Table 7.1) for the lowest blast performance level (i.e., heavy performance level, PL_{B3} in Figure 7.1). This is because the blast FRM was trained with the blast dataset given in Tables B.4 and B.6, which has no displacement ductility demands beyond the ductility limit of 6 for the heavy performance level.
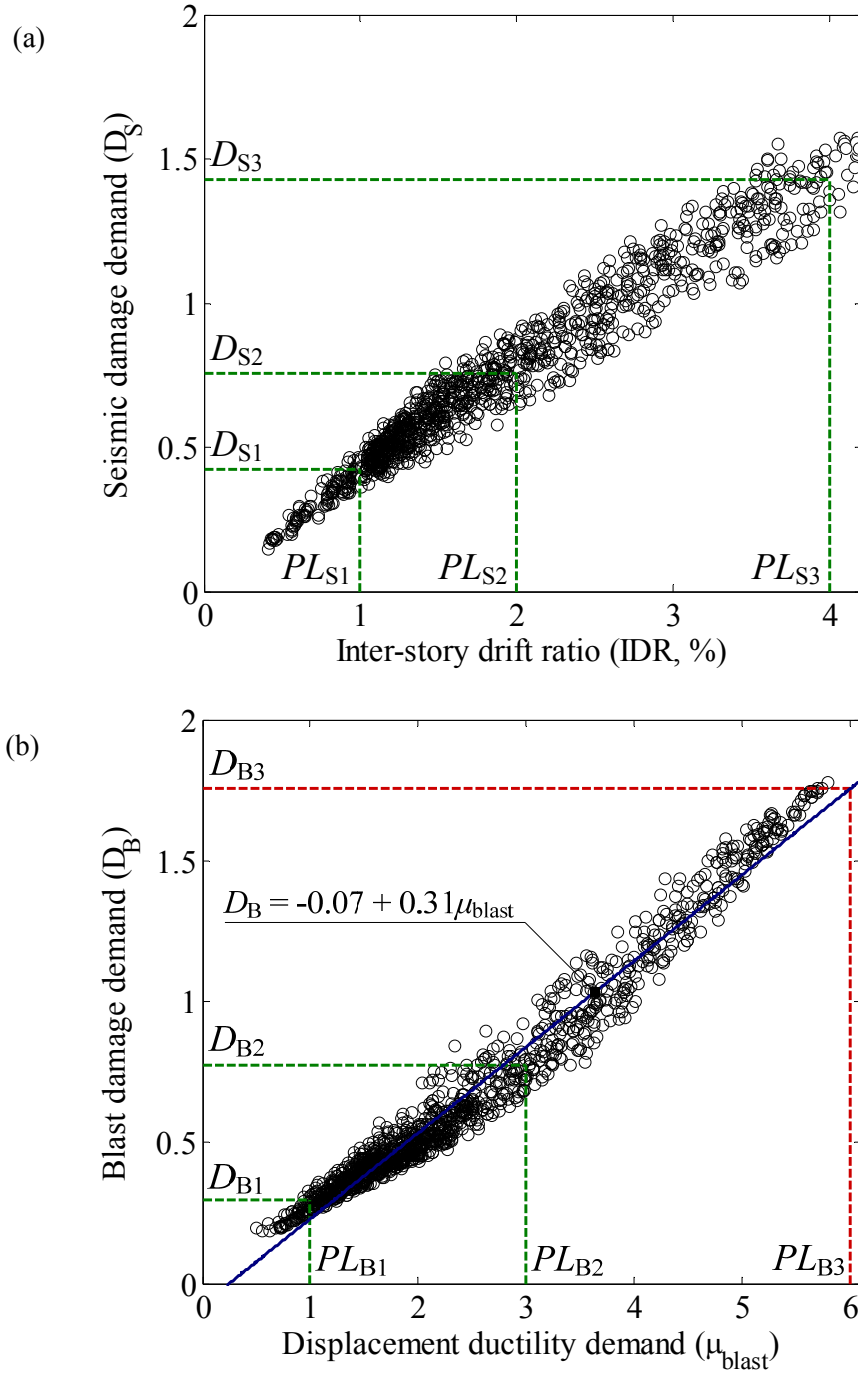
Figure 7.5. Seismic and blast energy-based damage limits for retrofitted frame: (a) IDR-D_S relationship; (b) μ_{blast}-D_B relationship with a linear regression model (Table 7.3)

As an alternative to directly finding the heavy performance level (PL_{B3}) in the relationship of μ_{blast}-D_B shown in Figure 7.5(b), this study slightly modified the initial combining

process (Figure 7.2), as shown in Figure 7.6. In the modified combining process, a regression analysis was added to find a fitted value (heavy damage limit, D_{B3}) corresponding to the heavy performance level (PL_{B3}). After finding the D_{B3} limit using the regression model, a minimum value between seismic (D_{S3}) and blast (D_{B3}) energy-based damage limits was selected as a multi-hazard energy-based damage limit (D_{M3}) for the severe performance level (PL_{M3}). A linear regression model using the entire dataset (referred to as the "single linear regression model") is included in Figure 7.5(b), and the fitted value corresponding to PL_{B3} was estimated as a heavy damage limit of 1.75 (i.e., D_{B3} = 1.75) using the regression model. To estimate the adequacy of the regression model, residual analyses were performed as illustrated Figures 7.7(a) and 7.7(b). The scatter-plot of the residuals against the fitted values has a nonlinear pattern (Figure 7.7(a)), and the quantile-quantile (Q-Q) plot to estimate distribution of the residuals shows the non-normal distribution of the residuals at the ends of the plot (Figure 7.7(b)) [Montgomery et al. 2015]. According to these residual analyses, the single linear regression model is not appropriate for predicting the energy-based damage limit (D_{B3}) for the heavy performance level (PL_{B3}) in the multi-hazard performance criteria, which indicates that the regression model may underestimate or overestimate D_{M3} value.

A previous study [Jeon et al. 2015] developed aftershock fragility curves for non-ductile RC frame structures, using bilinear regression models to minimize the sum of the square of residuals between actual and fitted values. Based on this previous work, the present study developed a tri-linear regression model, using the corresponding data points for each performance level as illustrated in Figure 7.8. Using the tri-linear regression model, the regression model within the heavy performance level (PL_{B3}), a PL_{B3} regression model (the red solid line in Figure 7.8), estimated a fitted value as the heavy damage limit of 1.86 (i.e., D_{B3} =

1.86 in Figure 7.8). The results of the residual analyses for the PL_{B3} regression model are shown in Figure 7.9. The tri-linear regression model given in Figure 7.8(b) is more appropriate than the single linear regression model given in Figure 7.5(b) to predict the value of D_{B3} because the scatter plot of the residuals in Figure 7.9(a) has a random pattern and small residual. The Q-Q plot in Figure 7.9(b) also shows a normal distribution.
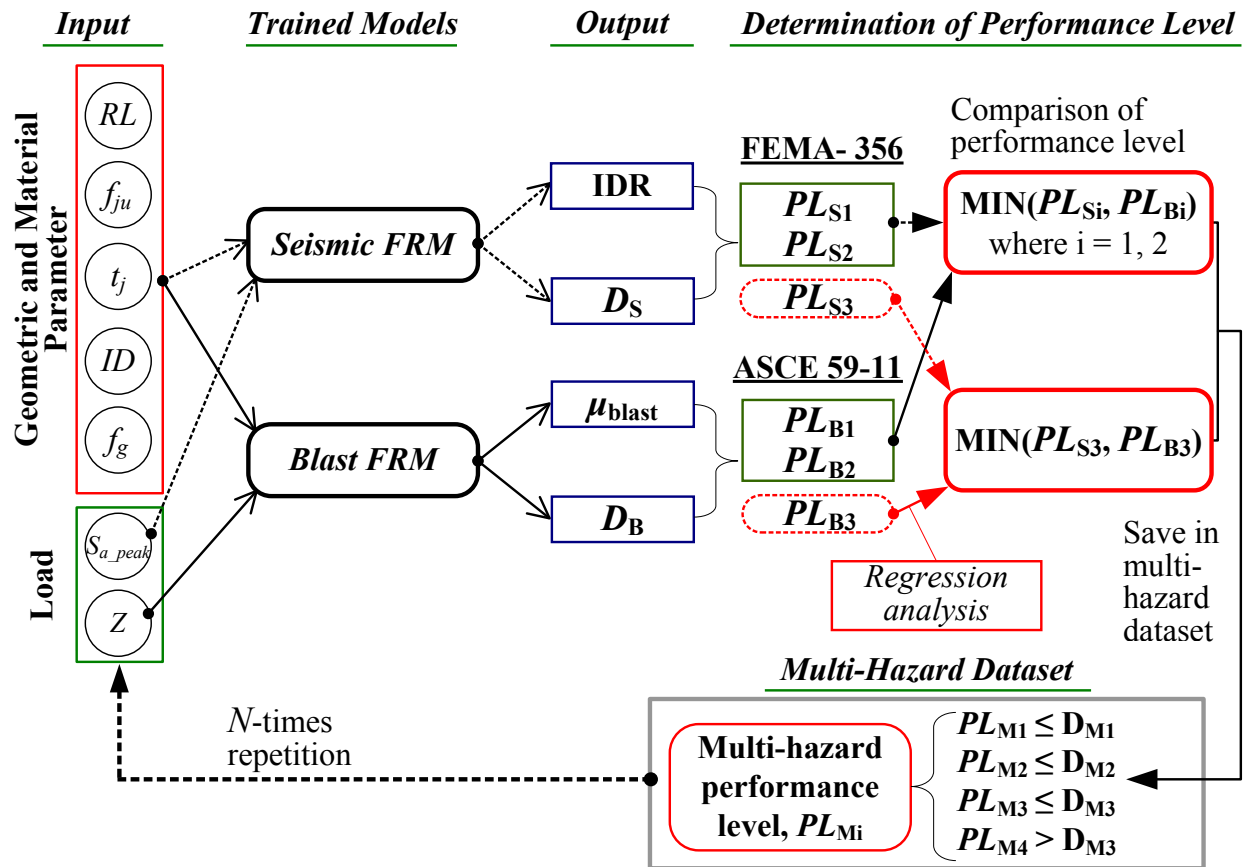
Figure 7.6. Modified combining process of seismic and blast performance criteria
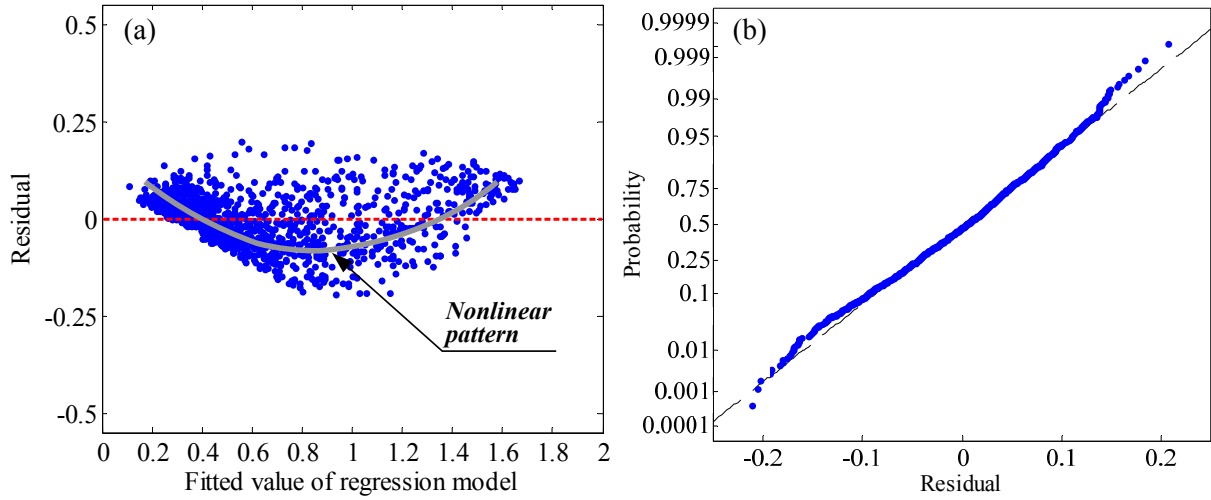
Figure 7.7. Residual analyses for a linear regression model: (a) residual plot; (b) Q-Q plot
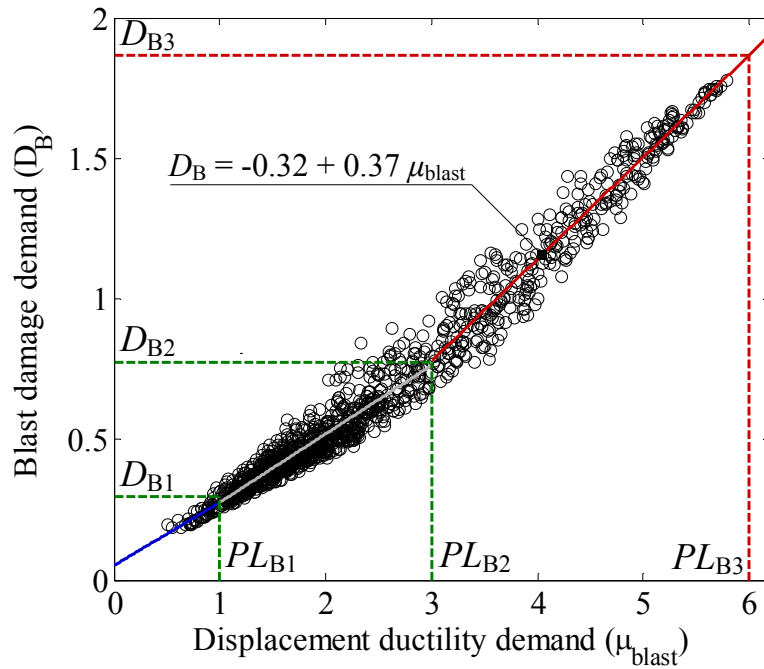
Figure 7.8. μ_{blast}-D_B relationship with triple linear regression models in terms of blast performance levels (Table 7.3)
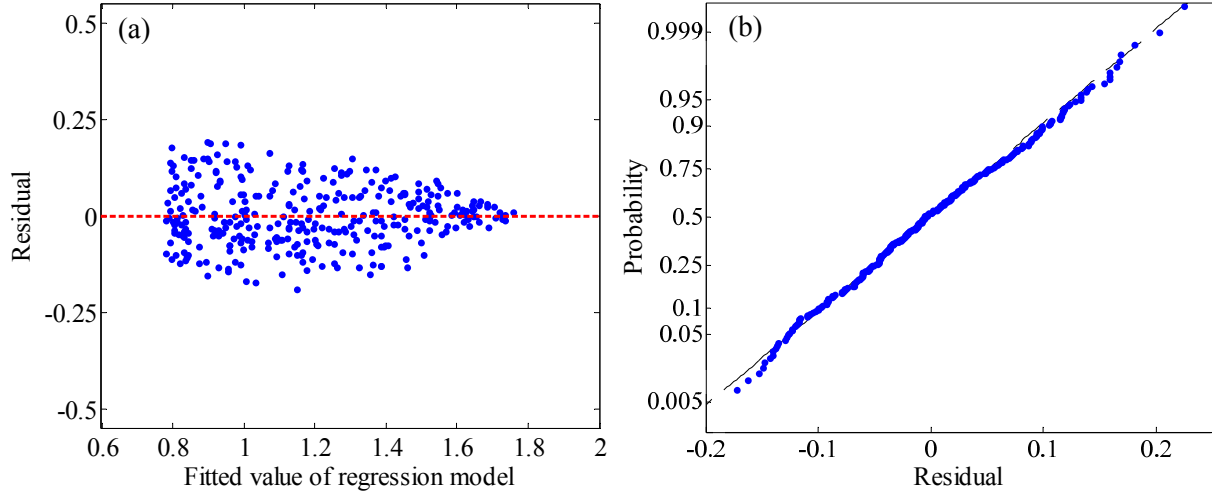
Figure 7.9. Residual analyses for a linear regression model in hazard level: (a) residual plot; (b) Q-Q plot

After determining the seismic (D_{Si}) and blast (D_{Bi}) damage limits for each performance level, the multi-hazard damage limits (D_{M1} and D_{M2}) in terms of the minor and moderate performance levels (PL_{M1} and PL_{M2}) were derived by the combining process illustrated in Figure 7.6. Additionally, the severe damage limit for the multi-hazard performance criteria ($D_{M3} = 1.43$ in Table 7.3) was selected as the minimum value between the seismic (D_{S3}) and blast (D_{B3}) damage limits for the CP (PL_{S3}) and heavy (PL_{B3}) performance levels. Table 7.3 summarizes the multi-hazard damage limits (D_{Mi}) for each performance level, along with the seismic (D_{Si}) and blast (D_{Bi}) damage limits. Based on the D_{Mi} limits in Table 7.3, a four-by-four performance evaluation matrix for the retrofitted condition was built, as illustrated in Figure 7.10. The four-by-four matrix, composed of the multi-hazard energy-based damage limits (D_{Mi}) given in Table 7.3, has 16 performance (or damage) zones from $\tilde{M}_{11}$ to $\tilde{M}_{44}$. The performance evaluation matrix for the retrofitted condition may be used to evaluate whether the multi-hazard performance for a non-ductile RC frame with a given retrofit system is within a pre-determined target performance level. This approach can also be used to rapidly determine the type and design of retrofit

schemes needed to ensure reaching a desired target performance level. A retrofit scenario using the multi-hazard performance matrices for the as-built and retrofitted conditions will be further discussed in the following section.
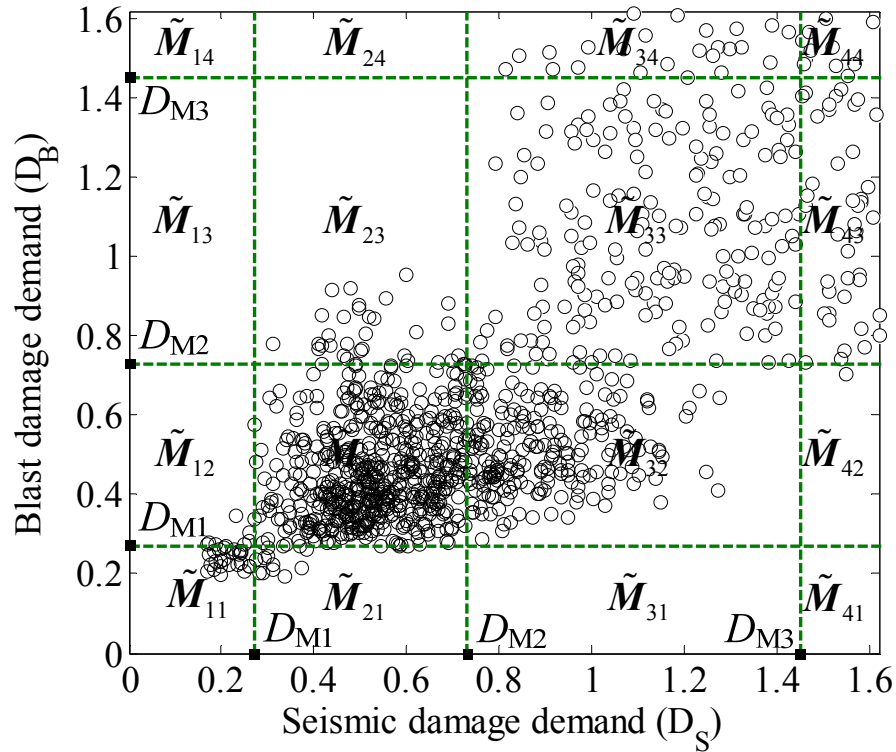
Figure 7.10. Four-by-four performance evaluation matrix for retrofitted frame building (Table 7.3)

Table 7.3. Summary of energy-based damage limits for retrofitted frame structure

Seismic performance level (PL_{Si})		Energy-based damage limit (D_{Si})	Blast performance level (PL_{Bi})		Energy-based damage limit (D_{Bi})	Multi-hazard performance level (PL_{Mi})		Energy-based damage limit (D_{Mi})
PL_{S1}	IO	≤ 0.42	PL_{B1}	Superficial	≤ 0.28	PL_{M1}	Minor	≤ 0.28
PL_{S2}	LS	≤ 0.76	PL_{B2}	Moderate	≤ 0.79	PL_{M2}	Moderate	≤ 0.76
PL_{S3}	CP	≤ 1.43	PL_{B3}	Heavy	≤ 1.86	PL_{M3}	Severe	≤ 1.43
PL_{S4}	Collapse	> 1.43	PL_{B4}	Element failure	> 1.86	PL_{M4}	Collapse or element failure	> 1.43

7.4 Evaluation of Retrofit Scheme using FRP Column Jacketing System in terms of Multi-Hazard Performance

7.4.1 Retrofit scenario

This study has focused on a retrofit scenario for non-ductile RC frames using FRP column jackets. The effectiveness of the retrofit scenario was evaluated using the multi-hazard performance evaluation matrices proposed in Section 7.3. The target performance level has been pre-determined for the present work to be better than a moderate level, from $\tilde{M}_{11}$ to $\tilde{M}_{22}$ in the performance matrix, for the retrofitted condition. The point labeled "*A*" in Figure 7.11 does not satisfy the target performance level and as such demonstrates the inadequate performance of the non-ductile frame structure without retrofit. The use of an FRP column jacketing system can enhance the performance so that the structure performs within the pre-determined target level of $\tilde{M}_{11}$ to $\tilde{M}_{22}$ in Figure 7.11. The geometric and material parameters associated with the FRP column jacketing system were varied within the model ranges given in Table 6.1 and were incorporated into the FRMs until the energy-based damage demands (D_S and D_B) for the given geometric and material parameters were reached within the target performance level. The geometric and material parameters satisfying the target performance were then selected for the retrofit scheme.

176
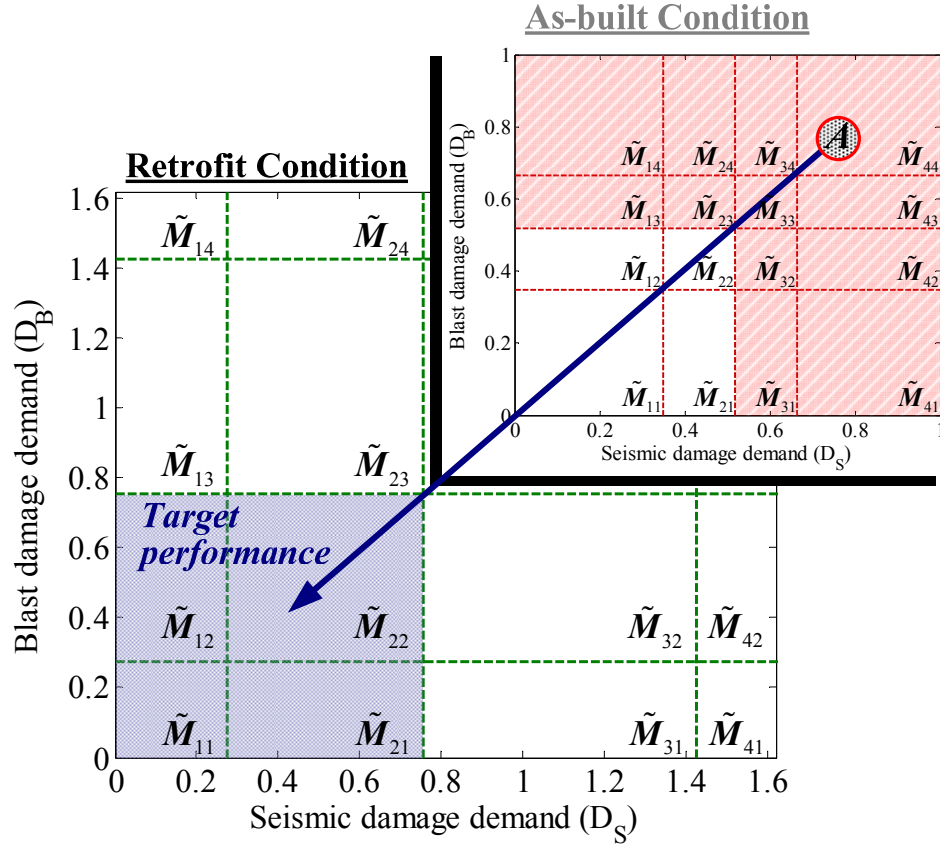
Figure 7.11. Retrofit scenario of FRP column jacketing system

7.4.2 Parametric study

To investigate the effect of five input parameters (retrofit location, ultimate tensile strength of the FRP material, jacket thickness, column inner diameter, and grout strength) associated with the retrofit system, these parameters were varied within the model ranges given in Table 6.1. The loading parameters were selected for the following loading scenario: a peak spectral acceleration (S_{a_peak}) = 2.0 g and scaled distance (Z) = 0.6 m/kg$^{1/3}$, which corresponds to a stand-off distance (R_D) = 5.0 m. The selected loading parameters induced the $\tilde{M}_{44}$ performance level in the as-built performance evaluation matrix, which, as a result, required the structure to be strengthened using a retrofit system to meet the desired $\tilde{M}_{22}$ performance level. The input

parameters for the retrofit system were incorporated into the FRMs, and the FRMs computed the energy-based damage demands (D_S and D_B) for the given parameters. Based on the FRM-based demands, the effects of the geometric and material parameters in terms of seismic and blast performance were estimated using the performance matrix for the retrofitted condition proposed in Section 7.3.2. This parametric study helped identify the critical parameters for the column jacketing system.

7.4.2.1 Effect of jacket strength and thickness

Figure 7.12 shows the damage demands calculated for the structure while varying the jacket thickness (t_j) parameter from 0.7 mm to 6.5 mm with respect to three different jacket strengths (minimum, nominal, and maximum training points; i.e., f_{ju_min} = 166 MPa; f_{ju_n} = 419 MPa; and f_{ju_max} = 1380 MPa given in Table 6.1). Other geometric and material parameters, such as column inner diameter (ID) and grout strength (f_g), were fixed as respective nominal values (i.e., ID = 444 mm, and f_g = 42.9 MPa) given in Table 6.1. Figure 7.12 demonstrates the effects of the parameters f_{ju} and t_j under the given loading condition. Increases in the parameters f_{ju} and t_j resulted in additional flexural capacity (i.e., flexural stiffness and strength) in the column elements and increased confining pressure (or confinement effect), which improves the peak confined concrete strength (f_{cc}') and ultimate axial strain (ε_{cu}) in an FRP-confined concrete column. These effects significantly decreased the values for the demands D_S and $D_{B,}$ as illustrated in Figure 7.12. Due to this modification of the input parameters, the structure, which initially had a $\tilde{M}_{44}$ multi-hazard performance under the given loading scenario in the as-built condition, now behaved within the pre-determined target performance ($\leq \tilde{M}_{22}$ in the as-built performance evaluation matrix).

178
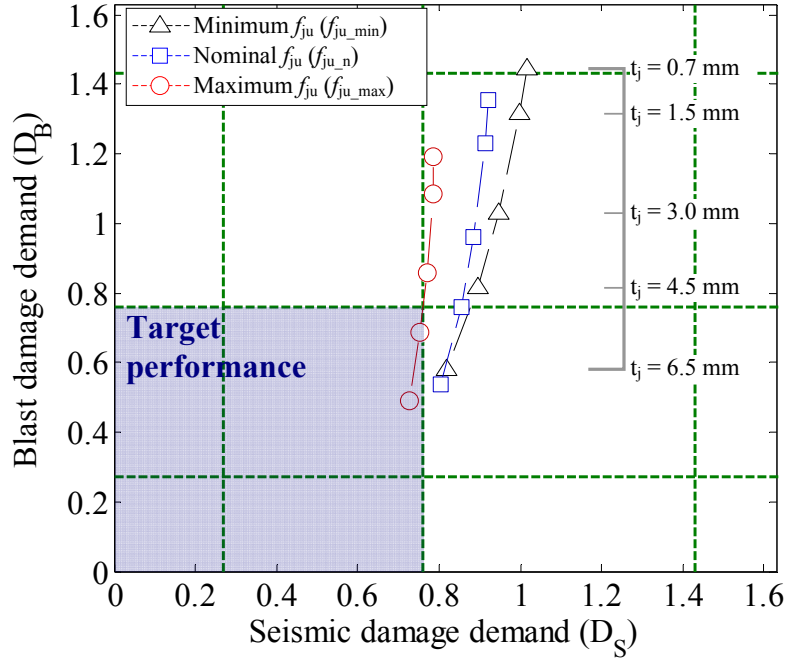
Figure 7.12. Effect of jacket strength (f_{ju}) and thickness (t_j) on seismic and blast energy-based damage demands (D_S and D_B)

7.4.2.2 Effect of retrofit location

To investigate the effect of retrofit location, Figure 7.13 compares the performance of a frame with a first-story retrofit installation to that of an all-story retrofit installation. The FRP column jacketing system used in Figure 7.13 consisted of nominal values for the parameters f_{ju}, ID and f_g (f_{ju_n} = 419 MPa, $ID_{\_n}$ = 444 mm, and f_{g_n} = 42.9 MPa in Table 6.1), and 0.7 mm to 6.5 mm for the t_j parameter. While the additional retrofit on the second story columns slightly decreased the D_B demand at the t_j parameter of 0.7 mm to 6.5 mm, it significantly reduced the D_S demand. In particular, as illustrated in Figure 7.13, the installation of the retrofit system with the t_j parameter of 6.5 mm to the columns on both stories satisfied the pre-determined target performance ($\leq \tilde{M}_{22}$ as described in Section 7.4.1). This was mainly due to a reduction in the maximum story drift demand by the additional retrofit on the second story columns. The

additional retrofit improved the global stiffness of the structure and uniformly distributed the normalized mode vectors over the first and second stories. This approach, described in Section 6.5.1, distributed the roof displacement gained from the capacity spectrum method (CSM) over the first and second stories by the normalized mode vectors, as given in Equation (6.12). The increase in the global stiffness reduced the roof displacement, and the uniform distribution of the mode vectors decreased the maximum value of the mode vectors. For these reasons, the additional retrofit in the second story improved the seismic performance of the structure.
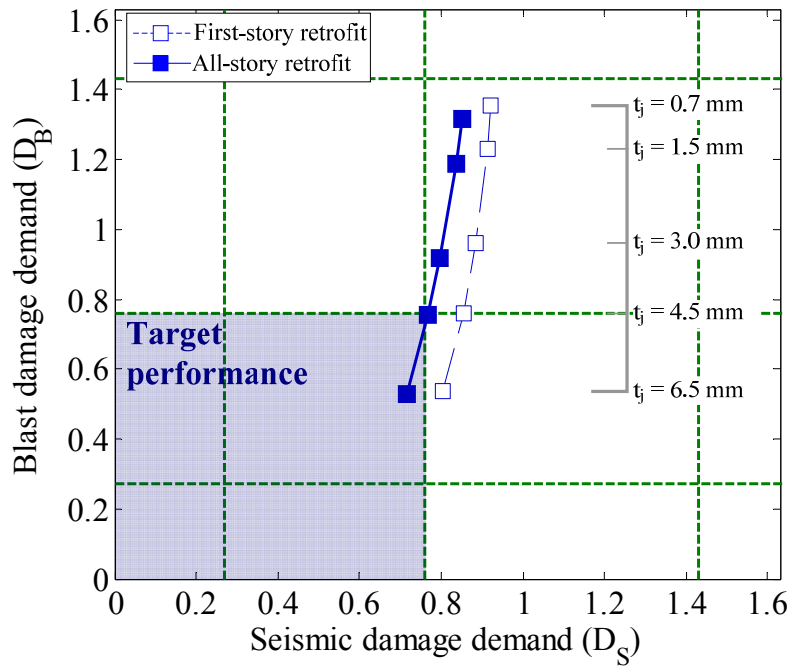
Figure 7.13. Effect of retrofit location (*RL*) parameter on energy-based damage demands (D_S and D_B)

7.4.2.3 Effect of inner diameter of FRP jacketing system and grout strength parameters

Figure 7.14 shows the seismic and blast damage demands (D_S and D_B demands) computed from the FRMs, varying the grout strength (f_g) parameter from 13.8 MPa to 89.3 MPa with respect to nominal and maximum training points for the column inner diameter parameter

(ID_n = 444 mm, and ID_{max} = 559 mm in Table 6.1). The jacket strength parameter was fixed at

419 MPa, a nominal training point for the f_{ju} parameter in Table 6.1. Two values for the jacket

thickness parameter were selected as 1.5 mm ($\approx$ a two-ply FRP jacket for the nominal f_{ju}) and 6.5

mm (a maximum training point for the t_j parameter in Table 6.1). As illustrated in Figure 7.14,

the value of the *ID* parameter had a marginal effect on the seismic performance when the t_j

parameter is held at 1.5 mm. Although an increase in the value of the *ID* parameter improved the

flexural stiffness and strength of the columns, the D_S demand was only slightly increased

because the increase in the value of the *ID* parameter reduced the confining pressure. The

reduction in the confining pressure resulted in having a lower value of the confinement ratio (CR

= 0.05) than the minimum value of 0.07 for the CR (CR_{min} = 0.07) proposed by Spoelstra and

Monit [1999]. For this reason, the ultimate displacement capacity was decreased in accordance

with the increase of the *ID* parameter from 444 mm to 559 mm. This decrease in the ultimate

displacement capacity amplified the D_S demand, computed using the Park-Ang damage model

(see Equation (2.3)). When the t_j parameter was increased from 1.5 mm to 6.5 mm for the FRP

column jacketing system with an *ID* parameter of 559 mm, the D_S demand decreased slightly

because the CR (= 0.17) for the FRP column jacketing system was higher than the minimum

value of the CR. The D_B demand was more significantly affected by the value of the *ID*

parameter than the D_S demand, as shown in Figure 7.14. This is because the reduction in the

displacement demands (i.e., reduction in a Δ_m response parameter given in Equation (2.3)) by the

increase in the flexural stiffness and strength was much higher than the decrease in the ultimate

displacement capacity (i.e., decrease in a Δ_u response parameter given in Equation (2.3)) caused

by the decrease in the confining pressure. Additionally, Figure 7.14 demonstrates that an increase

in the grout strength resulted in a slight decrease in the demands D_S and D_B. As compared to

other input parameters (i.e., retrofit location, jacket strength, jacket thickness, and column inner diameter parameters), the grout strength appears to have a relatively negligible effect on the seismic or blast performance of the retrofitted structure.
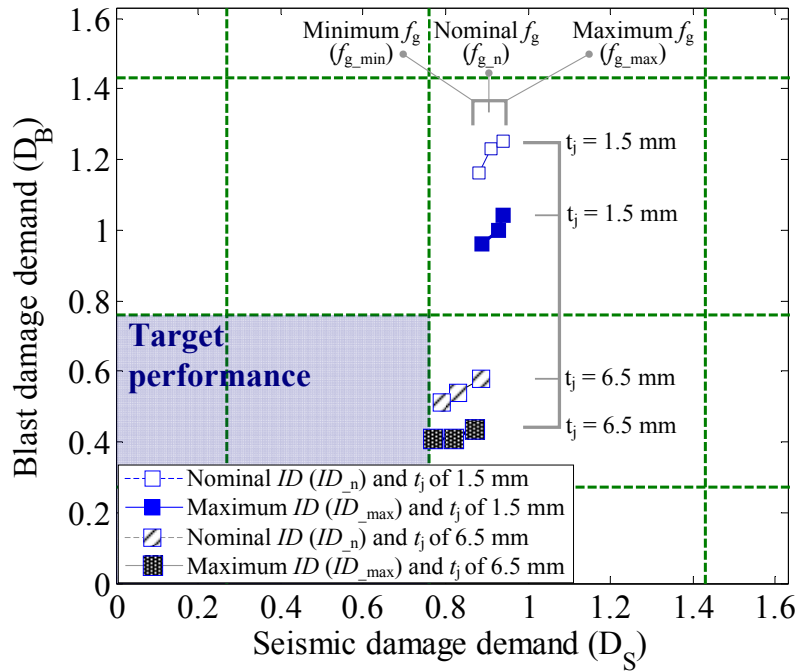
Figure 7.14. Effects of column inner diameter (*ID*) and grout strength (*f*g) parameters on the energy-based damage demands (*D*S and *D*B)

7.4.2.4 Summary of parametric studies

The parametric studies demonstrated that all identified parameters – except for grout strength – significantly affect the seismic performance and/or the blast performance of the retrofitted structure. Among them, the FRP jacket parameters f_{ju} and t_j, compared to the impact of other variables, can significantly improve both the seismic performance and the blast performance of the structure. The choice of a retrofit location (*RL*) parameter has a significant effect on the seismic performance, but only a marginal effect on the blast performance. While the blast performance is significantly enhanced by an increase in column diameter (*ID),* the seismic

performance is negatively affected by the increase in the size of the *ID* parameter when the confinement ratio (CR) does not meet the minimum required value.

7.4.3 Rapid decision-making process for retrofit design

This section presents and demonstrates a rapid decision-making process for the selection of a retrofit design which satisfies a given multi-hazard target performance level ($\leq \tilde{M}_{22}$ in the performance evaluation matrix) by using seismic and blast FRMs. It should be noted that this rapid decision-making process did not propose an optimal retrofit design, which can maximize the effectiveness of the retrofit system and minimize the retrofit cost, but found a cost-effective retrofit design that satisfies with the target performance by incorporating several possible retrofit cases into the FRMs. The as-built test frame described by Wright [2015] was selected as a representative two-story, two-bay non-ductile RC frame building for the purposes of defining the procedure (As-Built Case in Figure 7.15). The retrofitted test frame presented in Chapter 3 was also added as a reference retrofit case, designed for only seismic loading (Retrofit Case I in Table 7.4). Based on the performance of the reference retrofit case, a range of retrofit cases was developed. The example structure was assumed to be under a seismic load corresponding to a peak spectral acceleration (S_{a_peak}) of 1.5 *g*, which is similar to the peak shaker acceleration in the full-scale dynamic testing that initially led to a CP level in the as-built test frame. Additionally, the blast loading parameters, charge weight (W_{TNT}) and standoff distance (R_D), were assumed to be 680.4 kg and 5.0 m, respectively (i.e., scaled distance $Z = 0.6$ m/kg$^{1/3}$). This blast loading scenario induced column element failure for the as-built case. For this example, the retrofit scheme was determined using the following steps:

- Step 1: Examine the multi-hazard performance for As-Built Case using the FRMs. The performance was determined by the multi-hazard performance evaluation matrix proposed in Section 7.3. Since the as-built case reached an $\tilde{M}_{34}$ performance zone as shown in Figure 7.15, the as-built structure needed to be strengthened by an FRP column jacketing system to ensure the structure's performance was within the target performance zones ($\leq \tilde{M}_{22}$).

- Step 2: Evaluate the multi-hazard performance for Retrofit Case I described in Chapter 3, which is the reference retrofit specifically designed specifically to enhance seismic performance. This retrofit case satisfied the seismic target performance, but it did not meet the blast target performance. For this reason, the parameters dicussed in Section 7.4.2 were varied within the model ranges to ensure that the multi-hazard target performance was reached.

- Step 3: Develop a number of retrofit designs based on Retrofit Case I by modifying specific parameters as shown in Table 7.4. The f_g parameter was fixed because changes to this parameter only marginally affected the multi-hazard performance as described in Section 7.4.2.3.

- Step 4: Examine the multi-hazard performance for the various retrofit cases. As illustrated in Figure 7.15, adding the retrofit location (*RL*) and increasing the parameters f_{ju} and *ID* from Retrofit Cases II to IV did not contribute to any significant improvement in the blast performance of the structure. However, Retrofit Cases V and VI both satisfied the target multi-hazard performance by

either increasing the t_j parameter to 4.0 mm or increasing the f_{ju} parameter to 1380 MPa.

- Step 5: Select Retrofit Case V as the retrofit scheme for this example because Retrofit Case V increases only the FRP jacket thickness t_j parameter compared to the reference retrofit case to ensure the target multi-hazard performance ($\leq \tilde{M}_{22}$). This was expected to result in a more economical retrofit design compared to the design requiring an FRP jacket with a much higher strength.

Table 7.4. Geometric and material parameters for various retrofit cases

Retrofit Case	RL	f_{ju} (MPa)	t_j (mm)	ID (mm)	f_g (MPa)	Description
Retrofit Case I	First-story	1080	1.3	456	40.0	Same as the retrofitted test frame in Chapter 3
Retrofit Case II	First-story	1380	1.3	456	40.0	Increasing f_{ju} by maximum training point in Table 6.1
Retrofit Case III	All-story	1080	1.3	456	40.0	Adding RL to all-story columns
Retrofit Case IV	First-story	1080	1.3	559	40.0	Increasing ID by maximum training point in Table 6.1
Retrofit Case V	First-story	1080	4.0	456	40.0	Increasing t_j within the model ranges in Table 6.1
Retrofit Case VI	First-story	1380	4.0	456	40.0	Increasing f_{ju} and t_j within the model ranges in Table 6.1
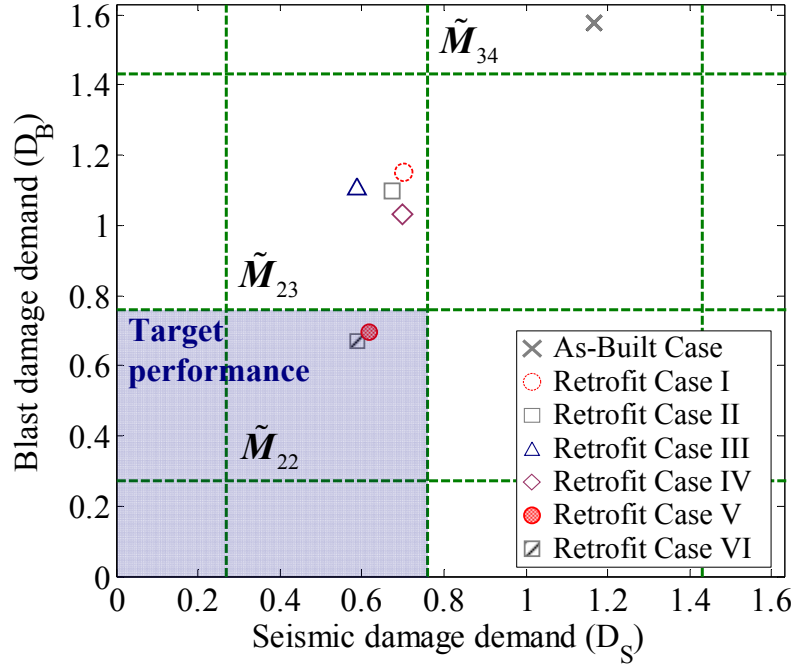
Figure 7.15. Various retrofit cases using FRP column jacketing systems

7.5 Summary

This chapter developed a procedure to derive energy-based damage limits (D_{Mi}) with respect to multi-hazard performance levels (PL_{Mi}) for non-ductile RC frames by combining seismic and blast performance criteria using fast-running models (FRMs). The damage limits for multi-hazard responses were used to construct performance evaluation matrices ($\tilde{M}_{11}$ to $\tilde{M}_{44}$) for the as-built and retrofitted conditions. These performance matrices were developed to rapidly evaluate both the performance of the existing non-ductile RC building structure (as-built frame) and the selection of a retrofit scheme with an FRP column jacketing system.

To investigate the effects of specific input parameters on the performance of a retrofitted structure, a loading scenario which induced an undesirable $\tilde{M}_{44}$ performance level for the as-built frame structure was selected. A series of parametric studies within the model ranges

developed in Chapter 6 were conducted for this loading scenario. Through the parametric studies, the ultimate tensile strength of the FRP jacket (f_{ju}) and jacket thickness (t_j) were identified as critical parameters, while the unconfined compressive strength of the grout material (f_g) was shown to have a negligible effect on the multi-hazard performance of the retrofitted structure. The addition of a second retrofit location (*RL*) significantly enhanced the seismic performance of the structure, and the size of the inner diameter of the FRP jacket (*ID*) had a relatively greater effect on the blast performance.

This chapter also presented and demonstrated a decision-making procedure for the initial design of an FRP jacket retrofit scheme, which will meet target performance levels for a given two-story, two-bay non-ductile RC frame. For this example structure, the multi-hazard performance of the retrofitted structure changed as specific geometric and material parameters of the FRP jacketing system were varied under an assumed multi-hazard loading scenario. Based on these changes in performance, an FRP retrofit system was selected that would meet target performance goals for the non-ductile RC frame system.

CHAPTER 8. CONCLUSIONS

8.1 Summary and Conclusions

Many existing reinforced concrete (RC) building structures designed in accordance with pre-1971 codes have seismically-deficient detailing in columns and beam-column joints, which can result in premature failure under seismic and blast loads. To enhance the seismic performance of the representative non-ductile RC frame studied in the present work, a fiber-reinforced polymer (FRP) column jacketing system was selected as a retrofit scheme. The FRP column jacketing system provides additional confining pressure to the concrete columns, which contributes to the enhancement of peak concrete compressive strength and ultimate axial strain in the material. This enhancement in material performance increases the flexural capacity and ductility for the existing RC columns. As such, the retrofit helps ensure the desirable performance of the non-ductile RC frame as specified in current design codes.

However, current design codes define performance criteria with different types of structural demand limits depending on loading type, such as inter-story drift-based limits for seismic loads and displacement ductility-based limits for blast loads. This difference may underestimate or overestimate the required retrofit design for existing non-ductile RC frames. Therefore, the present work developed a method to define multi-hazard performance criteria with identical demand limits under seismic and blast loads for non-ductile RC frames retrofitted with an FRP column jacketing system. The multi-hazard performance criteria can be utilized to conduct performance-based evaluation and retrofit design using an FRP column jacketing system for the non-ductile RC frame.

Using a mobile shaker system, a series of full-scale dynamic tests were conducted on a two-story, two-bay, non-ductile RC test frame retrofitted with an FRP column jacketing system in the first story. The full-scale dynamic shaker loading provided more realistic behavior of the test frame than previous shake table tests for reduced-scale specimens. Additionally, the dynamic responses for the retrofitted test frame were compared to those for an identical unretrofitted non-ductile RC test frame (as-built test frame) that was previously tested; this comparison served to quantify the effectiveness of the FRP column jacketing system. The installation of the retrofit system was shown to be effective in reducing the inter-story drift ratio and column rotation in the first story and mitigating the soft-story mechanism found in the as-built test frame.

Based on the measured dynamic responses, a numerical modeling methodology was developed for seismic loads associated with bond-slip effects between reinforcing bars and the surrounding concrete. The modeling methodology, which can represent bond-slip effects, was incorporated into numerical finite element (FE) frame models. To verify the modeling method, the simulated responses reproduced from the FE frame models with proper bonding conditions in as-built and retrofitted configurations were compared to the experimental responses in terms of displacement time history, story displacements, and peak inter-story drift ratios. The numerical simulation showed reasonable agreement with the experimental results, with a maximum variation of approximately 12.0 % for critical response parameters. This modeling process can be utilized to predict the seismic responses of non-ductile RC frames without retrofits and those with FRP-jacketed columns.

This study also proposed a numerical modeling methodology to simulate blast responses of the as-built and retrofitted FE frame models. The proposed modeling methodology includes bond-slip effects between reinforcing bars and surrounding concrete, as well as an advanced

blast load modeling technique, which can ensure a good balance between computational efficiency and the accurate prediction for blast loading. A numerical RC column model was developed using the proposed modeling methodology in order to compare to experimental results from blast tests performed by previous researchers. The simulated responses correlated well with experimental responses in terms of peak displacement, with less than 5.0 % variation. The modeling methodology was incorporated into the FE frame models, which were developed for predicting the seismic response.

Using artificial neural networks (ANNs), fast running models (FRMs) for seismic and blast loads were developed based on numerical datasets that included parameters associated with the FRP column jacketing system (e.g., retrofit location, jacket strength, jacket thickness, section enlargement using grout materials and grout strength) and loading parameters (e.g., peak spectral acceleration and scaled distance) as the inputs. The output parameters in the datasets were selected to be inter-story drift ratios and displacement ductility demands related to current code-defined limits, as well as seismic and blast damage demands computed from a standard damage model. To create numerical datasets, various input parameters for the FRP column jacketing system were incorporated into the FE frame models developed for predicting seismic and blast responses, and those models were simulated under various loading parameters. The seismic and blast FRMs were trained, validated, and tested using randomly-selected cases in the numerical datasets; the FRM-based results correlate well with the FE-based results. Additionally, the seismic and blast FRMs were tested with 14 randomly-selected sample cases, which showed less than 12 % variation between the FRM- and FE-based results. The results indicated that the FRMs allow rapid and reliable estimation for seismic and blast demands.

The seismic and blast FRMs were utilized to derive multi-hazard performance criteria with energy-based damage limits in terms of three different performance levels: *minor*, *moderate* and *severe*. The FRMs can rapidly generate a large number of response datasets. Based on the large datasets, the performance criteria was combined using seismic and blast energy-based damage limits corresponding to code-defined limits. Additionally, multi-hazard performance evaluation matrices for the as-built and retrofitted conditions were constructed using the multi-hazard damage limits. The performance matrices were useful for multi-hazard performance evaluation of the existing RC frames as well as the selection of retrofit schemes, which ensure a desirable multi-hazard target performance level.

To investigate the effects of specific identified parameters associated with the FRP column jacketing system, parametric studies were conducted under a given loading scenario, which exceeded the severe damage levels for seismic and blast loads. Through these parametric studies, the jacket strength and thickness were identified as critical parameters, while the grout strength was noted to have a negligible effect on multi-hazard performance. Adding column retrofits to the second story of the frame significantly enhanced its seismic performance. Column section enlargement had a greater effect on blast performance than seismic performance. This study also presents and demonstrates a decision-making procedure for determining a retrofit design, which meets the multi-hazard target performance using the performance evaluation matrix. The retrofit scheme was determined by varying specific parameters of the FRP column jacketing system within the model ranges.

8.2 Recommendations for Future Work

This study focused mainly on proposing multi-hazard performance criteria for a low-rise non-ductile RC building structure, retrofitted with an FRP column jacketing system based on the FRMs. To extend the scope of the multi-hazard performance criteria, additional research work will be needed as follows:

- The loading parameters used in this study were varied using peak spectral response accelerations and scaled distances. To consider various characteristics of seismic and blast loading, additional loading parameters should be included, such as spectral response accelerations at a period of 1.0 second and transition periods for seismic response spectrum curves (demand curves in a capacity spectrum method), and charge weights of TNT and standoff height for blast loads.

- For the as-built condition, the multi-hazard performance was evaluated using the FE numerical model that represented the full-scale as-built test frame specimen. However, the multi-hazard performance for the as-built frame can be varied depending on material properties of concrete and steel, aspect ratios (height-to-depth or length-to-depth) of column and beam elements, longitudinal reinforcement ratios, transverse reinforcement ratio, and types of transverse reinforcement. These parameters can affect failure modes of RC building structures under seismic and blast loading scenarios. To generalize multi-hazard performance criteria for existing non-ductile RC frames, a variety of input parameters associated with structural detailing should be added.

- For the retrofitted condition, the present work only focused on an FRP column jacketing system as the retrofit system. Seismic and/or blast resistance of existing non-ductile RC frames can be strengthened by various retrofit systems, such as infilled wall systems, FRP wrapping systems, near surface mounted rods, buckling-restrained bracing systems, or shape memory alloy bracing systems. To develop a retrofit approach considering various retrofit systems, the entire procedure to propose the multi-hazard performance criteria in this dissertation needs to be performed for the various retrofit systems.

- The multi-hazard performance criteria proposed in this study is based on a low-rise building structure. To include the effect of structural heights on the performance criteria, FE numeircal models for mid-rise and high-rise building structures should be developed using the modeling methodologies proposed in this dissertation.

- This study installed the retrofit system on an undamaged non-ductile RC frame. In reality, existing RC building structures constructed in the 1950s-1970s typically have experienced some level of deterioration from their service environment or previous hazard events. Such damage can affect the structural performance and selection of retrofit design under future events. Thus, numerical techniques representing various residual damage conditions before the application of the retrofit system should be developed. Additionally, the residual performance of the damaged building structure should be evaluated before and after the application of the retrofit system, and the effects of residual performance on the retrofit systems should be investigated. Finally, a decision-making procedure for the retrofit

scheme satisfying a desirable performance level needs to be proposed for damaged structures.

APPENDIX A. DATASHEET OF INPUT PARAMETERS

This appendix includes commercial datasheets of the ultimate tensile strength of FRP jackets (f_{ju}) and unconfined compressive strength of grouting materials (f_g). As discussed in Chapter 6, this study utilized commercial datasheets to determine the ranges of the input parameters for model training and their training points. The datasheets for the f_{ju} and the f_g are summarized, respectively, in Tables A.1 and A.2.

Table A.1. Summary of commercial FRP datasheets

Product List #	Product name	FRP material type	Elastic modulus, E_j (MPa)	Ultimate tensile strain, ε_{ju}	Ultimate tensile strength, f_{ju} (MPa)	Jacket thickness per a layer, t_j (mm)
1	Tyfo BC	GFRP	14900	0.015	224	0.86
2	Tyfo BCC	CFRP	47900	0.014	671	0.86
3	Tyfo PR	GFRP	20900	0.022	460	1.30
4	Tyfo SCH-41	CFRP	82000	0.009	697	1.00
5	Tyfo SEH-51A	GFRP	20900	0.018	368	1.30
6	Tyfo SEH-51A-SW1	GFRP	18800	0.016	301	1.30
7	V-Wrap C200-H	CFRP	86100	0.016	1380	1.02
8	PLC150.10	CFRP	95500	0.011	1080	0.66
9	PLC100.60	CFRP	49280	0.014	698	0.66
10	PLG60.60	GFRP	24140	0.017	431	0.66
11	PLG45.45	GFRP	22060	0.015	335	0.28
12	CF60.40	CFRP	31400	0.013	420	1.00
13	PileForm F	GFRP	10342	0.016	166	3.18
14	CSS-BCF018	CFRP	43000	0.013	559	1.00
15	CSS-BCF418	CFRP	41000	0.014	574	0.86

Product List #	Product name	FRP material type	Elastic modulus, E_j (MPa)	Ultimate tensile strain, ε_{ju}	Ultimate tensile strength, f_{ju} (MPa)	Jacket thickness per a layer, t_j (mm)
16	CSS-BGF018	GFRP	17000	0.018	306	0.66
17	CSS-CBGF424	GFRP	20000	0.014	280	0.86
18	CSS-CUCF22	CFRP	98000	0.009	882	1.00
19	CSS-CUGF27	GFRP	23000	0.017	391	1.30
20	Hex 100G	GFRP	23400	0.020	468	1.20
21	Hex 103C	AFRP	62000	0.009	564	1.20

Table A.2. Summary of commercial grout material datasheets

Product List #	Product name	Compressive strength, f_g (MPa)	
		1-day curing	28-day curing
1	FX-228	24.1	62.1
2	SikaGrout 212	24.1	51.7
3	SikaGrout 328	24.1	56.5
4	SikaGrout 428FS	22.4	89.6
5	Fastest Non-Shrink Grout	27.6	55.1
6	Non-Shrink General Purpose Grout	13.8	68.9
7	Non-Shrink Precision Grout	17.2	86.2
8	Non-Shrink Construction Grout	21.0	62.0
9	Five Star Grout	17.3	55.2
10	SeaShield 510 UW Grout	17.0	62.0

APPENDIX B. INITIAL AND ADDED DATASETS WITH SEISMIC AND BLAST DEMANDS

This appendix presents input and output parameters for initial and additional datasets utilized in model training, validation, and testing. The initial datasets were established by combining training points of seven input parameters (S_{a_peak} = peak spectral acceleration, Z = scaled distance, RL = retrofit location, f_{ju} = ultimate tensile strength of FRP material, t_j = jacket thickness, ID = inner diameter of the FRP jacketing system, and f_g = grout strength). The five input parameter combinations span a five-dimensional space. To better explain the combining method, a three-dimensional dataset is utilized. Figure B.1 shows a three-dimensional space for a three parameter space (i.e., x_1, x_2, and x_3 in Figure B.1) as a cube. The value at the center of each axis denotes the nominal, and minimum and maximum values at each axis represent the extreme training points. The figure describes three different combining methods for the three parameter space. Figure B.1(a) presents the sample cases with all nominal training points. Figure B.1(b) shows the sample cases for two parameters fixed as the nominal training points, while varying one of the parameters to an extreme. As illustrated in Figure B.1(c), one of the parameters fixed the nominal training point while varying two parameters to extremes.

By using the combining methods, the 71 sample cases considered as each initial dataset are summarized in Tables B.1 and B.2. The output parameters consisted of seismic demands (IDR = inter-story drift ratio, and D_S = seismic damage demand in Tables B.3 and B.5) and blast demands (μ_{blast} = blast displacement ductility demand, and D_B = blast damage demand in Tables B.4 and B.6). As described in Chapter 6, the IDRs were predicted by a capacity spectrum method (CSM) approach using the finite element (FE) frame models, and the blast displacement ductility

demand was determined based on the FE simulated results. The energy-based damage demands were computed using the Park-Ang damage model [Park and Ang 1987], and the parameters of the damage model were based on the FE simulated results. The seismic and blast demands with the input parameters in the initial datasets are summarized in Tables B.3 and B.4. To better predict the seismic and blast demands using the fast running models (FRMs) developed and validated in Chapter 6, additional datasets were added into the entire dataset. Tables B.5 and B.6 shows the additional datasets for the seismic loads and the blast loads, respectively.
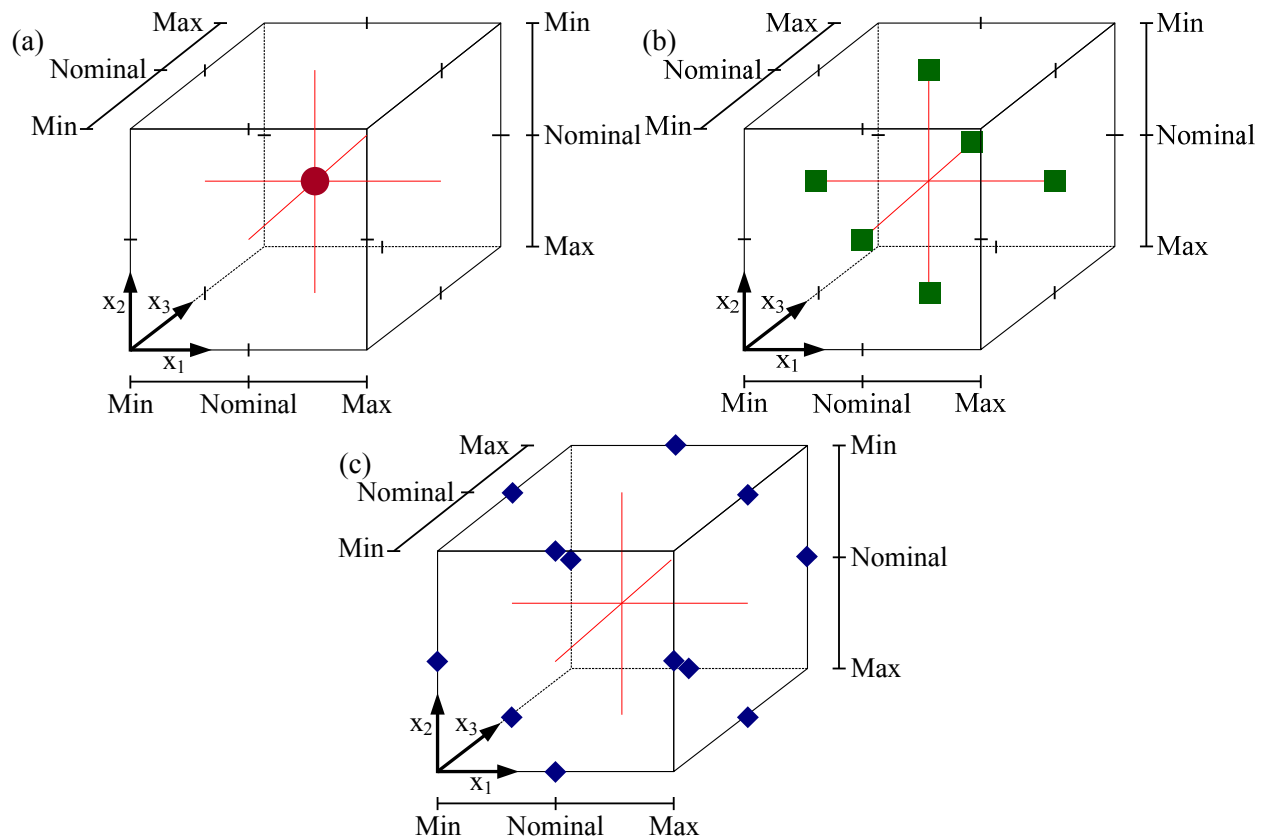
Figure B.1. Three-dimensional sample space: (a) all nominal points; (b) one extreme point; (c) two extreme points [Stewart 2010]

Table B.1. Initial dataset for seismic loading type

Case #	RL	S_{a_peak} (g)	f_{ju} (MPa)	t_j (mm)	ID (mm)	f_g (MPa)	Description of parameter combination
1	No-retrofit	3.0	No-retrofit	No-retrofit	No-retrofit	No-retrofit	S_{a_max}, As-built condition
2	No-retrofit	1.5	No-retrofit	No-retrofit	No-retrofit	No-retrofit	S_{a_n}, As-built condition
3	No-retrofit	0.5	No-retrofit	No-retrofit	No-retrofit	No-retrofit	S_{a_min}, As-built condition
4	First-story	1.5	419	3.6	444	42.9	Rest nominal
5	First-story	3.0	419	3.6	444	42.9	S_{a_max}, Rest nominal
6	First-story	0.5	419	3.6	444	42.9	S_{a_min}, Rest nominal
7	First-story	1.5	166	3.6	444	42.9	f_{ju_min}, Rest nominal
8	First-story	1.5	1380	3.6	444	42.9	f_{ju_max}, Rest nominal
9	First-story	1.5	419	6.5	444	42.9	t_{j_max}, Rest nominal
10	First-story	1.5	419	3.6	559	42.9	$ID_{\_max}$, Rest nominal
11	First-story	1.5	419	3.6	444	13.8	f_{g_min}, Rest nominal
12	First-story	1.5	419	3.6	444	89.3	f_{g_max}, Rest nominal
13	First-story	3.0	166	3.6	444	42.9	S_{a_max}, f_{ju_min}, Rest nominal
14	First-story	3.0	1380	3.6	444	42.9	S_{a_max}, f_{ju_max}, Rest nominal
15	First-story	0.5	166	3.6	444	42.9	S_{a_min}, f_{ju_min}, Rest nominal
16	First-story	0.5	1380	3.6	444	42.9	S_{a_min}, f_{ju_max}, Rest nominal
17	First-story	3.0	419	6.5	444	42.9	S_{a_max}, t_{j_max}, Rest nominal
18	First-story	0.5	419	6.5	444	42.9	S_{a_min}, t_{j_max}, Rest nominal
19	First-story	3.0	419	3.6	559	42.9	S_{a_max}, $ID_{\_max}$, Rest nominal
20	First-story	0.5	419	3.6	559	42.9	S_{a_min}, $ID_{\_max}$, Rest nominal
21	First-story	3.0	419	3.6	444	13.8	S_{a_max}, f_{g_min}, Rest nominal
22	First-story	3.0	419	3.6	444	89.3	S_{a_max}, f_{g_max}, Rest nominal
23	First-story	0.5	419	3.6	444	13.8	S_{a_min}, f_{g_min}, Rest nominal
24	First-story	0.5	419	3.6	444	89.3	S_{a_min}, f_{g_max}, Rest nominal
25	First-story	1.5	166	6.5	444	42.9	f_{ju_min}, t_{j_max}, Rest nominal
26	First-story	1.5	1380	6.5	444	42.9	f_{ju_max}, t_{j_max}, Rest nominal
27	First-story	1.5	166	3.6	559	42.9	f_{ju_min}, $ID_{\_max}$, Rest nominal
28	First-story	1.5	1380	3.6	559	42.9	f_{ju_max}, $ID_{\_max}$, Rest nominal

Case #	RL	S_{a_peak} (g)	f_{ju} (MPa)	t_j (mm)	ID (mm)	f_g (MPa)	Description of parameter combination
29	First-story	1.5	166	3.6	444	13.8	f_{ju_min}, f_{g_min}, Rest nominal
30	First-story	1.5	166	3.6	444	89.3	f_{ju_min}, f_{g_max}, Rest nominal
31	First-story	1.5	1380	3.6	444	13.8	f_{ju_max}, f_{g_min}, Rest nominal
32	First-story	1.5	1380	3.6	444	89.3	f_{ju_max}, f_{g_max}, Rest nominal
33	First-story	1.5	419	6.5	559	42.9	$t_{j\_max}, ID_{\_max}$, Rest nominal
34	First-story	1.5	419	6.5	444	13.8	t_{j_max}, f_{g_min}, Rest nominal
35	First-story	1.5	419	6.5	444	89.3	t_{j_max}, f_{g_max}, Rest nominal
36	First-story	1.5	419	3.6	559	13.8	$ID_{\_max}, f_{g\_min}$, Rest nominal
37	First-story	1.5	419	3.6	559	89.3	$ID_{\_max}, f_{g\_max}$, Rest nominal
38	All-story	1.5	419	3.6	444	42.9	Rest nominal
39	All-story	3.0	419	3.6	444	42.9	S_{a_max}, Rest nominal
40	All-story	0.5	419	3.6	444	42.9	S_{a_min}, Rest nominal
41	All-story	1.5	166	3.6	444	42.9	f_{ju_min}, Rest nominal
42	All-story	1.5	1380	3.6	444	42.9	f_{ju_max}, Rest nominal
43	All-story	1.5	419	6.5	444	42.9	t_{j_max}, Rest nominal
44	All-story	1.5	419	3.6	559	42.9	$ID_{\_max}$, Rest nominal
45	All-story	1.5	419	3.6	444	13.8	f_{g_min}, Rest nominal
46	All-story	1.5	419	3.6	444	89.3	f_{g_max}, Rest nominal
47	All-story	3.0	166	3.6	444	42.9	S_{a_max}, f_{ju_min}, Rest nominal
48	All-story	3.0	1380	3.6	444	42.9	S_{a_max}, f_{ju_max}, Rest nominal
49	All-story	0.5	166	3.6	444	42.9	S_{a_min}, f_{ju_min}, Rest nominal
50	All-story	0.5	1380	3.6	444	42.9	S_{a_min}, f_{ju_max}, Rest nominal
51	All-story	3.0	419	6.5	444	42.9	S_{a_max}, t_{j_max}, Rest nominal
52	All-story	0.5	419	6.5	444	42.9	S_{a_min}, t_{j_max}, Rest nominal
53	All-story	3.0	419	3.6	559	42.9	$S_{a\_max}, ID_{\_max}$, Rest nominal
54	All-story	0.5	419	3.6	559	42.9	$S_{a\_min}, ID_{\_max}$, Rest nominal
55	All-story	3.0	419	3.6	444	13.8	S_{a_max}, f_{g_min}, Rest nominal
56	All-story	3.0	419	3.6	444	89.3	S_{a_max}, f_{g_max}, Rest nominal
57	All-story	0.5	419	3.6	444	13.8	S_{a_min}, f_{g_min}, Rest nominal
58	All-story	0.5	419	3.6	444	89.3	S_{a_min}, f_{g_max}, Rest nominal
59	All-story	1.5	166	6.5	444	42.9	f_{ju_min}, t_{j_max}, Rest nominal

Case #	RL	S_{a_peak} (g)	f_{ju} (MPa)	t_j (mm)	ID (mm)	f_g (MPa)	Description of parameter combination
60	All-story	1.5	1380	6.5	444	42.9	f_{ju_max}, t_{j_max}, Rest nominal
61	All-story	1.5	166	3.6	559	42.9	f_{ju_min}, $ID_{\_max}$, Rest nominal
62	All-story	1.5	1380	3.6	559	42.9	f_{ju_max}, $ID_{\_max}$, Rest nominal
63	All-story	1.5	166	3.6	444	13.8	f_{ju_min}, f_{g_min}, Rest nominal
64	All-story	1.5	166	3.6	444	89.3	f_{ju_min}, f_{g_max}, Rest nominal
65	All-story	1.5	1380	3.6	444	13.8	f_{ju_max}, f_{g_min}, Rest nominal
66	All-story	1.5	1380	3.6	444	89.3	f_{ju_max}, f_{g_max}, Rest nominal
67	All-story	1.5	419	6.5	559	42.9	t_{j_max}, $ID_{\_max}$, Rest nominal
68	All-story	1.5	419	6.5	444	13.8	t_{j_max}, f_{g_min}, Rest nominal
69	All-story	1.5	419	6.5	444	89.3	t_{j_max}, f_{g_max}, Rest nominal
70	All-story	1.5	419	3.6	559	13.8	$ID_{\_max}$, f_{g_min}, Rest nominal
71	All-story	1.5	419	3.6	559	89.3	$ID_{\_max}$, f_{g_max}, Rest nominal

Table B.2. Initial dataset for blast loading type

Case #	RL	Z (m/kg$^{1/3}$)	f_{ju} (MPa)	t_j (mm)	ID (mm)	f_g (MPa)	Description of parameter combination
72	No-retrofit	0.4	No-retrofit	No-retrofit	No-retrofit	No-retrofit	Z_{min}, As-built condition
73	No-retrofit	0.8	No-retrofit	No-retrofit	No-retrofit	No-retrofit	Z_n, As-built condition
74	No-retrofit	1.6	No-retrofit	No-retrofit	No-retrofit	No-retrofit	Z_{max}, As-built condition
75	First-story	0.8	419	3.6	444	42.9	Rest nominal
76	First-story	0.4	419	3.6	444	42.9	Z_{min}, Rest nominal
77	First-story	1.6	419	3.6	444	42.9	Z_{max}, Rest nominal
78	First-story	0.8	166	3.6	444	42.9	f_{ju_min}, Rest nominal
79	First-story	0.8	1380	3.6	444	42.9	f_{ju_max}, Rest nominal
80	First-story	0.8	419	6.5	444	42.9	t_{j_max}, Rest nominal
81	First-story	0.8	419	3.6	559	42.9	ID_{max}, Rest nominal
82	First-story	0.8	419	3.6	444	13.8	f_{g_min}, Rest nominal
83	First-story	0.8	419	3.6	444	89.3	f_{g_max}, Rest nominal
84	First-story	0.4	166	3.6	444	42.9	Z_{min}, f_{ju_min}, Rest nominal
85	First-story	0.4	1380	3.6	444	42.9	Z_{min}, f_{ju_max}, Rest nominal
86	First-story	1.6	166	3.6	444	42.9	Z_{max}, f_{ju_min}, Rest nominal
87	First-story	1.6	1380	3.6	444	42.9	Z_{max}, f_{ju_max}, Rest nominal
88	First-story	0.4	419	6.5	444	42.9	Z_{min}, t_{j_max}, Rest nominal
89	First-story	1.6	419	6.5	444	42.9	Z_{max}, t_{j_max}, Rest nominal
90	First-story	0.4	419	3.6	559	42.9	Z_{min}, ID_{max}, Rest nominal
91	First-story	1.6	419	3.6	559	42.9	Z_{max}, ID_{max}, Rest nominal
92	First-story	0.4	419	3.6	444	13.8	Z_{min}, f_{g_min}, Rest nominal
93	First-story	0.4	419	3.6	444	89.3	Z_{min}, f_{g_max}, Rest nominal
94	First-story	1.6	419	3.6	444	13.8	Z_{max}, f_{g_min}, Rest nominal
95	First-story	1.6	419	3.6	444	89.3	Z_{max}, f_{g_max}, Rest nominal
96	First-story	0.8	166	6.5	444	42.9	f_{ju_min}, t_{j_max}, Rest nominal
97	First-story	0.8	1380	6.5	444	42.9	f_{ju_max}, t_{j_max}, Rest nominal
98	First-story	0.8	166	3.6	559	42.9	f_{ju_min}, ID_{max}, Rest nominal
99	First-story	0.8	1380	3.6	559	42.9	f_{ju_max}, ID_{max}, Rest nominal

Case #	RL	Z (m/kg$^{1/3}$)	f_{ju} (MPa)	t_j (mm)	ID (mm)	f_g (MPa)	Description of parameter combination
100	First-story	0.8	166	3.6	444	13.8	f_{ju_min}, f_{g_min}, Rest nominal
101	First-story	0.8	166	3.6	444	89.3	f_{ju_min}, f_{g_max}, Rest nominal
102	First-story	0.8	1380	3.6	444	13.8	f_{ju_max}, f_{g_min}, Rest nominal
103	First-story	0.8	1380	3.6	444	89.3	f_{ju_max}, f_{g_max}, Rest nominal
104	First-story	0.8	419	6.5	559	42.9	$t_{j\_max}, ID_{\_max}$, Rest nominal
105	First-story	0.8	419	6.5	444	13.8	t_{j_max}, f_{g_min}, Rest nominal
106	First-story	0.8	419	6.5	444	89.3	t_{j_max}, f_{g_max}, Rest nominal
107	First-story	0.8	419	3.6	559	13.8	$ID_{\_max}, f_{g\_min}$, Rest nominal
108	First-story	0.8	419	3.6	559	89.3	$ID_{\_max}, f_{g\_max}$, Rest nominal
109	All-story	0.8	419	3.6	444	42.9	Rest nominal
110	All-story	0.4	419	3.6	444	42.9	$Z_{\_min}$, Rest nominal
111	All-story	1.6	419	3.6	444	42.9	$Z_{\_max}$, Rest nominal
112	All-story	0.8	166	3.6	444	42.9	f_{ju_min}, Rest nominal
113	All-story	0.8	1380	3.6	444	42.9	f_{ju_max}, Rest nominal
114	All-story	0.8	419	6.5	444	42.9	t_{j_max}, Rest nominal
115	All-story	0.8	419	3.6	559	42.9	$ID_{\_max}$, Rest nominal
116	All-story	0.8	419	3.6	444	13.8	f_{g_min}, Rest nominal
117	All-story	0.8	419	3.6	444	89.3	f_{g_max}, Rest nominal
118	All-story	0.4	166	3.6	444	42.9	$Z_{\_min}, f_{ju\_min}$, Rest nominal
119	All-story	0.4	1380	3.6	444	42.9	$Z_{\_min}, f_{ju\_max}$, Rest nominal
120	All-story	1.6	166	3.6	444	42.9	$Z_{\_max}, f_{ju\_min}$, Rest nominal
121	All-story	1.6	1380	3.6	444	42.9	$Z_{\_max}, f_{ju\_max}$, Rest nominal
122	All-story	0.4	419	6.5	444	42.9	$Z_{\_min}, t_{j\_max}$, Rest nominal
123	All-story	1.6	419	6.5	444	42.9	$Z_{\_max}, t_{j\_max}$, Rest nominal
124	All-story	0.4	419	3.6	559	42.9	$Z_{\_min}, ID_{\_max}$, Rest nominal
125	All-story	1.6	419	3.6	559	42.9	$Z_{\_max}, ID_{\_max}$, Rest nominal
126	All-story	0.4	419	3.6	444	13.8	$Z_{\_min}, f_{g\_min}$, Rest nominal
127	All-story	0.4	419	3.6	444	89.3	$Z_{\_min}, f_{g\_max}$, Rest nominal
128	All-story	1.6	419	3.6	444	13.8	$Z_{\_max}, f_{g\_min}$, Rest nominal
129	All-story	1.6	419	3.6	444	89.3	$Z_{\_max}, f_{g\_max}$, Rest nominal
130	All-story	0.8	166	6.5	444	42.9	f_{ju_min}, t_{j_max}, Rest nominal

Case #	RL	Z $(\text{m/kg}^{1/3})$	f_{ju} (MPa)	t_j (mm)	ID (mm)	f_g (MPa)	Description of parameter combination
131	All-story	0.8	1380	6.5	444	42.9	f_{ju_max}, t_{j_max}, Rest nominal
132	All-story	0.8	166	3.6	559	42.9	f_{ju_min}, $ID_{\_max}$, Rest nominal
133	All-story	0.8	1380	3.6	559	42.9	f_{ju_max}, $ID_{\_max}$, Rest nominal
134	All-story	0.8	166	3.6	444	13.8	f_{ju_min}, f_{g_min}, Rest nominal
135	All-story	0.8	166	3.6	444	89.3	f_{ju_min}, f_{g_max}, Rest nominal
136	All-story	0.8	1380	3.6	444	13.8	f_{ju_max}, f_{g_min}, Rest nominal
137	All-story	0.8	1380	3.6	444	89.3	f_{ju_max}, f_{g_max}, Rest nominal
138	All-story	0.8	419	6.5	559	42.9	t_{j_max}, $ID_{\_max}$, Rest nominal
139	All-story	0.8	419	6.5	444	13.8	t_{j_max}, f_{g_min}, Rest nominal
140	All-story	0.8	419	6.5	444	89.3	t_{j_max}, f_{g_max}, Rest nominal
141	All-story	0.8	419	3.6	559	13.8	$ID_{\_max}$, f_{g_min}, Rest nominal
142	All-story	0.8	419	3.6	559	89.3	$ID_{\_max}$, f_{g_max}, Rest nominal

Table B.3. Seismic demands (output parameters) for initial dataset

Case #	RL	S_{a_peak} (g)	f_{ju} (MPa)	t_j (mm)	ID (mm)	f_g (MPa)	IDR (%)	D_S
1	No-retrofit	3.0	No-retrofit	No-retrofit	No-retrofit	No-retrofit	5.25	1.95
2	No-retrofit	1.5	No-retrofit	No-retrofit	No-retrofit	No-retrofit	2.44	0.93
3	No-retrofit	0.5	No-retrofit	No-retrofit	No-retrofit	No-retrofit	0.41	0.17
4	First-story	1.5	419	3.6	444	42.9	1.64	0.58
5	First-story	3.0	419	3.6	444	42.9	3.29	1.02
6	First-story	0.5	419	3.6	444	42.9	0.55	0.20
7	First-story	1.5	166	3.6	444	42.9	1.72	0.66
8	First-story	1.5	1380	3.6	444	42.9	1.58	0.55
9	First-story	1.5	419	6.5	444	42.9	1.58	0.43
10	First-story	1.5	419	3.6	559	42.9	1.57	0.43
11	First-story	1.5	419	3.6	444	13.8	1.62	0.59
12	First-story	1.5	419	3.6	444	89.3	1.78	0.68
13	First-story	3.0	166	3.6	444	42.9	3.45	1.10
14	First-story	3.0	1380	3.6	444	42.9	3.16	0.88
15	First-story	0.5	166	3.6	444	42.9	0.57	0.22
16	First-story	0.5	1380	3.6	444	42.9	0.53	0.19
17	First-story	3.0	419	6.5	444	42.9	3.16	0.86
18	First-story	0.5	419	6.5	444	42.9	0.53	0.14
19	First-story	3.0	419	3.6	559	42.9	3.14	1.18
20	First-story	0.5	419	3.6	559	42.9	0.52	0.20
21	First-story	3.0	419	3.6	444	13.8	3.23	1.22
22	First-story	3.0	419	3.6	444	89.3	3.56	1.36
23	First-story	0.5	419	3.6	444	13.8	0.54	0.22
24	First-story	0.5	419	3.6	444	89.3	0.59	0.23
25	First-story	1.5	166	6.5	444	42.9	1.77	0.56

Case #	RL	S_{a_peak} (g)	f_{ju} (MPa)	t_j (mm)	ID (mm)	f_g (MPa)	IDR (%)	D_S
26	First-story	1.5	1380	6.5	444	42.9	1.72	0.55
27	First-story	1.5	166	3.6	559	42.9	1.73	0.72
28	First-story	1.5	1380	3.6	559	42.9	1.58	0.58
29	First-story	1.5	166	3.6	444	13.8	1.43	0.39
30	First-story	1.5	166	3.6	444	89.3	1.73	0.72
31	First-story	1.5	1380	3.6	444	13.8	1.98	0.66
32	First-story	1.5	1380	3.6	444	89.3	1.96	0.66
33	First-story	1.5	419	6.5	559	42.9	1.49	0.41
34	First-story	1.5	419	6.5	444	13.8	1.61	0.61
35	First-story	1.5	419	6.5	444	89.3	1.53	0.58
36	First-story	1.5	419	3.6	559	13.8	1.67	0.61
37	First-story	1.5	419	3.6	559	89.3	1.59	0.55
38	All-story	1.5	419	3.6	444	42.9	1.47	0.49
39	All-story	3.0	419	3.6	444	42.9	2.93	0.99
40	All-story	0.5	419	3.6	444	42.9	0.49	0.16
41	All-story	1.5	166	3.6	444	42.9	1.55	0.45
42	All-story	1.5	1380	3.6	444	42.9	1.27	0.43
43	All-story	1.5	419	6.5	444	42.9	1.27	0.35
44	All-story	1.5	419	3.6	559	42.9	1.27	0.43
45	All-story	1.5	419	3.6	444	13.8	1.42	0.57
46	All-story	1.5	419	3.6	444	89.3	1.62	0.59
47	All-story	3.0	166	3.6	444	42.9	3.09	0.90
48	All-story	3.0	1380	3.6	444	42.9	2.54	0.85
49	All-story	0.5	166	3.6	444	42.9	0.52	0.15
50	All-story	0.5	1380	3.6	444	42.9	0.42	0.14
51	All-story	3.0	419	6.5	444	42.9	2.54	0.70
52	All-story	0.5	419	6.5	444	42.9	0.42	0.12
53	All-story	3.0	419	3.6	559	42.9	2.92	1.00

Case #	RL	S_{a_peak} (g)	f_{ju} (MPa)	t_j (mm)	ID (mm)	f_g (MPa)	IDR (%)	D_S
54	All-story	0.5	419	3.6	559	42.9	0.49	0.17
55	All-story	3.0	419	3.6	444	13.8	2.84	1.13
56	All-story	3.0	419	3.6	444	89.3	3.24	1.18
57	All-story	0.5	419	3.6	444	13.8	0.47	0.19
58	All-story	0.5	419	3.6	444	89.3	0.54	0.20
59	All-story	1.5	166	6.5	444	42.9	1.44	0.44
60	All-story	1.5	1380	6.5	444	42.9	1.29	0.42
61	All-story	1.5	166	3.6	559	42.9	1.52	0.71
62	All-story	1.5	1380	3.6	559	42.9	1.45	0.53
63	All-story	1.5	166	3.6	444	13.8	1.23	0.37
64	All-story	1.5	166	3.6	444	89.3	1.64	0.60
65	All-story	1.5	1380	3.6	444	13.8	1.49	0.67
66	All-story	1.5	1380	3.6	444	89.3	1.49	0.63
67	All-story	1.5	419	6.5	559	42.9	1.40	0.38
68	All-story	1.5	419	6.5	444	13.8	1.42	0.49
69	All-story	1.5	419	6.5	444	89.3	1.34	0.46
70	All-story	1.5	419	3.6	559	13.8	1.42	0.47
71	All-story	1.5	419	3.6	559	89.3	1.40	0.44

Table B.4. Blast demands (output parameters) for initial dataset

Case #	RL	Z (m/kg$^{1/3}$)	f_{ju} (MPa)	t_j (mm)	ID (mm)	f_g (MPa)	μ_{blast}	D_B
72	No-retrofit	0.4	No-retrofit	No-retrofit	No-retrofit	No-retrofit	5.20	1.87
73	No-retrofit	0.8	No-retrofit	No-retrofit	No-retrofit	No-retrofit	2.46	1.13
74	No-retrofit	1.6	No-retrofit	No-retrofit	No-retrofit	No-retrofit	0.31	0.18
75	First-story	0.8	419	3.6	444	42.9	1.75	0.41
76	First-story	0.4	419	3.6	444	42.9	2.83	0.62
77	First-story	1.6	419	3.6	444	42.9	0.29	0.06
78	First-story	0.8	166	3.6	444	42.9	1.79	0.41
79	First-story	0.8	1380	3.6	444	42.9	1.70	0.40
80	First-story	0.8	419	6.5	444	42.9	1.86	0.43
81	First-story	0.8	419	3.6	559	42.9	1.72	0.41
82	First-story	0.8	419	3.6	444	13.8	1.45	0.33
83	First-story	0.8	419	3.6	444	89.3	1.93	0.45
84	First-story	0.4	166	3.6	444	42.9	3.23	0.68
85	First-story	0.4	1380	3.6	444	42.9	2.55	0.57
86	First-story	1.6	166	3.6	444	42.9	0.32	0.08
87	First-story	1.6	1380	3.6	444	42.9	0.25	0.06
88	First-story	0.4	419	6.5	444	42.9	2.58	0.58
89	First-story	1.6	419	6.5	444	42.9	0.26	0.05
90	First-story	0.4	419	3.6	559	42.9	2.61	0.60
91	First-story	1.6	419	3.6	559	42.9	0.32	0.06
92	First-story	0.4	419	3.6	444	13.8	2.75	0.64
93	First-story	0.4	419	3.6	444	89.3	2.88	0.60
94	First-story	1.6	419	3.6	444	13.8	0.30	0.06
95	First-story	1.6	419	3.6	444	89.3	0.29	0.06
96	First-story	0.8	166	6.5	444	42.9	1.35	0.32

Case #	RL	Z (m/kg$^{1/3}$)	f_{ju} (MPa)	t_j (mm)	ID (mm)	f_g (MPa)	μ_{blast}	D_B
97	First-story	0.8	1380	6.5	444	42.9	1.63	0.29
98	First-story	0.8	166	3.6	559	42.9	1.80	0.46
99	First-story	0.8	1380	3.6	559	42.9	1.87	0.31
100	First-story	0.8	166	3.6	444	13.8	1.36	0.32
101	First-story	0.8	166	3.6	444	89.3	1.91	0.41
102	First-story	0.8	1380	3.6	444	13.8	1.30	0.30
103	First-story	0.8	1380	3.6	444	89.3	1.06	0.25
104	First-story	0.8	419	6.5	559	42.9	1.03	0.25
105	First-story	0.8	419	6.5	444	13.8	1.01	0.23
106	First-story	0.8	419	6.5	444	89.3	1.02	0.24
107	First-story	0.8	419	3.6	559	13.8	1.23	0.28
108	First-story	0.8	419	3.6	559	89.3	0.89	0.21
109	All-story	0.8	419	3.6	444	42.9	1.66	0.40
110	All-story	0.4	419	3.6	444	42.9	2.70	0.62
111	All-story	1.6	419	3.6	444	42.9	0.23	0.04
112	All-story	0.8	166	3.6	444	42.9	1.69	0.39
113	All-story	0.8	1380	3.6	444	42.9	1.57	0.37
114	All-story	0.8	419	6.5	444	42.9	1.73	0.40
115	All-story	0.8	419	3.6	559	42.9	1.56	0.33
116	All-story	0.8	419	3.6	444	13.8	1.43	0.33
117	All-story	0.8	419	3.6	444	89.3	1.79	0.41
118	All-story	0.4	166	3.6	444	42.9	3.14	0.68
119	All-story	0.4	1380	3.6	444	42.9	2.33	0.52
120	All-story	1.6	166	3.6	444	42.9	0.20	0.04
121	All-story	1.6	1380	3.6	444	42.9	0.25	0.03
122	All-story	0.4	419	6.5	444	42.9	2.37	0.55
123	All-story	1.6	419	6.5	444	42.9	0.27	0.03

Case #	RL	Z (m/kg$^{1/3}$)	f_{ju} (MPa)	t_j (mm)	ID (mm)	f_g (MPa)	μ_{blast}	D_B
124	All-story	0.4	419	3.6	559	42.9	2.41	0.56
125	All-story	1.6	419	3.6	559	42.9	0.20	0.03
126	All-story	0.4	419	3.6	444	13.8	2.70	0.59
127	All-story	0.4	419	3.6	444	89.3	2.81	0.56
128	All-story	1.6	419	3.6	444	13.8	0.25	0.06
129	All-story	1.6	419	3.6	444	89.3	0.23	0.04
130	All-story	0.8	166	6.5	444	42.9	1.30	0.31
131	All-story	0.8	1380	6.5	444	42.9	1.59	0.39
132	All-story	0.8	166	3.6	559	42.9	1.77	0.45
133	All-story	0.8	1380	3.6	559	42.9	1.87	0.43
134	All-story	0.8	166	3.6	444	13.8	1.23	0.30
135	All-story	0.8	166	3.6	444	89.3	1.80	0.38
136	All-story	0.8	1380	3.6	444	13.8	1.45	0.33
137	All-story	0.8	1380	3.6	444	89.3	1.11	0.28
138	All-story	0.8	419	6.5	559	42.9	1.03	0.26
139	All-story	0.8	419	6.5	444	13.8	0.97	0.23
140	All-story	0.8	419	6.5	444	89.3	0.99	0.24
141	All-story	0.8	419	3.6	559	13.8	1.23	0.29
142	All-story	0.8	419	3.6	559	89.3	0.89	0.22

Table B.5. Seismic demands (output parameters) for additional dataset

Case #	RL	S_{a_peak} (g)	f_{ju} (MPa)	t_j (mm)	ID (mm)	f_g (MPa)	IDR (%)	D_S
143	No-retrofit	2.8	No-retrofit	No-retrofit	No-retrofit	No-retrofit	4.18	1.41
144	No-retrofit	2.5	No-retrofit	No-retrofit	No-retrofit	No-retrofit	4.01	1.24
145	No-retrofit	2.0	No-retrofit	No-retrofit	No-retrofit	No-retrofit	2.71	1.12
146	No-retrofit	1.0	No-retrofit	No-retrofit	No-retrofit	No-retrofit	1.46	0.60
147	No-retrofit	0.9	No-retrofit	No-retrofit	No-retrofit	No-retrofit	1.26	0.42
148	No-retrofit	0.7	No-retrofit	No-retrofit	No-retrofit	No-retrofit	0.83	0.34
149	No-retrofit	0.3	No-retrofit	No-retrofit	No-retrofit	No-retrofit	0.27	0.11

Table B.6. Blast demands (output parameters) for additional dataset

Case #	RL	Z (m/kg$^{1/3}$)	f_{ju} (MPa)	t_j (mm)	ID (mm)	f_g (MPa)	μ_{blast}	D_B
150	No-retrofit	0.6	No-retrofit	No-retrofit	No-retrofit	No-retrofit	4.89	1.72
151	No-retrofit	0.8	No-retrofit	No-retrofit	No-retrofit	No-retrofit	2.89	1.45
152	No-retrofit	1.0	No-retrofit	No-retrofit	No-retrofit	No-retrofit	1.49	0.92
153	No-retrofit	1.2	No-retrofit	No-retrofit	No-retrofit	No-retrofit	0.88	0.62
154	No-retrofit	1.3	No-retrofit	No-retrofit	No-retrofit	No-retrofit	0.75	0.44
155	No-retrofit	1.4	No-retrofit	No-retrofit	No-retrofit	No-retrofit	0.33	0.27
156	First-story	0.4	419	0.7	444	42.9	5.87	1.72
157	First-story	0.4	1380	1.0	444	42.9	3.54	1.00
158	First-story	0.4	166	3.2	444	42.9	3.31	0.85
159	First-story	0.4	419	1.3	444	42.9	5.38	1.63
160	First-story	0.4	1380	2.0	444	42.9	4.39	1.33
161	All-story	0.4	419	0.7	444	42.9	5.81	1.66

REFERENCES

Abdelkarim OI, ElGawady MA. Analytical and finite-element modeling of FRP-concrete-steel double-skin tubular columns. Journal of Bridge Engineering 2014; 20(8): B4014005 1-12.

ACI Committee 318. Building code requirements for reinforced concrete. ACI 318-63, Farmington Hills, Americal Concrete Institute, Detroit, MI (US); 1963.

ACI Committee 318. Building code requirements for structural concrete and commentary. ACI 318-14, Farmington Hills, Americal Concrete Institute, Detroit, MI (US); 2014.

ACI Committee 440. Guide for the design and construction of externally bonded frp systems for strengthening concrete structures. ACI 440.2R American Concrete Institute, Detroit, MI (US); 2017.

Akkar S, Metin A. Assessment of improved nonlinear static procedures in FEMA-440. Journal of Structural Engineering 2007; 133(9): 1237-1246.

Al-Salloum YA. Influence of edge sharpness on the strength of square concrete columns confined with FRP composite laminates. Composites Part B: Engineering 2007; 38: 640-50.

Anderson JA, Rosenfeld E. Neurocomputing: Foundations of research. MIT Press, Cambridge, MA (US): 1988.

ASCE. Blast protection of buildings, ASCE/SEI 59-11, American Society of Civil Engineers, 2011.

ASCE. Seismic evaluation and retrofit of existing buildings. ASCE/SEI 41-13, American Society of Civil Engineers, 2014.

Aschheim M, Gülkan P, Sezen H, Bruneau M, Elnashai AS, Halling M, Love J, Rahnama M. Performance of buildings. Earthquake Spectra 2000; 16 (S1): 237-279.

ASTM. Test for static modulus of elasticity and Poisson's ratio of concrete in compression. ASTM C469-94, Philadelphia, PA (US); 2000.

ASTM. Standard test method for compressive strength of hydraulic cement mortars. ASTM C109, Philadelphia, PA (US); 2013.

ASTM. Standard test method for tensile properties of polymer matrix composite materials. ASTM D3039, Philadelphia, PA (US); 2014.

ASTM. Standard test method for compressive strength of cylindrical concrete specimens. ASTM C39, Philadelphia, PA (US); 2015a.

ASTM. Standard specification for deformed and plain billet steel bars for concrete Reinforcement. ASTM A615, Philadelphia, PA (US); 2015b.

ATC-19. Structural response modification factors. Applied Technology Council (ATC), Redwood City, CA (US); 1995.

ATC-40. Seismic Evaluation and Retrot of Concrete Building. Applied Technology Council (ATC), Redwood City, CA (US); 1996.

AUTODYN. Interactive non-linear dynamic analysis software, version 4.2, user's manual. Century Dynamics Inc.; 2001.

Aycardi LE, Mander JB, Reinhorn AM. Seismic resistance of reinforced concrete frame structures designed only for gravity loads: experimental performance of sub-assemblages. ACI Structural Journal 1994; 91(5):552-63.

Baker WE. Explosions in air. University of Texas Press, 54-77; 1973.

Bao Y, Kunnath SK, El-Tawil S, Lew HS. Macromodel-based simulation of progressive collapse: RC frame structures. Journal of Structural Engineering. 2008; 134(7): 1079-91.

Bao X, Li B. Residual strength of blast damaged reinforced concrete columns. International Journal of Impact Engineering 2010; 37(3): 295-308

Baylot JT, Bevins TL. Effect of responding and failing structural components on the airblast pressures and loads on and inside of the structure. Computers & Structures 2007; 85(11): 891-910.

Bentz E, Collins MP. Response-2000, user manual. University of Toronto, Toronto, Ontario (Canada); 2001.

Beres A, Pessiki S, White R, Gergely P. Implications of experiments on the seismic behavior of gravity load designed RC beam-to-column connections. Earthquake Spectra 1996; 12: 185-98.

Boyd SD, Acceleration of a plate subject to explosive blast loading - Trial results. Rep. No. DRTO-TN-0270, Defence Science and Technology Organisation, Melbourne (Australia); 2000.

Bracci JM, Reinhom AM, Mander JB, Kunnath SK. Deterministic model for seismic damage evaluation of RC structure. NCEER-89-0033. Technical Report: National Center for Earthquake Engineering Research, SUNY at Buffalo, NY (US); 1989.

Bracci JM, Reinhom AM, Mander JB. Seismic resistance of reinforced concrete frame structures designed for gravity loads: performance of structural system. ACI Structural Journal 1995a; 92(5): 597-609.

Bracci JM, Reinhorn AM, Mander JB. Seismic retrofit of reinforced concrete buildings designed for gravity loads: performance of structural model. ACI Structural Journal 1995b; 92(6): 711-23.

Bracci JM, Kunnath SK, Reinhorn AM. Seismic performance and retrofit evaluation of reinforced concrete structures. Journal of Structural Engineering 1997; 123(1): 3-10.

Buchan PA, Chen JF. Blast resistance of FRP composites and polymer strengthened concrete and masonry structures - A state-of-the-art review.Composites Part B: Engineering 2007; 38(5): 509-522.

Børvik T, Hanssen AG, Langseth M, Olovsson L. Response of structures to planar blast loads-A finite element engineering approach. Computers & Structures 2009; 87(9): 507-520.

Chen W, Hao H, Chen S. Numerical analysis of prestressed reinforced concrete beam subjected to blast loading. Materials & Design 2015; 65: 662-74.

Chopra AK, Goel RK. Capacity-demand-diagram methods based on inelastic design spectrum. Earthquake Spectra 1999; 15(4): 637-656.

Chopra AK, Goel RK. Evaluation of NSP to estimate seismic deformations: SDF systems. Journal of Structural Engineering 2000; 126(4): 482-490.

Chung YS, Meyer C, Shinozuka M. Automatic seismic design of reinforced concrete building frames. ACI Structural Journal 1990; 87(3): 326-40.

Corley WG, Sozen MA, Thornton CH, Mlakar PF. The Oklahoma city bombing: improving building performance through multi-hazard mitigation. Rep. No. FEMA-277. Federal Emergency Management Agency (FEMA): Washington, DC(US); 1996.

Corley WG, Mlakar PF, Sozen MA, Thornton, CH. The Oklahoma City bombing: summary and recommendations for multihazard mitigation. Journal of Performance of Constructed Facilities 1998; 12(3): 100-112.

Corley WG. Lessons learned on improving resistance of buildings to terrorist attacks. Journal of Performance of Constructed Facilities 2004; 18(2): 68-78.

Crawford JE, Wesevich J, Valancius J, Reynolds A. Evaluation of jacketed columns as a means to improve the resistance of conventional structures to blast effects. Proceedings, 66th Shock and Vibration Symposium, Biloxi, MS, 30 October - 2 November 1995.

Crawford JE, Malvar LJ, Wesevich JW, Valancius J, Reynolds AD. Retrofit of reinforced concrete structures to resist blast effects. ACI Struct. J. 1997; 94(4): 371-377.

Crawford JE, Lan S. Design and implementation of protection technologies for improving blast resistance of buildings. Presented at the Enhancing Building Security Seminar, Singapore; 2005.

Crawford JE. State of the art for enhancing the blast resistance of reinforced concrete columns with fiber-reinforced plastic. Canadian Journal of Civil Engineering 2011; 40(11): 1023-1033.

Crawford J, Wu Y, Choi H, Magallanes J, Lan S. Use and validation of the release III K&C concrete material model in LSDYNA. TR-11-36.6 Technical report, Karagozian & Case, Glendale, CA (US); 2012.

Crawford JE, Wu Y, Magallanes JM, Choi HJ. The importance of shear-dilatancy behaviors in RC columns. International Journal of Protective Structures 2013; 4(3): 341-377.

Deaton JB. Nonlinear finite element analysis of reinforced concrete exterior beam-column joints with nonseismic detailing. PhD thesis, Georgia Institute of Technology, Atlanta, GA (US); 2013.

Di Ludovico M, Manfredi G, Mola E, Negro P, Prota A. Seismic behavior of a full-scale RC structure retrofitted using GFRP laminates. J Struct Eng 2008; 135(5): 810-21.

Earthquake Engineering Online Archive. NISEE E-Library. Available at: http://nisee. berkeley.edu/elibrary/Image [Online]

Ehsani M, Tipnis A. Miami building first to benefit from innovative pile jacket. Concrete Repair Bulletin July/August 2011; 16-18.

El-Amoury AT. Seismic rehabilitation of concrete frame beam-column joints. PhD thesis. McMaster University, Hamilton, Ontario (Canada); 2003.

El-Attar AG, White RN, Gergely P. Shake table test of a 1/6 scale two-story lightly reinforced concrete building. NCEER-91-0017. Technical Report: National Center for Earthquake Engineering Research, SUNY at Buffalo, NY (US); 1991.

El-Attar AG, White RN, Gergely P. Behavior of gravity load designed reinforced concrete buildings subjected to earthquake. ACI Structural Journal 1997; 94(2): 133-45.

ElGawady M, Endeshaw M, McLean D, Sack R. Retrofitting of rectangular columns with deficient lap splices. J Compos Constr 2010; 14(1): 22-35.

Fajfar P. Capacity spectrum method based on inelastic demand spectra. Earthquake Engineering and Structural Dynamics 1999; 28(9): 979 - 993.

Fajfar P. A nonlinear analysis method for performance-based seismic design. Earthquake Spectra 2000; 16(3): 573-592.

Fam AZ, Rizkalla SH. Confinement model for axially loaded concrete confined by circular fiber-reinforced polymer tubes. ACI Structural Journal 2001; 98(4): 451-61.

FEMA-273. NEHRP Guidelines for the Seismic Rehabilitation of Buildings. Rep. No. FEMA-273, Federal Emergency Management Agency (FEMA): Washington, DC(US); 1997.

FEMA-356. Pre-standard and commentary for the seismic rehabilitation of buildings, prepared by ASCE. Rep. No. FEMA-356, Federal Emergency Management Agency (FEMA): Washington, DC(US); 2000.

FEMA-440. Improvement of nonlinear static seismic analysis procedures. Rep. No. FEMA-440, Federal Emergency Management Agency (FEMA): Washington, DC(US); 2005.

FEMA-547. Techniques for the seismic rehabilitation of existing buildings. Rep. No. FEMA-547. Federal Emergency Management Agency (FEMA): Washington, DC(US); 2006.

FEMA-P695. Quantification of building seismic performance factors Rep. No. FEMA-P695, Federal Emergency Management Agency (FEMA): Washington, DC(US); 2009.

Freeman SA, Nicoletti JP, Tyrell JV. Evaluations of existing buildings for seismic risk-A case study of Puget Sound Naval Shipyard, Bremerton, Washington. Proceedings of the 1st U.S. National Conference on Earthquake Engineering, 1975; 113 –122.

Galambos T, Mayes R. Lessons from dynamic tests of an eleven story building, Engng Struct. 1979; 1: 264-273.

Garcia R, Hajirasouliha I, Pilakoutas K. Seismic behavior of deficient RC frames strengthened with CFRP composites. Eng Struct 2010; 32(10): 3075-85.

Gencturk B, Elnashai AS. Development and application of an advanced capacity spectrum method. Engineering Structures 2008; 30(11): 3345-54.

Geneviève T, Amal B, Comparison of ALE and SPH methods for simulating mine blast effects on structures. Rep. No. DRDC-VALCAPRIER-TR-2010-326. Valcartier (Quebec, Canada): Defence Research and Development Canada (DRDC); 2010.

Gilson L, Van Roey J, Guéders C, Gallant J, Rabet L. A simple coupling of ALE domain with empirical blast load function in LS-DYNA. EPJ Web Conf. 2012, 26: 04018.

Güneyisi EM, Altay G. Seismic fragility assessment of effectiveness of viscous dampers in R/C buildings under scenario earthquakes. Structural Safety 2008; 30(5): 461-80.

Hakuto S, Park R, Tanaka H. Seismic load tests on interior and exterior beam-column joints with substandard reinforcing details. ACI Structural Journal 2000; 97(1): 11-25.

Haladuick, T. Numerical simulation of blast interaction with the human body: Primary blast brain injury prediction. Master thesis, Univ. of Waterloo, Waterloo, Ontario (Canada); 2014.

Hallquist J. LS-DYNA keyword user's manual, Livermore Software Technology Corporation, Livermore, CA (US); 2007.

Han Y, Liu H. Finite Element simulation of medium-range blast loading using LS-DYNA. Shock and Vibration 2015; 2015: 1-9.

Haroun MA, Mossalam AS, Feng Q, Elsanadedy HM. Experimental investigation of seismic repair and retrofit of bridge columns by composite jackets. Journal of Reinforced Plastics and Composites 2003; 22(14): 1243-1268.

Haroun MA, Elsanadedy HM. Fiber-reinforced plastic jackets for ductility enhancement of reinforced concrete bridge columns with poor lap-splice detailing. Journal of Bridge Engineering 2005; 10(6):749-57.

Harries K, Ricles J, Pissiki S, Sause R. Seismic retrofit of lap splices in nonductile columns using CFRP jackets. ACI Structural Journal 2006; 103(6): 226-236.

Hosoya H, Abe I, Kitagawa Y, Okada T. Shaking table tests of three-dimensional scale models of reinforced concrete high-rise frame structures with wall columns. ACI Structural Journal 1995; 92(6):765-80.

Hudson DE. A comparison of theoretical and experimental determination of building responses to earthquakes. In: Proc 2nd World conference on earthquake engineering, Japan; 1960. 1105-1119

ICRI. Guideline for the preparation of concrete surfaces for repair using hydro-demolition methods. Technical Guideline No. 310.3R-2014. Rosemont, IL (US); 2014.

Jeon JS, DesRoches R, Lowes LN, Brilakis I. Framework of aftershock fragility assessment–case studies: older California reinforced concrete building frames.Earthquake Engineering & Structural Dynamics 2015; 44(15): 2617-2636.

Ji X, Kato M, Wang T, Hitaka T, Nakashima M. Effect of gravity columns on mitigation of drift concentration for braced frames. J Constr Steel Res 2009; 65:2148-56.

Kim TW, Foutch DA, LaFAVE JM. A practical model for seismic analysis of reinforced concrete shear wall buildings. Journal of Earthquake Engineering 2005; 9(3): 393-417.

Kosko B. Neural networks and fuzzy systems: a dynamical systems approach to machine intelligence. Prentice-Hall, Inc., Englewood Cliffs, NJ (US); 1994.

Koutromanos I, Kyriakides M, Stavridis A, Billington S, Shing P. Shake-table tests of a 3-story masonry-infilled RC frame retrofitted with composite materials. J. Struct. Eng. 2013 SPECIAL ISSUE: NEES 2: Advances in Earthquake Engineering; 139: 1340-51.

Kunnath SK, Reinhorn AM, Park YJ. Analytical modeling of inelastic seismic response of R/C structures. Journal of Structural Engineering 1990;116(4):996-1017.

Kunnath SK, Reinhorn AM, Lobo RF. IDARC Version 3.0: A program for the inelastic damage analysis of reinforced concrete structures. NCEER-92-0022 Technical Report: National Center for Earthquake Engineering Research, SUNY at Buffalo, NY (US); 1992.

Kurama Y. Seismic behavior, performance, and retrofit of non-ductile reinforced concrete frame structures. Department of Civil and Environmental Engineering, Lehigh University; Bethlehem, PA (US); 1996.

Lan YM, Sotelino ED, Chen WF. State-of-the-art review of highway bridge columns retrofitted with FRP jackets. Department Report CE-STR-98-5; School of Civil Engineering, Purdue University; West Lafayette, IN (US); 1998.

Livermore Software Technology Corporation. LS-DYNA Keyword User's Manual Version 971/R7.0. Livermore, CA (US); 2013.

Luccioni BM, López DE, Danesi RF. Bond-slip in reinforced concrete elements. Journal of structural engineering 2005; 131(11):1690-8.

Lynn AC, Moehle JP, Mahin SA, Holmes WT. Seismic evaluation of existing reinforced concrete building columns. Earthquake Spectra 1996; 12(4):715-39.

Ma R. Seismic retrofit and repair of reinforced concrete columns using advanced composite materials. PhD thesis, University of Southern California, Los Angeles, CA (US); 1999.

Ma R, Xiao Y, Li KN. Full-scale testing of a parking structure column retrofitted with carbon fiber reinforced composites. J Construct Building Mater 2000; 14(2): 63-71.

Malvar LJ, Crawford JE, Wesevich JW, Simons D. A plasticity concrete material model for DYNA3D. International Journal of Impact Engineering 1997; 19(9-10): 847-73.

Malvar LJ, Crawford JE, Morrill KB. Use of composites to resist blast. Journal of Composites for Construction 2007,11(6): 601-610.

Malvar LJ, Crawford JE. Dynamic increase factors for steel reinforcing bars. 28th DDESB Seminar. Orlando (US); 1998.

Mander JB, Priestley MJN, Park R. Observed stress-strain behavior of confined concrete. ASCE J Struct Eng 1988; 114(8):1827-48.

Martinelli P, Filippou FC. Simulation of the shaking table test of a seven-story shear wall building. Earthquake Engineering & Structural Dynamics 2009; 38(5): 587-607.

MathWorks. MATLAB. The MathWorks, Inc., Natick, MA (US); 2014.

Miranda E. Estimation of inelastic deformation demands of SDOF systems. Journal of Structural Engineering (ASCE) 2001; 127(9):1005-1012.

Mirmiran A, Shahawy M, Samaan M, Echary HE, Mastrapa JC, Pico O. Effect of column parameters on FRP-confined concrete. Journal of Composites for Construction. 1998; 2(4): 175-85.

Morrill KB, Malvar LJ, Crawford JE. Retrofit design procedure for existing RC buildings to increase their resistance to terrorist bombs. Proceedings of the 9th International Symposium on Interaction of the Effects of Munitions with Structures (IEMS), Berlin, Germany. 3-7 May 1999.

Mutalib AA, Hao H. Development of PI diagrams for FRP strengthened RC columns. International Journal of Impact Engineering 2011; 38(5): 290-304.

Nam JW, Kim HJ, Kim SB, Kim JHJ, Byun KJ. Analytical study of finite element models for FRP retrofitted concrete structure under blast loads. International Journal of Damage Mechanics 2009; 18(5): 461-90.

NEES@UCLA. Network for earthquake engineering simulation at the University of California, Los Angeles. Los Angeles (CA): University of California, Los Angeles; 2015. < http://nees.ucla.edu/>

Neuberger A, Peles S, Rittel D. Scaling the response of circular plates subjected to large and close-range spherical explosions. Part I: Air-blast loading. International Journal of Impact Engineering 2007; 34(5): 859-73.

Ofengeim DK, Drikakis D. Simulation of blast wave propagation over a cylinder. Shock Waves 1997; 7(5): 305-317.

Olovsson L, Souli M. ALE and fluid-structure interaction capabilities in LS-DYNA. In: 6th International LS-DYNA users conference, Dearborn, MI (US); 2000.

Osteraas JD, Somers P, Carpenter J, Ferner H, Holmes W, Krawinkler H, Longstreth M, Ryan P, Wight J. Reinforced concrete buildings. Earthquake Spectra 1996; 12(S1): 49-74.

Osteraas JD. Murrah building bombing revisited: A qualitative assessment of blast damage and collapse patterns. Journal of Performance of Constructed Facilities 2006; 20(4): 330-335.

Park YJ, Ang AH-S. Mechanistic seismic damage model for reinforced concrete. ASCE, Journal of Structural Engineering 1985; 111(4): 722-739.

Park YJ, Ang AH-S, Wen YK. Damage-limiting a seismic design of buildings. Earthquake Spectra 1987; 3(1): 1-26.

Patel S. Rehabilitation of non-ductile reinforced concrete building columns against brittle shear failure using fiber reinforced polymer jackets. MSc thesis, Lehigh University, Bethlehem, PA (US); 2000.

Paulay T, Priestley MJN. Seismic design of reinforced concrete and masonry buildings. John Wiley & Sons, Inc, New York; 1992.

Pessiki SP., Conley CH, Gergely P, White RN. Seismic behavior of lightly-reinforced concrete column and beam-column joint details. NCEER-90-0014. Technical Report: National Center for Earthquake Engineering Research, SUNY at Buffalo, NY (US); 1990.

PileMedic. PileMedic^{TM} PLC150.10 Product Datasheet. PileMedic, LCC, Tucson, AZ (US); 2009. Available at: http://pilemedic.com/data/PileMedic%20PLC150.10.pdf [Online]

Prada C, Fink M. Eigenmodes of the time reversal operator: A solution to selective focusing in multiple-target media. Wave Motion 1994; 20(2): 151-163.

Priestley MJN. Displacement-based seismic assessment of reinforced concrete buildings. J Earthquake Eng 1997; 1(1):157-92.

Qu Z, Ye L, Wada A. Seismic damage mechanism control of RC ductile frames from a stiffness point of view. In: Proc 8th international conference on urban earthquake engineering, Tokyo, Japan; 2011.

Rigby, SE. Blast wave clearing effects on finite-sized targets subjected to explosive loads. PhD thesis, Univ. of Sheffield, Sheffield (UK); 2012.

Rodriguez-Nikl T. Experimental simulations of explosive loading on structural components. PhD Dissertation, University of California, San Diego, La Jolla, CA (US); 2006.

Rossetto T, Gehl P, Minas S, Galasso C, Duffour P, Douglas J, Cook O. FRACAS: A capacity spectrum approach for seismic fragility assessment including record-to-record variability. Engineering Structures. 2016; 125: 337-48.

Saatcioglu M, Razvi SR. Strength and ductility of confined concrete. J Struct Eng, ASCE 1992; 118(6):1590-607.

Sause R, Harries KA, Walkup SL, Pessiki S, Ricles JM. Flexural behavior of concrete columns retrofitted with carbon fiber reinforced polymer jackets. ACI Structural Journal 2004;101(5):708–16.

Schwer LE. A brief introduction to coupling load blast enhanced with multi-material ALE: The best of both words for air blast simulation. In: 9th European LS-DYNA Forum 2010, Bamberg (Germany), 1-10; 2010.

Schwer LE, Teng H, Souli M. LS-DYNA Air blast techniques: Comparisons with experiments for close-in charges. In: 10th European LS-DYNA Conference 2015, Wurzburg (Germany), 1-20; 2015.

Seible F, Priestley MJN, Innamorato D, Weeks J, Policelli F. Carbon fiber jacket retrofit test of circular shear bridge column. CRC-2. Advanced Composites Technology Transfer Consortium Rep. No. ACTT-94/02, University of California, San Diego, La Jolla, CA (US); 1994.

Seible F; Hegemier GA; Priestly MJN; Ho F; Inmamorato D. Rectangular carbon jacket retrofit of flexural column with 5% continuous reinforcement. Advanced Composites Technology Transfer Consortium Report No. ACTT-95/03, University of California, San Diego, La Jolla, CA (US); 1995a.

Seible F, Hegemier GA, Priestley MJN, Innamorato D, Ho F. Carbon fiber jacket retrofit test of circular flexural columns with lap spliced reinforcement. Advanced Composites Technology Transfer Consortium Report No. ACTT-95/04, University of California, San Diego, La Jolla, CA (US); 1995b.

Seible F, Priestley MJN, Innamorato D. Earthquake retrofit of bridge columns with continuous carbon fiber jackets, Volume II, Design Guidelines. Rep. No. ACTT-95/08. San Diego (CA): University of California, San Diego, La Jolla, CA (US); 1995c.

Seible F, Priestley MJN, Hegemier GA, Innamorato D. Seismic retrofit of RC columns with continuous carbon fiber jackets. Journal of Composites for Construction 1997; 1(2): 52-62.

Seifi A, Hosseini A, Marefat MS, Zareian MS. Improving seismic performance of old-type RC frames using NSM technique and FRP jackets. Engineering Structures 2017; 147: 705-23.

Sezen H, Elwood KJ, Whittaker AS, Mosalam KM, Wallace JW, Stanton JF, Structural engineering reconnaissance of the August 17, 1999 earthquake: Kocaeli (Izmit), Turkey Earthquake. PEER 2000/09 Technical Report, Pacific Earthquake Engineering Research Center, University of California, Berkeley, CA (US); 2000.

Sezen H. Seismic behavior and modeling of reinforced concrete building columns. Ph.D. thesis, Department of Civil and Environmental Engineering, University of California, Berkeley, CA (US); 2002.

Shi Y, Hao H, Li ZX. Numerical simulation of blast wave interaction with structure columns. Shock Waves 2007, 17(1-2): 113-133.

Shi Y, Hao H, Li ZX. Numerical derivation of pressure–impulse diagrams for prediction of RC column damage to blast loads. International Journal of Impact Engineering 2008, 35(11): 1213-1227.

Shi Y, Li ZX, Hao H. Bond slip modelling and its effect on numerical analysis of blast-induced responses of RC columns. Structural Engineering and Mechanics 2009, 32(2): 251-267.

Simpson PK. Artificial neural system – foundation, paradigm, application and implementations. Pergamon Press, New York, NY (US): 1990.

Slavik T. Coupling of empirical explosive blast loads to ALE air domains in LS-DYNA. In: 7th European LS-DYNA Users Conf. Salzburg (Austria). 2009. 1-10.

Spoelstra MR, Monti G. FRP-confined concrete model. Journal of Composites for Construction. 1999; 3(3):143-50.

Stewart LK. Testing and analysis of structural steel columns subjected to blast loads. PhD thesis. University of California, San Diego, La Jolla, CA (US); 2010.

Stewart LK, Morrill KB. Residual capacity prediction of blast-loaded steel columns using physics-based fast running models. International Journal of Safety and Security Engineering. 2015; 5(4): 289-303.

Tabatabaei ZS, Volz JS. A comparison between three different blast methods in LS-DYNA: LBE, MM-ALE, Coupling of LBE and MM-ALE. In: 12th International LS-DYNA users conference, Livermore, CA (US); 2012.

Tai CH, Teng JT, Lo SW, Liu CW. A three-dimensional numerical investigation into the interaction of blast waves with bomb shelters. JSME International Journal Series B Fluids and Thermal Engineering 2005, 48(4): 820-829.

Teng M-H, Sotelino ED, Chen W-F. Performance evaluation of reinforced concrete bridge columns wrapped with fiber reinforced polymers. ASCE J Compos Constr 2003; 7(2): 83-92.

Trajkovski J, Kunc R, Perenda J, Prebil I. Minimum mesh design criteria for blast wave development and structural response-MMALE method. Latin American Journal of Solids and Structures 2014, 11(11): 1999-2017.

UFC 3-340-02, Structures to Resist the Effects of Accidental Explosions. Dept. of the Army and Defense Special Weapons Agency, Washington DC (US); 2008.

US Army. Fundamentals of protective design for conventional weapons. Army Technical Manual TM 5-855-1; 1985.

Vidic T, Fajfar P, Fischinger M. Consistent inelastic design spectra: strength and displacement, Earthquake Engng. Struct. Dyn. 1994; 23(5): 507-521.

Wang LM, Wu YF. Effect of corner radius on the performance of CFRP-confined square concrete columns: Test. Eng Struct 2008; 30(2):493-505.

Weatherby JH. Investigation of bond slip between concrete and steel reinforcement under dynamic loading conditions. PhD thesis, Louisiana State University, Baton Rouge, Los Angeles, CA (US); 2003.

Williams GD. Analysis and response mechanisms of blast-loaded reinforced concrete columns. PhD thesis, Univ. of Texas, Austin, TX (US); 2009.

Williams MS, Sexsmith RG. Seismic damage indices for concrete structures: a state-of-the-art review. Earthquake spectra 1995, 11(2): 319-349.

Wojciechowski J, Balcerzak M, Bojanowski C, Kwasniewski L, Gizejowski M. Example Validation of Numerical Modeling of Blast Loading. In Applied Mechanics and Materials 2011, 82: 410-415.

Woodson SC, Baylot JT. Structural collapse: quarter-scale model experiments. Technical Report SL-99-8, US Army Engineer Research and Development Center, Vicksburg, Mississippi (US); 1999.

Wright TR. Full-scale seismic testing of a reinforced concrete moment frame using mobile shakers. PhD thesis, Georgia Institute of Technology, Atlanta, GA (US); 2015.

Wu YF, Wei YY. Effect of cross-sectional aspect ratio on the strength of CFRP-confined rectangular concrete columns. Engineering Structures 2010; 32(1): 32-45.

Wu Y, Crawford JE. Numerical modeling of concrete using a partially associative plasticity model. Journal of Engineering Mechanics 2015; 141(12): 04015051

Xiao Y, Ma R. Seismic retrofit of RC circular columns using prefabricated composite jacketing. Journal of Structural Engineering 1997; 123(10): 1356-64.

Xiao Y, Wu H, and Martin GR. Prefabricated composite jacketing of RC columns for enhanced shear strength. J. Struct. Eng. 1999; 125(3): 255–64.

Xiao Y, Wu H. Compressive behavior of concrete confined by carbon fiber composite jackets. Journal of Material for Civil Engineering 2000; 12(2): 139-46

Yan Z, Pantelides CP, Reaveley LD. Fiber reinforced polymer jacketed and shape modified compression members: I-experimental behavior. ACI Structural Journal 2006a; 103(6): 885-93.

Yan Z, Pantelides CP. Fiber reinforced polymer jacketed and shape modified compression members: II-model. ACI Structural Journal 2006b; 103(6), 894-903.

Yan Z, Pantelides CP. Concrete column shape modification with FRP shells and expansive cement concrete. Constr Build Mater 2011; 25(1):396–405.

Youssf O, ElGawady MA, Mills JE, Ma X. Finite element modelling and dilation of FRP-confined concrete columns. Engineering Structures 2014; 79: 70-85.

Yu E, Skolnik D, Whang D, Wallace JW. Forced vibration testing of a four story RC building utilizing the nees@UCLA mobile field laboratory. Earthquake Spectra 2008; 24: 969-95.